IEKP-KA/2005-24

Entwicklung der raumfahrtqualifizierten Datenakquisition für den Übergangsstrahlungsdetektor des AMS-02 Experiments auf der Internationalen Raumstation

Florian P.L. Hauler

Zur Erlangung des akademischen Grades eines
DOKTORS DER NATURWISSENSCHAFTEN
von der Fakultät für Physik der Universität (TH)
Karlsruhe

genehmigte

DISSERTATION

von

Dipl.-Phys. Florian Hauler
aus Karlsruhe

Tag der mündlichen Prüfung: 16.12.2005
Referent: Prof. Dr. Willem de Boer, Institut für Experimentelle Kernphysik
Korreferent: Prof. Dr. Thomas Müller, Institut für Experimentelle Kernphysik

Universität Karlsruhe (TH)
Institut für Experimentelle Kernphysik (IEKP)

WS 2005/2006

Dissertation

Development of the Space Qualified Data Acquisition for the Transition Radiation Detector of the AMS-02 Experiment on the International Space Station

Florian Philipp Leopold Hauler

16.12.2005

Prof. Dr. Wim de Boer

Prof. Dr. Thomas Müller

to my family and my friends

I hope this thesis gives an answer to their question:
What is a physicist actually doing in his job?

Figure 0.1: Experiment logo of AMS-02.

Contents

Chapter 1

Introduction

Figure 1.1: Drawing of the AMS-02 detector mounted on the International Space Station. Source: Lockheed Martin.

The Earth continuously experiences particle impacts of highest energies, whose origin lies in outer space. This phenomenon was first discovered in 1912 by the Austrian physicist Viktor Franz Hess. Before that time people thought, that the natural radioactivity measured on the ground could be traced back to radioactive nuclei located in the Earth's crust. To proof this assumption, Prof. Hess boarded a hot air balloon equipped with several electrometers to measure the intensity of ionizing radiation in heights up to 5000 m. His results were surprising. He found while ascending, that the intensity of ionizing radiation increases and concluded that its origin lies in outer space. For his research he was awarded the Nobel Prize in 1936.
Many other researchers followed his example and investigated primary cosmic radiation by measuring its secondary radiation which is created when high energetic cosmic particles interact with atomic nuclei in the Earth's atmosphere. Figure 1.2 shows the cosmic-ray energy spectrum as it is known today. This spectrum can be described by an inverse power law in energy with differential fluxes:

$\Phi \propto E^{-2.7}$ up to the region of the knee at 10^{15} eV,
$\Phi \propto E^{-3.0}$ from the knee to the ankle at 10^{19} eV,

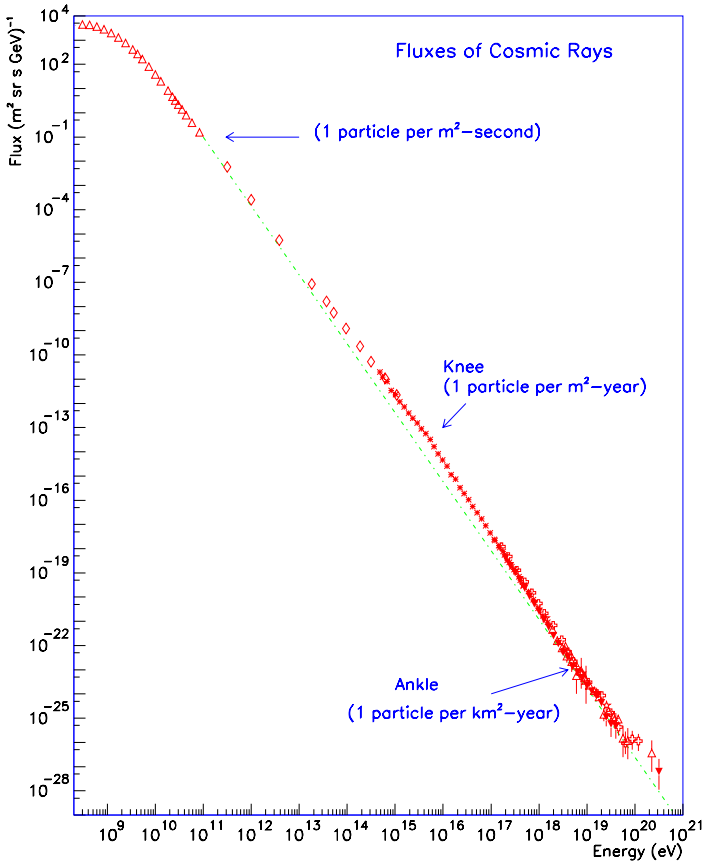

Figure 1.2: Cosmic-ray energy spectrum. From [She01].

$\Phi \propto E^{-2.8}$ above the ankle, although at these energies statistics are low.

In order to measure the spectrum of cosmic radiation, two different methods are used today. The first method is the indirect measurement, where large ground based experiments are used to measure the secondary particle flux. From the amount of secondary radiation it is possible to deduce the energy of the primary particle. Since at very high particle energies the particle flux decreases rapidly, large sensitive detector areas or a long measurement time is required. As an example KASCADE[1]-grande at the Forschungszentrum Karlsruhe or the Pierre-Auger Observatory in the province Mendoza of Argentina are experiments of this indirect measurement.
The second method is the direct measurement of cosmic particles. Up to energies of about 10^{15} eV particle detectors on balloons which fly up to 40 km height or satellites can be used to perform a direct measurement of primary cosmic radiation. As an example BESS[2], HEAT[3] CAPRICE[4], IMAX[5] and ISOMAX[6] may be mentioned. Unfortunately balloon experiments

[1]KASCADE, KArlsruhe Shower Core and Array DEtector
[2]BESS, Balloon-borne Experiment with a Superconducting Spectrometer
[3]HEAT, High-Energy, Antimatter Telescope
[4]CAPRICE, The Cosmic Anti Particle Ring Imaging Cherenkov Experiment
[5]IMAX, Isotope Matter Antimatter Experiment
[6]ISOMAX, Isotope Magnetic Experiment

have a very limited measurement time, are restricted in their weight and have a small acceptance of 0.3 $m^2 \cdot sr$ (BESS).
New opportunities arise with the development of AMS-02 - a particle spectrometer, which will be mounted on the International Space Station (ISS). There, AMS-02 will be able to measure the primary charged cosmic particle flux with unprecedented statistics up to the multi-TeV region for at least three years, limited only by the amount of superfluid Helium needed for its superconducting magnet. AMS-02 features a large acceptance of 0.5 $m^2 \cdot sr$. Its power consumption limit of 2 kW and its weight limit of about 6.7 t imposes a big technical challenge. The main physics goals are the search for antimatter, the measurement of the $^{10}Be/^{9}Be$ ratio and the indirect search for dark matter. A good start already has been made with its precursor experiment AMS-01 which performed measurements during its 10 days Space Shuttle flight STS-91, where the feasibility of launching a particle physics spectrometer with delicate silicon sensors was proven. Despite the fact that this was an engineering flight, already at this time precious scientific data could be acquired [A+02]. No antinuclei heavier than protons could be detected and no hints for the nature of dark matter could be found. Unlike AMS-01, AMS-02 will be equipped with a transition radiation detector, that allows to distinguish light and heavy particles of equal charge and energy, such as p and e^+ or $\bar{p}$ and e^-, by means of their different Lorentz factors $\gamma = E/mc^2$. In the energy range from 5 to 300 GeV a proton rejection factor between 10^2 and 10^3 at 90% positron detection efficiency can be obtained. Together with the electromagnetic calorimeter a total rejection factor of 10^5 to 10^6 can be reached.
AMS-02 is scheduled to be transported into space three years after the successful resumption of shuttle flights which were suspended after the Columbia disaster on February 1st, 2003. In the meantime a smaller experiment, PAMELA[1] is scheduled to be launched onboard a Russian satellite by the beginning of 2006 with a similar physics program, although equipped with a smaller acceptance of 0.002 $m^2 \cdot sr$.

This thesis describes the activities that were performed to develop, produce and test the space-qualified electronics for the transition radiation detector of AMS-02 on the ISS. The first part of Chapter 2 describes the AMS-02 detector: the superconducting magnet, the tracker and its subsystems, the transition tadiation detector, the ring imaging cherenkov counter, the time-of-flight system, the electromagnetic calorimeter and the star tracker. The second part gives a summary of the AMS-02 physics scope. It mentions the search for antimatter, as well as the measurement of the Be^{10}/Be^{9} ratio. A detailed section is dedicated to the indirect search for dark matter, since this is one of the major research fields of this institute. Chapter 3 offers a brief overview about the environment AMS-02 has to face during the Space Shuttle lift into orbit and onboard the ISS. It touches technical details of the shuttle and the space station, as well as the hostile environment in terms of radiation, material effects and thermal influence.
In Chapter 4 the physics background is described which is needed to design and to operate a transition radiation detector. It starts with a description of the nature of transition radiation, continues with the detection principles of radiation using proportional counters and closes with the explanation of an application example, the proton rejection analysis.
Chapter 5, which is the main chapter of this thesis, starts with the presentation of the global AMS-02 DAQ and slow control system, and then focuses in detail on the TRD electronics boards. It continues with the description of the electronics development/production steps and the space qualification procedures and presents the test benches that were designed to perform the functional tests after production. In the end of this chapter, the DAQ and slow control

[1] PAMELA, a Payload for Antimatter Matter Exploration and Light-nuclei Astrophysics

commanding is described on an introductory basis.
Finally Chapter 6 shows the outcome of the two electronics verification testbeams that were conducted in October 2002 and in October 2003, presents the cosmics stand which was set up in the beginning of 2005 and describes the DSP programming effort that was undertaken to develop the data reduction algorithm and the pedestal calibration.
Chapter 7 gives a summary and outlook.

Chapter 2

AMS-02 - a Particle Detector Designed for Operation on the ISS

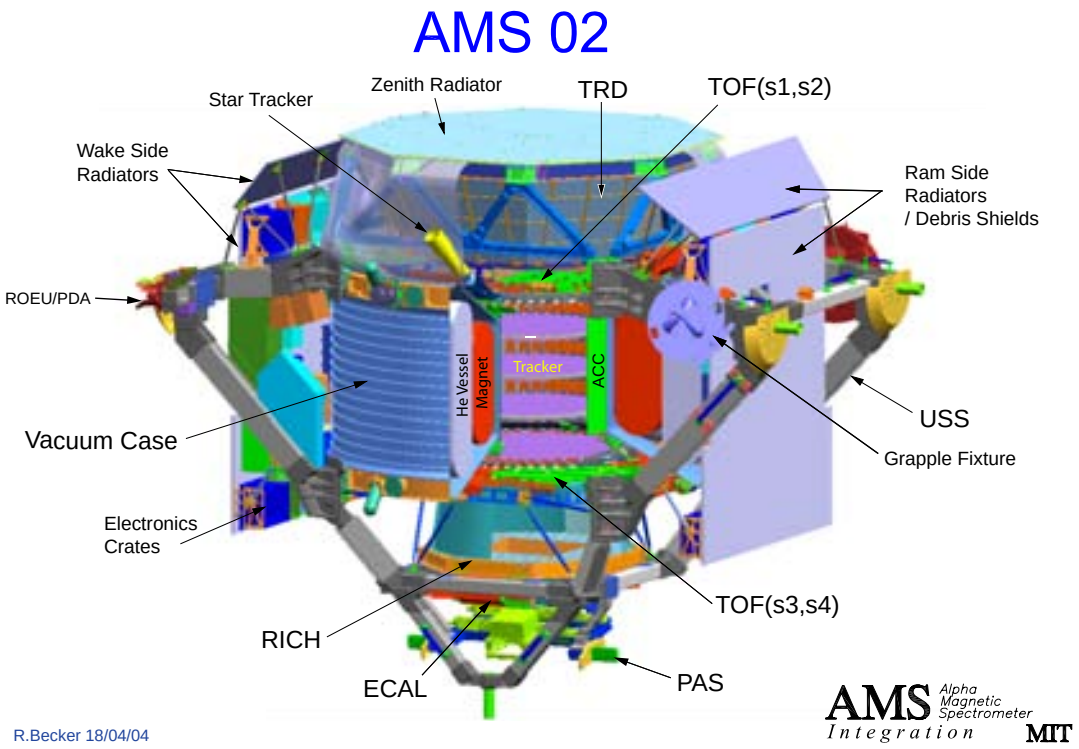

Figure 2.1: Cross section of AMS-02. Additionally to the detectors described in this chapter, this figure depicts the Unique Support Structure (USS), which connects the detector to the Space Shuttle and to the ISS. Furthermore, thermal radiators, debris shields and electronics crate racks are shown.

The Alpha Magnetic Spectrometer-02 (AMS-02) is an experiment which will be mounted on the International Space Station (ISS) to measure primary cosmic ray spectra in space for three years. It will measure cosmic ray spectra of individual elements up to $Z \leq 26$ and up to the TeV region and high energetic γ-rays up to hundreds of GeV. The AMS-02 spectrometer consists of a *silicon tracker*, a *Time-of-Flight* (TOF) detector, a *Ring Imaging Cherenkov Counter* (RICH), an *Electromagnetic Calorimeter* (ECAL), an *Amica Star Tracker* (AST), *AntiCoincidence Counters* (ACC) and a *Transition Radiation Detector* (TRD). A cross section of AMS-02 is shown in Figure 2.1. AMS-02 provides excellent particle identification capabilities.

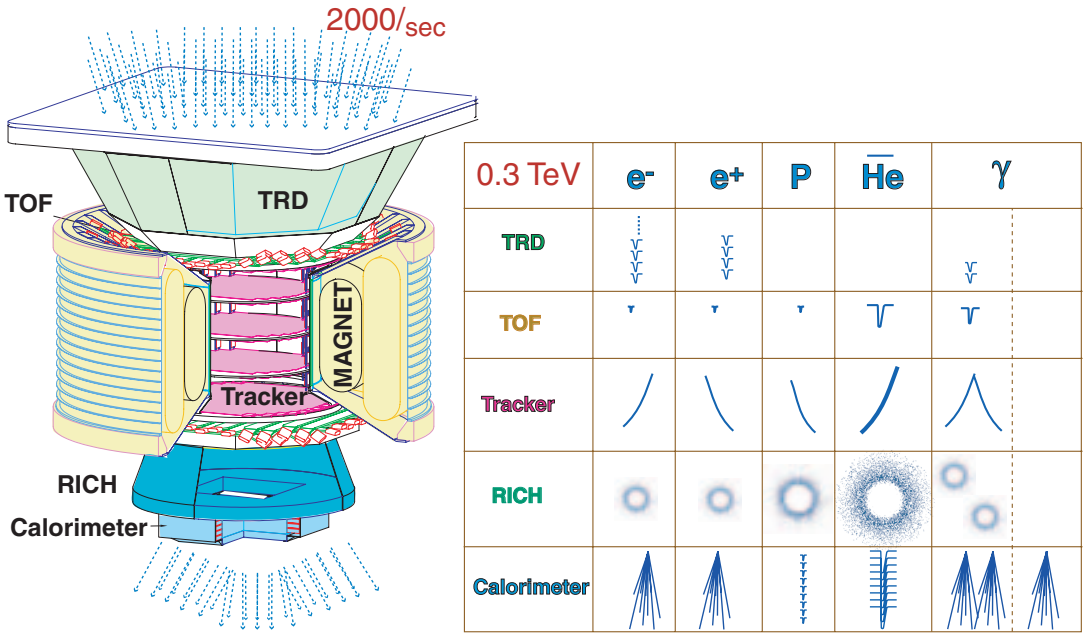

Figure 2.2: AMS-02 and the expected signatures in the various subdetectors.

It measures the charge of the traversing particle independently in tracker, RICH and TOF subdetectors. The velocity is measured by the TOF, TRD and RICH subdetecors.
The tracker measures the particle's momentum in a magnetic field, which is provided by a superconducting magnet. Its accuracy is 10 μm in the bending direction and 30 μm in the non-bending one, allowing the determination of the particle's momentum up to 2 TV/c rigidity. Additionally, the tracker is equipped with an IR laser alignment system which is used to continuously monitor the X- and Y- position of the tracker layers with respect to each other and detect displacements caused by the start vibrations of the shuttle or by thermal variations. The superconducting magnet is cooled by 2500 l of superfluid Helium (Helium-II). It consists of a pair of large dipole coils together with two series of six smaller racetrack coils distributed between them. The racetrack coils increase the magnitude of the dipole field and reduce the stray field outside the magnet in order to prevent a torque on the ISS resulting from the interaction with the magnetic field of the Earth. The magnet will provide a central dipole field of 0.86 T.
The TOF subdetector is composed of four layers of plastic scintillator paddles, of which two are located above and two below the magnet. It measures the time a particle needs to fly through the four layers with an accuracy of 120 ps. Additionally, this subdetector provides coordinate information and energy loss. With this information the velocity, the direction and the relative charge (Ze/e) of the particles that pass through the detector can be determined.
The RICH subdetector is mounted below the lower two TOF planes and consists of a NaF and silica aerogel radiator plane at the top and a photodetector plane at the bottom, separated by 45 cm drift space. A hole with the size of the ECAL, located in the middle of the photodetector plane, assures that no interaction with the RICH occurs before the particle crashes into the ECAL. A conical mirror surrounds the drift volume to increase the acceptance. The RICH measures the velocity of a singly charged particle within an accuracy better than per mil and

provides particle flight direction information. Another main aim of the RICH is to separate isotopes up to an atomic number of Z≃26.
The ECAL subdetector is placed at the bottom of AMS-02. It is a three-dimensional sampling calorimeter composed of 1 mm scintillating fibers sandwiched between grooved lead plates. The radiation length of the ECAL is 17 X_0. By means of shower shape analysis light and heavy particles such as e^+ and p or $\overline{p}$ and e^- can be distinguished, providing a way to suppress the proton background of a positron measurement up to a level of 10^3 - 10^4 up to 500 GeV. This is of special importance when the particle energies are too high for the tracker to distinguish between light and heavy particles of the same charge any more, but still the electromagnetic shower form inside the ECAL is different.
The TRD is designed to provide non-destructive particle identification additionally to the ECAL. The capability for e^+/p separation will be better than 10^2 referring to an electron efficiency of 90% up to particle energies of 250 GeV. It consists of 20 layers of 6 mm diameter straw tubes separated by 20 mm radiator material. Therefore the TRD can be used to obtain track information of the traversing particle outside the central magnetic field. The straw tubes, filled with an 80/20 gas mixture of Xe/CO_2, are used as proportional counters.
The ACC subsystem surrounds the tracker. This scintillation based anticounter system vetos against events that show signals of particles which hit the barrel of anticounters around the tracker. In addition, the system will detect backscattering off the ECAL. Therefore only particles are selected that pass straight through the detector.
The star tracker is a pair of optical telescopes with CCD-cameras to measure the pointing direction in space AMS-02 looks at. [Lam03]
The signatures of different particles at 0.3 TeV in the various subdetectors are shown in Figure 2.2.

This chapter describes the AMS-02 detectors in detail and gives a short overview about the physics goals of AMS-02. Most of the figures in this chapter are taken from [AMS05], otherwise the source is indicated.

2.1 The Superconducting Magnet

The information given in in this section is a summary of the references [B^+04, B^+02, B^+00, AMS05].

2.1.1 Magnet Design

The superconducting magnet provides the necessary magnetic field for the momentum measurement in the tracker. The magnetic field configuration as shown in Figure 2.3 was chosen to feature a negligible dipole momentum to avoid any interaction with the Earth's magnetic field causing an undesirable torque on the ISS. The coil system comprises a set of 14 superconducting coils around the inner cylinder of the vacuum tank. It was designed to produce the maximum field in the appropriate direction inside its bore tube, while minimizing the stray field outside the magnet. The magnetic dipole field, perpendicular to the experiment axis, is created by the pair of largest coils, placed opposite to each other. The remaining twelve smaller racetrack coils[1] control the stray field and also increase the magnitude of the overall magnetic dipole field. The central magnetic flux density is B = 0.86 T with the bending power of $BL^2 = 0.862$ Tm^2.

[1] flux return coils

The magnet is cooled by superfluid Helium (Helium-II). The Helium-II is stored in a Helium vessel next to the magnet coils, with both magnet and vessel enclosed in a vacuum case. The coil placement within the vacuum case and the Helium vessel is shown in Figure 2.4. The AMS-02 magnet parameters are given in Table 2.1. All magnets are wound from the same

Central Magnetic Field $B_x(0,0)$	0.860 T
Dipole Bending Power	0.862 Tm^2
Maximum Stray Magnetic Field at R = 2.3 m	15.2 mT
Maximum Stray Magnetic Field at Y = 2.3 m	7.6 mT
Maximum Stray Magnetic Field at R = 3.0 m	3.9 mT
Peak Magnetic Field on the Dipole Coils	6.59 T
Peak Magnetic Field on the Flux Return Coils	5.91 T
Maximum Torque on Geomagnetic Field	0.272 Nm
Nominal Operating Magnet Current	459.5 A
Stored Energy	5.15 MJ
Nominal Magnet Inductance	48 H

Table 2.1: AMS-02 magnet parameters.

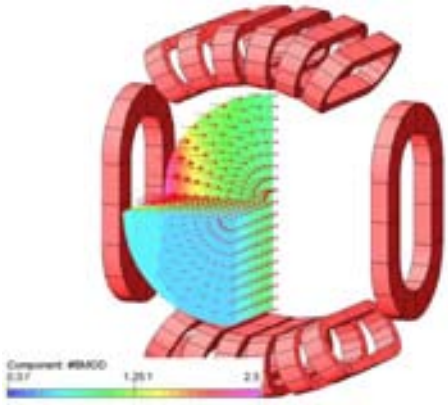

Figure 2.3: Field configuration between the two main magnet coils.

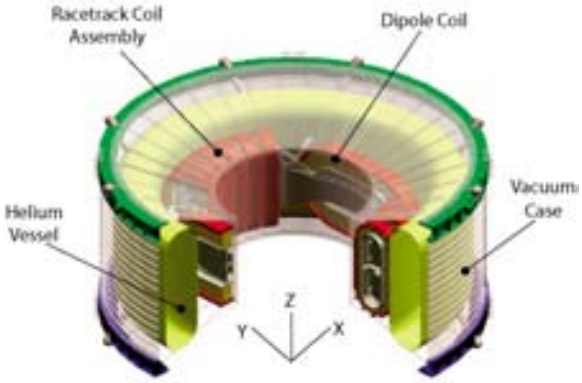

Figure 2.4: Layout of the AMS-02 superconducting magnet including Helium vessel and vacuum case.

conductor. It consists of a NbTi/Cu superconducting wire embedded in a high purity aluminum stabilizer. Aluminum has been selected because of the strict weight requirements. The superconducting strand was produced by Outokumpu Poricopper Oy, Finland. It is a multifilamentary wire made of 552 high homogeneity 22.4 μm NbTi filaments. Since pure NbTi has a rather low thermal conductivity its superconductivity tends to be unstable. To overcome this problem intimate contact with a material of high thermal conductivity at the operating temperature has to be made. Therefore the filaments are embedded in a copper matrix which is encased in high purity aluminum. The Cu matrix is needed for manufacturing reasons but since the aluminum is extremely conductive and much less dense, it provides maximum thermal stability for minimum weight. See Figure 2.5 for a cross section of an AMS-02 conductor with dimensions of 2.00 mm $\times$ 1.55 mm and a diameter of the round copper strand of 0.76 mm.
NbTi is a Type-II superconducter with a critical temperature of $T_c = 10$ K. Unlike in Type-I

superconductors the change from superconducting state to normalconducting state does not happen abruptly, but passes gradually when reaching its critical temperature T_c. For all the coils a total of 55 km of superconducting strand is required. Each of the two large dipole coils has 3360 turns and the smaller flux return coils have 1457 turns each.
As in all superconducting magnets the undesired hazard of a quench, which represents a transition from the superconducting state to the normalconducting state, has to be considered. Possible unrecoverable damage can be:

- In the region where the quench began, heating might be so quick that the conductor is likely to melt. In a system of coils the breakdown of the magnetic field of one coil can lead to increased current flow and field in the other coils by inductive coupling causing excessive stresses within the windings and between the coils.
- The excessively produced vapor has to be vented before a dangerous pressure builds up.

All these hazards were considered in the design of the magnet. The aluminum stabilized conductor is sufficiently thermal conductive in order to quickly spread the heat generated during a quench throughout the coil, preventing the peak temperatures from becoming dangerous. All 14 coils are connected in series, thus carrying the same current at all times. The coils are permanently monitored by an electronic protection system. If the first sign of a quench in one coil is detected, heaters are powered to quench all 14 coils simultaneously thus distributing the stored energy between all the coils.

2.1.2 Mechanical System

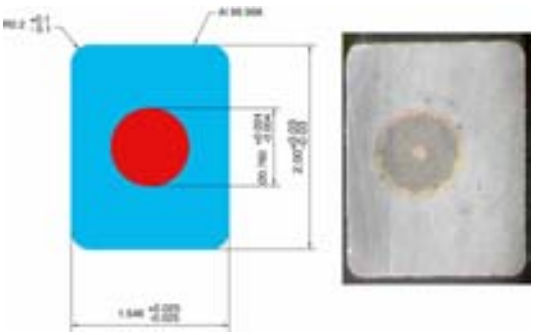

Figure 2.5: Cross section of a magnet conductor.

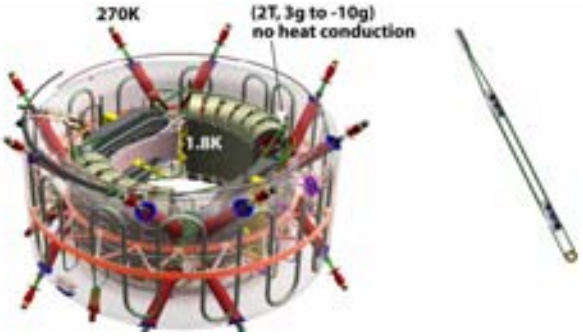

Figure 2.6: Mechanics of strap attachment.

The magnet has a cold mass of more than 2000 kg which has to be supported from the experiment structure, in particular the vacuum tank which has a temperature of around $T \approx 270 \pm 40$ K. Therefore the design of the support straps is crucial, since they have to carry the load without conducting much heat across the large temperature gradient. Still this inertial load is small compared to the magnetic loads during magnet operation: for example, the dipole coils feel a net attraction to each other of around 250 tons. However, the magnetic loads are reacted within the structure of the coil set and none are transmitted to the vacuum tank or parts of the AMS-02 system. Significant inertial loads can occur only during launch, reentry or landing of the Space Shuttle, once on orbit inertial loads disappear completely. Since

the magnet is only charged during operation on the ISS, magnetic and inertial loads are never superimposed. During normal operation, when inertial loads are very small or non-existent the function of the straps is only to position the magnet correctly within the vacuum tank.
During launch and landing the straps have to resist large forces and also require high stiffness to prevent low frequency resonance which could lead to mechanical damage. This leads to large cross sections for the straps and therefore to high levels of heat conduction, which would reduce the endurance of the superfluid Helium system and thus shorten the lifetime of the experiment. To minimize the heat conduction, the straps need to be as thin as possible, but this yields poor strength, low stiffness and a low resonant frequency.
In the design of the straps all requirements were taken into account. Each strap consists of a pair of composite bands connected in parallel. One band is thin, with low stiffness and strength, permanently connected between the cold mass and the vacuum tank. The other band is much thicker and stronger, but was designed with a passive disconnect feature. It only forms a thermal path during launch and landing. All the other times, when it is not needed, the disconnect is opened by differential thermal contraction between the bands and the removal of the high inertial load. In this way the thermal conduction from the vacuum tank to the cold mass of the magnet is dramatically reduced. During operation on the ground or in space the high-stiffness band is not engaged, only the low-stiffness band keeps the magnet in place with a reduced thermal conduction of 3 mW per support. During launch, for only a few minutes, the high-stiffness band engages causing a much higher thermal conduction.

Figure 2.7: Picture of the AMS-02 coils: left and right are the dipole coils, in between are the racetrack coils for the flux return.

All in all a total of 16 straps support the magnet as can be seen in Figure 2.6. The magnet support straps have to pass through the volume of the Helium container to connect the magnet coils with the outer cylinder of the vacuum tank. To avoid contact between the liquid Helium and the straps resulting in a high heat load, the 16 support straps are placed into tubes traversing the Helium container. A photo of the real magnet coils can be seen in Figure 2.7

2.1.3 Magnet Cooling and Cryogenics

So far there have been four large liquid Helium payloads in space developing and demonstrating the technology to handle liquid Helium in space. These major missions are the Infrared Astronomical Satellite (IRAS), the Cosmic Background Explorer (COBE) and the Superfluid Helium On-Orbit Transfer (SHOOT), launched by NASA and the Infrared Space Observatory (ISO) launched by the European Space Agency. IRAS, COBE and ISO were all infrared telescopes, SHOOT was an experiment to demonstrate the technology of superfluid Helium transfer under zero-gravity conditions.
The cryogenic system for the AMS-02 magnet uses the techniques developed for all the previous space-born systems and combines well-established technology for cooling terrestrial superconducting magnets. The design target of the cryogenic system is to keep the magnet coils superconducting under all operating conditions, while maximizing the lifetime of the experiment.

Helium-II - a Superfluid Cooling Liquid for AMS-02 magnet

Helium, the second most abundant element in the known universe after hydrogen, composed of two neutrons and two protons, offers a low boiling point of 4.2 K suitable for cryogenic cooling of a superconducting magnet. However, when Helium is cooled at ambient pressure below the lambda-point of T = 2.17 K it exhibits characteristics of two distinct fluids. Firstly, a normal viscous liquid and the other one being a superfluid liquid without internal friction. This new phase, called Helium-II - while the other one is called Helium-I, offers some nice features suitable for a cryogenic system of a superconducting magnet in space. Firstly, the specific latent heat and density of Helium-II are both higher than in He-I. Since the amount of cryogenic Helium that can be carried is limited, this offers an endurance benefit: the higher density allows to effectively fit more Helium into the vessel than it would be possible with He-I. The higher specific latent heat is beneficial for the cooling capability. Secondly in zero gravity there are no convection currents, causing thermal stratification in He-I. It would not be possible to tell whether the complete system is cold, or only in the part of it, where the temperature has been measured. In contrast, the very high thermal conductivity of Helium-II ensures that the temperature remains isothermal throughout the whole system.
Helium-II is created from He-I by removing the Helium vapor above a container of liquid Helium via pumping. By doing this the boiling point of Helium-II can even be reduced further to 1.8 K, by lowering the environmental pressure down to p = 16 mbar. On Earth this will be achieved with large vacuum pumps. In orbit, however, space itself will be used as a pump and the low temperature can be achieved by venting the Helium container to space.
In order to protect AMS-02 from the effect of sudden Helium heating and pressurization, burst discs are used to prevent excessive pressure.

Phase Separation Using the Thermo-Mechanical Effect

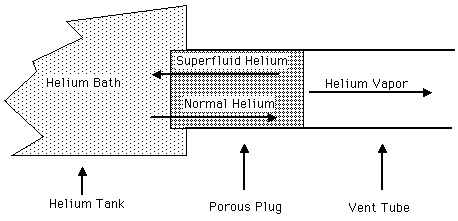

Figure 2.8: Principle of the passive phase separator. From [Nat05a].

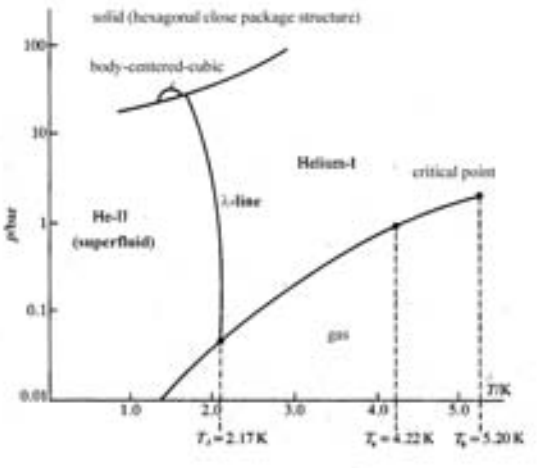

Figure 2.9: Phase diagram of Helium. From [Atk90].

Handling liquid Helium in space requires the use of special techniques. The liquid Helium is stored in a toroidal vessel of 2500 l. But how to separate the liquid Helium-II phase from the

gaseous Helium phase under zero-gravity? On Earth the easiest thing to do would be to place a vapor vent on the highest point of the vessel, using gravity to ensure that liquid remains on the bottom and vapor is released from the top. Under zero-gravity there is no top or bottom. The solution to this problem is a passive phase separator.
Figure 2.8 illustrates the principle of phase separation used in the SHOOT experiment. The vent plug has pores that are large enough that both, the normal and the superfluid Helium can flow through. Once the Helium has passed the plug and reaches the outside surface in the vent tube where it is exposed to the vacuum of space, it evaporates. With the evaporation process the Helium cools the porous plug. The phase separator takes advantage of the thermo-mechanical-effect: superfluid Helium flows from cold to warm. Now the Helium inside the Helium bath looks to the Helium at the outer surface of the plug as a hot spot. As a consequence it starts to flow back to the Helium bath. Normal Helium continues to flow through the porous plug to the outer surface, evaporates, cools and flows back as superfluid Helium keeping the bath at the desired temperature.
In AMS-02 the phase separator, developed by Linde in Germany, is welded into the top of the vessel. It consists of a porous plug of sintered stainless steel in a steel housing. The Helium bath has a temperature of T = 1.8 K at a pressure of P = 16 mbar. As can be seen from the phase diagram in Figure 2.9 at this pressure there are only the Helium-II phase and the He-gas phase present, making it impossible to benefit from the He-I phase. During flight, a slight temperature difference of $\Delta T = 30$ mK is maintained between the two faces of the plug - the warmer side directed to the Helium bath, the colder side to deep space, keeping the Helium-II phase inside the vessel. Helium gas which evaporates inside the vessel and cools the liquid can escape through the porous plug. The boiled off vapor is constrained to flow through pipes connected to a series of four concentric shields surrounding the magnet and helium vessel. By cooling these shields with the vapor, the heat leak into the cryogenic system is reduced to a minimum. Two of the shields are rigid, made of aluminum honeycomb material with fiberglass skin, minimized in thickness yet being able to withstand the loads during launch and landing. The other two shields are made from thin sheets of soft aluminum.

The Cooling System

Stirling cryocoolers
The rate of consumption of superfluid Helium will be reduced by four Stirling cycle coolers connected to the outer vapor shield. They are expected to remove a total of about 12 W at a temperature of 58 K. Each cooler consumes 100 W, which has to be removed together with the heat from the outer shield to a quarter panel zenith radiator on the top of the experiment by means of a double redundant capillary pumped loop.

Mass gauging
How to measure the liquid content in the Helium vessel? Under zero-gravity a normal Helium probe would be useless. Instead a calorimetric method can be used to determine the mass of Helium in the vessel: a small heat pulse is applied to the Helium and the temperature is monitored some distance away with an accurate thermometer. This is feasible because superfluid Helium has a high thermal conductivity making the whole liquid isothermal. If the energy dissipated into the liquid is known and the temperature rise could be exactly determined, then the mass of Helium can be deduced.

Coil cooling system
The coils are not mounted inside the Helium vessel for two reasons. Firstly the mechanical layout of the vessel would become very complicated and secondly a quench of the magnet in the liquid Helium could transfer the heat so quickly that the Helium pressurizes in an instant and is lost by venting through pressure relief devices in the vessel. This means that the coils have to be cooled by thermal conduction to the superfluid medium. A thermal bus bar made of copper, filled with Helium-II, is used since it offers a most important characteristic for this application: high thermal conductivity at low temperatures during normal operation and low thermal conductivity, such as He-I above T =2.17 K, following a quench in order to prevent heat being transferred too rapidly. The thermal bus bar forms a closed circuit during magnet cooldown. Inside the bar Helium-II is pressurized to 1 bar to suppress boiling. A part of the thermal bus bar resides in the superfluid Helium vessel acting as a heat exchanger. Heat transported from the coils to the thermal bus bars will be conducted by Gorter-Mellink conduction to the Helium in the vessel.

Persistent switches
The magnet has to be charged from a power supply outside the vacuum tank. Once it is charged the power supply can be disconnected and the magnet can be operated in persistent mode. This is done by persistent switches which, when closed, form a superconducting link across the terminals of the magnet. The leads which supply the current from the power supply to the magnet are therefore designed for minimum heat leak when they are carrying no current. This requirement causes the cross section of the leads to be relatively small and therefore the resistance to be relatively high. As a result the leads create substantial amount of heating during charging. This heat has to be removed by Helium-II which is stored in the Helium vessel at 16 mbar. Unfortunately this pressure is too low to ensure a sufficient flow of Helium to cool the leads. A thermo-mechanical pump is mounted in the Helium vessel to pump Helium-II to the leads to provide cooling when required.
A thermo-mechanical pump operates similar to the phase separator described earlier in this chapter. Here a small heater is used to induce a slight temperature difference across the porous plug, with the warm side towards the leads and the cold side towards the Helium vessel. Helium-II travels to the warmer region and cools the leads.
In addition, a disconnect feature is built in near the warm end of the leads, providing a complete thermal and electrical break in the leads when the persistent switch is closed.

2.2 The Tracker and its Subsystems

The information given in in this section is a summary of the references [C$^+$03b, Haa04, Cec04, Cec03, AMS05].

2.2.1 Tracker Design

The tracker measures the particle's momentum in a magnetic field by detecting the particle's trajectory in eight circular planes equipped with silicon sensors. A picture of a tracker layer during assembly is shown in Figure 2.10. The magnetic field with a bending power BL^2 of 0.8 Tm^2 is provided by the superconducting magnet described in the previous section. When a particle with the electric charge z·e travels through a magnetic field with the flux density $\overrightarrow{B}$

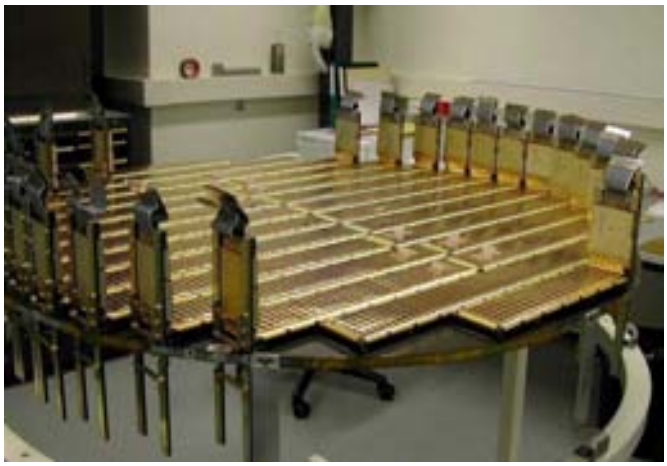

Figure 2.10: Picture of tracker layer 2 during assembly, completely equipped with ladders. The tracker planes consist of ladders composed of double-sided silicon sensors.

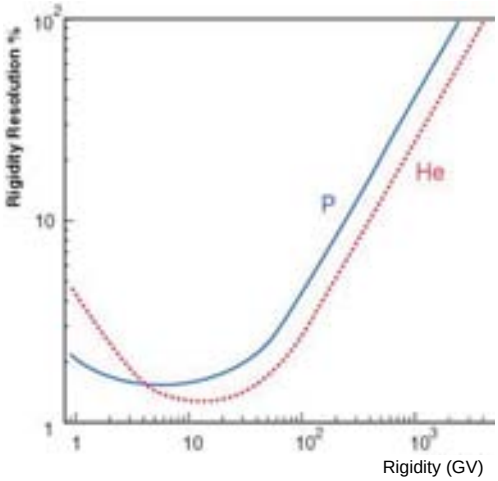

Figure 2.11: Tracker rigidity resolution for protons and Helium. From [Bat02].

perpendicular to its velocity vector, it gets deflected by the Lorentz force:

$$\overrightarrow{F_L} = Z \cdot e(\overrightarrow{v} \times \overrightarrow{B}). \tag{2.1}$$

The Lorentz force F_L is balanced by the centrifugal force and causes the particle to move on a circular trajectory with radius R.

$$F_c = \frac{mv^2}{R} = ZevB = F_L. \tag{2.2}$$

This equation relates the radius R of the particle's trajectory to the momentum of a particle with charge Z·e. Since the particle's charge has still to be derived by another measurement, the direct result of this measurement is the magnetic rigidity R·B:

$$RB = \frac{p}{Ze} \tag{2.3}$$

The rigidity resolution for protons and Helium is given in Figure 2.11. At 100 GV/c the momentum resolution dp/p for protons is still about 3%. Once the particle's charge is determined, the momentum can be calculated from the rigidity.
When a charged particle traverses the silicon sensors of the eight tracker layers, it loses a certain amount of energy. This is referred to as the energy loss -dE/dx, described by the Bethe-Bloch formula. The measurement of the specific energy loss allows to identify the charge of the detected nuclei via the relationship $dE/dx \propto z^2$. For more information about the interaction between charged particles and matter see Section 4.2.1.
The silicon tracker is composed of around 2300 double-sided silicon sensors arranged on 192 ladders in eight circular layers transverse to the magnet axis. In each ladder there are 1024 channels yielding 196608 tracker channels all in all. The total tracker size amounts to 6.4 m^2 of silicon. The silicon sensor material is n-type, high resistivity (> 6 $k\Omega$cm) silicon. Implanted on the ohmic side (n-side) there are n^{++}-strips with a pitch of 104 μm and a read-out pitch of 208 μm. Intermediate p^+ blocking strips minimize the influence of surface charges on the

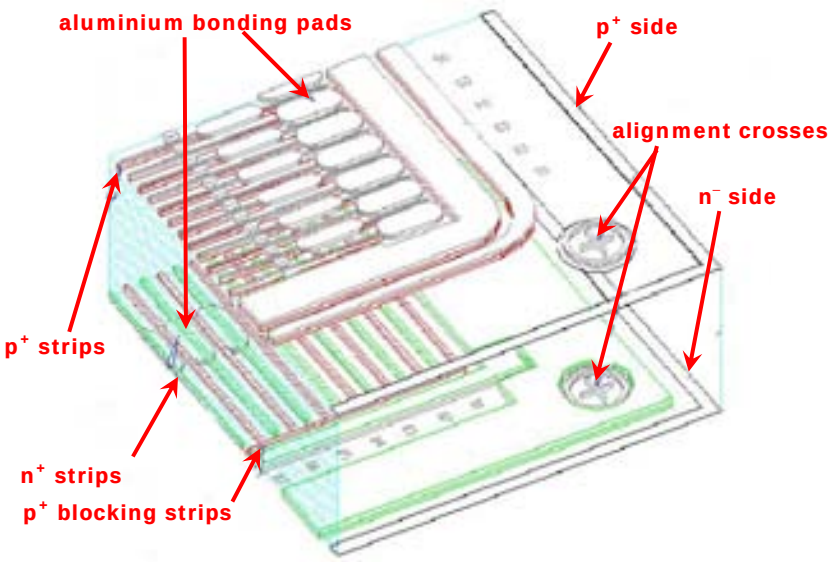

Figure 2.12: Cross section of the double-sided silicon sensors used in the tracker.

position measurement. Implanted on the junction side (p-side) there are p^{++}-strips with a pitch of 27.5 μm and a readout pitch of 110 μm. The strips on the p-side having a finer pitch are used to measure the bending coordinate and the orthogonal strips on the n-side measure the non-bending coordinate. The resulting position measurement accuracy is 10 μm in the bending direction and 30 μm in the nonbending one, allowing the determination of the particle's momentum up to 2 TV/c rigidity. The cross section of an AMS-02 silicon sensor is shown in Figure 2.12. In the operational mode the 300 μm thick sensors are reverse-biased and fully depleted. The most probable charge distribution of a minimal ionizing particle (MIP) traversing the silicon sensor is approximately 25.000 electron/hole pairs by ionization [HZ+98]. In the presence of the electric field, the created charge carriers drift in opposite directions to the two surfaces where the charge is collected on metallized readout strips. Drift times are about 8 ns for electrons and about 25 ns for holes. From there the signal is fed capacitively to the readout electronics, where the position of the traversing particle can be determined by the relative signal heights of adjacent strips. The sensors were manufactured at silicon factories

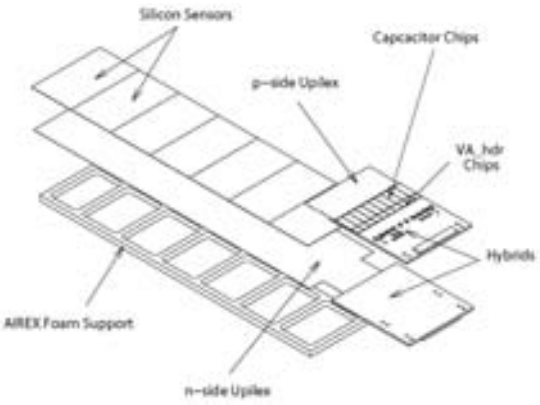

Figure 2.13: Sketch of a tracker ladder.

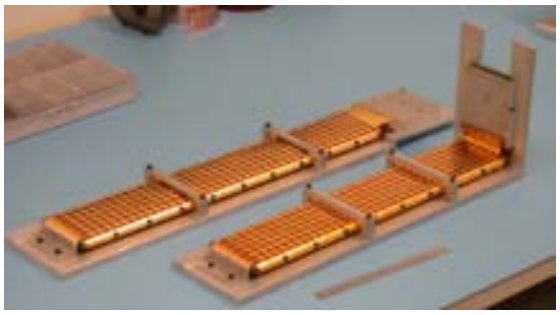

Figure 2.14: Photo of two tracker ladders.

in Switzerland[1] and in Italy[2]. All in all over 4000 sensors have been produced to select 2500 sensors of the best quality in terms of electrical parameters and noisy strips in order to assemble the Silicon tracker ladders.
An exploded drawing of a tracker ladder is shown in Figure 2.13 and a photo of an assembled ladder is given in Figure 2.14. A metallized Upilex film of 50 μm thickness is glued directly to the n-side of the silicon sensors and is used as routing cable to bring the n-side signals to the front end hybrids. Another Upilex film of smaller size is used to connect the p-side signals to the front end hybrids. The silicon sensors are supported by 5 mm thick Airex foam, glued to the Upilex film on the n-side. The exposed surface of the foam is treated with a layer of 100 μm carbon fiber. Small aluminum frames are glued on the carbon fiber surface. The aluminum frames are fixed with screws to the tracker plane. The required precision for the alignment of the silicon sensors is <5 μm. Finally, a double-metalized Upilex film, which surrounds each ladder, is used as electromagnetic shielding. The tracker planes are constructed of a composite structure of carbon fiber layers surrounding an aluminum honeycomb interior. The diameter of the inner planes is 1.0 m and of the outer planes is 1.4 m. The ladders are arranged without any overlap, taking into account a minimal decrease of plane hermeticity. This is justified by a significant complication of the mechanics when using an overlapping design.
The total weight of the detector is 186 kg and its power consumption is 734 W.

2.2.2 The Tracker Alignment System

As mentioned before, the tracker measures the particle's track on its eight layers with an accuracy down to 10 μm. However, in space the environmental conditions can worsen the mechanical accuracy. During the start of the Space Shuttle intense vibrations occur, having an impact on its mechanical accuracy. Furthermore, rapid periodic changes in the thermal settings due to solar radiation and cooling while in the shadow of the Earth may contribute to a decrease of mechanical accuracy. With AMS-01 it was found that variances of up to 30 μm occured, although the carbon fiber support structure was normally stable at the 15 μm level. Moreover it was found that the excursions were correlated with changes in thermal conditions correlated to changes in spacecraft attitude. For long observation periods, the stability is especially important, since this limits the ultimate momentum resolution for high rigidity particles. Furthermore, mechanical instability can introduce significant systematic errors in the pointing accuracy of the AMS-02 tracker, particularly when measuring converted photons from astrophysical point sources.
The Tracker Alignment System (TAS) shoots laser beams into the eight tracker layers, generating signals that mimic straight (infinite rigidity) tracks. The beams are narrow, with a diameter less than 0.5 mm and have a divergence smaller than 1 mrad. It is expected that these artificial straight tracks allow the tracing of changes of the tracker geometry within a position accuracy of better than 5 μm and an angular accuracy of better than 2 μrad.
The laser beams are generated with high-quality DBR (Distributed Bragg Reflector) laser diodes mounted outside the tracker volume. The photons are conducted by mono-mode optical fibres nearly loss free to 2×5 beamport boxes, which are mounted on the outer face of the two outer tracker support planes. From there the laser beams enter the tracker volume. The wavelength of the beams is 1082 nm, chosen such as to penetrate all eight Si detector layers of the tracker. Only a small fraction of the laser photons are absorbed in the silicon (10% in the 300 μm thick silicon sensor). However, a bigger effect is the strong effective attenuation of a

[1] Colibrys SA, Maladière 83, CH-2007 Neuchâtel
[2] ITC-irst, Via Sommarive 18, I-38050 Povo

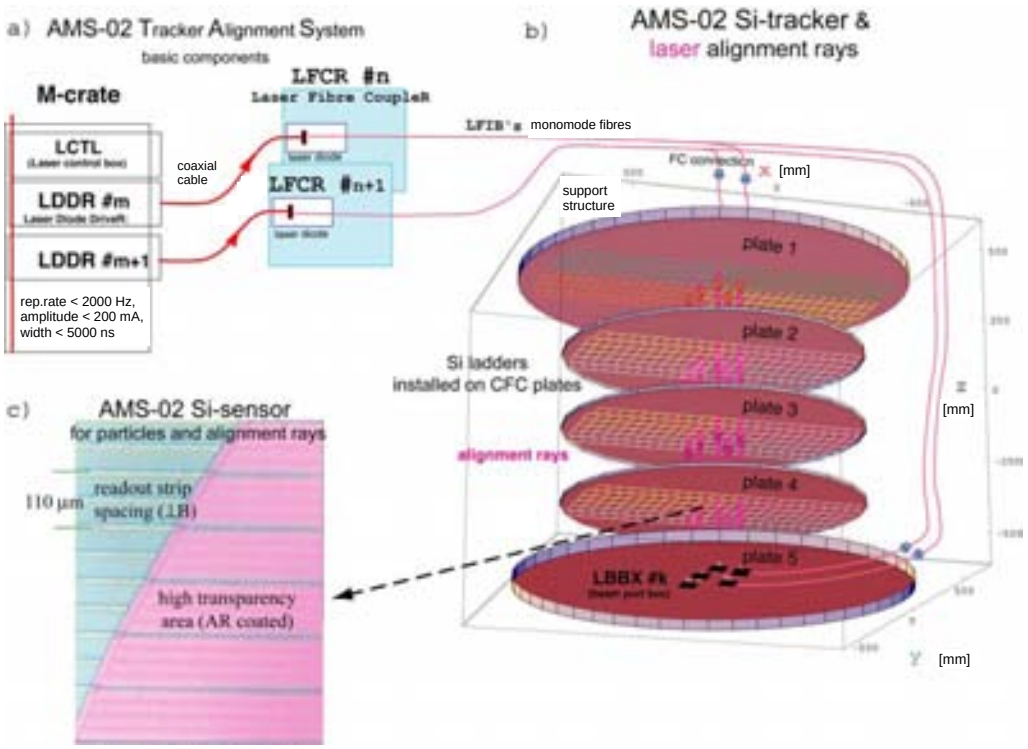

Figure 2.15: Overview of the tracker alignment system. (a) TAS components in the M-crate. (b) Geometry of upward and downward going laser beams. The laser beams are injected on the upper tracker plate and the lower tracker plate by five beamport boxes on each plate. (c) Micrograph of and Anti Reflective (AR) area.

factor ∼10 per layer due to reflection caused by the high refractive index of Si. Therefore the tracker sensors in the alignment beams have been treated with antireflective coating optimized for the wavelength chosen. The residual reflectivity is ∼1%. Furthermore, to avoid obstruction by the aluminized readout strips, the metallization has been reduced to 10 μm in the coated areas, achieving a transparency of 50% and the eighth layer of the tracker still receives about 0.8% of laser intensity.
The laser alignment will be performed during data taking. This allows to recognize any possible changes in the tracker geometry and to correct for deformations offline. The TAS has a weight of about 3 kg and a low power consumption of 1 mW. Figure 2.15 depicts the tracker alignment system with its connection to the M-crate.

2.2.3 The Tracker Thermal Control System

The tracker has to be cooled by an active cooling system. The hybrids are mounted on carbon fiber-metal bars, which conduct the heat dissipated by the front end electronics.
The Tracker Thermal Control System (TTCS) is a two-phase, mechanically pumped loop system using CO_2 at about 80 bar as cooling liquid. CO_2 is used since it poses no safety related problems and has a low liquid/vapor density ratio of order of 1-10. Before entering the tracker volume the liquid CO_2 temperature is controlled by pre-heaters to remain just below the boiling point. In the tracker volume it passes thermal bars on the outer and outermost inner planes,

where the heat from the front-end hybrids is collected in series. At each heat input, a small fraction of the liquid gets evaporated. After passing the last hybrid up to 30% of the liquid has been vaporized. To cool the tracker volume isothermally the evaporator circuit is split into upper and lower loops to cool the upper and lower layers of the tracker.
When the vapor/liquid mixture reaches the outside of the tracker volume, it is redirected to the condensers on the thermal wake and ram radiator panels facing outer space. There it is cooled down below the boiling point and afterwards is returned back to the pump input, closing the circuit. The relative flow to the wake and ram radiators has not to be technically controlled, since it is self-adjusting. The fluid preferentially flows towards the cooler radiator. For redundancy there are two separate loops. Figure 2.16 illustrates the main components of the TTCS.

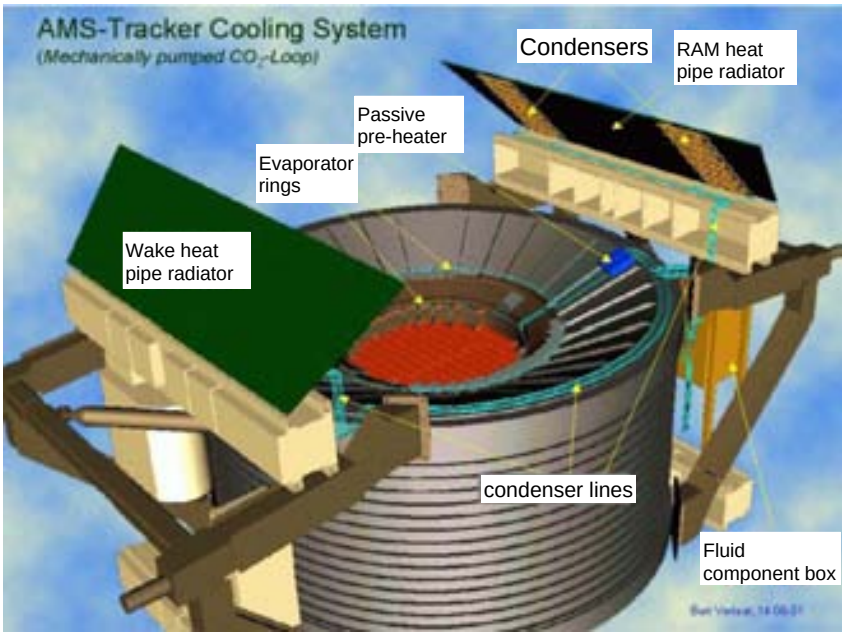

Figure 2.16: Model of the tracker thermal control system. Thermal bars conduct heat from the hybrids to the evaporator rings, where a small part of the CO_2 gets vaporized. From there the CO_2 liquid/vapor mixture is pumped to the wake and ram radiator to be cooled below the boiling point.

2.3 The Transition Radiation Detector

The information given in in this section is a summary of the references [KS+04, K+04, Hau04, G+03, S+02, M+03, K+01a, K+01b, AMS05].

2.3.1 Transition Radiation Detector Design

Transition Radiation (TR) consists of soft X-rays which are emitted when charged particles traverse the boundary between two media with different dielectric constants ϵ_1 and ϵ_2. This radiation originates from the reformation of the particle's field when traveling from the medium with ϵ_1 to the medium with ϵ_2 (see Chapter 4). The production depends on the particle's mass

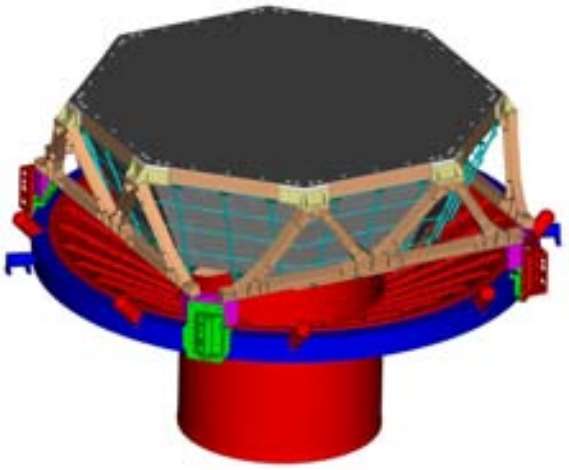

Figure 2.17: Drawing of the Transition Radiation Detector (TRD). The TRD is supported by an M-shaped structure.

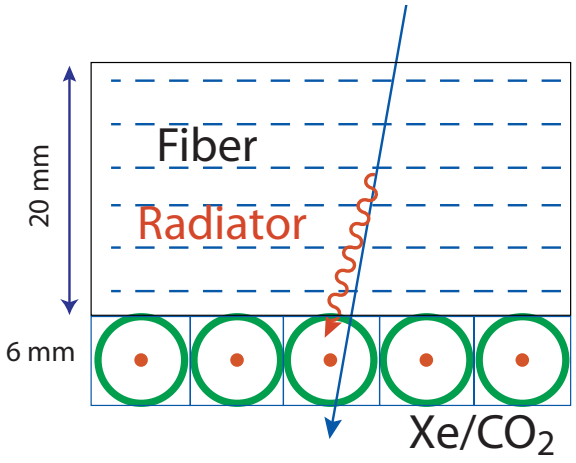

Figure 2.18: Sketch of one TRD layer consisting of fiber fleece as radiator and gas filled proporional tubes as detector.

and energy. The Transition Radiation Detector (TRD) is used to distinguish particles of the same momentum and electric charge but of different masses, such as electrons and protons. A drawing of the TRD is given in Figure 2.17.

In the momentum range from 10 to 300 GeV/c, light particles such as electrons and positrons have a much higher probability of emitting TR photons than heavy particles such as protons and antiprotons. At a single boundary, the probability of transition radiation photon emission is still very small, on the order of 10^{-2}. This is enhanced by using fleece as a radiator made of 0.06 g/cm^3 polypropylene/polyethylene[1]. The TRD is composed of 20 layers made of 20 mm thick radiators and 6 mm diameter proportional mode straw tube modules. One layer is illustrated in Figure 2.18. The straw tubes are filled with a Xe/CO_2 (80/20) gas mixture and operated at 1600 V to detect the ionization trace of the traversing particle and the transition radiation photon created in the radiator material before. By statistical signal height analysis in all 20 layers, the probability can be evaluated whether the traversing charged particle which causes ionization in the gas of the proportional tubes was accompanied by a transition radiation photon, which is absorbed by the photoeffect in the gas of the proportional tube.
In this way a rejection factor of $10^2 - 10^3$ for p^+ and e^- can be achieved against e^+ and $\overline{p}$ in

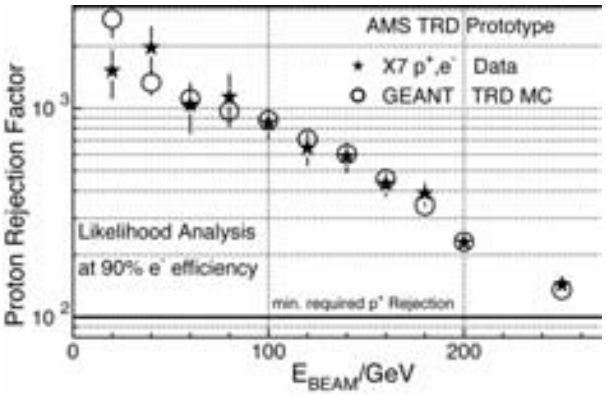

Figure 2.19: Proton rejection factor measured in a CERN X7 testbeam and analysed using a likelihood analysis and Geant 3 Monte Carlo simulation.

[1]LRP-375 BK manufactured by Freudenberg Vliesstoffe KG, Germany

the aforementioned momentum range. The proton rejection factor as measured in a CERN X7 testbeam with a 20 straw tube layer prototype detector, is shown in Figure 2.19. The results show good agreement with the GEANT 3 simulation. It can be seen, that in an energy range from 10 to 250 GeV the proton rejection factor lies clearly above the minimal required factor of 10^2.

2.3.2 Mechanics and Straw Tubes

Mechanical Support

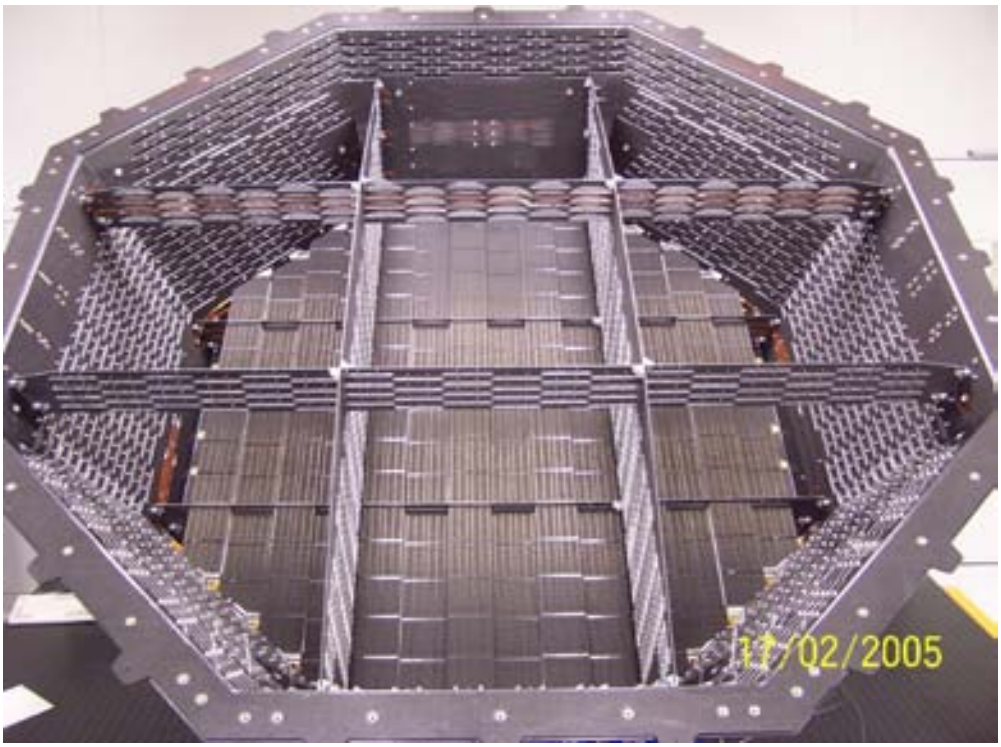

Figure 2.20: Conical octagon made of aluminum honeycomb material. Straw tubes and frontend electronics are not mounted on this picture.

The mechanical structure of the TRD has the form of a conical octagon with a width from 1.5 m at the bottom to 2.2 m at the top. It is made of an aluminum-honeycomb material with carbon-fiber skins. On the sidewalls slots are machined with a precision of 100 μm, where the straw tube modules are attached to. The dimensions are verified on a high precision optical measuring device. A picture of the octagon is shown in Figure 2.20. Detailed finite element calculations have been performed to verify that the large TRD octagon structure satisfies all dimensional and safety requirements with the result of the modal analysis showing that the first natural eigen-frequency is 54 Hz, above the required 50 Hz. The octagon is supported by an aluminum "M"-shaped structure which is mounted on the Unique Support Structure (USS). The USS holds AMS-02 in the Space Shuttle and finally fixes it to the ISS. The complete TRD including Gas System and Electronics weighs less than 500 kg.

Straw Tubes

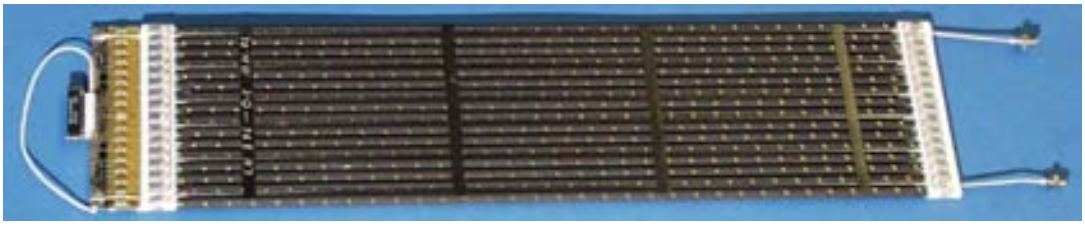

Figure 2.21: Picture of a small straw tube module.

The straw tube modules as shown in Figure 2.21 are made of 16 straws, each one fabricated from two overlapping multilayer foils, predominantly made out of 25 μm Kapton material. Each of these Kapton foils is covered with 0.2 μm aluminum metallization and 6 μm Carbon polyimide on one side. The two foils are glued together by applying a 10 μm polyurethane layer on the other side, winding them back-to-back and heat sealing them afterwards. The total wall thickness is 72 μm. The cross section of a straw tube wall is shown in Figure 2.22. At each end the straws are closed by polycarbonate end pieces, which serve as manifolds to distribute the gas. The gas distribution channel in the endpieces is arranged in the way that the gas flux flows through the first eight straws in one direction and is reversed through the second half of the straws. The sense wire is made of 30 μm gold plated tungsten, tensioned with 1 N. It is fixed by a Cu-Te crimp-plug, which is centered by the straw tube end pieces. The length of the straw modules varies from 0.8 m to 2 m. To stabilize the straw tubes six longitudinal carbon fibre stiffeners are glued between the straws and additional transverse stiffeners are glued onto the modules. They modules are arranged in the conical octagon structure, such that the upper and lower four layers of tubes run along the B-field direction and the twelve central layers in the perpendicular direction. In all, there are 328 modules, for a total of 5248 straws.

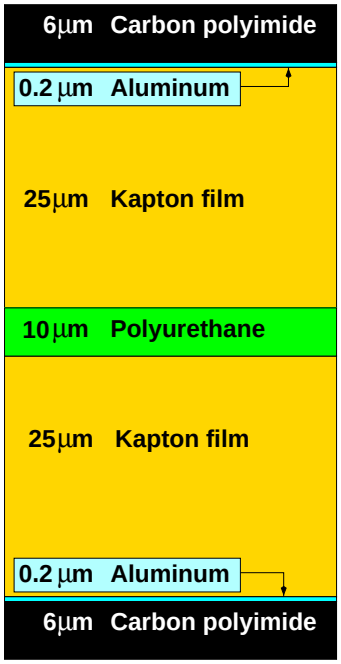

Figure 2.22: Wall cross section of a TRD straw tube.

Fleece Radiator

The LRP-375 BK fleece material consists of polypropylene(85%)/polyethylene(15%) fibers with a mean diameter of $\sim$10 μm, and an overall density of 0.06 g/cm^3. The fleece is cut into pieces of about 20 mm thickness and a length chosen to cover the complete straw module. The total TRD has an accumulated area of $\sim$50 m^2 to be covered with radiator material. The fleece has to be chemically cleaned by a CH_2Cl_2 soxhlett extraction process to comply with the NASA outgassing limits and therefore deposition limit of 10^{-14} g/s/cm^2 on any ISS surface.

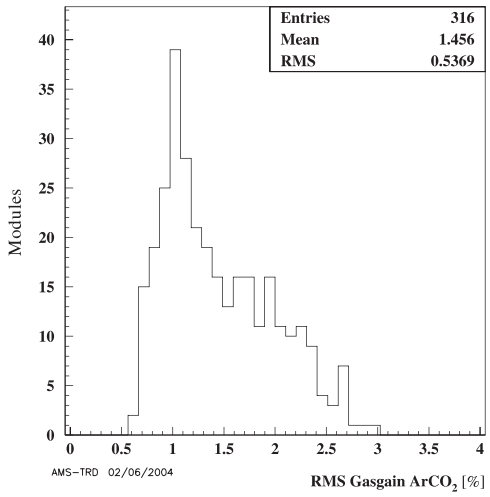

Figure 2.23: Gas gain measurement during module production.

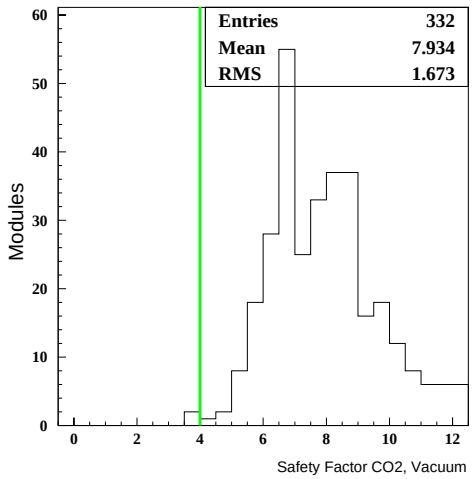

Figure 2.24: CO_2 leakage measurement during straw module production. CO_2 leakage is expressed in terms of gas supply safety factor.

Gas Tightness

The gas tightness of the straw modules is the most critical design issue. The available gas supplies of 49.5 kg of Xe and 4.5 kg of CO_2 have to last for three years of operation in space. At standard conditions this corresponds to 8420 l of Xe and 2530 l of CO_2. Since insufficient gas tightness can limit the operational time of the TRD, great efforts have been made to keep the CO_2-leak rate of the straw modules as small as possible. The CO_2 leak rate for one meter of straw tube was determined to be 1.85×10^{-5} l mbar/s per module meter. This leak rate is attributed to diffusion through the straw walls. For the full TRD (500 module meters) this results in 9.3×10^{-3} l mbar/s. An additional leak rate of the polycarbonate endpieces has to be taken into account. One single endpiece accounts for a leak rate of 0.9×10^{-5} l mbar/s, for all 328×2 endpieces this totals to 5.9×10^{-3}l mbar/s. Taking together the CO_2 leak rate of the straw walls and of the endpieces this results in a total leak rate of 1.5×10^{-2} l mbar/s, corresponding to a CO_2 loss of 287 l over three years or a safety factor of 8.8 with respect to the CO_2 supply. This is assured by testing each of the 5248 straws individually before producing a module.

Production Tests

During straw production, single straws are tested for gas tightness in a test stand where He at 2.8 bar for five minutes is used to achieve fast and accurate measurements. The complete modules are tested for low dark currents (< 1 nA) at a high voltage of 1500 V with $Ar/CO_2(80/20)$. The gas gain homogeneity is determined by measurement of the gas gain as a function of the position along each straw in a module which is placed on a precision granite block. The calibration is done using the converted 5.9 keV photons from an Fe^{55} source. The mean homogeneity of all measured gas gains is 1.5 %. The gas gain homogeneity at a nominal gas gain of 3000 is

shown in Figure 2.23. Each straw module is measured by a pressure drop test at 1.7 bar in a vacuum vessel. The results of this tests are shown in Figure 2.24. The safety factor averaged over all modules selected for flight is 7.9.

2.3.3 The Xe/CO_2 Gas System

The TRD straw tubes contain Xe/CO_2 mixed 4:1 in volume at ∼1 bar. The TRD gas system is a recirculating gas system, which has to store, mix, and distribute the gas through the TRD modules. The system is built up of a supply box (Box-S), a circulation box (Box-C) and manifolds. Figure 2.25 illustrates the TRD gas system.

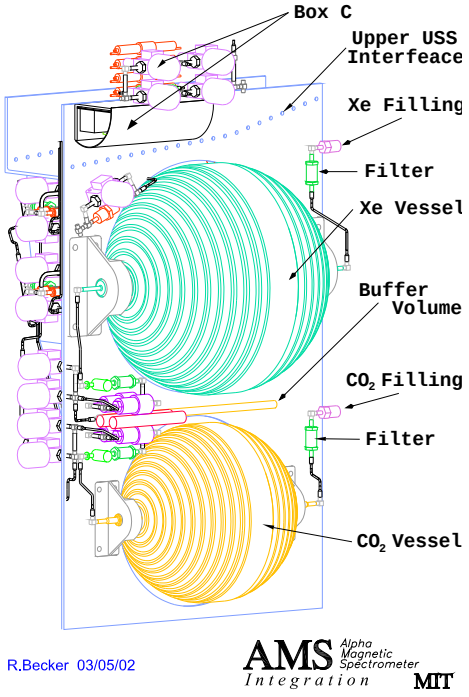

Figure 2.25: TRD gas supply system. Box-S consists of the Xenon and CO_2 vessels. Vessel D is located on the backside and cannot be seen.

Box-S stores the Xe and CO_2 in separate vessels, which contain 49.5 kg of Xe at a pressure of ∼107 bar and 4.5 kg of CO_2 at a pressure of ∼65 bar, 54 kg in total. Leak-before-burst vessels ensure safety in the event of high temperatures causing overpressure in the vessels during a time when gas cannot be vented, e.g. when the system has no electrical power. All valves have a two-fold redundancy. The gases are transferred in controlled amounts, by measuring partial pressures to a mixing vessel (vessel D), from which the mixture is released into Box-C. Figure 2.26 illustrates a filling cycle. Box-C contains redundant pumps to circulate gas through the TRD to ensure uniform gas properties. It also contains a CO_2 analyzer and monitor tubes for measuring the gas gain with an Fe^{55} source to assess the properties of the gas. The pumps and CO_2 sensor are mounted inside a gas tight vessel. In the event of a pump or valve failure, pressure integrity of the system will not be lost.

About once a day, gas will be mixed inside the vessel D. Several times per day small amounts of gas are released into Box-C to correct for changes in total or partial pressures in the gas circuit which will occur due to gas leakage. Then the flow of gas splits into 41 separate gas circuits, each consisting of eight straw modules connected in series with a maximum active volume of eight liters. Each gas circuit is individually connected to the input and output manifolds via computer controlled isolation valves. Pressure sensors in the manifolds at the input and output of the gas circuits can detect leaks in order to isolate a leaky segment. If a large leak is detected in a segment, it is closed automatically by the slow control computer. A pressure drop in Box-C causes all valves to be closed by the gas system electronics, regardless whether the slow control computer is running or not.

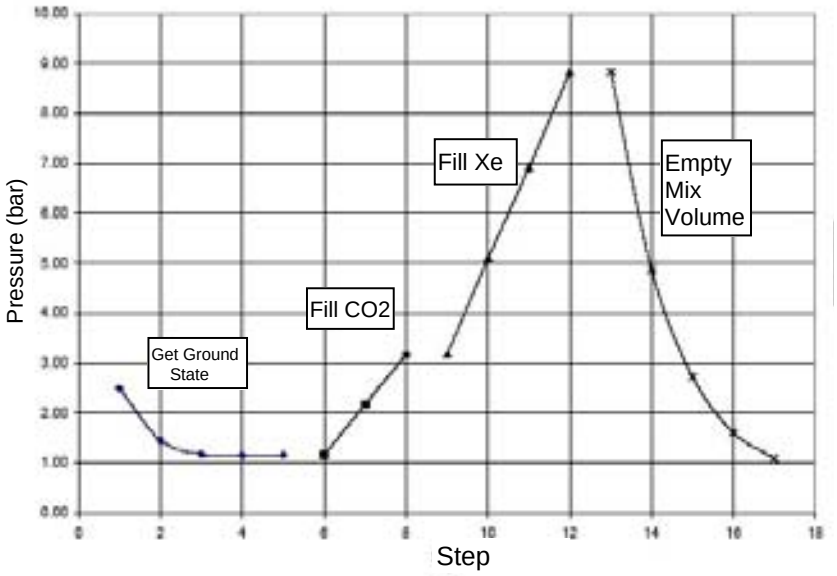

Figure 2.26: Computer controlled Xe/CO_2 fill cycle. Pressure measurement shows the buildup of gas while mixing. In the end pressure decreases while the gas is filled into Box-C.

2.4 The Ring Imaging Cherenkov Detector

The information given in in this section is a summary of the references [B+03, AMS05].

2.4.1 Ring Imaging Cherenkov Detector Design

The purpose of the AMS-02 RICH[1] is to measure the velocity of a charged particle with a relative accuracy of about 1 per mil. A drawing of the RICH is given in Figure 2.27. The determination of the velocity is based on the Cherenkov effect.

When a charged particle traverses a dielectric material with a phase velocity faster than c/n, where c is the speed of light and n is the refractive index of the material, a characteristic electromagnetic radiation is emitted. During its passage, the atoms next to the particle's path become polarized, turning the atoms into electric dipoles. As long as $v < c/n$, all the dipoles are distributed symmetrically around the particle's trajectory, the resulting field when integrating over all the dipoles is compensated. But when the

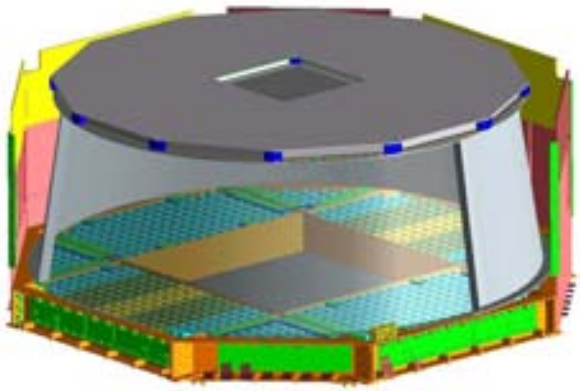

Figure 2.27: Drawing of the RICH subdetector.

[1] RICH, Ring Imaging Cherenkov Detector

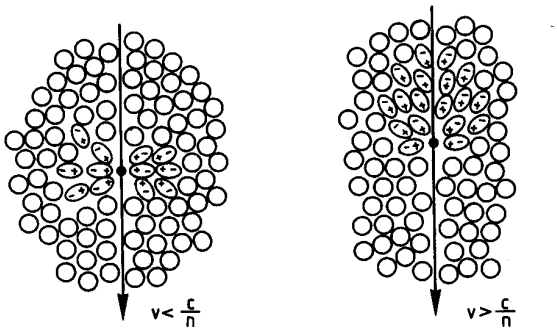

Figure 2.28: Polarization due to the passage of a charged particle. From [Gru93].

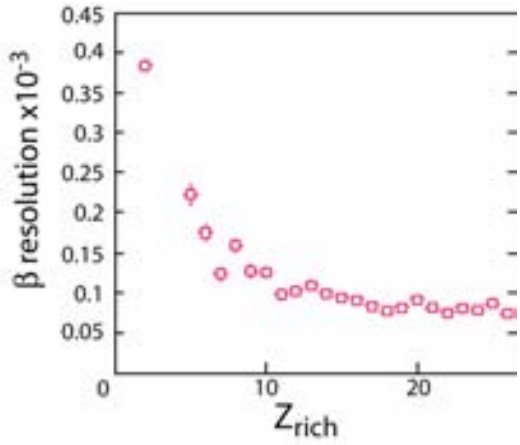

Figure 2.29: Velocity resolution dependence on different ions measured with an n = 1.03 radiator.

particle is faster than the speed of light in the medium, $v > c/n$, the symmetry is broken and a resulting dipole field is created, as is illustrated in Figure 2.28. This dipole field causes emission of an electromagnetic radiation cone, which can be detected by photomultipliers.
The geometry of the radiation cone depends on the velocity v of the charged particle and of the refractive index n(ω) of the material. The half opening angle of the cone θ_C is given by

$$cos\theta_C = \frac{1}{n\beta}. \tag{2.4}$$

Cherenkov radiation starts to be emitted at a threshold velocity

$$\beta_{min} = \frac{1}{n(\omega)}. \tag{2.5}$$

From this threshold onwards, Cherenkov radiation is emitted in forward direction. The opening angle increases until $\beta = 1$ and

$$\theta_C = arccos\frac{1}{n(\omega)}. \tag{2.6}$$

The number of radiated photons in a frequency range $d\omega$ when passing the length dx in the material is given by

$$\frac{d^2N}{d\omega dx} \propto Z^2 sin^2\theta_C. \tag{2.7}$$

Therefore the velocity is determined by measuring the Cherenkov cone opening angle and the charge of the incoming particle can be estimated by the number of radiated Cherenkov photons. Figure 2.29 shows the β resolution in dependency of the particle charge Z and Figure 2.30 demonstrates the charge separation capability of the AMS-02 RICH. Clearly visible are the individual ion peaks of up to Z = 26. A sample of Cherenkov rings can be seen in Figure 2.31. This demonstration of a charge measurement was performed during a testbeam in October 2002. The beam was composed of A/Z = 2 ions with a rigidity of 40 GV/c.

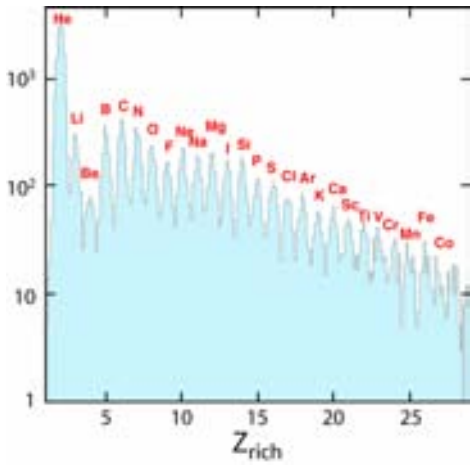

Figure 2.30: RICH charge distribution measurement at a testbeam in October 2002 for $Z > 1$, taken with an $n = 1.03$ radiator. Protons are suppressed.

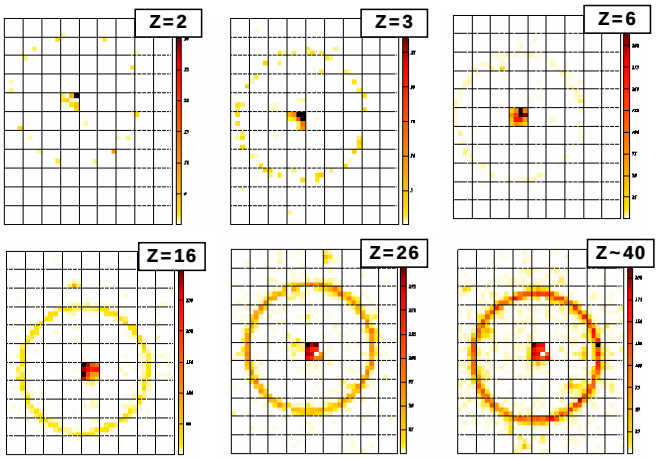

Figure 2.31: Samples of Cherenkov rings created with single $A/Z = 2$ ion events.

2.4.2 Radiator and Mirror

The RICH subdetector is mounted below the lower two time-of-flight planes and the electromagnetic calorimeter. This subdetector has a truncated conical shape with 60 cm upper radius, 67 cm lower radius and a height of 47 cm. A supporting plate on the top holds a 3 cm thick layer of dielectric material, called the radiator. A conical mirror encloses the drift volume to increase the acceptance. The lower plane is the photon detection plane which supports an array of 680 light guides and photomultipliers as well as the front end electronics. In the middle of the plane is a 64 x 64 cm^2 square hole to let particles pass unaffected by the detection plane reach the electromagnetic calorimeter. Two radiator materials are used. Except of the central part, the radiator material is silica aerogel - a mixture of $m(SiO_2)$ and $2m(H_2O)$, with m representing an integer value. This material has a porous structure containing bubbles with a size smaller than optical wavelengths. The corresponding refractive index is an average between the ones of air and the mixture. It has a linear dependency with the density of the aerogel material. By means of different treatments during the production process the aerogel density can be designed between 0.1 to 0.3 g/cm^3, making a radiator refractive index accessible greater than for gases but smaller than for liquids and solids ($1.025 < n < 1.075$). In the central part of the RICH a radiator made of NaF, which has a higher refractive index of n = 1.336 is placed, creating a wider Cherenkov cone. This is done to increase the photon detection efficiency for those particles that fall upon the central hole of the detection plane. All in all 80 rectangular blocks of silica aerogel of size 11.5 x 11.5 x 3 cm^3 and 16 central blocks of NaF of size 8.5 x 8.5 x 0.5 cm^3 are used.
Most of the photons go directly into the photon detectors of the lower plane, about 30% are pointed outside the lower detector plane. To collect these photons as well, a conical mirror has been designed to reflect them into the sensitive area of the lower plane, in this way increasing the active size of the RICH subdetector. The lower diameter of the cone is 134 cm and the upper diameter is 114 cm. A thin film of reflective coating made up of 100 nm of aluminum and 300 nm of SiO_2 is applied on the inner surface of the cone. The coating provides a reflectivity of $> 85\%$ at a wavelength of 420 nm.

The residual field where the photomultipliers are placed is around 300 Gauss. This requires the photomultipliers to be shielded. The HAMAMATSU R7600-00-M16 photomultiplier has been chosen due to its reduced size, fast response under low operational voltages (800 V), large anode uniformity and low sensitivity to external fields.

2.5 The Time-of-Flight System and Anticoincidence Counters

The information given in in this section is a summary of the references [C$^+$03a, AMS05].

2.5.1 The Time-of-Flight Detector

The AMS-02 TOF[1] detector allows to measure particle velocity and to discriminate between upwards and downwards traveling particles. A drawing of the TOF is given in Figure 2.32. The time resolution of the TOF system is about 120 ps. Downwards traveling particles are discriminated from upwards traveling particles at the level of 10^9. The geometrical acceptance of the TOF and consequently of AMS-02 for charged particles is 0.4 m^{2}sr. Moreover it generates the fast trigger for charged particles or converted photons. The time resolution as a function of charge was measured during a testbeam in 2003 and is shown for two counters in Figure 2.33. A measurement of absolute charge can be performed additionally to other detectors in AMS-02 such as the RICH. This energy deposition is to first order proportional to the square of the particle charge. The energy resolution is sufficient to distinguish particles up to the charge Z $\sim$ 20. A combined charge measurement of TOF and RICH was done during a testbeam in 2002 and is shown in Figure 2.34.

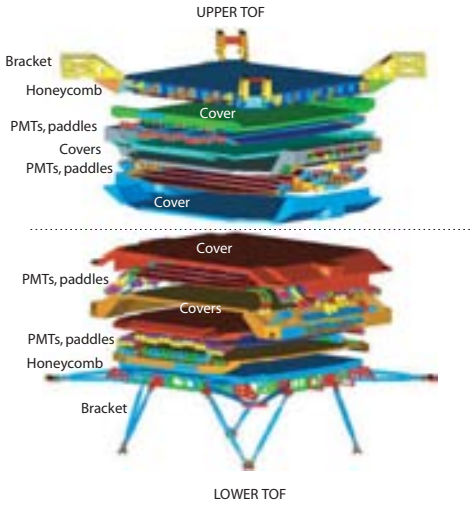

Figure 2.32: Drawing of the time-of-flight system.

The TOF subdetector is composed of four circular planes of plastic scintillator paddles, of which two are located above and two below the magnet. The paddles are 12 cm wide with a length between 117 cm to 134 cm, which overlap each other by 0.5 cm to avoid geometrical inefficiencies. Each of the four planes is composed of eight or ten paddles. The thickness of the scintillator paddles is 1 cm, which is a compromise between minimum thickness and light output needed. In two adjacent planes the paddles are oriented perpendicular to facilitate efficient background rejection. This overlapping and crossed paddle geometry provides a granularity of about 12 x 12 cm^2. At each end the scintillator paddles are connected by independently powered photomultiplier tubes through light guides.
The paddles for the upper and lower TOF plane pairs are mounted on a honeycomb panel. Carbon fiber enclosures provide support and light tightness. The TOF detector is mounted via brackets to the Unique Support Structure.
A major design constraint is the residual of the magnetic field in the region of the TOF planes, which ranges up to 3 kG. Photomultiplier tube (PMT) performance is strongly affected by the

[1] TOF, Time-Of-Flight

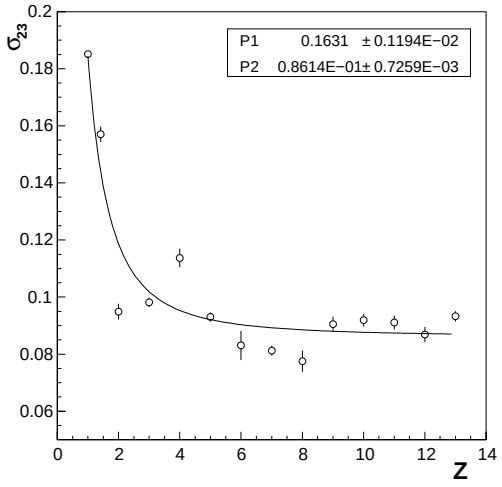

Figure 2.33: Time resolution of the TOF detector (in [ns]) as a function of particle charge taken with two counters C2 and C3 during a testbeam in 2003.

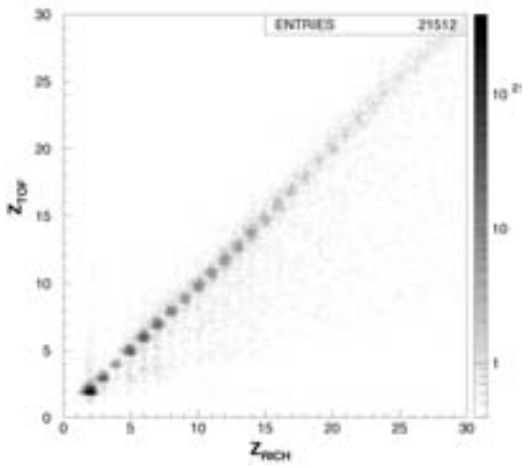

Figure 2.34: Combined charge measurement of RICH and TOF detectors from a testbeam in 2002.

presence of a magnetic field. Consequently a thorough investigation of PMTs to be operated under these conditions preceded the selection of the HAMAMATSU R5946 photomultiplier. It was found that the PMTs perform best when they are aligned within 45° of the field direction. This has been a primary design consideration in the placement of the PMTs. To position the PMTs correctly into the magnetic field, the light guides have curved geometries. The magnetic field and the placement of the PMTs in the scintillator planes is illustrated in Figure 2.35. In total 144 PMTs are used in the TOF system. The PMTs feature a spectral response range from 300 nm to 600 nm with a maximum response at 420 nm, corresponding to a quantum efficiency of about 20%. Figure 2.36 shows an assembly drawing of a TOF paddle and a photograph of an assembled paddle. The central section is an ELJEN EJ-200 scintillator adjoined at each end by clear curved or bent light guides up to 15 cm long to align the PMT correctly in the magnetic field.
The TOF system can operate in vacuum over a temperature range from -20°C to +50°C. Its weight is less than 280 kg and as a power consumption, including all electronics, of less than 170 W.

2.5.2 Anticoincidence Counters

The ACC[1] system surrounds the tracker like a barrel. 16 scintillation panels (Bicron, BC414) of 8 mm thickness fit tightly inside the inner bore of the superconducting magnet. The purpose of the ACC system is to detect particles which enter the tracker laterally outside the main acceptance and to veto against them. This prevents the charge measurement in the tracker to get falsified by particles entering laterally and leaving hits close to the tracks of interest.
The light from the scintillation panels is collected by Kuraray Y-11(200)M wavelength shifter fibers with 1 mm diameter, which are embedded in grooves milled into the scintillation panels. On both ends of the scintillation panels, two output ports with 37 fibers each are linked to transition connectors. They are placed on the upper and lower conical flanges of the magnet

[1] ACC, Anticoincidence Counter

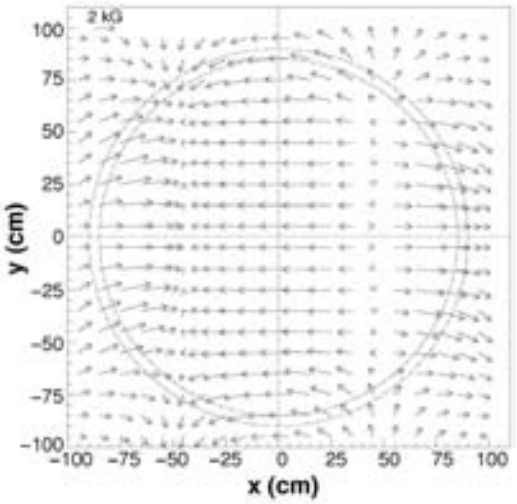

Figure 2.35: Residual magnetic field at the time-of-flight planes. The dashed circles indicate the position of the photomultiplier tubes.

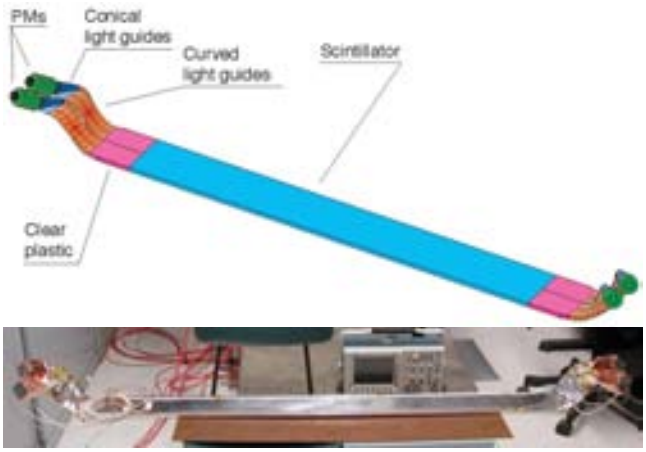

Figure 2.36: Assembly drawing of a time-of-flight paddle (upper drawing) and photo of an assembled paddle (below).

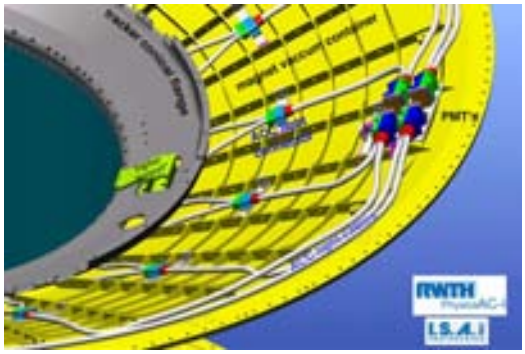

Figure 2.37: The light transport system of the ACC system. The light is guided through the fibers embedded in the panels, to the PMTs located on the outer rim of the vacuum case.

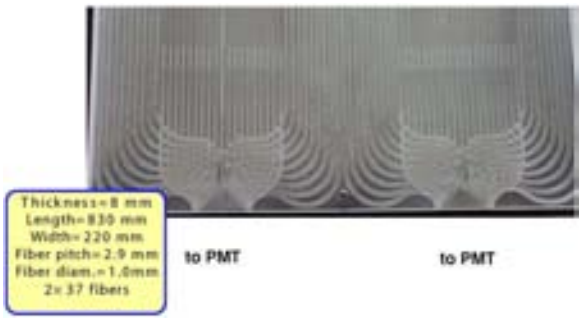

Figure 2.38: Picture of an ACC panel end. The grooves for the wavelength shifter fibers rejuvenating at the end of the panel can be seen.

vacuum case. From these connectors onwards clear fibers guide the light to Hamamatsu R5946 photomultiplier tubes, mounted on the rim of the vacuum case. The placement of the PMTs is illustrated in Figure 2.37 and a picture of the ACC panels is presented in Figure 2.38.
The photomultiplier tubes have to work in a moderate magnetic field of about 1.2 kG, since they are placed approximately 40 cm from the racetrack coils. To reduce the effects of the magnetic field the photomultiplier tubes are oriented with their axes parallel to the stray field. One scintillation panel is read out by two photomultiplier tubes. For a minimum ionizing particle (MIP) the output charge of the photomultiplier tubes is approximately 13 pC.
The signals from the PMTs veto against the AMS-02 trigger in order to reject events outside the tracker acceptance. [AMS05]

2.5.3 The Trigger

The AMS-02 TOF system provides the fast trigger (FT) for the other subdetectors. When a particle traverses the four TOF scintillator planes, and the ACC scintillators do not veto, the Trigger electronics notifies all other subdetector that a particle has passed AMS-02. Subsequently the other subdetectors are read out. Furthermore, the TOF system also flags particles with charges greater than one, making it possible to suppress protons at trigger level.

2.6 The Electromagnetic Calorimeter

The information given in in this section is a summary of the references [AMS05, C+02].

2.6.1 Design of the Electromagnetic Calorimeter

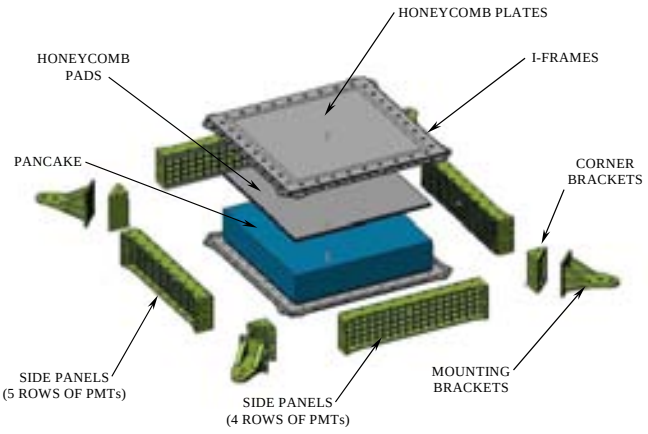

Figure 2.39: The mechanical layout of the electromagnetic calorimeter. The active detector volume is labeled pancake. Photomultiplier tubes are mounted on the sidepanels. The ECAL is fixed to the USS with the corner brackets.

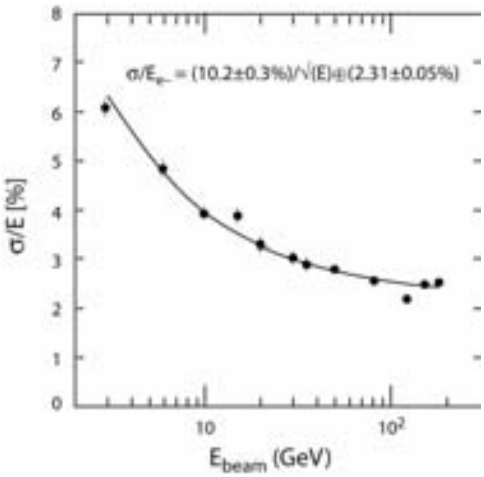

Figure 2.40: Energy resolution of the electromagnetic calorimeter. The energy resolution can be parameterized by the formula given in the plot.

The AMS-02 Electromagnetic Calorimeter (ECAL) is placed at the bottom of AMS. The ECAL provides a precise three-dimensional imaging of the longitudinal and lateral shower development. Shower shape analysis of positrons and protons provides a way to suppress the proton background up to a level of 10^4. The composition of the ECAL is shown in Figure 2.39. The energy resolution is given in Figure 2.40.
While electrons and photons in the MeV range loose their energy mainly by photoeffect and Compton scattering, the dominating process in the GeV range is bremsstrahlung and subsequent electron/positron pair creation. The created electron and positron emit again bremsstrahlung photons and an electromagnetic avalanche emerges. The avalanche grows until the mean particle energy drops below a critical energy E_c, when $E_0/N < E_c$ and the avalanche dies out. A good description of the longitudinal shower profile is given by the parametrization

$$\frac{dE}{dt} = \frac{E_0 \cdot f^{g+1} \cdot t^g e^{-ft}}{\Gamma(g+1)}, \tag{2.8}$$

where Γ(g) is the Gamma function

$$\Gamma(g) = \int_0^\infty e^{-x} x^{g-1} dx, \tag{2.9}$$

and t = x/X_0 is the shower depth in units of the radiation length X_0; g and f are fit parameters and E_0 is the initial primary energy. This formula can be qualitatively understood when realizing that for small shower depths t the amount of secondaries grows like t^g. With increasing depth the energies of the shower particles decrease. Finally the amount of particles reaches a maximum. Beyond the maximum absorption processes dominate and the shower dies out. This is described in the formula by the term e^{-ft}. In this parametrization the maximum of the shower is reached when

$$t_{max} = \frac{g}{f}. \tag{2.10}$$

The shower depth is given by

$$t_{max} = ln\Big(\frac{E_0}{E_c}\Big) + c, \tag{2.11}$$

where c is +0.5 for gamma induced cascades or -0.5 for electron induced cascades, E_c is the critical energy of the detector material and E_0 the energy of the primary particle. With increasing longitudinal depth, the transversal size of the shower increases due to multiple scattering. For a homogenous calorimeter[1] the lateral size can be described best with the Molière radius:

$$R_m = \frac{21\ MeV}{E_c} X_0\ [g/cm^2]. \tag{2.12}$$

A typical longitudinal electromagnetic shower profile is shown in Figure 2.41.

The ECAL is composed of a lead/scintillating fiber sandwich with an active area of 648 x

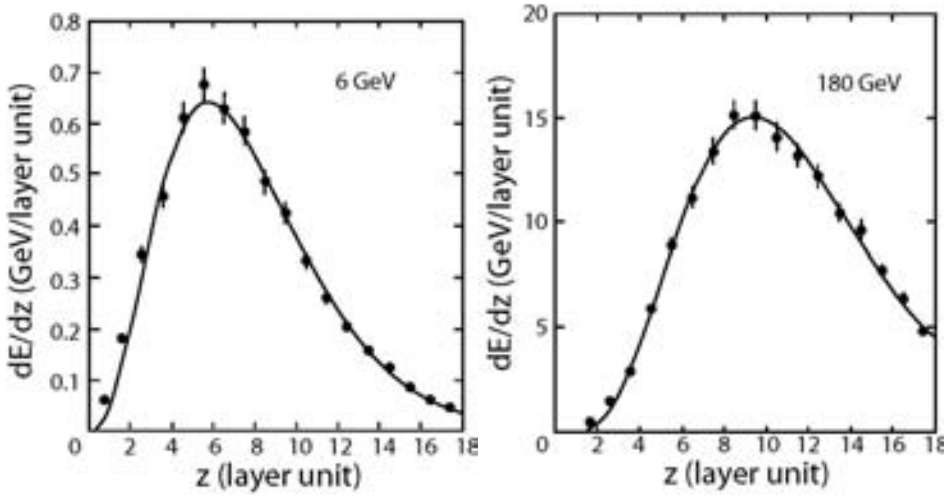

Figure 2.41: Longitudinal electromagnetic shower profile for 6 GeV and 180 GeV.

648 mm^2 and a thickness of 166.5 mm. It is build up of 18.5 mm thick superlayers, made of eleven grooved, 1 mm thick lead foils interleaved with layers of 1 mm diameter scintillating fibers, glued together with epoxy. In each superlayer all the fibers point in one direction. To

[1]This holds not for a sampling calorimeter, since its layers are composed of different materials

obtain the 3-dimensional imaging capability, the superlayers are stacked together with the fiber pointing direction changing by 90° from superlayer to superlayer. In four layers the fibers are oriented parallel to the x-axis and in five layers the fibers are oriented parallel to the y-axis. The average density of the calorimeter is 6.9 ± 0.2 g/cm^3. The total weight is about 496 kg with a thickness corresponding to about 17 radiation lengths. A photo of the assembly of three ECAL layers is depicted in Figure 2.42. The mechanical structure is formed by an aluminum alloy

Figure 2.42: Photo of the assembly of three ECAL layers. In adjacent layers the pointing direction of the fibers change by 90° to obtain the three-dimensional imaging capability.

support frame, composed of four lateral panels, where the photomultiplier tubes are mounted. On the top and bottom honeycomb plates are attached. With the mounting brackets the ECAL detector is attached to the unique support structure.
The fibers are read out by four-anode Hamamatsu R7600-00-M4 photomultipliers. Each anode covers an active area of 9 x 9 mm^2, where 35 fibers are read out, defining the volume of a cell in the ECAL. The complete ECAL is subdivided into 1296 cells, corresponding to 324 PMTs. Each of the superlayers is read out by 36 PMTs which are arranged alternatingly on opposite ends. The residual magnetic field around the ECAL is below 20 G. To maintain the performance of the PMTs a magnetic shielding covers not only the PMT base but also the light guides, the HV divider and the front end electronics. The light collection system is illustrated in Figure 2.43. The PMT shielding is a 1 mm thick soft iron square tube with 30.5 mm sides and a length of 74 mm.

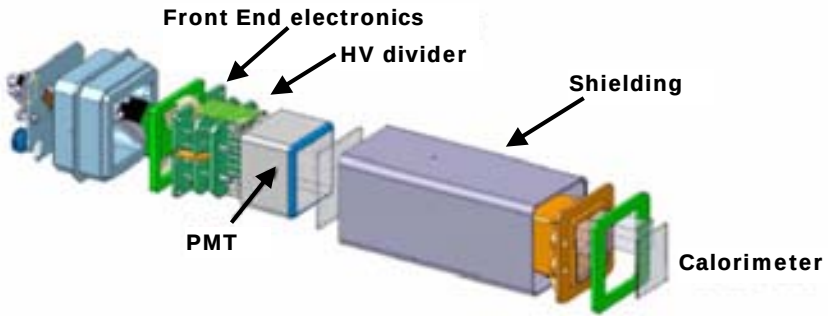

Figure 2.43: Light collection system of the ECAL. A magnetic shielding covers the light guides, the HV divider and the front end electronics to maintain the performance in the magnetic field.

2.6.2 Standalone ECAL Gamma Trigger

The ECAL subdetector provides a very efficient standalone trigger for photons with energies down to 2 GeV. This trigger benefits from the good energy resolution and from the excellent imaging capabilities of the ECAL. The trigger is activated in two steps. Firstly, the count of the PMTs above a threshold in the 6 central layers is evaluated making a *fast decision* available within 180 ns. Secondly a level 1 trigger decision is provided well before 1 μs, obtained by the fast reconstruction of the particle direction. Only particles with an inclination smaller than 20° are accepted, ensuring that the trajectory of the particle passed cleanly through the other AMS-02 subdetectors. The expected trigger efficiency is 90% at 2 GeV and more than 99% for energies larger than 10 GeV. Once the trigger decision has been taken, the trigger signal is forwarded to the AMS-02 global trigger.

2.7 The AMICA Star Tracker and GPS

The information given in in this section is a summary of the references [Car03, Car05, AMS05].

2.7.1 The AMICA Star Tracker

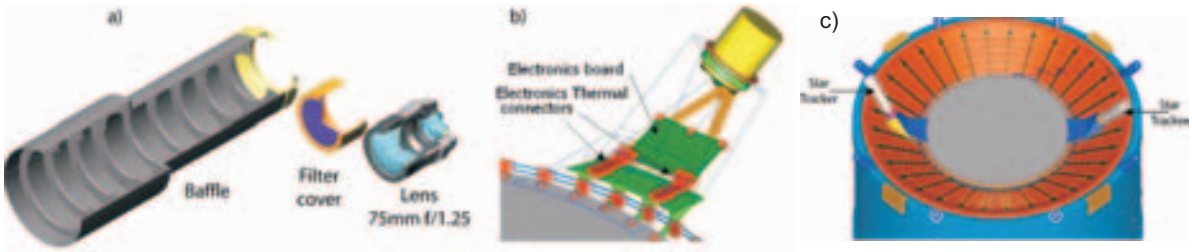

Figure 2.44: Schematics of the star tracker system. Star tracker optics (a), support (b), position on AMS-02 (c).

The AMICA[1] star tracker is a pair of optical telescopes with CCD[2]-cameras, which measures the orientation in space by photographing the stars and comparing this image to a sky map. With this information the pointing direction of AMS-02 can be determined with arc-sec precision and the angular orientation of the stellar field with slightly lower precision.
The CCD-cameras have a frame acquisition frequency of 30 Hz. The lense has a 75 mm focal length and f/1.25 with 60 mm aperture and is filtered to pass 475 mm to 850 mm light for noise reduction, to prevent saturation as well as to protect it from infrared and ultraviolet light. A baffle with a length of 369 mm prevents that direct or reflected light from the space station enters the lense system. It is tapered with an outer diameter of 104 mm at the camera end and 130 mm at the outer end. The CCD has 512 × 512 pixels, each 16 × 16 μm^2. The support structure is made of zero thermal expansion coefficient reinforced carbon fiber composite to ensure mechanical stability. The cameras are oriented in a way such as to maximize their view towards space, avoiding the rotating solar panels, the radiators and the central parts of the space station. The controller unit is based on a 21020 DSP. Separated program, data and image

[1] AMICA, Astro Mapper for Instrument Check of Attitude
[2] CCD, Charge Coupled Device

memory is available. A housekeeping board measures voltages, currents and temperatures. With a photodetector oriented in the same way as the telescope, the sky background intensity can be determined. If the background intensity of the CCD or on the photodetector exceeds a given threshold due to moon or sun reflections or other sources of light, the CCD intensifier is switched off in order to prevent damages. The star tracker acquires stars brighter than 7^{th} magnitude within a field of 6.25° x 6.25°.

2.7.2 GPS

A precision of a few microseconds is required to correlate measurements from AMS-02 to other measurements in the electromagnetic spectrum. Therefore a GPS[1] unit will be mounted on AMS-02. It will be the ALCATEL Topstar 3000D. Two antennas will be mounted in different directions to ensure that the signals from sufficient GPS satellites can always be acquired. Time information will be gathered and will be included together with a local timer of the trigger system in the event data.

2.8 AMS-02 Thermal Control

The information given in in this section is a summary of the reference [AMS05].

Electronic and mechanical equipment used in spacecrafts usually operates efficiently and reliably in a narrow temperature range similar to the temperature we are used to on Earth, such as room temperature. The main reason for this is, that originally most of the components were designed for terrestrial use and later adapted for use in spacecrafts. Typically AMS-02 electronics equipment requires to be maintained in an operational temperature range between -20°C and +50°C. Depending on the subsystem the temperature range can go down to -10°C and +20°C, e.g. for the cryocoolers.
To guarantee the proper thermal environments of space, several factors have to be taken into consideration. AMS-02, mounted on the ISS, resides in vacuum, where aerodynamic heating due to atmospheric drag can be ignored. Likewise convective interaction between AMS-02 and its environment has not to be taken into account. The only way AMS-02 interacts with its environment is by thermal radiation. The radiative interaction is characterized by the exchange of energy by means of direct solar radiation, solar radiation reflected from the Earth - also known as albedo radiation, thermal energy radiated from Earth and radiation from the spacecraft to deep space. A short overview of these kinds of radiation is given in Section 3.4. The primary external factor in the thermal environment is solar illumination. Different areas of the detector are subject to rapidly varying solar illumination alternating with exposure to deep space. The incoming solar radiation depends primarily on the angle between the ISS orbital plane and the direction to the Sun - the so-called beta angle. Figure 2.45 illustrates the definition of the beta angle and Figure 2.46 the variation of the beta angle in time. With the ISS position of 51° of orbital inclination and the tilt of the Earth's axis the beta angle varies between -75.1° and +75.1°, depending on the seasons. For beta angles greater than 70° the orbit is entirely in sunlight, while for beta angles near 0° about 40% of the orbit lies in the Earth's shadow. For the majority of the time the beta angle is between -50° and +50°.
The experiment itself dissipates around 2000 W. The major part (1500 W) is dissipated in the electronics boxes and radiated to outer space through the wake and ram radiators. The wake

[1] GPS, Global Positioning System

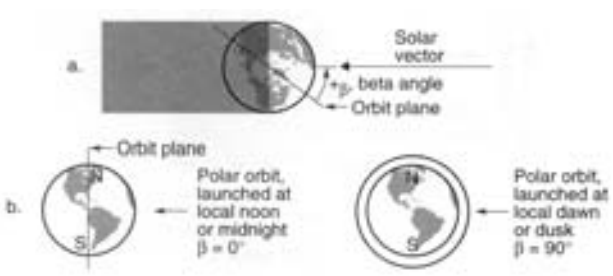

Figure 2.45: Definition of the beta angle. From [Gil02].

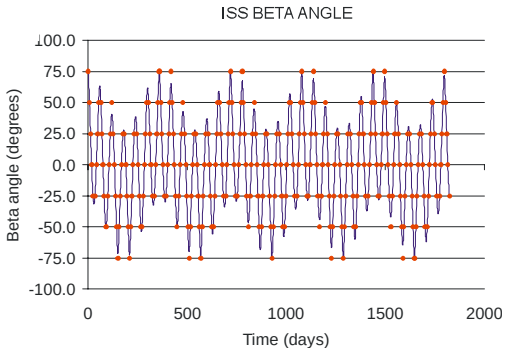

Figure 2.46: Beta angle variation in time.

and ram radiators are mounted directly to the boxes. Heat from the electrical components is conducted from the printed circuit boards, to the box walls or frames which hold the boards and from there directly to the inside surface of the radiators. The radiators are made of an Al:Rohacel:Al sandwich. Inside the radiators Ammonia heat pipes ensure the transfer of the heat from the inside to the outside and also distribute the heat evenly over the entire radiator area of 4 m^2.
To protect the low temperature of 1.8 K in the magnet and in the surrounding tank of superfluid Helium, the vapor cooled shield closest to the outside of the toroidal vacuum case is kept at 68 K, maintained by the four cryocoolers which must remove 432 W of heat. This heat is transported through loop heat pipes with ammonia as the working fluid up to the zenith radiator, from where the heat is removed, the fluid condensed and recirculated by capillary pressure. Two times 70 W are removed from the tracker via the tracker radiators of the TTCS. The small amounts of heat generated by the Lower TOF (4 W), RICH (37 W) and ECAL (72 W) are radiated by small surfaces attached directly to these detectors. Additionally the ECAL uses the unique support structure beams to which it is attached as heat sinks. To prevent heat flow back into the magnet insulating shims between structural members are used and Multi Layer Insulation (MLI) between different volumes to maintain thermal insulation. In this way, between the TRD (20 W) plus upper TOF (3 W) and the vacuum case a 20-layer MLI blanket keeps the radiation load on the vacuum case below 3 W.

Because of the complexity of AMS-02 a thermo-vacuum test for the whole detector is planned at the European Space Agency ESTEC facility in the Netherlands. The purpose of this test is to verify the functional performance of the experiment as well as its thermal control hardware under thermal vacuum conditions.

2.9 Physics with AMS-02

Since AMS-02 will reside in space on the International Space Station for at least three years, it will be able to perform accurate, high statistics, long duration measurement of energetic primary charged cosmic ray spectra and gamma ray spectra. In contrast to ground based experiments AMS-02 grossly profits from its position in space, where measurements are not affected by any disturbing atmosphere. Compared to balloon experiments which have a flight time of several weeks to several months, AMS-02 will provide a significant longer operational

time, with the only limitation being the amount of superfluid Helium which is estimated to last for three years. After that time, AMS-02 will still be able to operate, although without any momentum measurement.
Three major physics goals will be presented in the next subsections: the search for antimatter, the Be^{10}/Be^{9} ratio measurement, and the indirect search for dark matter. Since this is one of the major fields of interest at the IEKP of the Universität Karlsruhe, an emphasis will be put on the indirect search for dark matter.

2.9.1 Search for Antimatter

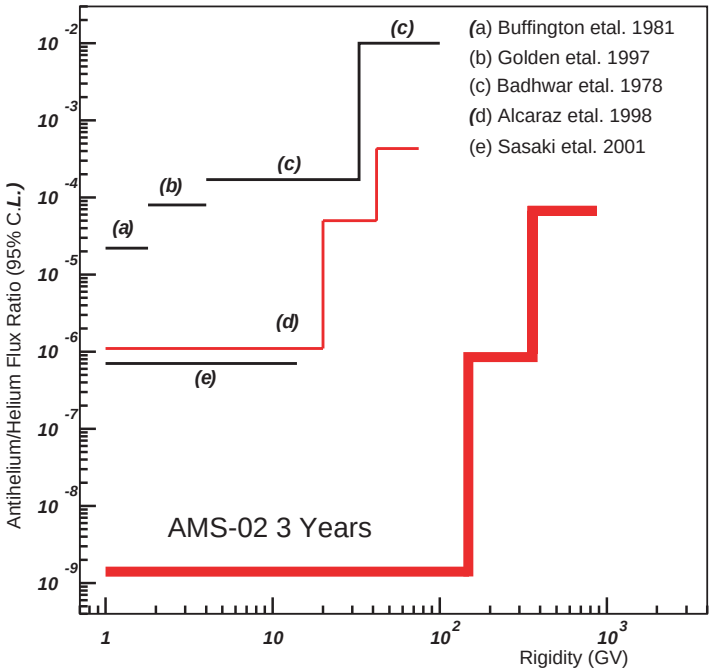

Figure 2.47: Projected AMS-02 limits on the $\overline{He}/He$ flux ratio compared to previous measurements.

The Big Bang theory expects the amount of antimatter to equal the amount of matter in the very beginning. In the early stages after the Big Bang, kT was large compared to the hadron masses. Therefore, it is expected that many types of hadrons, protons and neutrons including their antiparticles as an example, were in thermal equilibrium with radiation, thus being created and annihiliated in reversible interactions.

$$p + \overline{p} \leftrightarrows \gamma + \gamma \tag{2.13}$$

Exactly as normal matter, this antimatter could have formed atoms, stars and galaxies. Light emitted from such antigalaxies could not be distinguished from light emitted from normal galaxies. But, comparable to normal galaxies, also the stars in antigalaxies would emit antiparticles in big amounts which could propagate into matter dominated regions and therefore should be detectable near the Earth. From the measurement of primary cosmic ray nuclei we find today, that there is a paucity of antimatter in our own galaxy. Even on a wider scale within our cluster of galaxies, no evidence for the intense γ-ray and X-ray emission that would follow annihilation

of matter with antimatter was found. In the interstellar medium there is a large number of secondary antiprotons which were created from interactions with high energetic cosmic rays. In contrast to that, the probability of the creation of secondary antiparticles with (Z≥2) is very little. This means that if an antiparticle such as $\overline{C}$ or $\overline{Fe}$ is found, it is thinkable that a whole domain of antimatter exists somewhere far away from our matter dominated region. Such an antinucleus had to be created by a thermonuclear process in an antistar. Moreover, the detection of $\overline{He}$ could hint for the existence of primordial antimatter. For a three year measurement a $\overline{He}/He$ limit of the order of 10^{-9} will be obtained for rigidities up to 130-140 GV/c. The search for antimatter benefits from the large acceptance of 0.5 m^2sr and the little material along the particle's trajectory through AMS-02, thus minimizing the probability for large angle nuclear scattering which could be confused with the signal of anti-nuclei. Figure 2.47 illustrates the expected sensibility on the $\overline{He}/He$ flux ratio compared to previous measurements. [AMS05, Per03, Orb03, dB94]

2.9.2 Age of Cosmic Rays

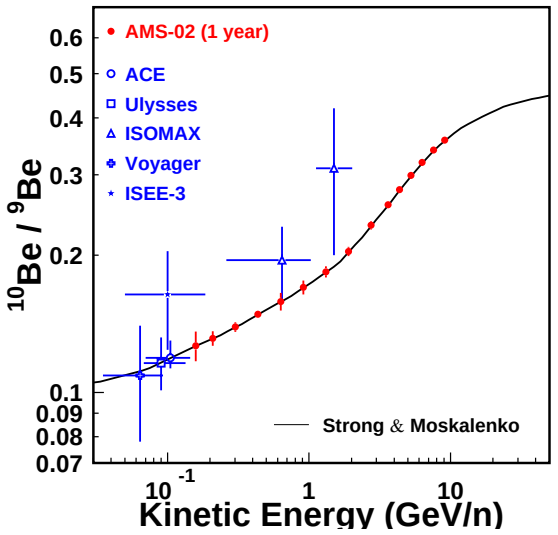

Figure 2.48: Projected AMS-02 one year measurement of the $^{10}Be/^{9}Be$ ratio. Solid line represents the diffusion/convection model prediction.

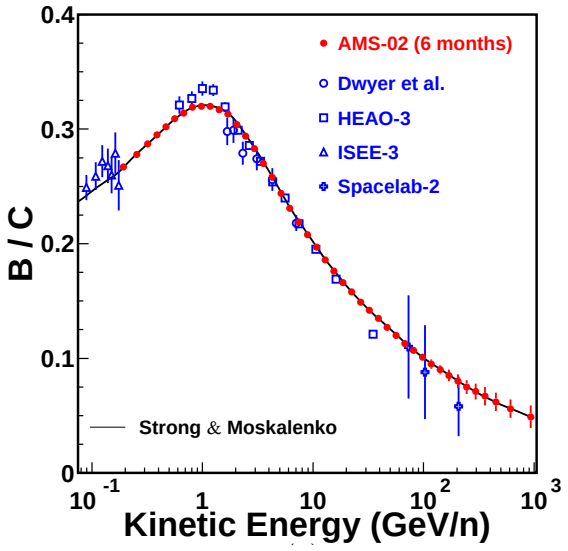

Figure 2.49: Projected six months measurement of the B/C ratio.

Due to the excellent velocity resolution of the RICH, AMS-02 will be able to measure the radioactive ^{10}Be with respect to its stable neighbor isotope ^{9}Be. ^{10}Be has a half-life of 1.6×10^6 years. So this unstable nucleus serves as radioactive clock, providing constraints on the confinement time of galactic cosmic rays (GCR) within the Galaxy. A high ^{10}Be/^{9}Be ratio indicates that most of the cosmic rays are relatively young, otherwise a small ratio indicates that the cosmic rays had to travel longer and the ^{10}Be had more time to decay. Figure 2.48 shows the projected AMS-02 one year measurement of this ratio. Beryllium is a *secondary* constituent[1] of the cosmic rays which was produced by spallation in interaction of heavier *primary* cosmic ray nuclei such as carbon, nitrogen and oxygen with the interstellar material in our galaxy.

[1] more secondary fragments are lithium and boron

The mean density of interstellar material traversed by cosmic rays can be determined: By comparing stable secondary to primary nuclei ratio in cosmic rays for a given propagation model it is possible to derive the mean matter cosmic rays encounter during propagation. As an example, B nuclei as secondary particles are created from primary C nuclei by interaction with the interstellar medium. The projected AMS-02 measurement is shown in Figure 2.49 for a six months measurement time. [AMS05, H$^+$04, H$^+$01]

2.9.3 Indirect Search for Dark Matter

In 1933 Zwicky observed that galaxies in the Coma cluster seem to be moving too rapidly to be held together by the gravitational attraction of visible matter. Also, in the 1960s Vera Rubin found from the observation of star velocities in spiral galaxies, that they move faster than expected from the amount of visible matter in the galaxies. When considering a star of mass m at a distance r from the galactic center with tangential velocity v, we can equate gravitational and centrifugal forces:

$$\frac{mv^2}{r} = \frac{mM(<r)G}{r^2} \tag{2.14}$$

As an example a spiral galaxy consists of a central bulge, where most of the luminous material is concentrated, plus a thin disc. Inside the bulge the mass distribution is $M(<r) \propto r^3$ and therefore $v \propto r$. Outside the hub the mass $M(<r)$ is approximately constant and therefore a velocity distribution $v \propto r^{-1/2}$ is expected. Therefore, an increase at small r and a decrease at large r is expected. In reality the rotation curves are quite flat at large r values, as observed for many spiral galaxies. This leads to the suggestion that the majority of the galactic mass, typically 80-90%, is in the form of dark matter in a halo around the hub and the disk. Since this dark matter is more widely distributed than the visible matter, the dark matter particles can at most have weak interactions. Otherwise it would cluster like the visible baryonic matter near the center of the galaxies. The clustering of the galaxies hints that these particles are non-relativistic, thus massive. This kind of *cold* dark matter is known as Weakly Interacting Massive Particles (WIMPs). It is concluded from recent measurements of the anisotropies of the cosmic microwave background (from WMAP[1]) [S$^+$03] and others, that the amount of visible matter can account for only about 5% of the present energy density of the universe. Dark matter is estimated to about 23%. The majority of about 72% is assigned to dark energy or vacuum energy which is manifested in the Casimir effect. But how can the existence of dark matter be proven and what is the nature of dark matter?
In contrast to direct searches for dark matter in experiments such as DAMA or Edelweiss, which focus on the cryogenic detection signatures of scintillation light, heat and ionization caused by recoil atoms of interaction with dark matter, the indirect search for dark matter in AMS-02 is based on the analysis of diffuse gamma-ray, antiproton and positron spectra.
Even without knowing of which nature WIMPs are, it is possible to deduce their annihilation cross section. We are searching for cold dark matter, meaning that they must be non-relativistic when they "freeze out" in an early evolution stage of the universe. This freeze-out occurs when the WIMP ($\chi\overline{\chi}$) annihilation rate falls below the expansion rate of the universe:

$$N < \sigma v > \leq H, \tag{2.15}$$

where N is the WIMP number density, v is the relative velocity of both annihilation partners and σ is the annihilation cross section. H is the Hubble parameter at the time of freeze-out.

[1] WMAP, Wilkinson Microwave Anisotropy Probe

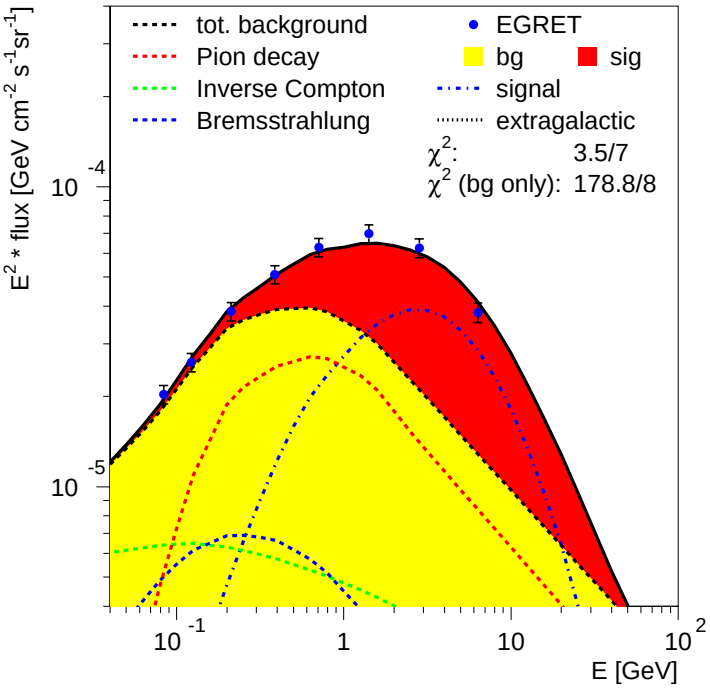

Figure 2.50: Fit of the background to EGRET data between 0.1 GeV and 0.5 GeV. The gamma excess at energies above can be explained by photons produced by dark matter annihilation. [dB05]

This formula can be understood when considering that the left term represents a collision rate which in equilibrium should be of the order of the age of the universe. Otherwise there is just not enough time for enough collision to achieve equilibrium.
From the relic density and the Hubble constant it is possible to find a thermally averaged annihilation cross section of

$$< \sigma v >= 2 \times 10^{-26} cm^3/s, \tag{2.16}$$

which is a cross section expected for weakly interacting particles. According to the rules of particle physics the annihilation products are predominantly quark-antiquark pairs, which form stable particles by hadronization such as protons, antiprotons, electrons, positrons, neutrinos and gamma rays. While the trajectory of charged particles is affected by interstellar magnetic fields and scattering, the detection of gamma-rays point directly back to the source, thus providing a perfect way to observe the intensity of the gamma ray emissions in the various sky regions. Therefore by observing the intensity of the gamma ray emissions it is possible to reconstruct the dark matter density distribution. This implies the necessity to distinguish between the gamma-rays from DM Annihilation (DMA) and the ones from the background on a statistical basis. The gamma rays from the background are dominated by proton-proton interactions in the interstellar space which generate a soft gamma ray spectrum due to the steeply falling power law spectrum of the protons. The DMA yields mono-energetic quarks, which produce a harder gamma-ray spectrum with a shape different from the background. Since the spectral shapes of gamma-rays from both background and DMA are well known, they can be fitted to the data with free normalization factors. From this it is possible to determine the relative contributions from DMA and the galactic and extragalatic background.

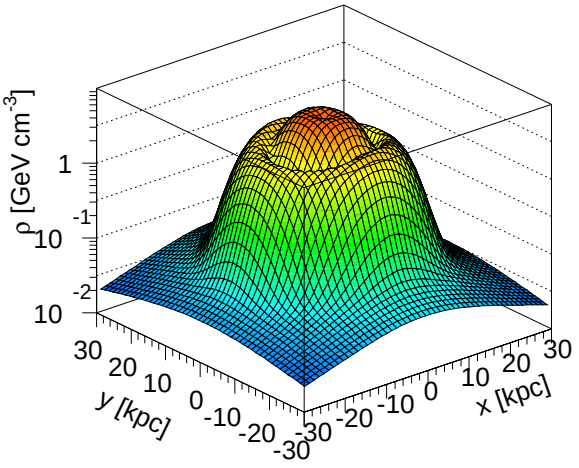

Figure 2.51: Halo profile in the xy plane of the galactic disc. [dB05]

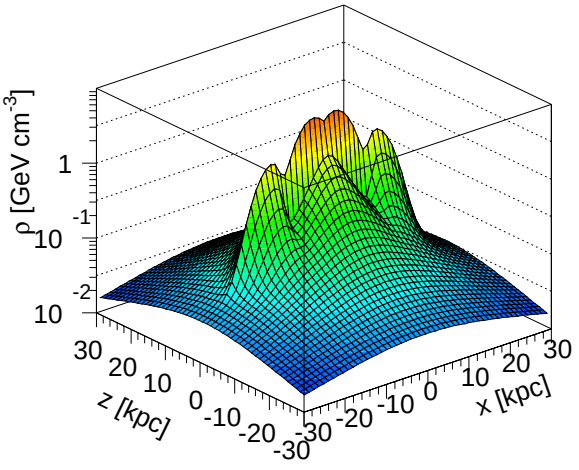

Figure 2.52: Halo profile in the xz plane of the galactic disc. [dB05]

In the years 1991 to 2000 a detailed gamma ray distribution over the whole sky was measured by the Energetic Gamma Ray Emission Telescope (EGRET) as part of the four instruments on the Compton Gamma Ray Observatory (CGRO). An excess of gamma rays above the expectation from the conventional background was observed. Different background models do not describe the shape of the gamma spectra very well in all sky directions. Figure 2.50 demonstrates a fit of the background and DMA with free normalizations to the gamma ray spectrum towards the galactic center. The contributions from the background and the contribution from DMA are illustrated. Below 0.5 GeV the DMA hardly contributes, allowing to normalize the background between 0.1 GeV and 0.5 GeV with the absolute predictions from the well-known program GALPROP. The difference between the data and the GALPROP background is defined as the EGRET excess, which can be well described by the contribution of gamma-rays originating from the hadronization of mono-energetic quarks for a WIMP mass of 65 GeV. An increased WIMP mass shifts the DM contribution to the right. In this way an estimate of the WIMP mass between 50 GeV and 100 GeV can be given. The background normalization was performed at lower energies, so the data and GALPROP shapes can only differ at higher energies thus changing the DMA normalization somewhat. By varying the GALPROP background between different models, a DMA normalization factor between 20 and 100 can be obtained in comparison with the DM annihilation cross section discussed above. This is the right order of normalization factors expected, since the DMA signal is proportional to the DM density squared and any clustering of DM will boost the signal compared with homogenous DM. So this normalization factor is known as boost factor. This excess of data over the background is apparent in all sky directions and has the same spectral shape everywhere which is characteristic for a signal from DMA. When fitting the shapes of background and DMA in 180 sky directions it is possible to determine the distribution of DM in the sky from the normalization factor needed. The flux in a given sky direction is composed of the product of annihilation cross section, boost factor and line-of-sight integral over the DM density squared. Outside the disc a profile can be asumed with a flat core at the center and a $1/r^2$ decrease at distances larger than the scale length of four kpc, as expected for a flat rotation curve. This profile which is common for many spiral galaxies describes the distribution of the EGRET excess well

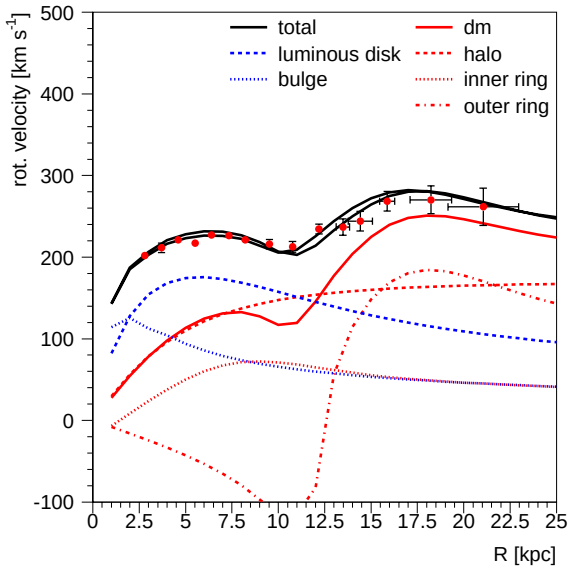

Figure 2.53: Rotation velocity plot with contributions from inner and outer DM ring. [dB05]

outside the galactic disc but fails to describe the data in the disk. Inside the disk an additional substructure was found in the form of doughnut shaped rings at radii of four and 14 kpc with a Gaussian width in radius of a few kpc. The position of our solar system is located at 8 kpc from the center between this inner and outer ring. Figure 2.51 shows the best fitted halo profile for the DM density distribution in the galactic disk (xy-projection) and Figure 2.52 shows the xz-projection. It was found that the location and shape of the inner ring coincides with a ring of molecular hydrogen which forms from atomic hydrogen in the presence of dust or heavy nuclei. The outer ring coincides with the ring of stars discovered in 2003 which cannot be part of the disc due to its small velocity dispersion and the large scale height in the kpc range. This ring is thought to originate from the infall of a dwarf galaxy. In this case an additional DMA is expected here. An explanation for the presence of this structure in the galactic disc, and not somewhere else could be that the infall occurred early and the disc may precess until angular momenta of disc and halo get aligned. To calculate the DM mass from the outer ring, one has to multiply the total WIMP number density found times the WIMP mass, which yields a few 10^{10} solar masses, roughly a factor 50 higher than the observed baryonic mass in the ring. This ring mass is comparable to the baryonic mass of our Galaxy which suggests that the ring may have a substantial influence on the rotation curve, slowing down the rotation speed inside the ring and increasing the rotation speed outside the ring. The resulting calculated rotation velocity curve is compared with data in Figure 2.53.
So far only the dark matter search using the gamma-ray spectrum has been presented. As mentioned above from the hadronization process also positrons and antiprotons are created, which also should yield an excess over the conventional background. Figures 2.54 and 2.55 show these plots compared with HEAT[1], AMS-01 and BESS[2] data. For this indirect search for dark matter, no assumptions were made concerning the nature of dark matter except that the annihilation produces hard gamma rays consistent with the fragmentation of monoenergetic

[1]HEAT, High Energy Antimatter Telescope
[2]BESS, Balloon-borne Experiment with a Superconducting Spectrometer

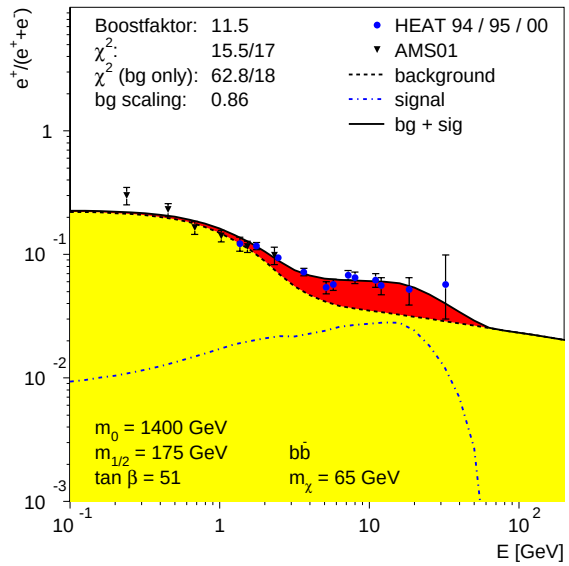

Figure 2.54: Positron fraction. [dB05]

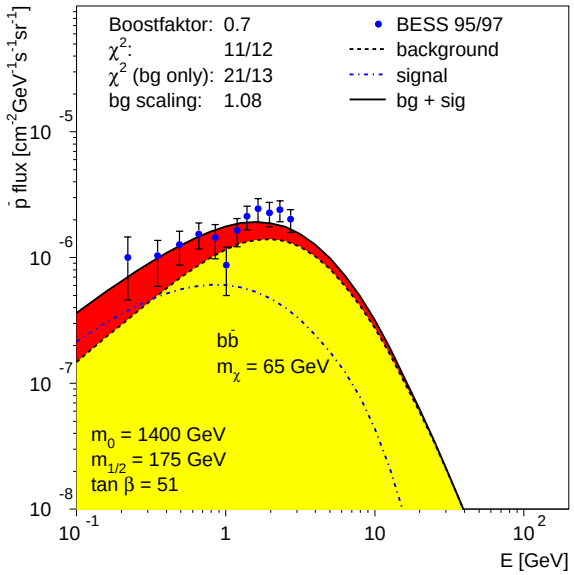

Figure 2.55: Antiproton spectrum. [dB05]

quarks between 50 and 100 GeV. A possible WIMP candidate is predicted by SUperSYmmetry (SUSY), which is an extension to the Standard Model of particle physics. SUSY presupposes a symmetry between fermions and bosons, which is achieved by doubling the particle spectrum of the Standard Model. For every fermion with spin 1/2 one introduces a boson with spin 0 and for every boson with spin 1, a fermion with spin 1/2 is introduced. Heavier SUSY particles can decay to lighter ones in processes where R parity is conserved - a new multiplicative quantum number. Standard Model particles have R parity 1 and SUSY particles have R parity -1. This R-parity conservation prevents the lightest supersymmetric particle to decay further. Usually the LSP is identified with the neutralino, a neutral Majorana fermion which is the lightest of the states arising from a linear combination of the photino $\tilde{\gamma}$, zino $\tilde{Z}^0$ and two higgsinos $\tilde{H}_1^0$ and $\tilde{H}_2^0$.

$$\tilde{\chi}^0 = N_1\tilde{\gamma} + N\tilde{Z}^0 + N_3\tilde{H}_1^0 + N_4\tilde{H}_2^0 \quad with \quad \sum_{i=1}^{4} |N_i|^2 = 1 \tag{2.17}$$

AMS-02 will measure the positron spectrum, the antiproton spectrum and the gamma-ray spectrum to contribute to the indirect search for dark matter. [Per03, AMS05, dB94, JKG96, dBHSZ03, dB04, dBHSZ04, dBGK+]

Chapter 3

Operation in Space on the International Space Station

The following chapter describes the technical and natural environment AMS-02 has to face during the Space Shuttle start and on orbit, when mounted on the ISS. Since this chapter touches research fields, which are not directly related to the topic of this thesis, it is kept as brief as possible. Nevertheless, this knowledge is essential to the successful design of AMS-02 including its electronics and was kept in mind at any time during development and production.

3.1 The Space Shuttle

NASA started the shuttle program on January 5th, 1972 to proceed with the development of a reusable low cost Space Shuttle system. The first Space Shuttle rolled out on September 17th, 1976. It was not fully functional and could not be used for space flight but it completed a very successful series of landing tests which served as the first real validation of the gliding abilities of the design. Five fully functional orbiters were built. Space Shuttle Columbia was first launched April 12th, 1981. The next shuttles to be delivered were Challenger in July 1982, Discovery in November 1983, Atlantis in April 1985. After the Challenger disaster, in which the spacecraft and the crew of seven astronauts were lost in an explosion during launch in January 1986, the orbiter Endeavour was built as a replacement using spare parts originally built for the other orbiters. It was delivered in May, 1991. Space Shuttle Columbia was lost, with all seven crew members, during re-entry on February 1st, 2003. This event had significant impact on the schedule for AMS-02, since the Space Shuttle fleet was grounded for more than two years, blocking the further construction of the ISS and delaying the AMS-02 shuttle start.

Figure 3.1: Picture of a NASA Space Shuttle launch. From [Wik05a].

The Space Shuttle system consists of four main elements: the orbiter spacecraft, two solid rocket boosters, an external tank and three Space Shuttle engines. A picture of a Space Shuttle during launch is shown in Figure 3.1. A major system feature is that the orbiter and the two

solid rocket boosters are reusable. The orbiter carries up to eight persons, in case of emergency even a total of ten persons. The acceleration load is never greater than 3 g[1]. The shuttle has a large payload bay taking up much of its length of 37 m (122 feet). Its wingspan is 24 m (78 feet). Mounted on the payload bay door inner surfaces, there are heat radiators. The payload bay doors are kept open for thermal control while the shuttle is on orbit. Propellant fuel for the three main engines, called the Main Propulsion System (MPS) is liquid hydrogen and liquid oxygen is used as oxidizer. The propellant is carried in separate containers located in the large external tank and is supplied to the main engines. The propellant mixture in the solid rocket boosters is composed of ammonium perchlorate as oxidizer (69.6% by weight) and aluminum (16%) as fuel. Furthermore, there are iron oxide as a catalyst (0.4%) and a polymer (12.04%) that acts as a binder to hold the mixture together. The maximum launch payload is 28.800 kg (63,500 lb). For spacecraft control in orbit such as orbit circularization, orbit transfer, rendezvous and deorbit, the Orbital Maneuvering System (OMS) is used. The orbiters's Reaction Control System (RCS) provides the thrust for attitude maneuvers like pitch, yaw and roll and for velocity changes along the orbiter axis. There is a forward RCS located in the forward fuselage nose area and an aft RCS located with the orbital maneuvering system in the OMS/RCS pods. The propellants for both systems are MMH/N_2O_2.
The Space Shuttle is launched in the upright position. Thrust is provided by the two Solid Rocket Booster and by the three Space Shuttle engines. Two minutes after launch the boosters are burnt out and are separated from the external tank. The solid rocket boosters fall into the ocean and are recovered for reuse. The three Space Shuttle engines keep on firing for about eight minutes more, and stop just before the shuttle enters into an orbit. At that time the external tank is separated from the orbiter. It follows a ballistic trajectory back to a remote area of the ocean. The external tank is not recovered for reuse.
In case of a failure which affects vehicle performance, such as a main engine failure or a cabin leak, the selection of an abort mode might be required. There are four types of intact abort modes.

- *Abort To Orbit (ATO)*
  In this abort mode the vehicle will achieve a temporary orbit that is lower than the nominal orbit. This mode requires less performance than foreseen for the original orbit and allows to evaluate problems in order to either deorbit or raise the orbit and continue the mission.

- *Abort Once Around (AOA)*
  The vehicle flies once around the Earth before making a normal entry and landing. Two OMS burns are required in this mode, with the second one being a deorbit maneuver.

- *Return to Launch Site (RTLS)*
  The orbiter flies downrange to dissipate propellant, turns around under power to return directly to a landing site near the launch area.

- *Transatlantic Landing (TAL)*
  This mode allows the orbiter to land intact on the other side of the Atlantic Ocean. The spacecraft follows a ballistic trajectory, no OMS thrusts are required. This mode was designed to improve the options available, when a main engine fails after the last RTLS opportunity but before the last time an AOA can be accomplished.

[1] 1 g is the surface gravitational acceleration of 9.8 m/s^2.

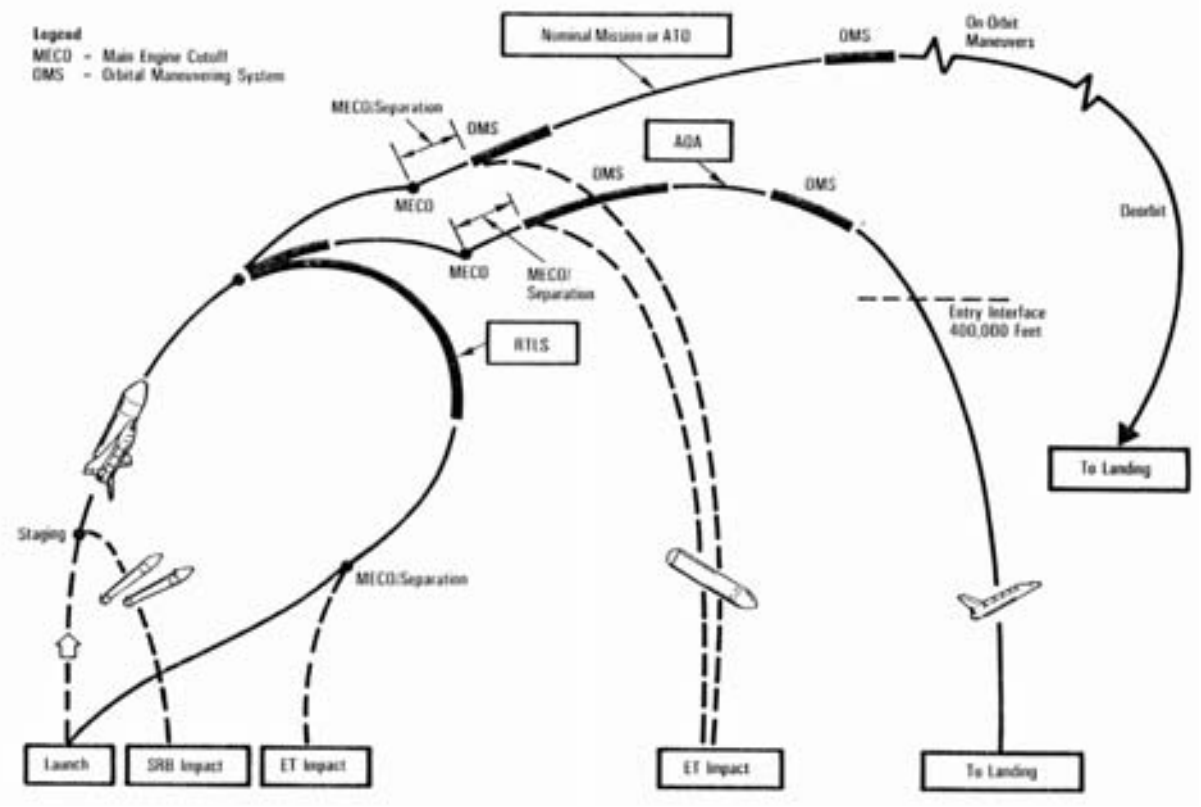

Figure 3.2: Mission profile of a Space Shuttle launch. From [Nat88].

Contingency aborts are possible when more severe failures have happened or an intact abort is not possible. Generally, the spacecraft would be lost. A normal mission profile including possible abort modes is shown in Figure 3.2.

To initiate the deorbit maneuver, primary RCS engines are used to rotate the orbiter tail first in the direction of the velocity. Then the OMS engines are fired to decrease the orbiter's velocity. In this process the orbiter reduces its velocity from about 7.74 km/s (25,405 feet/s) to approximately 91 m/s (300 feet/s). In the beginning of the reentry sequence, still the primary RCS engines are used to control the orbiter's attitude. The entry interface is considered to be at 122 km (400,000 feet) altitude. As soon as aerodynamic pressure builds up, the flight control surfaces become active and the RCS engines are inhibited. During entry the orbiter outer skin reaches nearly 1649°C (3,000°F). The Thermal Protection System consisting of materials selected for stability, high temperature and weight efficiency, is used to protect the orbiter. Reinforced Carbon-Carbon is used e.g. on the wing leading edges and the nose gap where temperature exceed 1260°C (2,300°F.)
The unpowered spacecraft glides to Earth and lands on a runway like a normal airplane. When it reaches ground its speed varies between 343 and 362 km/h (213 and 225 miles/h).
[Nat88, Wik05a]

Figure 3.3: Full view of the International Space Station. Photographed on December 2nd, 2002 by a crew member on board the Space Shuttle Endeavour following the undocking. The newly installed Port One (P1) truss now complements the Starboard One (S1) truss in center frame.

3.2 The International Space Station (ISS)

The International Space Station is build by a partnership of five space organizations: the National Aeronautics and Space Administration (NASA), the Russian Federal Space Agency, the Japan Aerospace Exploration Space Agency (JAXA), the Canadian Space Agency (CSA/ASC) and the European Space Agency (ESA). The ISS is being built in orbit around the Earth at an altitude of approximately 400 km. It orbits the Earth at a period of about 92 minutes at an inclination of about 52°. Every day the station loses roughly 100 m of altitude due to atmospheric drag. From time to time this has to be adjusted by the ISS regulation systems. A photo of the ISS in its latest stage of expansion as of November 2002 is shown in Figure 3.3.
The International Space Station is being built with more than 50 assembly and utilization flights involving at least three space vehicles: the American Space Shuttle, the Russian Soyuz and the Russian Proton rocket. Currently Russian Progress M1 flights provide logistics. In the future the European Autonomous Transfer Vehicle (ATV) and the Japanese H-2 transfer vehicle will join these supply transports. Also, the Space Shuttle can use the Multi-Purpose Logistics Module (MPLM) build by Agenzia Spaziale Italiana (ASI) under contract of NASA to allow transportation of pressurized payloads. Three MPLMs are available: Leonardo, Raffaello and Donatello. The assembly began in November 1998 when a Russian Proton rocket placed the Zarya module in orbit. In December of the same year the Space Shuttle brought

the Unity Module into orbit and attached it to the Zarya module. The first permanent crew, called the Expedition One Crew, arrived at the ISS on November 2nd, 2000 with the Russian Soyuz Rocket. The assembly continued with the Space Shuttle until February 1st, 2003, when the Space Shuttle fleet was grounded following the loss of the Space Shuttle Columbia during reentry into the atmosphere. Since that time the crew exchanges have been accomplished using Soyuz spacecraft instead of Space Shuttles.
The further extension of the ISS however had to be delayed until the Space Shuttle fleet returns to flight. Currently the space station consists of the following modules:

- *Zarya*[1]
  This module is also known as the Functional Cargo Block. Zarya provides electrical power storage, propulsion and guidance to the ISS during the initial stage of assembly. Later, when other modules with specialized functionality are constructed, Zarya will be used primarily as storage. Zarya was built in Russia, although it was officially owned and paid for by the United States.

- *Unity*
  Unity is the first of three connecting modules that will be built for the ISS. It has six berthing ports, each on one side. Essential space station resources, such as fluids, environmental control and life support systems, electrical and data lines are routed through Unity to supply other work and living modules. Unity was built by the United States.

- *Zvezda*[2]
  Zvesda is the Russian service module providing living quarters, a life support system, a communications system, electrical power distribution, a data processing system, a flight control system and a propulsion system. These quarters and systems will be supplemented or replaced by future ISS modules.

- *Destiny*
  The American Destiny Laboratory Module will support experiments and studies in cancer, diabetes and materials. There are five life support systems racks providing electrical power, cooling water, air revitalization, temperature and humidity control.

- *Quest Joint Airlock Module*
  This module is designed to be the primary airlock for the ISS providing the ability to host spacewalks with both the American EMU[3] and Russian Orlon spacesuits

- *Docking Compartment*
  The Russian Docking Compartment is currently connected to the Zvezda module. It provides capability for Russian-based Extra Vehicular Activities (EVAs) and docking ports for the Soyuz-TMA and Progress-M spacecrafts.

Modules to be added in the future are:

- *Node 2 (NASA)* - providing air, electrical power, water and other life support systems

- *Multipurpose Laboratory Module (Russia)* - serving as crew work and rest area and for experiments docking and cargo

[1] Russian: Sunrise
[2] Russian: Star
[3] EMU, Extravehicular Mobility Unit

- *Columbus Orbital Facility (ESA)* - the European science module
- *Japanese Experiment Module (JAXA)*
- *Centrifuge Accommodations Module (NASA)* - providing controlled gravity for experiments
- *Russian Research Module* - facilities for Russian experiments and research
- *Science Power Module (Russia)* - supplying the ISS with additional power of four solar arrays. The European space agency builds a robotic arm to be mounted for maintaining the Science Power Module.
- *Cupola (ESA/NASA)* - adds the feature of direct viewing for robotic operations to the ISS

Further parts of the ISS are the *ISS trusses*, *Photovoltaic Modules (PVMs)* and the *Canadarm2*. The *ISS trusses* form a structural backbone to the station and provide mountings for unpressurized modules, radiators, solar arrays and other equipment. AMS-02 will be mounted on the S3 truss. An explosion drawing of the International Space Station with the elements on orbit today and future elements is shown in Figure 3.4.
Electrical power is the most critical resource because it allows the crew to live comfortably, perform scientific experiments and to safely operate the station. The *Photovoltaic Modules* generate and store power to provide two sources of primary power at U≅160 V DC, called power channels. Each power channel is able to deliver continuous power throughout the ISS both during insolation and eclipse. Near the users the primary power is converted by DC/DC converters to secondary power with U≅124 V DC and distributed along a variety of paths to the individual users. Also the DC/DC converters isolate the secondary system from the primary system to maintain uniform power quality throughout the station. This two-level power system allows to compensate for factors such as electrical line losses, hardware degradation and solar array aging, while still providing consistent secondary voltage for ISS users. In the Secondary Power System, there is no redundancy. To gain redundancy a critical user has to select between input power sources that use different power channels and therefore different secondary power paths. Once the ISS is completed, four photovoltaic modules (S6, S4, P4, P6) will be present providing eight power channels. With a full complement of batteries, the power storage system is designed to require only 35% depth of discharge to supply the ISS with nominal power during the period of orbital eclipse. If the power generation functions fail, the batteries can supply power for one complete orbit following a period of orbital eclipse with a reduced ISS power consumption.
The *Canadarm2* is 17.6 m in length with a mass of 1,800 kg and a diameter of 35 cm. It is capable of handling large payloads of up to 116,000 kg. *Canadarm2* can reach many parts of the station by an inchworm-like movement, where it connects end-by-end on special fixture which provide power, data and video connections. Also it can move with the Mobile Base System, traversing the main trusses.
There are six subsystems providing data and communication transmission. The *Internal Audio Subsystem (IAS)* distributes audio onboard the station and to external interfaces. The *Ultrahigh Frequency Subsystem*[1] *(UHF)* is used for voice, command and telemetry communication between the station and the orbiter or to the astronauts wearing Extravehicular Mobility

[1] This subsystem is also known as the Ultrahigh Frequency Communication System (UCS)

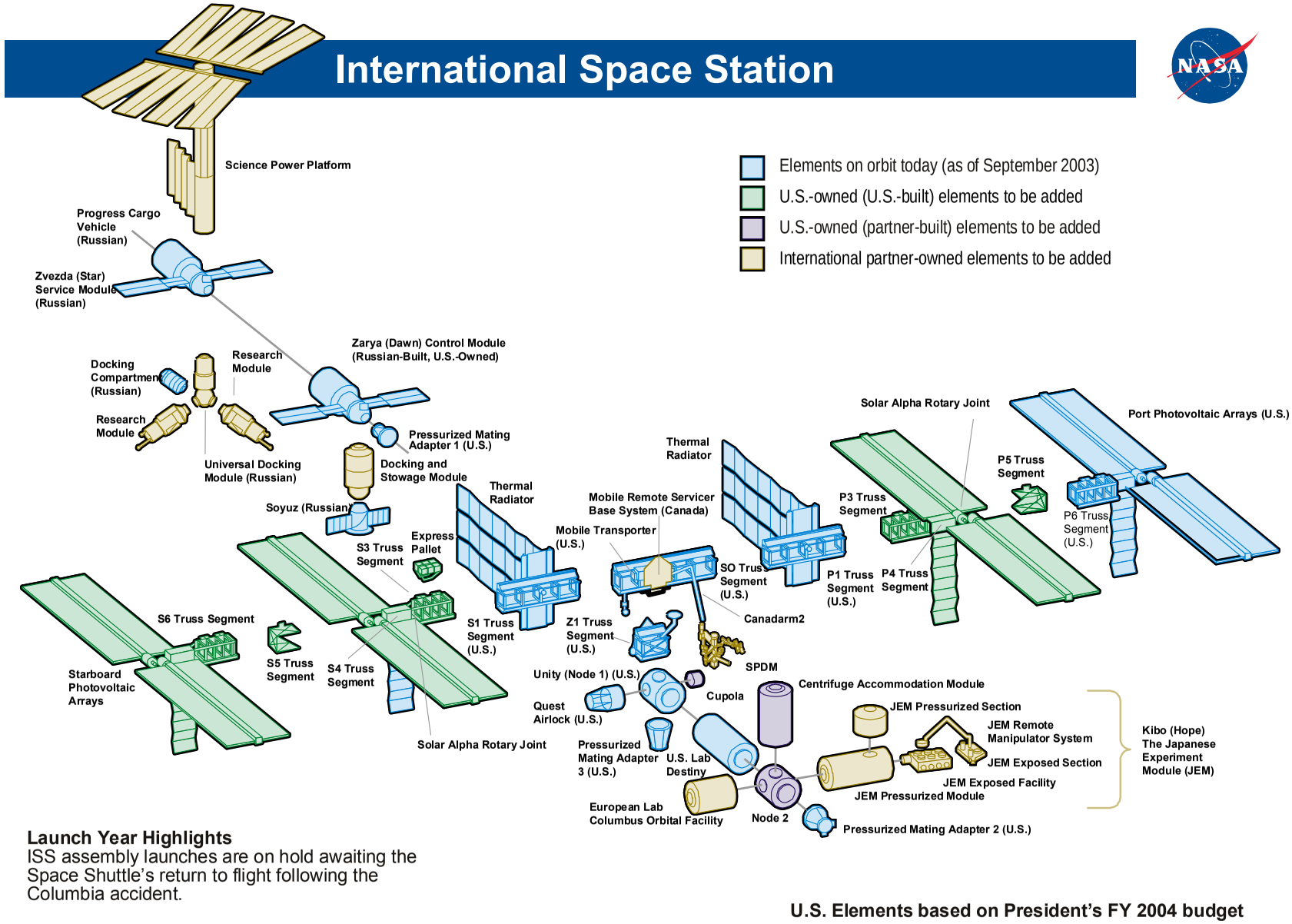

Figure 3.4: Explosion drawing of the International Space Station.

Units (EMU) for voice, biomedical and EMU data transfer during spacewalks. The *Video Distribution Subsystem (VDS)* distributes video onboard the station and to external interfaces, including the Ku-band for downlink, which is described below. The following two subsystems represent the communication channels to Earth and are therefore of utmost importance for AMS-02 communication:

- *The S-band subsystem (S-band)*
  The S-band transmits voice, commands, telemetry and files between the ground and the station via TDRS satellites (Tracking and Data Relay System Satellites). It is the primary communication system for command and control of the ISS. In case of a loss of one channel of audio or one of the antennas, it can be operated in a degraded mode. The S-band transmits and receives at a high data rate of 192 kbps return link (from the station via TDRS to ground control) and a forward link of 72 kbps; at a low data rate of 12 kbps return and 6 kbps forward. Forward data is encrypted on the ground to ensure safety of the uplinked commands. The S-band coverage is about 50% per orbit.

- *The Ku-band subsystem (Ku-band)*
  The purpose of the Ku-Band subsystem is to provide a high data rate downlink for the US Segment of the ISS. It can be used for real-time or recorded video, payload data, ISS systems telemetry and two-way transfer of files. The capacity of the Ku-band is large. However, there is much data to be transmitted from the various experiments, video and recorded systems telemetry, making it necessary to reconcile the amount of data to the capacity of the subsystems. The Ku-band capacity is about 50 Mbps and can be expanded in the future to 150 Mbps, with an overhead of about 6.8 Mbps. Data can be sent from up to twelve different channels. Up to four channels can contain video images. The Ku-band coverage is about 70% per orbit.

[AN05, Div98, Wik05b]

3.3 Environmental Considerations

The Earth's protective shield, the atmosphere, together with the gravitational force, the familiar one g environment, provides a suitable stable environment in which the human species has been able to evolve. Additionally, its technical acquisitions are strongly affected by this familiar environment. As soon as technical equipment has to work in space flight, it implies the ability to work with its removal. This has significant and sometimes unexpected implications since space environment influences the behavior of materials and the way in which systems behave as a whole. Needless to say, a spacecraft not only has to withstand the hostile environment of space but also has to cope with the environment of all previous phases of its life, namely manufacture, prelaunch, launch, before operating in its dedicated domain.

3.3.1 Launch

During launch high levels of vibrations occur associated both with the noise field and structural vibrations. Furthermore, modest-to-high levels of accelerations during ascent are expected, mechanical shock due to pyrotechnic device operation, a thermal environment that differs from both laboratory and space environment and a rapidly declining ambient pressure.

The sources of the severe acoustic/vibration environment during launch are both the operation of the launch vehicle's main engines and also the aerodynamic buffeting as the vehicle rises through the lower region of the Earth's atmosphere. Two peak levels occur. The first one during lift-off, when the rocket motor fires and the exhaust products are reflected from ground. During ascent the contribution from ground reflection decreases but still a variety of mechanical spacecraft components such as a liquid fuel turbopump operation continues to excite the vehicle's structure. Moreover, the vibration excites the launch shroud to generate a secondary acoustic field which may be even more harmful to light flexible components such as solar arrays. The second peak level during launch occurs during transonic flight, when the launch shroud gets excited by the unsteady flow field around the vehicle. To verify that a cargo element can survive these vibrations, extensive vibration qualification tests have to be performed during development.
The static peak acceleration has to be taken into account, as well, which is for the Space Shuttle 3 g. This is of special importance for astronauts in manned space flight. Greatest protection is provided when the astronaut is on his or her back during launch.
Mechanical shock is experienced when latches or explosive bolts are used at ignition of rocket motor stages and their following separation, launch vehicle/payload separation or during docking or landing. These events cause high-acceleration levels lasting only a few milliseconds. As an example for the Ariane rocket, during payload separation the peak excitation is some 2000 g at frequencies above 1.5 kHz.
The thermal heating experienced during launch is caused by the aerodynamic frictional forces of the vehicle moving at high velocity through the atmosphere. The temperature reached is determined by the specific heat of the shroud material and a balance between friction heating and radiative and convective heat losses.
During launch the ambient atmospheric pressure declines from 1 bar to 0 bar within the short time of about 2 minutes. In case of the shuttle, the venting of the cargo bay can be controlled. Provisions have to be foreseen to allow proper venting of cargo elements, such as electronics boxes.
Great care has to be taken that electromagnetic interference (EMI) does not cause the activation of part of the payload, which could represent a possible hazard. [Sta03]

3.3.2 Solar Radiation

The Sun provides all the heat input to the solar system, excluding planetary radioactive decay processes. The Sun's mass accounts for 99.9% of the total. Fundamentally the Sun is a giant thermonuclear fusion reactor with a surface temperature of ∼5800 K. The photosphere is the visible surface of the Sun, being actually a layer of about 100 km thickness, yet very thin compared to the 700000 km radius. Its spectrum approximates to that of a black body, with discrepancies at some wavelengths arising in the solar atmosphere. There are two primary regions of the solar atmosphere causing these discrepancies. The first region represents the chromosphere which extends to a few thousand kilometers above the photosphere with a temperature peaking at ∼10000 K. Enhanced ultraviolet radiation is emitted from this region. The second one is the upper atmosphere, called the corona which becomes more tenuous and extends to several solar radii. With a nominal temperature of 2×10^6 K, it emits substantial amounts of X-rays. The nominal release of energy from the Sun is about 3.85×10^{26} W.
Another outward flux from the Sun is the solar wind. It is basically a flow of plasma expelled at high velocity. It forms the outermost layer of the solar atmosphere, which is continuously

driven outward as a result of the Sun's radiation pressure. When it reaches the Earth, the speed of the wind is ∼450 km/s with a density of ∼9 protons/cm^3 and a kinetic temperature of ∼100000 K.
Periods of high solar activity appear when there are a large number of sunspots. Actually sunspots are regions which are cooler than the surrounding surface. They emit less radiation and thus appear as dark spots. The enhanced emission of radiation during the presence of a large number of sunspots, most notably at X-ray and γ-ray energies is associated with solar flares, which occur at sites near sunspots. The general level of activity has a well-defined 11-year cycle. [Sci05, Sta03]

3.3.3 Orbit Environment

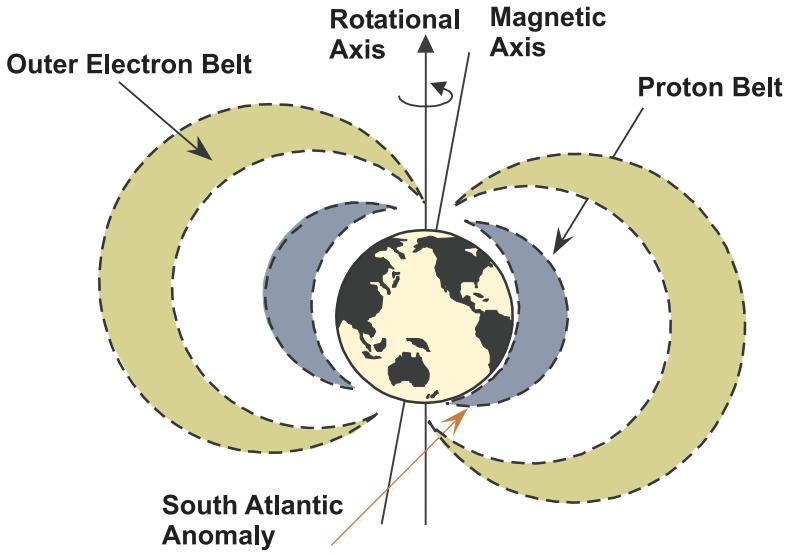

Figure 3.5: Sketch of the Earth with its Van-Allen belts.

In the near-Earth environment, several types of ionizing radiations exist that impact upon spacecraft systems. Energetic protons and electrons are trapped in the Earth's magnetic field and generally follow the magnetic field lines. The locations around the Earth where these particles are trapped are called the *Van-Allen radiation belts*[1]. Additionally, there may be significant fluxes of heavy ions such as helium, nitrogen and oxygen, whose atmospheric densities depend on solar and geomagnetic activity. A dominant feature of the radiation environment is the region known as the South Atlantic Anomaly, where due to the offset and tilt of the geomagnetic axis relative to Earth's rotation axis, parts of the radiation belt are brought to lower altitudes causing enhanced radiation. The effects of these particles are degradation of electronics parts due to accumulated dose, degradation of solar array performance due to displacement damage, single event upsets (SEU) and dielectric charging. Electrons and protons contribute both to the total dose. Protons dominate in low altitude orbits (less than about 800 km) and electrons dominate in high altitude orbits including geosynchronous orbits. Figure 3.5 illustrates the location of the van-Allen Belts around the Earth.

[1] James Alfred Van-Allen (born September 7th, 1914), American physicist associated with the University of Iowa

Another phenomenon is electrostatic charging of a spacecraft traveling through the near space environment. Consequently currents will occur between the space vehicle and the plasma and any charged imbalance may be equalized by arcing. There are two major sources of currents: firstly the ambient plasma itself and secondly photoelectron emission due to solar sunlight, particularly due to its short wavelength component.
Impacts of meteoroids and micrometeoroids, which are solid objects whose mass and size vary over many orders of magnitudes, generally cause degradation of surface thermal properties. Even the possibility of component failure exists. Near large gravitational masses such as the Earth they occur more often.
Another danger imposes man-made debris, consisting of aluminum oxide dust particles from solid rocket exhausts, instrument covers, nuts, bolts, rocket upper stages additionally to the naturally occurring micrometeoroid environment. Its size varies between 0.001 mm to 10 m in diameter. Particles greater than 1 mm cause a threat to the International Space Station. Smaller particles can have a flux that is high enough to erode surfaces and possess enough energy to penetrate protective coatings. [Sta03]

3.3.4 Material Outgassing

At spacecraft altitudes in which a pressure of 10^{-11}-10^{-15}Pa resides, outgassing of materials occur. This process, also known as sublimation, refers to the vaporization of surface atoms of a material whose ambient pressure is comparable with its own vapor pressure. The rate of outgassing increases when the temperature rises. Structural problems arising from outgassing are unlikely due to its small effect, however, the subsequent deposition of materials on both optical and electrically sensitive surfaces is hazardous. For plastic materials as an example, high vapor-pressure components evaporate rapidly, although initially mass loss is usually associated with the loss of adsorbed gases and water vapor. [Sta03]

3.3.5 Atomic Oxygen Erosion

Atomic oxygen is the major atmospheric species in LEO[1] which forms an aggressive environment for materials used on space vehicles in LEO. This arises firstly from its chemical activity and secondly from the fact that it travels about ∼8 km/s relative to the vehicle due to the vehicle's orbital velocity. Effects are the formation of stable oxide, scattering or reflection and chemiluminescent glow. Volatile products are formed, causing surface recession. The net effect of this erosion is to degrade the optical, thermal, mechanical and electrical material properties irreversibly. This must be taken into account when choosing materials for systems to be used in space. Silver is one of the few metals attacked by atomic oxygen. Due to its extensive use on solar arrays, bare exposure has to be avoided. Other materials affected by this erosion with increasing erosion yields are for example aluminum-coated Kapton, FEP Teflon, silicones and polyethylene. Chemiluminescent glow at visible wavelength can be observed on the Space Shuttle and around small spacecraft. It is thought to be caused by surface mediated O + NO recombination, forming excited NO_2 molecules that then radiate. Protective coatings can be applied, which are resistive to the attack of atomic oxygen. [Sta03]

[1] LEO, Low Earth Orbit

3.3.6 Other Material Effects

Material strength and fatigue life are also modified in a high-vacuum environment. Physical reasons for such changes are that gases absorbed into surface cracks either aid or hinder crack propagation. Another possible physical cause is that oxidation and gas diffusion absorbed into the material bulk influences material properties. Generally, it can be stated that fatigue life is improved. A prominent example of a material whose strength is improved in vacuum is that of glass: threefold improvement in strength has been observed at a pressure that is 1/1000 of atmospheric pressure.
Another material modification can be caused by the exposure to ultraviolet (UV) radiation. Many polymers are particularly sensitive to UV photons, whose energy is high enough to modify their chemical bonding structure (embrittlement) . Other effects are electrical changes in form of resistivity modification and optical changes affecting both thermal characteristics and opacity. This is especially important for solar arrays since the solar cell coverglass and its attendant adhesive are subject to darkening causing a reduced cell illumination and enhanced operating temperature, which degrades solar cell performance. [Sta03]

3.3.7 Radiation Effects

Radiation effects on electronics are commonly distinguished in total dose effects and single event effects (SEE). Total dose effects are caused by the deposition of energy by many particles. The key phenomena that take place result from the impact of the high-energy particle upon both the energetic band structure and lattice structure of the semiconductor material. The damage caused by a massive particle, such as a proton, is significantly higher than that from an electron due to the higher momentum carried by the proton. When a charged particle traverses the semiconductor material it leaves a track of ionization. The ionization process results in an impulsive release of charge, causing a single event upset (see later). Additionally, if a proton is stopped in the material, a significant displacement of a lattice atom will occur, which can result in local ionization and a local disruption in the energetic band structure. This leads to the creation of additional energetic states between the conduction and valence bands. A modified energetic band structure in the semiconductor results in a reduction of efficiency of solar cells.
Radiation analysis has to be performed during the design process of a spacecraft. If the expected dose is too high, shielding can be implemented or radiation hard electronics components can be used. In general, shielding is beneficial. However, in some cases large thicknesses of shielding can worsen the effects. Considering for example single event effects, a heavy ion passing through a certain thickness of material can be slowed down to an energy region where its linear energy transfer (LET), and therefore the ability to produce ionization, is increased. Moreover, secondary particles can be produced as a result of the interaction of the primary particle with the atoms of the shielding material. For example, secondary neutrons produced by proton fluxes can pose a problem for manned mission in orbits where the proton flux is high. This can be the case in altitudes greater than 500 km, or for solar protons in high inclination orbits. Activation can result in dose problems on long, manned missions such as the Space Station.
Singe event effects are caused by the deposition of energy by single particles. Several types of SEEs are distinguished.

- *Single Event Upsets (SEU)*
  A single event upset occurs when a heavy ion traverses the sensitive area of an integrated

circuit, producing sufficient charge in the form of electron-hole pairs to cause a change in the logic state of the device. This event causes a so-called *soft error* since it is reversible and causes no permanent damage. Effects can be bit flips in memory cells or registers. A reset or rewriting of the device results in normal device behaviour thereafter.

- *Single Event Latchup (SEL)*
  A single event latchup is a condition that causes loss of electronics device functionality due to high current caused by a latched low impedance state. This can occur in complementary metal oxide semiconductors (CMOS).The high operating current state can cause subsequent errors, e.g. in power supplies as a consequence of the high current. A SEL is cleared by a power off-on reset. If power is not removed quickly, a catastrophic failure may occur due to excessive heating or bond-wire failure.

- *Single Event Burnout (SEB)*
  A single event burnout can occur when an incident ion produces a conducting path for example in a metal oxide semiconductor (power MOSFETs) material causing the device to latch up and subsequently if this conditions lasts for a sufficiently long time to be completely burnt out and destroyed.

The parameter that characterizes a particle's ability to cause an SEE is its energy deposition rate, known as dE/dx, stopping power or LET. When designing an electronics systems there are different approaches to deal with possible SEE effects: error toleration, error correction and error prevention. The first one is costly and time consuming since it involves the specification of tolerance levels for various parts of the system and the determination of the maximum permissible error rate. Tests must be conducted to ensure that catastrophic failure is excluded and that the defined tolerance levels are met.
Error-correction techniques imply the use of redundant units, self-checking circuits, error-detecting and error-correction codes, serial calculation with error correction, concurrent programme execution, repetitive execution and watchdog timers. Error prevention involves the choice of components, which will not upset. [Sta03, Aer05, Nat05b]

3.4 Thermal Considerations

The only way AMS-02 interacts with its environment is by thermal radiation. The radiative interaction is characterized by the exchange of energy by means of direct solar radiation, solar radiation reflected from Earth *(albedo radiation)*, thermal energy radiated from Earth *(planetary radiation)* and radiation from the spacecraft to deep space. Fig 3.6 illustrates the different kinds of radiation.

- *Solar radiation*
  The spectral energy distribution of the *solar radiation* resembles a Planck curve with an effective temperature of 5800 K. 99% of the radiated solar energy lies between 150 nm and 10 μm with a maximum near 450 nm - the yellow part of the spectrum. Outside the Earth's atmosphere at the Earth's average distance from the Sun the solar radiation intensity called the solar constant, is about 1371 $\pm$ 5 W/m^2. It varies annually with the distance to the sun, from 1321 W/m^2 to 1423 W/m^2 at closest approach. The solar radiation intensity J_S at any distance from the Sun can be found from the relationship:

$$J_S = \frac{P}{4\pi d^2}, \tag{3.1}$$

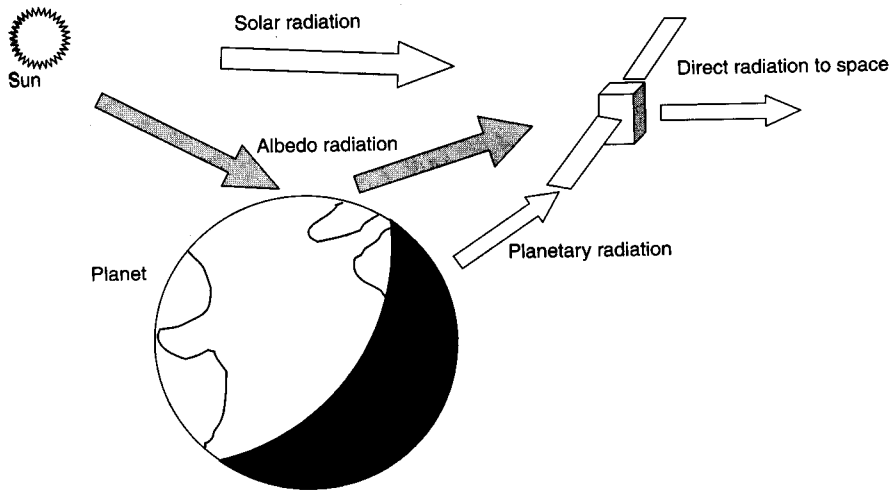

Figure 3.6: Different kinds of thermal input on orbit. From [Sav03].

with P as the total power output from the sun, 3.856 x 10^{26} W.

- *Albedo radiation*
  The fraction of the solar radiation that is reflected from the surface and atmosphere of planet is called the *albedo radiation*. The albedo radiation is highly dependent on the local surface and atmospheric properties. On the Earth it varies from as high as 0.8 from clouds to as low as 0.05 over surfaces such as water and forest. Normally an orbital average value can be used for thermal design purposes, for the Earth this is in the range 0.31 - 0.39. In low orbits however accurate calculation of albedo inputs may need to be performed as a function of orbital position, since it is a complex function of the reflective characteristics, spacecraft altitude and the angle between the local vertical and the sun rays. In orbit of the ISS the albedo varies from 0.2 to 0.4.

- *Planetary radiation*
  Planetary radiation depends on the temperature of the Earth. Because it is relatively low, the Earth radiates all of its heat at infrared wavelengths effectively between about 2 and 50 μm with a peak intensity around 10 μm. Essentially the atmosphere is opaque over much of the infrared spectrum with transparent windows at around 7 and 13 μm. As a consequence the radiation a space craft sees comes from the upper atmosphere with a black-body temperature of around 218 K. Superimposed to this radiation is the radiation from the Earth's surface passing through the infrared windows. For the orbit of the ISS the Earth's outgoing long wave radiation varies between 206 and 286 W/m^2.
  When designing the thermal system, changes in the thermal-optical properties, namely emissivity and absorptivity, of the exposed surfaces has to be taken into account.

To consider all those different kinds of radiation inputs in the thermal design of AMS-02, extensive thermal modeling for AMS-02 is carried out by Carlo-Gavazzi-Space (CGS), Milano, Italy. [Sav03, Moo02]

Chapter 4

Theory of Transition Radiation Detectors

Today's Transition Radiation Detectors (TRDs) are widely used in high energy physics experiments, such as ATLAS, ALICE, HERA-B or AMS-02. While in most cases the TRDs are used in proton machines and a suppression of charged background pions against electrons is desired, the main task of the AMS-02 TRD is the rejection of proton background against positrons.
This introduction and the following subsections are a brief summary of the transition radiation theory, which is described in more detail in [Gar60, TM61, Gar71, CHMP74, AYM75, Dol86, Che78, Dol93, ESA00, WPM$^+$04].

In this chapter, some characteristics of transition radiation are given, followed by an overview of the detection principles applied in a transition radiation detector.

4.1 Transition Radiation

Transition radiation is the electromagnetic radiation that is emitted when a charged particle crosses the interface between two media with different dielectric constants ϵ_1 and ϵ_2. The existence of this transition radiation was first predicted in 1946 by Ginzburg and Frank.
The creation of transition radiation is analogous to the radiation created by a non-uniformly moving charge, which is known as bremsstrahlung. The difference lies in the fact that during the production of bremsstrahlung the particle velocity changes, while during the production of transition radiation, the phase velocity changes.
In high energy physics experiments, a transition radiation detector can provide nondestructive information for particle identification, in addition to calorimetric measurements. First studies of transition radiation were performed in the optical region. The main benefit of using this radiation in high energy physics becomes apparent when ultrarelativistic particles are used as sources for transition radiation, since in this case the radiation appears in the X-ray region. From Garibyan's theory, some remarkable and important features for transition radiation in the X-ray region can be derived.

1. The total energy loss by a charged particle due to transition radiation is proportional to γ[1]. This provides a means to identify two kinds of particles of the same charge and energy, but with different masses, such as relativistic positrons and protons. In this case, positrons emit transition radiation in the X-ray region while protons do not.

2. The radiation is extremely forward peaked within an angle of order $1/\gamma$. This implies that the radiation is hardly separated from the original particle, causing a detector such

[1] γ=E/mc^2

as a proportional chamber to detect both the transition radiation photon and energy loss (dE/dx) of the charged particle. If desired a strong magnetic field can be applied to separate them.

3. In an interface between two dielectric media, the number of photons radiated per particle is of the order of the fine structure constant $\alpha = 1/137$. This number is actually quite low, but by using a multilayer dielectric radiator spaced in vacuum this radiation yield can be increased cumulatively. Instead of a stack of regular foils, also a highly irregular structure such as the AMS-02 radiator fleece can be used (see Section 2.3).

To get an impression of the features of transition radiation, we must first look at the angular distribution of the differential radiation intensity, when a particle traverses a single interface. Two-fold integration yields the total radiation intensity and the average number of photons per transition. In the next subsection then, the yield will be calculated, when a particle not only traverses an interface between two dielectric materials but a material layer with two interfaces in a different dielectric medium. This will take into account interference effects due to phase differences between the two photons created on each interface. Since real radiators are composed of a stack of foils, another subsection will deal with the physics of a periodic radiator. The following formulas are given in cgs units.

4.1.1 Emission on a Single Interface

At high photon frequencies a material can be considered as an electron gas. Therefore, the dielectric constant of a medium is related to the plasma frequency $\omega_P = \sqrt{4\pi n_e e^2/m_e}$, where m_e is the electron mass and n_e is the number of electrons per volume.

$$\epsilon(\omega) = 1 - \omega_P^2/\omega^2 = 1 - \xi^2 \tag{4.1}$$

For a highly relativistic particle traversing an interface the angular distribution of the radiated photon intensity W can be written as

$$\frac{d^2W}{d\omega d\Theta} = \frac{2\alpha\hbar\Theta^3}{\pi}\left(\frac{1}{\gamma^{-2}+\Theta^2+\xi_1^2} - \frac{1}{\gamma^{-2}+\Theta^2+\xi_2^2}\right)^2, \tag{4.2}$$

where $\alpha = \frac{e^2}{\hbar c}$ is the fine structure constant, ω is the energy of the radiated photon, ω_i is the plasma frequency of a medium i, and $\xi_i = \omega_i/\omega$.
This expression is valid for relativistic particles $\gamma \gg 1$, for high frequencies $\omega \gg \omega_i$ and for small angles $\theta \ll 1$. The radiation is sharply peaked in the forward direction at the narrow angle $\theta \simeq 1/\gamma$.

Integration over the angle θ reveals the differential energy spectrum

$$\frac{dW}{d\omega} = \frac{\alpha\hbar}{\pi}\left[\left(\frac{\omega_1^2+\omega_2^2+2\omega^2/\gamma^2}{\omega_1^2-\omega_2^2}\right)ln\left(\frac{\gamma^{-2}+\omega_1^2/\omega^2}{\gamma^{-2}+\omega_2^2/\omega^2}\right) - 2\right]. \tag{4.3}$$

Further integration with respect to the frequency yields the total radiation emitted at a single interface

$$W = \frac{\alpha\hbar}{3}\frac{(\omega_1-\omega_2)^2}{\omega_1+\omega_2}\gamma. \tag{4.4}$$

Clearly observable is the linear dependency of the radiation intensity on γ. This linear increase comes primarily from the hardening of the emitted X-rays, rather than from an increase in the overall number of photons.

Equation 4.3, which describes the differential energy spectrum, can be approximated in three regions defined by ω:

$$\frac{dW}{d\omega} \approx \begin{cases} \frac{2\alpha\hbar}{\pi}\left(ln\frac{\omega_1}{\omega_2} - 1\right) & \omega < \gamma\omega_2 \\ \frac{2\alpha\hbar}{\pi} ln\frac{\gamma\omega_1}{\omega} & \gamma\omega_2 < \omega < \gamma\omega_1 = \omega_c \\ \frac{\alpha\hbar}{6\pi}\left(\frac{\gamma\omega_1}{\omega}\right)^4 & \omega_c = \gamma\omega_1 < \omega \end{cases} \tag{4.5}$$

Obviously a *cut-off* frequency $\omega_c = \gamma\omega_1$ exists at which frequencies exceeding this value rapidly drop to small values. Figure 4.3 in Section 4.1.3 illustrates this differential energy spectrum. Clearly visible are the three regions mentioned above.
The photon yield per interface is rather low and of the order

$$N_\gamma = \int \frac{1}{\omega}\frac{dW}{d\omega} \simeq \alpha. \tag{4.6}$$

Due to this small probability for an energetic photon emission, many interfaces, or foils, are used in a transition radiation detector.

4.1.2 Emission on Two Interfaces of a Material Layer

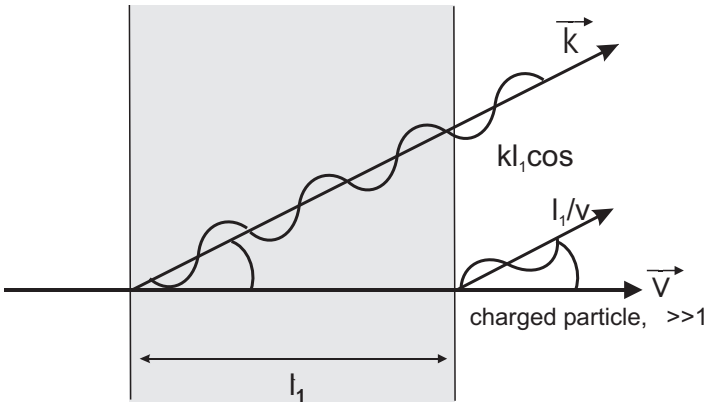

Figure 4.1: Transition radiation interference on one material layer.

To estimate the radiation yield on a layer of material, one has to take into account that the radiation fields created on both layer surfaces sum up. Consequently phase differences have to be considered. Figure 4.1 illustrates the two-surface interference. For relativistic particles, the amplitudes of the forward radiation from both surfaces are of the same magnitude. Generally, the resulting electric field $\overrightarrow{E}$ can be described, when neglecting backward emission, reflections on boundaries and change in θ because of refractions:

$$\overrightarrow{E}(\omega, \overrightarrow{\theta}) = \sum_{j=1}^{n} \cdot \overrightarrow{E^j}(\omega, \overrightarrow{\theta}) e^{\left(-\sum_{m\geq j}\sigma_m + i\phi_m\right)} \tag{4.7}$$

Here $\overrightarrow{E^j}$ is the single surface amplitude, $e^{-i\sigma_m}$ is an absorption factor in the mth layer, $\overrightarrow{\theta}$ is the difference between the unit vectors representing the photon and particle directions, and ϕ_m is the phase difference due to the different speeds of the particle and the photon in one layer. Since in this section we are only observing one single layer, we can neglect any absorption in consecutive layers for the moment. The phase difference is composed of two parts. When the field created on the first interface reaches the second interface it has the phase difference $\overrightarrow{k} \cdot \overrightarrow{x} = k\ l\ cos\theta$, with l as the layer thickness. The generation of the second field occurs later in time due to the limited particle velocity $\overrightarrow{v}$. Moreover since the field polarization on the second interface is opposed to the first one, this field has an additional phase difference π. The corresponding phase lag is $\pi + \omega t/v$. When summing up these two fields, an interference factor appears in the radiation intensity:

$$\left|e^{iklcos\theta} - e^{i\omega l/v}\right|^2 = 4\ sin^2(klcos\theta - \omega l/v)/2) = 4\ sin^2(\phi/2) \tag{4.8}$$

Consequently equation 4.3 is modulated by a factor $4sin^2(\phi/2)$. Using several approximations[1], it is possible to write ϕ_m as:

$$\phi_m = (\omega l_m/2c)(\gamma^{-2} + \theta^2 + \xi_m^2) = \frac{l_m}{z_m} \tag{4.9}$$

with the formation zone:

$$z_m = \frac{2c}{\omega}\frac{1}{\gamma^{-2} + \theta^2 + \xi_m^2} \tag{4.10}$$

The formation zone represents the distance along the particle's trajectory, after which the spatial separation between the primary particle and the emitted photon is of the order of the photon wavelength. The resulting differential angular radiation intensity can therefore be written as:

$$\left(\frac{\partial^2 W}{\partial\omega\partial\theta}\right)_{single\ layer} = 4\ sin^2(\phi/2) \cdot \left(\frac{\partial^2 W}{\partial\omega\partial\theta}\right)_{single\ interface} \tag{4.11}$$

If the layer thickness l_m is much smaller than the formation zone of the layer, the yield is strongly suppressed by the interference factor. Otherwise if the layer thickness is much bigger than the formation zone, the interference factor can be approximated by 2, meaning that the radiation yield from two interfaces is simply twice the yield of a single interface.

4.1.3 Regular and Irregular Radiator

Similarly we can calculate the radiation intensity for a *periodic* radiator as illustrated in Figure 4.2. The amplitude for the electric field of n equally spaced layers in a gas is the sum of the N single layer amplitudes each advanced by phase ϕ. Neglecting any absorption we obtain the formula:

$$\overrightarrow{E_n}(\omega, \overrightarrow{\theta}) = \overrightarrow{E_1}(\omega, \overrightarrow{\theta})(1 + e^{i\phi} + e^{2i\phi} + ... + e^{(n-1)i\phi}). \tag{4.12}$$

Each phase difference is composed of the phase difference in one layer and the phase difference in the medium between the layers. In the scenario for a foil layer (l_f and k_f) next to a gas layer (l_g and k_g) the phase difference can be written:

$$\phi = (k_f cos\theta - \omega/v)l_f + (k_g cos\theta - \omega/v)l_g. \tag{4.13}$$

[1] $k_m = \sqrt{\epsilon}_m\omega/c \simeq (1 - \frac{1}{2}\xi_m^2)\omega/c$, $cos\theta \simeq 1 - \frac{1}{2}\theta^2$, $\beta^{-1} \simeq 1 + \gamma^{-2}/2$

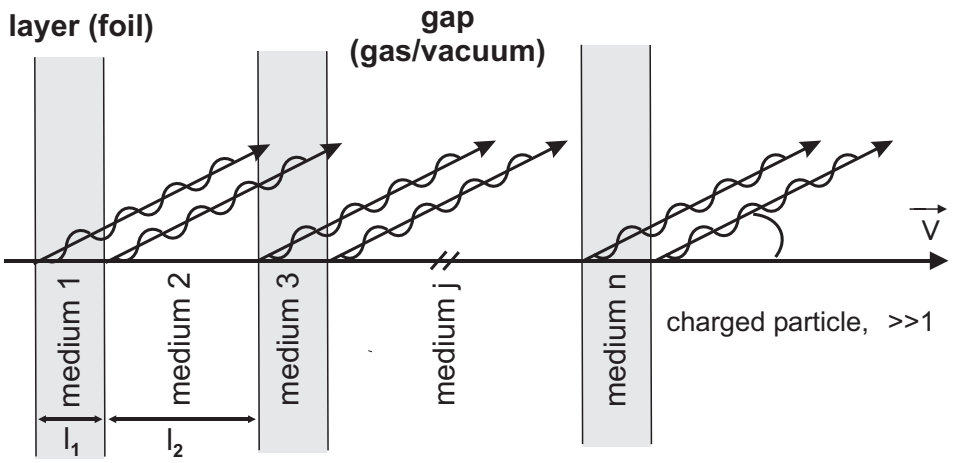

Figure 4.2: Transition radiation interference on multiple material layers. If the material layers are equally spaced, the radiation of each consecutive layer obtains a multiple of phase shift ϕ.

The resulting differential radiation intensity can be written as

$$\left(\frac{\partial^2 W}{\partial\omega\partial\theta}\right)_{N\ layers} = I^{(n)} \cdot \left(\frac{\partial^2 W}{\partial\omega\partial\theta}\right)_{one\ layer} \tag{4.14}$$

with $I^{(n)}$ the interference factor given by

$$I^{(N)} = \left|\frac{1-e^{Ni\phi}}{1-e^{i\phi}}\right|^2 = \frac{sin^2(N\phi/2)}{sin^2(\phi/2)}. \tag{4.15}$$

Transforming the phase difference ϕ into an expression containing the layer thickness l_1, the gap thickness between the layers l_2 and the corresponding formation zones z_1 and z_2 gives:

$$\frac{\partial^2 W_N}{\partial\omega\partial\theta} = \frac{\partial^2 W_0}{\partial\omega\partial\theta} 4sin^2\left(\frac{l_1}{z_1}\right)\frac{sin^2[N(l_1/z_1+l_2/z_2)]}{sin^2(l_1/z_1+l_2/z_2)} \tag{4.16}$$

An appreciable yield from the N-layer stack can only be obtained, if the spacing between the layers is in the order of the medium formation zones between the layers. If this spacing is larger than the formation zone, a transition radiation yield is expected to be comparable to the incoherent sum of the radiation of N single layers. In this sum, the single layer formula can be used for each layer.
Compared with the total yield of the single interface, which increases linearly with γ, the total yield of a stack of layers is limited by saturation effects as the Lorentz factor increases. Since the formation zones z_1 and z_2 are strongly dependent on the Lorentz factor of the particle, they will eventually become larger than the layer thickness l_1 and/or the layer spacing l_2. As a consequence this limits the total transition radiation yield to reaching a plateau value. The Lorentz factor at which the saturation becomes appreciable in the case of a multilayer radiator has been calculated in [Che78] to be:

$$\gamma_{sat} \simeq 0.6\omega_1\sqrt{l_1 l_2}/c \tag{4.17}$$

So far all absorption terms have been ignored. In the case of the incoherent sum of single layer intensities absorption can be considered by introducing an additional factor N_{eff}, which takes into account the absorption of transition radiation photons in the radiator material:

$$N_{eff} = \frac{1 - e^{-N\sigma}}{1 - e^{-\sigma}} \tag{4.18}$$

It can easily be seen that for an increasing stack of layers the radiation yield approaches a saturation limit which represents the equilibrium between emitted and reabsorbed transition radiation photons:

$$lim_{n\to\infty} N_{eff} = (1 - e^{-\sigma})^{-1} \tag{4.19}$$

As a summary the total intensity after n layers can be written as:

$$\left(\frac{\partial^2 W}{\partial\omega\partial\theta}\right)_{n\ layers} = N_{eff} \cdot \left(\frac{\partial^2 W}{\partial\omega\partial\theta}\right)_{single\ layer} = \frac{1 - e^{-N\sigma}}{1 - e^{-\sigma}} \cdot \left(\frac{\partial^2 W}{\partial\omega\partial\theta}\right)_{single\ layer} \tag{4.20}$$

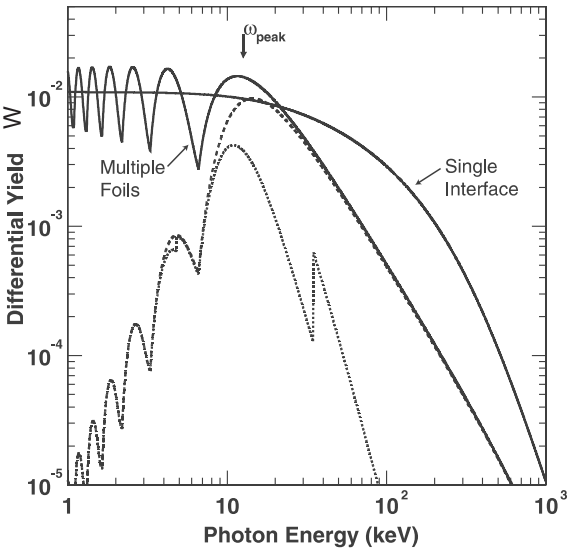

Figure 4.3: Differential transition radiation yield ($\partial W/\partial\omega$) versus photon energy for single interface and multiple layers. The dashed line represents the multilayer spectrum modified by self absorption processes. The dotted line shows the yield which would be captured in a single 1 cm thick layer of Xenon. All spectra are normalized to a single interface yield. ($\gamma = 10^4$, $l_1 = 35\ \mu m$, $l_2 = 1000\ \mu m$, $\omega_1 = 21.2\ eV$, $\omega_2 = 0.75\ eV$) From [WPM+04].

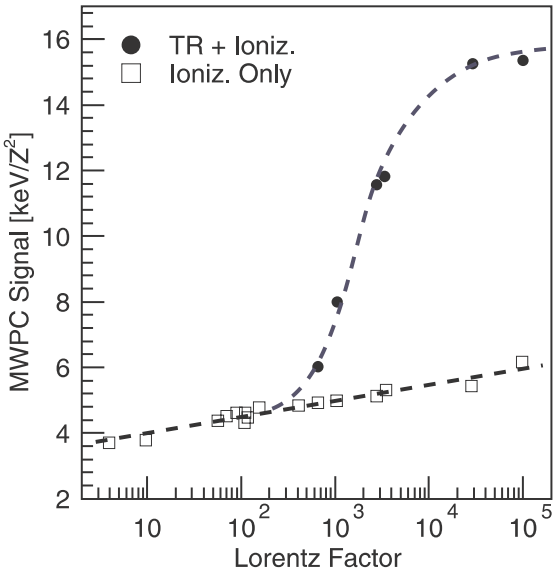

Figure 4.4: MWPC detector signal versus Lorentz factor. Nicely observable is the energetic separation between the energy deposition due to pure ionization of the primary particle and ionization with additional energy deposition due to the photo effect of transition radiation in the Xenon gas. The saturation effect at high Lorentz factors around 10^4 is visible. From [WPM+04].

For practical reasons *irregular* radiators composed of fleece, foam or fibers can be used rather than a regular stack of layers. Compared to a regular radiator, the yield is reduced by 10% to 30% [Orb03].

Figure 4.3 shows the differential transition radiation yield versus photon energy for a single interface and multiple interfaces. Figure 4.4 compares the multiwire proportional chamber signal of pure ionization and with additional transition radiation photon energy deposition. In order to choose an appropriate material for a radiator, it is necessary to realize that the absorption in the radiator material increases as Z^4/ω^3, while the transition radiation total energy is proportional to the plasma frequency, which varies with $Z^{1/2}$. Consequently it is advisable to choose a radiator material with small Z. In addition the radiation yield can be optimized as soon as the working range of the detector and therefore the Lorentz factor γ has been chosen, by keeping the layer thickness as close as possible to its formation zone limits.

4.2 Detection of Transition Radiation

Common transition radiation detectors use proportional chambers filled with Xenon gas to detect the transition radiation photons. Due to the small emission angles these photons are detected together with the ionization energy loss of the primary particle. The performance of the TRD therefore depends on the proper statistical separation of ionization and transition radiation signal. To optimize the TRD, the photon absorption (by photoelectric effect) should be maximized, while the ionization energy loss should be minimized. Therefore, a low-density high-Z material, such as Xenon gas, is used. According to [Orb03] for the AMS-02 TRD, TR photons have a probability of about 60% to be absorbed inside the next detector layer, made of 6 mm proportional tubes filled with $Xe/CO_2(80/20)$. Nevertheless since almost all TRDs are composed of several layers of combined radiator and detector, photons not absorbed in one detector layer are available as *feed-through* photons for possible absorption in the downstream detector layers.
In the next subsections particle interaction processes are reviewed in order to explain the principle of charged particle detection by dE/dx energy loss and photon detection by photoelectric effect, Compton scattering and pair creation. Most formulas in this section are taken from [Gru93].

4.2.1 Charged Particle Detection

When a charged particle passes matter, it interacts electromagnetically with the electrons bound within the material. This is the basic principle of charged particle detection. During these interactions the passing particle transfers part of its energy to its interaction partner electron. This electron can either be raised to a higher atomic shell if the detector material is a gas or to a higher energy level in a solid state detector. If the energy is high enough, the electron can leave the atom completely. This process is called ionization and is described for moderately relativistic charged particles by the *Bethe-Bloch formula* :

$$-\frac{dE}{dx} = \frac{N_A e^4}{4\pi m_e \epsilon_0^2 c^2} \cdot \frac{Zz^2}{A} \cdot \frac{1}{\beta^2} \cdot \rho \cdot \left[ln\left(\frac{2m_e c^2 \gamma^2 \beta^2}{I}\right) - \beta^2 - \frac{\delta}{2}\right], \tag{4.21}$$

where e and m_e is the charge and mass of an electron, Z and A is the atomic and mass number of the material, $\beta = v/c$, I is a mean ionization potential, N_A as Avogadro's number, z the charge of the ionizing material, ρ the density of the absorber material and δ the density correction which takes into account the shielding effect of atomic electrons on the extended electric field of relativistic particles.
The energy loss described by this formula decreases like $1/\beta^2$ and reaches a broad minimum

close to $\beta\gamma \approx 4$. Relativistic particles which feature an energy loss close to this minimum are denoted as minimum ionizing particle (MIP). For $\gamma > 4$ the energy loss rises again due to the logarithmic term in the bracket of Equation 4.21. This logarithmic rise is partly caused by big energy transfers on few electrons, called δ-electrons[1]. These electrons can ionize gas atoms and even escape from the detector volume. For thin absorbers, such as gases, high fluctuations around the mean energy loss can be observed. Here, the energy loss can be approximated by an asymmetric Landau distribution. Responsible for these high fluctuations are again rare energy transfers to atomic electrons, which create δ-electrons. For thick absorbers the Landau tail is reduced and for very thick absorbers the energy loss can be approximated by a Gaussian distribution.
Equation 4.21 just represents energy losses due to ionization. For high energies radiative losses due to bremsstrahlung become more and more important and have to be appropriately considered. Moreover Equation 4.21 is not valid for electrons or positrons, since already at low energies in the MeV-range, the energy loss for electrons is modified by bremsstrahlung. Since the primary electrons and the absorber electrons have the same mass, it is not possible to distinguish between primary and secondary electron. For electrons the energy loss can be expressed as:

$$-\frac{dE}{dx} = \frac{N_A e^4}{4\pi m_e \epsilon_0^2 c^2} \cdot \frac{Z}{A} \cdot \frac{1}{\beta^2} \cdot \rho \cdot \left[ln\frac{\gamma m_e c^2 \beta\sqrt{\gamma - 1}}{\sqrt{2}I} + \frac{1}{2}(1-\beta^2) - \frac{2\gamma - 1}{2\gamma^2} ln2 + \frac{1}{16}\left(\frac{\gamma - 1}{\gamma}\right)^2 \right] \tag{4.22}$$

For positrons again a different formula exists which can be looked up at [Gru93]. Additionally, for positrons there is an important difference: as soon as they come to rest they annihilate with another electron under emission of normally two photons.

4.2.2 Photon Detection

Photons have to interact with matter before it is possible to detect them. The basic principle is that photons transfer their energy to charged particles in the detector material, which create a detector signal by consecutive energy losses. The photon can either be totally absorbed, as is the case for the photoelectric effect or for pair creation, or it undergoes a scattering process on an electron, which represents the Compton effect. Absorption and scattering are a statistical processes which can be described by an exponential law. The photon intensity can be expressed as

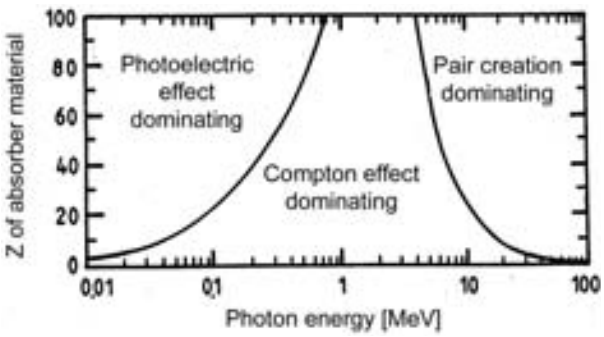

Figure 4.5: Areas of different dominating photon interactions as function of photon energy and absorber charge Z. From [Gru93].

$$I = I_0 e^{-\mu x}. \tag{4.23}$$

Here μ is the mass absorption coefficient, which can be related to the photon interaction process cross sections σ_i as:

$$\mu = \frac{N_A}{A} \sum_i \sigma_i, \tag{4.24}$$

where N_A is the Avogadro number, A is the mass number of the absorber. The cross sections are strongly dependent on the photon energy. For small photon energies ($E_{Ionization} \leq E_\gamma \leq$

[1] δ-electrons are also known as knock-on electrons

100 keV the photoelectric effect dominates. In an intermediate energy range ($E_\gamma \approx 1\ MeV$) the compton effect prevails. At very high energies ($E_\gamma > 1\ MeV$) the cross section of pair creation becomes the dominating effect. Figure 4.5 illustrates the dominating ranges of each cross section.
For the transition radiation detector, photon energies in the soft X-ray region are created, hence the photoelectric effect is the most important effect in this specific case.

Photoelectric Effect

Electrons bound in atoms can absorb the full energy of photons, which is not possible for free electrons due to momentum conservation reasons. The third interaction partner is the atomic nucleus. The electron which has absorbed the incoming photon leaves the atom with the energy of the photon reduced by the binding energy of its atomic shell. This is expressed by the Einstein equation:

$$E_{kin} = \hbar\omega - E_{bind} \tag{4.25}$$

Generally, the photoelectric cross section has a complicated dependence on Z. Additionally the cross section is modified in the energy regions next to the material dependent absorption threshold energies. The photoelectric effect occurs with enhanced probability, when the energy of the photon is equal to the binding energy of the electron. The tighter the electron is bound to the nucleus, the higher the absorption probability due to the closeness of the third interaction partner. For X-ray photons most of the photo electrons are electrons from the inner shells. Depending on the photon energy the cross section can be approximated between

$$\sigma^K_{Photo} \sim Z^4 \quad \text{and} \quad \sigma^K_{Photo} \sim Z^5. \tag{4.26}$$

After the electron has left the shell, it may now be occupied again by other electrons from higher atomic shells, in this way setting free the difference in potential energy. This difference can be emitted by characteristic X-rays or it can be conferred directly on electrons of the same atom. If this energy is now larger than the binding energy of the electron in its shell, it may leave the atom in this way creating an *Auger electron*. The energy of Auger electrons is small compared to the energy of the photoeffect electrons.

Compton Effect

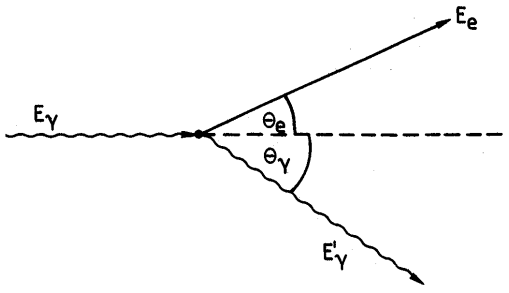

Figure 4.6: Scheme of Compton effect kinematics.

The principle of the Compton effect is shown in Figure 4.6. A photon scatters off an electron and confers part of its energy on the electron. The photons and electrons are deflected at the

angles θ_e and θ_γ respectively. The resulting energy of the scattered photon E'_γ can be calculated as

$$E'_\gamma = \frac{1}{1 + \frac{E\gamma}{m_e c^2} \cdot (1 - cos\theta_\gamma)} E_\gamma, \tag{4.27}$$

where E_γ is the initial photon energy. The maximum energy loss for the scattered photon occurs at deflection angle $\gamma_e = \pi$ (backward scattering) and is denoted as the so called Compton energy E_C. The Compton spectrum of a monochromatic γ-emitter represents a continuum in the energy range from 0 to $E_{\gamma'} = E_\gamma - E_C$. The cross section is proportional to the charge number Z of the absorber atoms:

$$\sigma_c \sim Z. \tag{4.28}$$

Pair Creation

In this process the photon creates an electron positron pair in the presence of the Coulomb field of a nucleus. This process starts to be possible at a certain photon energy, which is composed of the two rest masses of two electrons plus the recoil energy of the nucleus.

$$E_\gamma \geq 2m_e c^2 + 2\frac{m_e^2}{m_{nucleus}} c^2 \tag{4.29}$$

The cross section of pair creation is

$$\sigma_{Paar} \sim Z^2. \tag{4.30}$$

4.3 The Proportional Chamber

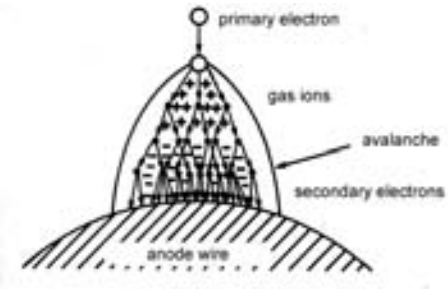

Figure 4.7: Avalanche creation around a wire in a proportional chamber. From [Gru93].

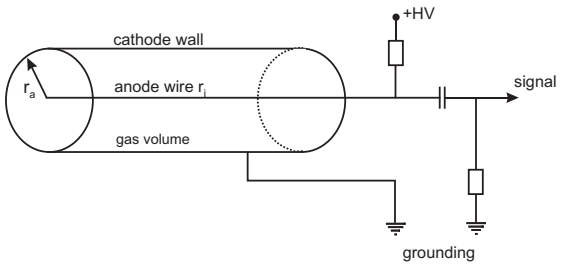

Figure 4.8: Connection scheme of a proportional chamber.

The proportional counter is composed of a cathode cylinder with conductive walls. In the middle of this cylinder a conducting anode wire is strung with a small diameter of 20-50 μm. The cylindrical volume is filled with a noble gas mixture, such as Ar/CO_2 or Xe/CO_2 (80/20) as is used for the proportional tubes of the TRD. High voltage of about 1500 V is applied between the anode wire and the cathode. Consequently a radial electric field $\overrightarrow{E}$ is created inside the cylinder between the wire and the wall, which can be expressed as:

$$\overrightarrow{E} = \frac{U_0}{ln\ r_a/r_i} \cdot \frac{1}{r} \tag{4.31}$$

with r_a the radius of the cylinder and r_i the radius of the wire. In the gas, charged particles traversing the proportional counter create e^-/i^+ pairs by ionization, photons create e^-/i^+ pairs

by all the effects described before, depending on the photon energy. The electric field separates electrons and ions by accelerating electrons to the anode wire and ions to the cylinder wall. From time to time they hit gas atoms and can transfer a part of their kinetic energy. The energy gain in the electric field between the hits is given by

$$\Delta E_{kin} = -e \int_{r_1}^{r_2} \overrightarrow{E}(r) \cdot d\overrightarrow{r} = \frac{eU_0}{ln\ r_a/r_i} \cdot ln\ r_2/r_1 \tag{4.32}$$

Due to the 1/r dependence of the electric field, the electrons enter a high field region around the anode wire. The energy gained in this area is high enough to ionize atoms by hits. These liberated electrons are again accelerated in the area of high electric field and create even more ionization. An avalanche is started. The avalanches are created almost entirely within a region of about 20 μm around the wire. The proportional chamber is operated in a voltage region, where the amount of secondary created e^-/i^+ pairs is proportional to the primary ionization. Figure 4.7 illustrates the development of an avalanche. Interesting to note, the induced signal which is decoupled via a capacitor and read out by a charge sensitive amplifier, is created mainly due to the slowly drifting ions rather than the fast electrons. The ratio between the signal induced by ions and electrons is given by

$$\frac{\Delta U^+}{\Delta U^-} = \frac{\frac{Ne}{C}\frac{ln\ r_a/r_0}{ln\ r_a/r_i}}{\frac{Ne}{C}\frac{ln\ r_0/r_i}{ln\ r_a/r_i}} = \frac{ln\ r_a/r_0}{ln\ r_0/r_i}, \tag{4.33}$$

where r_0 is the avalanche starting point next to the wire. Figure 4.8 shows the connection scheme of a proportional counter.
Xenon is an appropriate proportional gas, due to its high charge number Z. The gas for the AMS-02 TRD has a 20% admixture of CO_2. The reason for this is twofold. Firstly, as soon as the ions reach the cathode, they get neutralized by accepting electrons and the binding energy is liberated by the emission of an ultraviolet photon. Secondly photons can be created by the de-excitation of Xe-atoms, which have become previously excited during avalanche formation. Both kinds of photons can convert at the cathode by photoelectric effect and start a new avalanche. This effect can be suppressed by the addition of a poly-atomic quencher gas, such as CO_2. These molecules can absorb the emitted ultraviolet photons and release this energy by dissociation or elastic collisions.

4.4 Gas Amplification

The electron/ion multiplication in the avalanche at a certain gas density and high voltage is referred to as gas amplification. The theoretical description of the gas amplification in the proportional mode is based on the Townsend coefficient α, which describes the multiplication of electrons/ions in the detector gas:

$$dN = N \cdot \alpha \cdot ds, \tag{4.34}$$

with dN as the increase in electron number per length ds. The Townsend coefficient α cannot be calculated, since it depends on the excitation dependent and electric field dependent ionization cross sections in the gas. Therefore, it has to be measured for each gas mixture. With the assumption that the electric field is sufficient to generate secondary charge carriers at the distance s_{min} from the anode wire with radius a, the gas amplification G can be calculated as:

$$G = \frac{N}{N_0} = exp\left(\int_{E(s_{min})}^{E(a)} \frac{\alpha(E)}{dE/ds} dE \right). \tag{4.35}$$

The electric field next to the anode wire can be expressed as:

$$E(r) = \frac{\lambda}{2\pi\epsilon_0 \cdot r}, \tag{4.36}$$

with λ the charge per unit length L. Therefore, the gas amplification can be written:

$$G = exp\left(\int_{E(s_{min})}^{E(a)} \frac{\lambda \cdot \alpha(E)}{2\pi\epsilon_0 \cdot E^2} dE \right). \tag{4.37}$$

Using Diethorn's approach, who assumed that α is proportional to the electric field E:

$$\alpha = \beta \cdot E, \tag{4.38}$$

it is possible to write:

$$lnG = \frac{\beta \cdot \lambda}{2\pi\epsilon_0} \cdot \frac{\lambda}{2\pi\epsilon_0 \cdot a \cdot E_{min}}. \tag{4.39}$$

If now, one identifies β with ln2/ΔV with e $\cdot\Delta$V as the average ionization energy, and considers that E_{min} increases linearly with the gas density ρ:

$$E_{min}(\rho) = E_{min} \cdot \frac{\rho}{\rho_0}, \tag{4.40}$$

where ρ_0 is the gas density at standard conditions[1], one obtains

$$lnG = \frac{\lambda \cdot ln2}{2\pi\epsilon_0 \cdot \Delta V} \cdot ln \frac{\lambda}{2\pi\epsilon_0 \cdot a \cdot E_{min} \cdot (\rho/\rho_0)} \tag{4.41}$$

When considering the TRD straw tube geometry with an applied high voltage U, the charge per unit length λ can be replaced by:

$$\lambda = \frac{Q}{L} = U \cdot \frac{C}{L} = \frac{2\pi\epsilon_0 \cdot U}{ln(R/a)}. \tag{4.42}$$

Using this, finally the gas amplification can be expressed as:

$$G = \left(\frac{U}{ln(R/a) \cdot a \cdot E_{min}(\rho_0) \cdot (\rho/\rho_0)} \right)^{\frac{ln2 \cdot U}{ln(R/a) \cdot \Delta V}}. \tag{4.43}$$

E_{min} and ΔV are the so called Diethorn parameters. They depend on the kind of gas mixture used and are experimentally determined by fitting this formula through points defined by the measured gas gain, high voltage, anode wire radius, straw tube radius, ambient pressure and temperature ($\rho \sim P/T$). [BR93]

4.5 Outlook: Proton Rejection Analysis

The main purpose of the TRD in the AMS-02 detector is to perform proton rejection. Two different methods are interesting: the Cluster Counting Method and the Likelihood Method. In order to give a short overview about the first method, two definitions will be explained. Firstly, the proton rejection is defined as the ratio of the numbers of incident protons to those

[1] gas standard conditions: T=0°C, P=1013 mbar

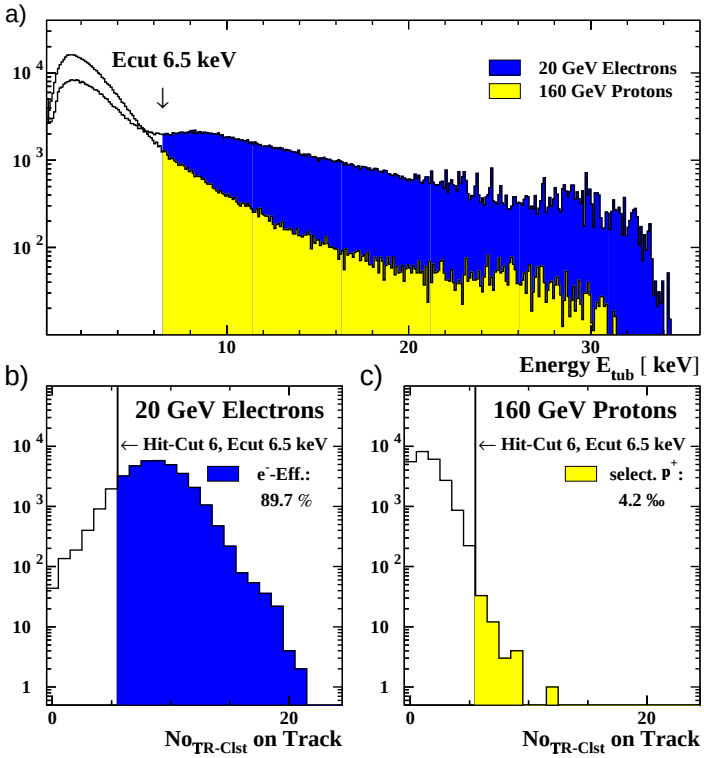

Figure 4.9: Proton rejection analysis: the Cluster Counting method. a) Definition of Energycut (Ecut); b),c) The Hitcut is chosen such that the electron efficiency is 90%. From [Orb03].

selected, whereas the total number of electron events is not reduced below 90% by applying the same cuts. Secondly, the electron efficiency corresponds to the fraction of accepted electrons to the total number of incident electrons.

$$e^- \text{ efficiency} = \frac{\text{number of accepted } e^-}{\text{total number of } e^-} \tag{4.44}$$

$$p^+ \text{ rejection} = \frac{\text{total number of } p^+}{\text{number of selected } p^+} \tag{4.45}$$

In the Cluster Counting Method, hits on a track are counted in each event that are above a certain energy threshold, referred to as *Energycut* or *Ecut*. The difference between a 160 GeV proton spectrum and a 20 GeV electron spectrum is shown in Figure 4.9a). The applied energy cut of E=6.5 keV results in the electron and proton distributions displayed in Figures 4.9b) and c). To choose whether an event is electron-like or proton-like, the definition of a *Hitcut* is required. This Hitcut defines the minimum number of hits, that is required to select an event as electron-like. With the selection of this cut the electron efficiency and the proton impurity of the data sample are defined.
For a fixed Hitcut, the Ecut can be varied and the derived proton rejection factor can be plotted as a function of electron efficiency as is shown in Figure 4.10a. Here, two different Hitcuts are displayed on a sample of 20 GeV electrons and 160 GeV protons. Even at 95% electron efficiency the proton rejection is twice as high as the minimum requested proton rejection of 100. The embedded small plot shows that in this example a Hitcut of 5 or 6 already relate to the best

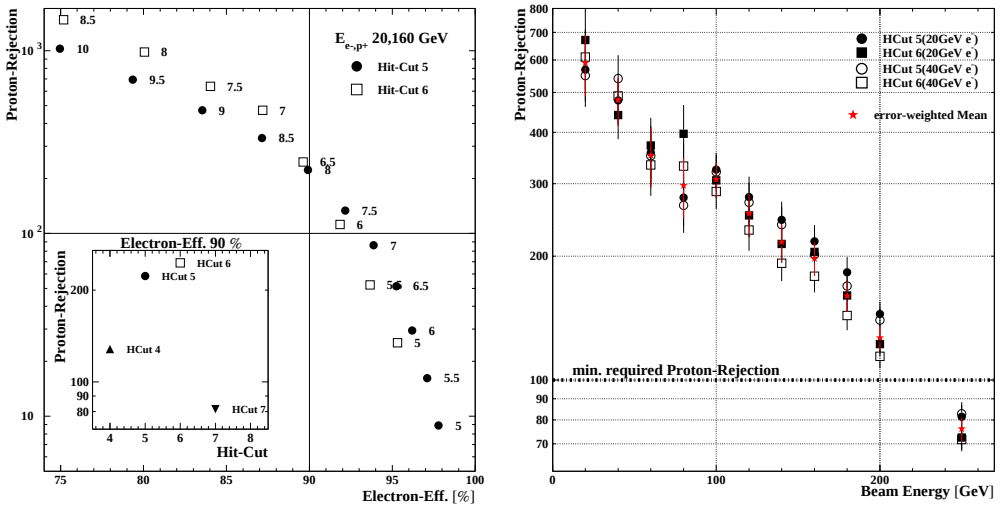

Figure 4.10: a) Proton rejection as a function of electron efficiency. Attached numbers indicate the applied Ecut [keV]. b) Proton rejection as a function of beam energy. Visible is an exponential declension down to an average rejection of 76 at 250 GeV proton energy. From [Orb03].

possible rejection factors.
With a fixed Hitcut and by keeping the electron efficiency constant at 90%, the proton rejection can be plotted against proton beam energy as shown in Figure 4.10b. For this plot an electron sample of 20 GeV and an electron sample at 40 GeV was used. The distributions show a steep declension down to 250 GeV proton energy, where an average proton rejection of 76 still can be reached. Aa a more sophisticated method, the Likelihood analysis can be used to reduce the remaining background by roughly a factor of 2. For further details about the Likelihood method the reader is referred to [Orb03].

Chapter 5

Space Qualified Electronics

The requirements for the AMS-02 electronics are more demanding than those for common space electronics. AMS-02 is vastly more complex and calls for more resources in terms of power, weight, schedule and money. The Data Acquisition (DAQ) system widely abandons the use of space qualified components because of their high costs. Instead, it uses primarily high grade commercial components and still achieves reliability by interconnecting redundant units. Great efforts were made to ensure that these components work in space. They were tested for bit flips and latch ups in heavy ion beam tests. Total Ionizing Dose (TID) tests have been made to verify that they withstand the ∼1 kRad/year radiation in space. On board and crate level, thermal vacuum tests and vibration tests were performed to ensure the survival of the electronics and its affiliated mechanics during launch and on impact of extreme temperature conditions.
The following chapter gives an introductory overview about the data acquisition system of AMS-02 and focuses in detail on the development of the power supply and readout electronics of the transition radiation detector, which is the main topic of this thesis.

5.1 Overview of AMS-02 DAQ

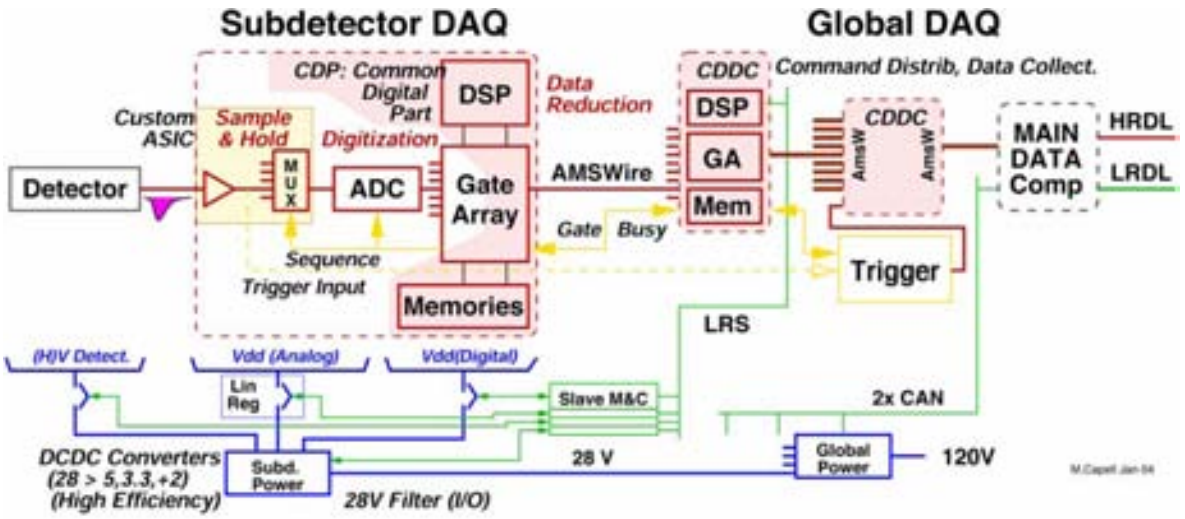

Figure 5.1: Scheme of a common subdetector DAQ node connected to the global DAQ. A unified approach for all subdetectors saves manpower and money resources. From [AMS05].

Compared to other collaborations such as CMS[1] or ATLAS[2] at CERN, AMS-02 is a relatively small collaboration. As a consequence, time, money and manpower are especially valuable. Whenever possible, common developments are preferred to problem specific solutions. The Common Digital Part (CDP), as an example, is used in almost every subdetector DAQ node, regardless whether it is working in TRD, tracker or ECAL electronics. Its slightly modified brother, the Command Distributor and Data Concentrator (CDDC) is used in the data collecting nodes of higher level DAQ. Figure 5.1 illustrates a complete DAQ-chain of subdetector electronics. The heart of each data processing subdetector node is the CDP, which consists of a DSP[3], a gate array and memories. As soon as a subdetector is triggered, the gate array generates signal sequences to control and read out the affiliated subdetector front end electronics, which consists of custom ASIC[4] chips and ADCs[5]. The ASIC preamplifies, shapes, samples and holds the signals for a certain time. Subsequently, the stored signals of the various channels are multiplexed to the ASIC output which is connected to an ADC. There, the signals get digitized and clocked into the gate array to be stored in a buffer memory. The DSP recognizes when a raw event is available, processes it by a subdetector specific routine to reduce its size. The processed event is stored again in the buffer memory. On request the stored event is sent through a serial point-to-point link to the CDDCs in the higher level DAQ nodes, until it reaches the main computer, which is linked to the ISS data infrastructure. Power arrives at the AMS-02 power distribution system from the ISS solar array systems with 120 V where it is converted into 28 V. From there it reaches the subdetector specific power supply boxes, which house DC/DC converters to adapt the incoming voltage to the specific needs of the boards in each subsystem. The CDDCs next to the subdetector CDPs also provide slow control functionality. They are the masters of Lecroy buses, leading to the Lecroy bus slaves which control the DC/DC converters, high voltage boards and linear regulators of each subsystem.

5.2 AMS-02 Global DAQ and Slow Control

5.2.1 Global DAQ and Slow Control Hierarchy

Figure 5.2 illustrates the general DAQ level structure of AMS-02. All DAQ levels are bidirectionally interconnected by 10 MByte/s point-to-point links, called AMSWire[6] links. Scientific data is transferred from the lower DAQ nodes (on the left) to the higher ones (on the right). Commands are issued from the higher DAQ nodes to the lower ones. The xDR[7] nodes are connected to the front ends of each subdetector. All scientific data is collected on the xDR nodes, where a subdetector specific DSP program reduces the amount of data to be sent to the higher DAQ and therefore for later storage. Each xDR node comprises one CDP with two redundant AMSWire links to the higher DAQ. The real data reduction boards consist of two redundant CDPs. Therefore they are named xDR2, in this way indicating their two-fold redundancy. Four AMSWire links are used to connect this board to the next DAQ level. After the data has been processed in the CDP, it is buffered and upon request, asynchronously with

[1] CMS, Compact Muon Solenoid - experiment at CERN
[2] ATLAS, A Toroidal LHC ApparatuS experiment at CERN
[3] DSP, Digital Signal Processor
[4] ASIC, Application-Specific Integrated Circuit
[5] ADC, Analog Digital Converter
[6] AMSWire is based on the Spacewire specification, will be described later.
[7] x is a substitute of the subsystem abbreviation. DR stands for Data Reduction.

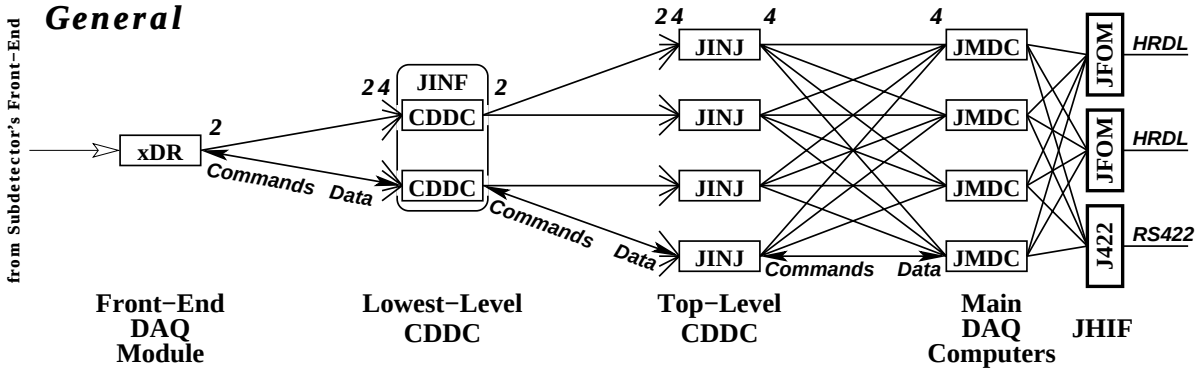

Figure 5.2: AMS-02 DAQ system structure. Data is gathered at the xDR nodes, where the amount of data to be transmitted is reduced to a minimum. The JINF board gathers and buffers the data from a subset of xDR nodes. On request data is sent to a higher instance of the DAQ tree, to the JINJ and to the JMDC. Interfaces to HRDL and RS422 link data to the ISS infrastructure. All links are bidirectional. From [AMS05].

subsequent triggers, sent to the next level in the DAQ tree, which is represented by the JINF boards. One JINF board consists of two redundant CDDCs, which are built up similar to the CDPs but with a different front end and larger memories. Each CDDC is connected to the lower-level CDPs by a maximum of 24 AMSWire links. This maximum is defined by the tracker subsystem, where twelve Tracker Data Reduction (TDR2) boards containing 24 CDPs with two AMSWire links each, have to be connected to the two CDDCs of one JINF board. The event data from connected xDR nodes is collected in the JINF board, buffered and again upon request sent to the next level of the DAQ tree, represented by the four JINJ boards. A maximum of 24 AMSWire links can be connected to the JINJ boards. Here again event data is collated, buffered and upon request passed over to one of the four JMDCs[1]. Once JMDC receives the complete data from one event, it analyzes it to ensure, that it might contain interesting physics data and also to monitor the performance of the detector. The JMDC computer is based on the IBM PowerPC 750 microprocessor, implemented into a custom built computer with a compact PCI format bus (cPCI). The PowerPC 750 features a 32-bit implementation of the PowerPC Reduced Instruction Set (RISC) architecture and low power consumption. It is connected to a 2 GByte solid state memory buffer, which is required when the HRDL[2] is not available, to the AMS-02 CAN-bus for monitoring and command transfers, to the AMSWire links of the DAQ tree and to the HRDL and LRDL[3] including the equivalent data links for the shuttle.

Originally, slow control communication paths and DAQ communication paths were kept separated. Slow control commands were planned to be issued from JMDC via CAN-bus to 8051-processor based slow control boards called USCMs[4], which were supposed to be present in most subsystems such as the TRD and the tracker subsystems and from there to the slow control slaves. For two-fold redundancy two USCMs were placed in parallel, powered by a dedicated DC/DC converter. In the end of 2003 a weight reduction program made it necessary

[1] JMDC, J Main DAQ Computer
[2] High Rate Data Link
[3] Low Rate Data Link
[4] USCM, Universal Slow Control Module

to omit the USCMs together with their DC/DC converters in a lot of subsystems (see Section 5.7). Slow control functionality was taken over partly by a newly developed JINF with added slow control capability. This new board was labelled as JINFv2. Consequently slow control commands for these subsystems are no longer issued via CAN-bus but send via AMSWire links from JMDC to the JINFv2 boards, where they are redistributed to their dedicated slow control slaves. However, still a lot of subsystems are controlled via CAN-bus and USCM boards as shown in Figure 5.3.

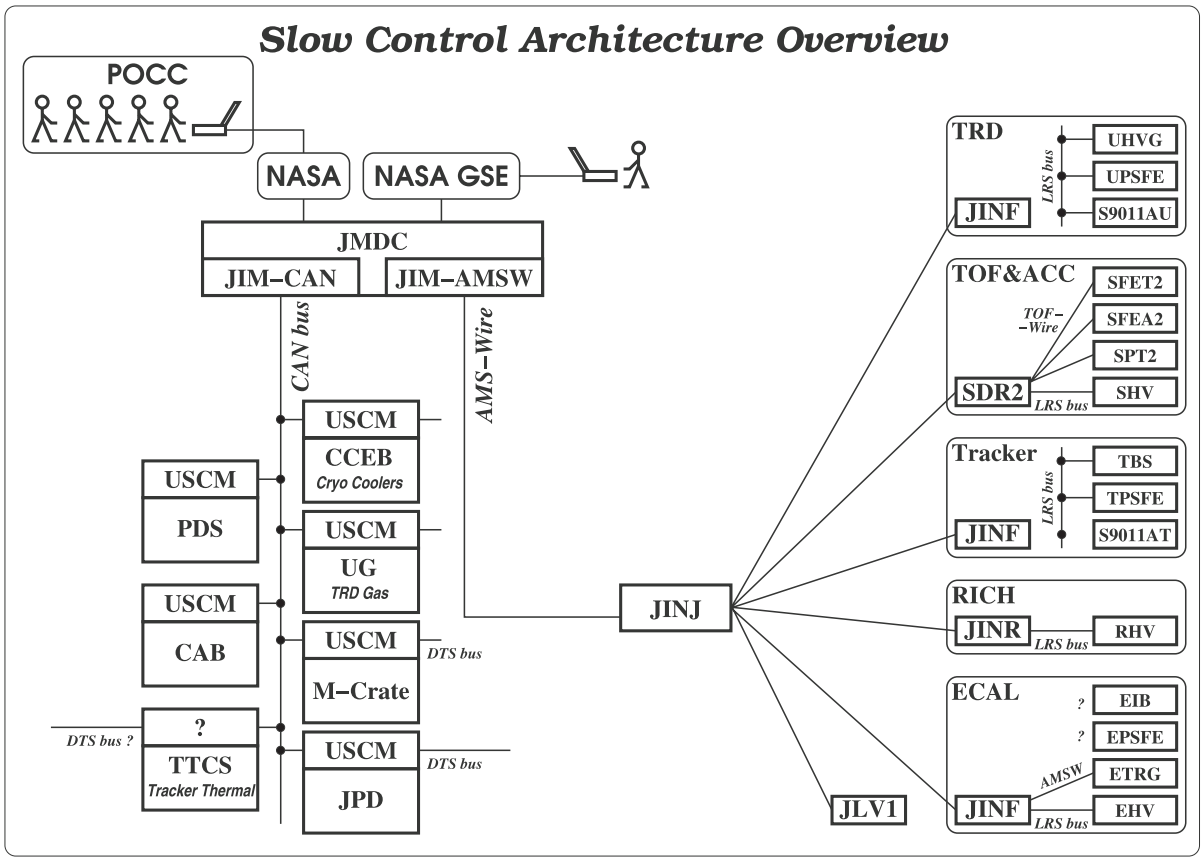

Figure 5.3: Slow control commands are issued on two different commanding paths within AMS-02. For the TRD, TOF, tracker, RICH, ECAL subdetectors slow control commands are issued over the point-to-point AMSWire links. For all other subsystems slow control commands are communicated over CAN-bus. Modified from [AMS05].

5.2.2 Interfaces to the International Space Station

Power Interface

AMS-02 has two power feeds, each one connected to one of the eight ISS solar arrays. The power is provided at voltages between 109 and 126 V, with 120 V nominal. From the ISS power budget AMS-02 is allocated a maximum of 2000 W. This is extended to 2300 W for the final 30 minutes of magnet charging. The power feeds are connected to the AMS-02 Power Distribution System (PDS), which is designed to meet the stringent NASA requirements in

terms of isolation, grounding, electromagnetic compatibility and inrush current. The PDS is equipped with a thermal interlock that diverts power into the PDS heaters as soon as AMS-02 is turned on until the PDS temperature is within the operational range. Electromagnetic interference filters protect the station from noise generated by the experiment and vice versa the experiment from noise generated by noise sources on the station. The two power feeds supply two power buses to which DC/DC converters are connected. They transform the incoming 120 V into 28 V provided to the subsystem consumers with an efficiency of $> 90\%$. These DC/DC converters represent the first power isolation barrier of AMS-02. Wired OR circuit breakers at the output of the DC/DC converters on the two power buses allow each of the subsystem boxes to be supplied with power from either of the two AMS-02 power feeds. Some magnet subsystems are supplied directly by 120 V. The PDS is monitored and controlled by a pair of of USCMs running in hot redundancy.

Low Rate Data Link (LRDL) Interface

Telemetry and commanding data are issued through the LRDL. It is based on the MIL-STD 1553B dual serial bus, which is split to each of the four JMDCs, while one is selected to actively manage the link. To prevent a single-point of failure at the point of bus splitting, AMS-02 is equipped with two splitters which can be selected by swapping a cable outside AMS-02 during an Extra-Vehicular Activity (EVA). Since telemetry and commanding data is critical to the operation of the experiment, the LRDL is linked on the ISS to both, the Ku-band and the S-Band, providing two parallel data paths. See Section 3.2 for more details on the Ku-band and S-band. AMS-02 is allocated about 20 KBits/s on the LRDL with an expected duty cycle of up to 70%. Ten bytes of critical health data are transmitted with near to 100% duty cycle. These can be monitored by the ISS crew or NASA ground controllers, which have the facility to issue some key commands, such as putting the experiment into standby state.

High Rate Data Link (HRDL) Interface

The main amount of data is conducted out of AMS-02 through the HRDL. The HRDL link is based on fiber optics communication. It can transport data with up to 90 MBit/s. On the ISS the HRDL is connected to the Ku-band radio down link, which supports up to 43 MBit/s. Of this transfer rate an orbit average of 2 MBit/s is allocated for AMS-02. All of the four JMDCs are connected to the HRDL. Since the HRDL link between AMS-02 and the ISS, represents a possible single-point of failure, the HRDL link is made redundant. As for the LRDL, an astronaut can swap the HRDL cable during an extravehicular activity. With the HRDL, AMS-02 is linked to ACOP[1], where scientific data is stored on hard disks (see Section 5.2.3).

5.2.3 AMS Crew Operations Post

The AMS Crew Operations Post (ACOP) is a special computer designed for AMS-02. It is brought to the ISS on a previous flight before AMS-02 is launched. ACOP is mounted inside the US lab module of the ISS in an express rack. The main purpose of ACOP is to archive the data from the experiment, which arrives through the HRDL fiber optic data link. Additionally it allows to monitor and command the experiment, if necessary. ACOP will be based on a CompactPCI format system with a single board computer, similar to the JMDC, but

[1] ACOP, AMS-02 Crew Operations Post

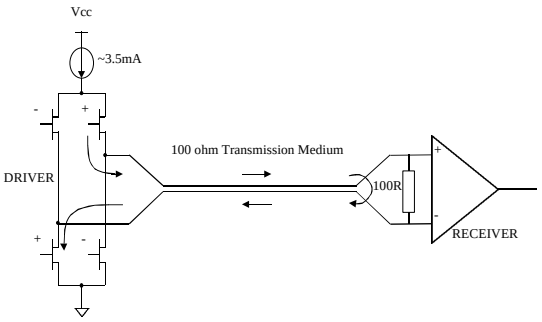

Figure 5.4: Sketch of an AMSWire driver connected to its receiver. A constant current source of around 3.5 mA provides the current that flows out of the receiver, along the transmission medium, through the 100 Ω termination resistors. Two pairs of transistor switches in the driver control the direction of the current flow and thus the logical level. From [Eur00].

with extended memory and peripherals on board. A Compact Flash (CF) carrier will store the operating system and programs. Four exchangeable hard disk will be used to archive the data. VGA graphics and a flight-qualified LCD screen will be available. The total hard disk capacity should be sufficient for one month. Additional crew exchangeable hard disk will be available to extend this period to up to six months. The recorded hard disk will be transported to ground as a permanent archive. With ACOP the crew is able to monitor and control AMS-02, this is of importance when charging the magnet.

5.2.4 Communication Standards

AMSWire

Based on the ESA SpaceWire standard, AMSWire is a bi-directional, serial point-to-point link protocol. Data is transmitted using two differential wire pairs in each direction, yielding a total of eight signal wires, four in each direction. AMSWire uses Data-Strobe (DS) encoding. The first differential pair contains data information and the second differential pair strobe information. The data values are transmitted directly. The strobe signal changes its state, whenever the data remains constant from one bit to the next. Using this coding scheme the transmission clock is encoded in data and its associated strobe. By XORing the data and associated strobe line together, the transmission clock can be recovered. The reason for DS encoding is to improve the skew tolerance to almost 1-bit time compared to 0.5-bit time for simple data and clock encoding. AMSWire follows the Master-Slave concept. A slave does not send any reply, unless it receives a request from any of its masters. AMSWire signals are transmitted through a cable, across a PCB or a backplane using Low Voltage Differential Signal (LVDS) technique. The driver-receiver scheme is shown in Figure 5.4. The benefits of LVDSs are: near constant total drive current (±3.5 mA) which decreases switching noise on power supplies, high immunity

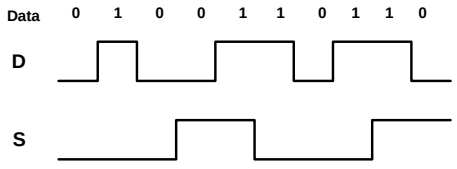

Figure 5.5: Example of Data-Strobe-encoding used in AMSWire. From [Eur00].

against potential differences between driver and receiver (± 1V) and high immunity against induced noise. Furthermore, LVDS technique implies low EMI since the small equal and opposite currents on the differential lines create small electromagnetic fields which tend to cancel one another. LVDS drivers have a small power consumption of about 50 mW. To terminate the AMSWire link a simple 100 Ω resistor is applied. The AMSWire data rate is 100 Mbps, fixed for both directions. AMSWire connectors are of micro-miniature-d type and have eight signal contacts plus a screen termination contact. Further information about AMSWire can be found in [Lin01] and about SpaceWire in [Eur00].

CAN-Bus

CAN (Controller Area Network) is a serial bus system which was originally developed by BOSCH[1] for automotive applications in the early 1980s. The CAN specification v2.0 was introduced in 1991. Today CAN is widely used in passenger cars, trucks and buses, trains, maritime electronics, medical equipment, factory automation, aircraft and aerospace electronics. Physically the CAN-bus can be implemented by two lines with differential signals. On these two lines a bit is described as two oppositional potential level changes. The lines are commonly referred to as CAN-H and CAN-L. Possible electromagnetic disturbances affect both lines. But since only the differential outcome is relevant, disturbances are effectively suppressed. Multiple CAN nodes are usually present on one bus which encloses the danger of logical conflicts causing electrical shorts, when two nodes try to send complementary bits simultaneously. This is avoided by using open-collector technique. The condition with two contrary levels on CAN-H and CAN-L is referred to as dominant bit, representing a logical "0" and the condition with two identical levels is referred to as recessive bit, representing a logical "1". The connection of the CAN node by the bus represents a Wired-And connection scheme. The schematic of a CAN driver is shown in Figure 5.6. The differential CAN-bus is terminated by two 120 Ω resistors at each end. By this, reflections are avoided and the potential of both lines get referenced against each other. The CAN data rate can be up to 1 MBit/s[2]. The constraint is that all CAN nodes have to process the message simultaneously which poses a limit on either the bus length or on the data rate. With 1 MBit/s a bus length of 40 m is possible, while for 10 kbit/s a bus length of 6.7 km can be reached. CAN provides a multi-master hierarchy, allowing the construction of redundant systems. If one network node is defective, the network is still able to operate. CAN is based

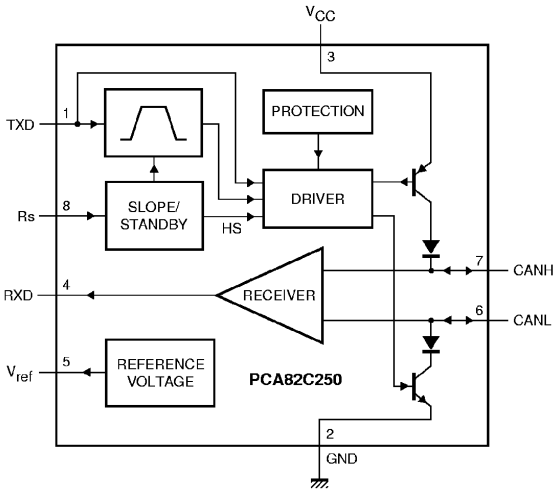

Figure 5.6: Differential CAN driver with open collector wiring. The PNP transistor is connected to VCC to control the CAN-H line and the NPN-transistor is connected to GND to control the CAN-L line. From [ME-05].

[1] Robert Bosch GmbH, http://www.bosch.de, Germany which focuses mainly on the development of electronics for automotive applications.

[2] as defined in ISO 11898-2 high speed

on broadcast communication, meaning that a sender transmits information to all devices on the bus. Each message possesses a message identifier. A receiver is not addressed directly. Instead, all receiving devices read the message and then decide if it is relevant to them by evaluating its identifier. By using this content specific addressing scheme, adding more CAN nodes can be accomplished in an easy way. Sophisticated error detection mechanisms guarantee data integrity. Every transmitter that is sending, compares simultaneously the bit levels to be transmitted with the bit levels detected on the bus. In this way global errors or local bit errors on the transmitter can be detected reliably. The transmitter sends the result of its own CRC[1] calculation in its message. Receivers calculate the CRC in the same way as the transmitter and compare their result to the received value. In case of disagreement a CRC error is recognized. All receivers check the consistency of the message being received and acknowledge a consistent message or flag an inconsistent message. The transmitter detects this acknowledgement error condition and breaks off the current communication. Automatically the transmitter restarts the communication. Permanent failures can be distinguished from short disturbances by CAN nodes. Defective nodes are switched off. To reduce power consumption CAN-devices may be set into sleep mode. More information about the CAN protocol can be found in [Rob91, CAN05].

5.2.5 The Common Parts of AMS-02 Electronics: CDP and CDDC

The Common Digital Part (CDP) as shown in Figure 5.7 is the heart of each AMS-02 DAQ board. It is composed of an Analog Devices DSP 2187L, a 512 KB AMD AM29LV004B Flash Memory, an 128 KB Samsung Static Random Access memory (SRAM) K6R1016V1C and a Field Programmable Gate Array (FPGA). Depending on the development stage, two different FPGAs have been built in the CDP. In early development stages the reprogrammable Altera Apex EP20K200EBC356 and later on the radiation hard, but only single programmable Actel A54SX32A gate arrays have been used. The basic working principle of the CDP node is, that upon an incoming LV1 trigger the sequencer starts moving digitized scientific data from the front ends into the SRAM. The DSP recognizes the raw event in the SRAM memory and processes it and stores the processed event in the output buffer of the SRAM. The CDP receives its commands by the AMSWire receivers and stores them into the SRAM. Afterwards they are read out and analyzed by the DSP. As soon as a command arrives requesting the processed event, the event data is transmitted from the SRAM to the requesting node by the AMSWire transmitter. The most important CDP components are described in the following.

Digital Signal Processor

The Analog Devices DSP-2187L endows the CDP with processing power. It is a single-chip microcomputer with built in 32 K of 24-bit program memory and 32 K of 16-bit data memory. The DSP is clocked by a 25 MHz clock to provide a 20 ns instruction cycle. One instruction is executed in a single cycle, yielding 50 MIPS[2] processing power. The DSP is powered by 3.3 V and consumes about 168 mW neglecting output loads, when running at full speed. Two low power states are available. The first one with a consumption of 32 mW and a second one down to 12 mW by slowing down the internal clock signal. The processor remains in the low power state until an interrupt occurs. Additionally a power-down state can be used to reduce the power consumption even more. Up to eleven interrupts are available, four of them are dedicated external interrupts. Internally the DSP uses five buses, a program memory address

[1] CRC, Cyclic Redundancy Check
[2] MIPS, Million Instruction per Second

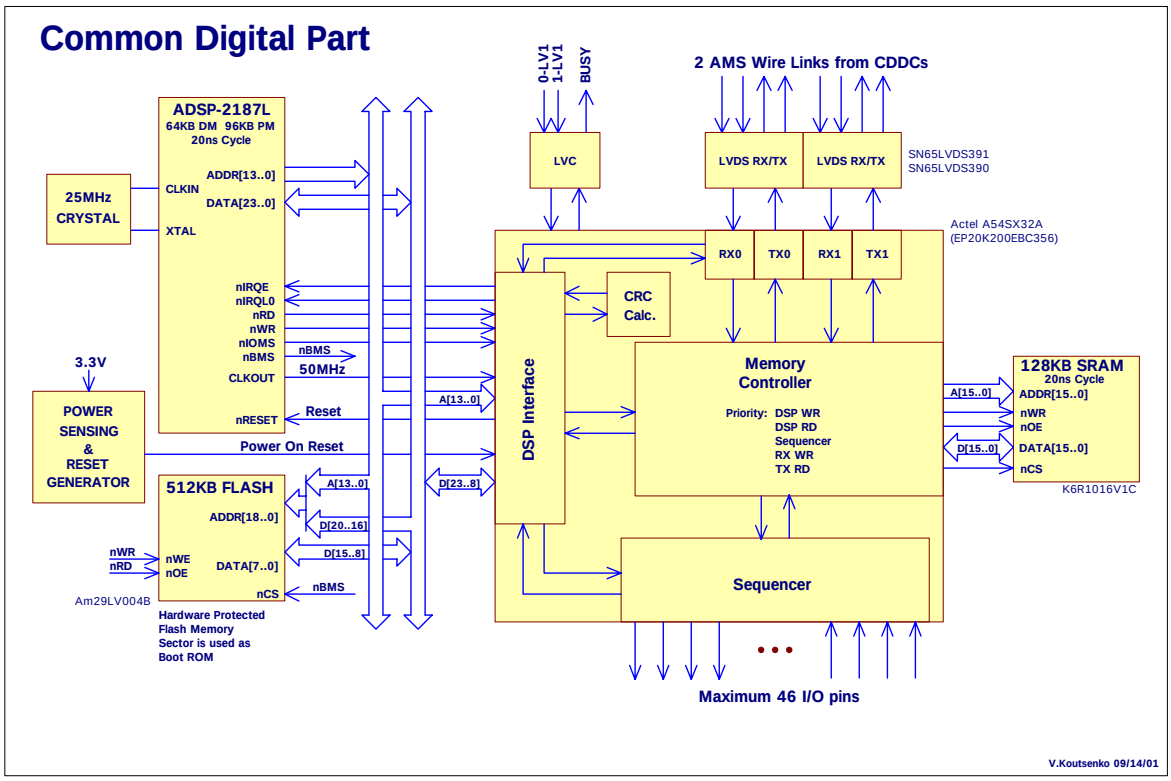

Figure 5.7: Overview of the Common Digital Part. It consist of a 16-bit Analog Devices digital signal processor, a flash memory, an SRAM, LVDS drivers/receivers and a Field Programmable Gate Array (FPGA). In an early development stage, a rewritable Altera APEX20K FPGA and later on the radiation hard Actel FPGA A54SX32A-PQ208 was used.

bus, a program memory data bus, a data memory address bus, a data memory data bus and a result bus. Since the program memory can store both instructions and data, two operands can be fetched at the same time: one operand from the program memory through the program memory bus and one operand from the data memory though the data memory bus. In parallel the DSP generates the next program address, fetches the next instruction, performs one or more data moves as described before, updates one or two address pointers and performs a computational operation. These features allow the programmer to develop highly efficient code as will be described in Chapter 6.3. Externally the two address buses share a single address bus, allowing to access memory off-chip. With this 14-bit address bus and the 24-bit data bus, access to the flash memory and to the DSP interface of the gate array is available. Through the DSP interface and the memory controller in the gate array the SRAM memory can be accessed. The processor contains three independent computational units the ALU[1], the MAC[2] and the shifter, which are connected by the data-, program- and the result bus. Two serial ports are available, although they are not used in the CDP. More information about the DSP can be found in [Ana98].

[1] ALU, Arithmetic and Logic Unit
[2] MAC, Multiplier, Accumulator

Flash Memory

The AMD AM29LV004B is a 4 MBit CMOS flash memory segmented in 512 K x 8 bit. A flash memory is a non-volatile memory. After a power cycle, the memory content is still present. This flash memory is powered by 3.3 V. According to the data sheet this flash chip guarantees 1000000 write cycles per sector and 20-years data retention at 125°C. It is divided into one 16 KByte, two 8 KByte, one 32 KByte and seven 64 KByte sectors. The DSP boots from the flash memory. The first three sectors of the flash memory contain the bootstrap code, the boot loader and three identical versions of the ROM monitor. The ROM monitor is the base program which serves AMSWire requests and allows to load user specific programs from the flash memory. The first three sectors are hardware protected against modifications or erasure. Upon boot, the bootstrap code in the first 96 bytes at the very beginning of the flash memory memory is loaded into the DSP program memory at address 0x0000. The DSP program execution starts at address 0x0000 of the program memory and the bootstrap code loads the boot loader from the flash memory into program memory. The boot loader observes the three versions of the ROM monitor for intactness by CRC calculation and loads the first version which passed the test into program memory address 0x0000 using BDMA[1] transfer with context reset. In case all three versions of the ROM monitor are corrupted, majority logic is used to reconstruct a new ROM monitor out of the three corrupt versions. The remaining eight sectors of the flash memory allow to store configuration data or detector specific program files, containing the actual event building code. [Ana00]

SRAM

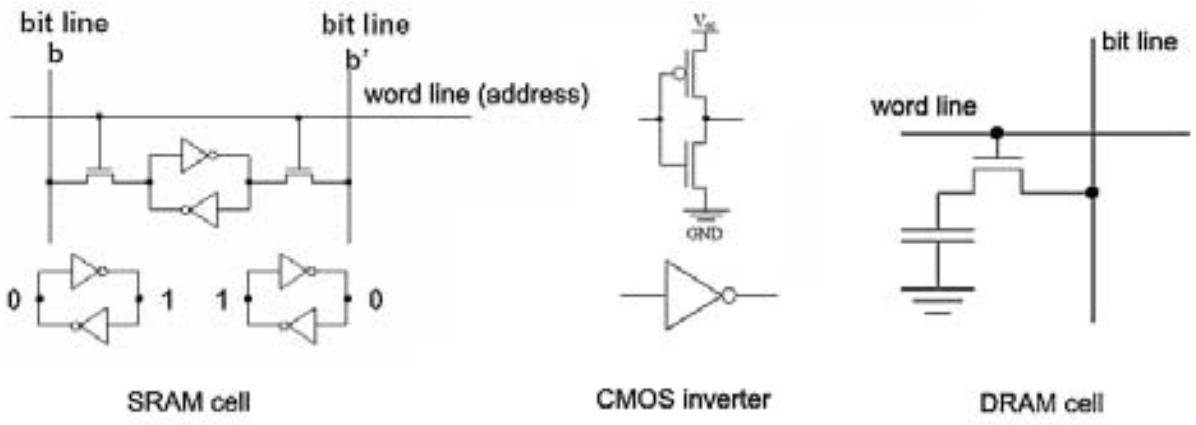

Figure 5.8: Principle of SRAM memory. Two cross-coupled inverters store the memory information. Commonly six transistors are required to form a memory cell.

The SAMSUNG K6R1016V1C memory is a 64 K × 16 bit CMOS static random access memory (SRAM). It features low power dissipation of down to 5 mA in standby and about 93 mA in operation. It is accessed by the CDP with 20 ns cycle but can be accessed with a 15 ns cycle. Common DRAM[2] memories used as the main memory of today's personal computers

[1]BDMA, Byte Memory Direct Memory Access
[2]DRAM, Dynamic Random Access Memory

store information on transistor accessed capacitors and therefore suffer leakage and require periodic refreshing. In contrast to that, the SRAM uses a more complex technique involving four transistors to form two cross-coupled inverters and two more to access the memory. In this way it takes typically six MOSFETs to store one bit. This obviously requires more space on the chip than the simpler DRAM memory, which makes the SRAM more expensive. Figure 5.8 shows the schematic of an SRAM memory cell. The larger package of SRAM chips allows to feed in all address lines at the same time, in other words it does not require address multiplexing. Since SRAM chips do not require refreshing and all address bits can be applied at the same time, SRAMs are much faster than DRAMs. For the same reasons it is easier to work with SRAMs than with DRAMs.
Among other tasks the SRAM in the CDP is used to store raw and processed events. The memory access is controlled by the gate array.

FPGA

The Field Programmable Gate Array (FPGA) represents the interface to all peripherals. The FPGA contains the logic to receive and transmit AMSWire requests, CRC calculation, the interface to the DSP and the memory controller to access the SRAM memory. These features are common in all CDP and CDDC nodes. The main difference between the CDP nodes of the various subdetectors and to the CDDC represents the sequencer, which does not exist in CDDC nodes. Since the subdetector front ends are different in terms of ASIC type, ADC type, timing and amount of channels, they require different sequences to make the ASIC multiplex the analog detector signals to the ADC and the digitized data from the ADC to the FPGA. Naturally the CDDC does not contain any sequencer but additional AMSWire receivers and transmitters to connect up to four masters and 24 slaves. While the common part of the logic has been developed by MIT, the subdetector specific part has to be provided by individuals of the subdetector collaborations. The best choice is certainly the front end designer, since he knows best about its requirements. For the TRD electronics the front end sequences were defined by RWTH Aachen and were technically implemented by the Universität Karlsruhe together with MIT. The FPGA firmware has been developed using VHDL[1] language. This language describes the desired behavior of the logic under development and does not use logic components, such as flip-flops as descriptive elements. More information about the technical implementation of the sequencer in the CDP code can be found in [Jun05]. The description of the sequences is given in Section 5.4.1.

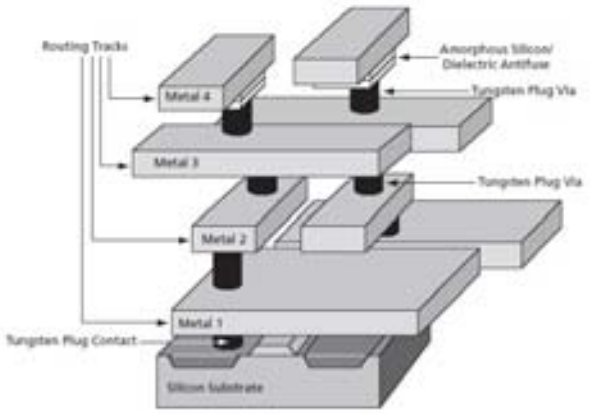

Figure 5.9: Principle of Actel's antifuse technology for the SX-A chip family. The picture illustrates the principle for the A54SX72A device which has four layers of metal with the antifuses between Metal 3 and Metal 4. The A54SX32A device has three layers with the antifuse between Metal 2 and Metal 3.

[1]VHDL, Very High Speed Integrated Circuit Hardware Description Language

Altera Apex 20K SRAM FPGA
The firmware development was performed on prototype boards housing Altera Apex EP20K200 QC208 PLDs[1]. It is supplied by 2.5 V and a 50 MHz clock provided by the DSP. The Apex architecture uses SRAM configuration elements in contrast to the Actel antifuse technology. These devices are more suitable for the development stage than antifuse devices, since they can be reprogrammed lots of times. The firmware of Altera Apex 20K PLDs is volatile. It has to be loaded any time, when a power cycle has preceded. This can be done either manually by a dedicated programming cable[2], which is connected on one end to a serial or parallel port of a PC and on the other end to the JTAG[3] connector linked to the Apex. The Apex can also be programmed by dedicated configuration devices, namely small Flash EEPROM[4] chips, named EPCT32. Upon start-up the Apex retrieves configuration information from these chips and can be used instantly. The configuration flashes also have to be programmed. This can be done using the same programming cable on the same JTAG connector, since the Apex and the configuration devices are both linked to it. Due to their SRAM technology the Apex PLDs are not considered as radiation tolerant and therefore replaced by Actel antifuse FPGAs in the final electronics design. Since these devices were used on prototype boards, they are of no importance for the final layout of the TRD electronics. [Alt04]

Actel Antifuse FPGA A54SX32A
The final design uses the ACTEL A54SX32A FPGA in the PQ-208 package. It is supplied by 2.5 V and a 50 MHz clock provided by the DSP. Technically the ACTEL SX-A FPGA family is based on the metal-to-metal antifuse concept. It is fabricated in a 0.22/0.25 μm CMOS process. The entire floor of each chip is spanned with an uninterrupted grid of logic modules. These logic modules need to be interconnected to be used. This is done by the programmable metal-to-metal antifuse interconnect elements embedded between layers M3 and M4. Locating the interconnection elements in other layers than the logic elements is an advantage, since all the precious place on the silicon substrate can be used to place the logic elements and no space is wasted for interconnections. Figure 5.9 shows the layer configuration of the A54SX72A FPGA. The difference to the A54SX32A device in the layer configuration is that metal layer 4 is missing and the antifuses are located between metal layer 3 and metal layer 2. The antifuse elements are formed by a combination of amorphous silicon and dielectric material between the metal of the interconnect layer and the tungsten via to the lower plane. After being programmed these interconnects form a permanent low-impedance connection of about 25 Ω with a capacitance of 1.0 fF for low signal impedance. Firmware development was done using VHDL language. SRAM based FPGA technology, as used in the Altera Apex FPGA described above, is susceptible to SEEs[5]. Both transient corruption of single bit information, known as soft errors, and loss of FPGA configuration, known as firm errors, are possible. Firm errors incorporate the hazard of system level functional failure and are very difficult to prevent and correct. Antifuse FPGAs are immune against firm errors. [Act05]

[1] PLD, Programmable Logic Device
[2] MasterBlaster or ByteBlasterMV
[3] JTAG, Joint Test Action Group
[4] EEPROM, Electrically Eraseable Programmable Read Only Memory
[5] SEE, Single Event Effect, (effect on electronics due to radiation)

5.3 The TRD DAQ electronics subsystem design

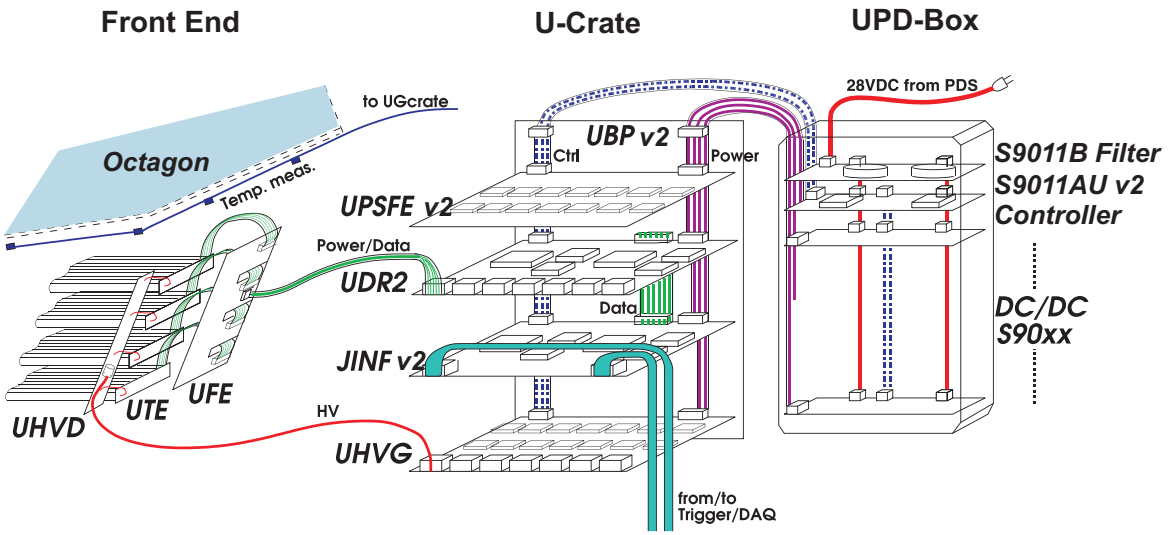

Figure 5.10: TRD DAQ electronics subsystem design. The TRD electronics consists of three spatial separated major parts: Front end electronics, the U-Crate and the UPD-Box. The front end part in the picture is mounted at the walls outside the octagon, close to the mounting slots for the straw tube modules. All in all there are two U-Crates and two UPD-Boxes, one set mounted on the wake and one set mounted on the ram radiator. A list of board abbreviations is available in Table 5.1.

The electronics for the TRD as illustrated in Figure 5.10 consists of the front ends (attached to the detector), the data acquisition electronics, the slow control electronics, the high voltage system (inside U-Crate) and the DC/DC converters (inside UPD-box). The *U* in the abbreviations for all subdetector specific electronic boards stands for the German word *Übergangsstrahlung*, meaning *transition radiation*. A list with the meaning of all the abbreviations is given in Table 5.1. The TRD DAQ electronics subsystem consists of three parts.
The first part is represented by the front end electronics, which is under responsibility of RWTH Aachen. It consists of three kinds of boards: the UFE-boards, the UTE-boards and the UHVD-boards. The Tube End boards (UTE) are placed at the very end of the straw tube modules. Their function is to decouple the signal from the high voltage on the straw tube wires through capacitors to the front end electronics boards (UFE). The High Voltage Distribution (UHVD) boards provide the means to connect the HV cable and to route the high voltage to the straw modules. These are mounted together with the UFE boards on the walls outside the octagon. They consist of two IDEAS VA32 chips, which multiplex the 64 signals from four straw tube modules to a 12-bit serial ADC. All in all there are 82 sets of front end boards to read out the whole detector.
The second part is the U-Crate, which houses four different kind of boards on a backplane (UBP): the UPSFE, the UDR2, the UHVG and the JINF. The power for the UFE boards is controlled and regulated by the Power Supply For Front Ends board (UPSFE). It consists of 14 linear regulators, two Actel FPGAs and slow control circuitry to switch on and off not only

Front End	
UFE	TRD Front End Board
UTE	TRD Tube End Board
UHVD	TRD High Voltage Distribution Board
UFS	TRD Front End Simulator
U-Crate	
UPSFE	TRD Power Supply for Front Ends
UDR2	TRD Data Reduction Board
JINF	Command Distributor and Data Concentrator
UHVG	TRD High Voltage Generator
UBP	TRD Backplane
UPD-Box	
S9011AU	Controller for TRD DC/DC Converters
S9011B	28 VDC Filter

Table 5.1: List of TRD electronics abbreviations.

its linear regulators onboard but all the other boards in the crate, except for the JINF. Three UPSFEs are located in one crate, each providing power for 14 UFE boards. One linear regulator supplies two UFE boards. Consequently in nominal conditions seven linear regulators are in use, the other seven linear regulators are kept in cold redundancy. Six High Voltage Generators (UHVG) supply the straw tubes wires with up to about 1600 V. The UHVG boards are composed of double-redundant Cockroft-Walton HV generators with 16 stages controlled by Lecroy MHV100 chips. The six Data Reduction Boards (UDR2) are composed of two double redundant CDPs, which generate the readout sequences for the UFE boards, and interface circuitry to access seven UFE boards. The main task of the UDR2 boards is to reduce the amount of incoming data from the front ends to a minimum, by discarding data from channels which show no signal, and to send only the reduced amount of data to the higher DAQ. The raw data of the TRD at a 2 kHz trigger rate is approximately 20 MByte/s. Assuming only single event hits with signals in all 20 layers, the data rate would be reduced to 78 KByte/s. Since the UDR2 is the only link between the U-Crate and the front ends, the power for the front ends is routed from the UPSFE through the UDR2 to front ends. Upon request the JINF board, which consists of two CDDCs, collects the event data of all the six UDR2 boards and transfers it to the main AMS-02 DAQ system for storage on the ISS and downlinking to Earth. All in all, there are two U-Crates, which house 16 VME-sized boards each.
To supply these boards with their dedicated operating voltages, the 28 V coming from a central Power Distribution System (PDS) inside AMS-02 has to be transformed by custom-made DC/DC converters which provide transformation efficiencies of up to 80%. These DC/DC converters are housed in the UPD-Box, which represents the third part of the TRD DAQ electronics subsystem. For each U-Crate one UPD-box contains seven double-redundant DC/DC converters, a filter and control electronics.
Due to the low power consumption of the utilized components and due to the high efficiencies of the DC/DC converters, the complete TRD DAQ electronics has a power consumption of less than 100 W.

5.4 Front End Electronics

5.4.1 The Front End Board UFE

Figure 5.11: Photo of a UFE-board.

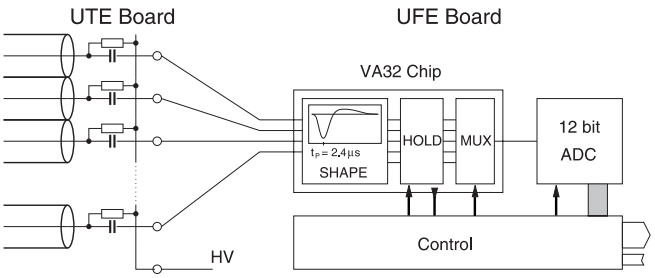

Figure 5.12: Scheme of TRD front end electronics.

The UFE board acquires and digitizes physics data. A picture of a UFE board can be seen in Figure 5.11. One UFE board is connected to a group of four straw tube modules with 16 straw tubes each, thus being able to perform pre-amplification, shaping and signal digitalization for a total of 64 channels. As illustrated in Figure 5.12, the wire signals are fed into two Viking VA32HDR12[1] chips. Each chip contains 32 preamplifiers, CR-RC shapers and sample-and-hold circuits and a multiplexer which switches the signal of all 32 channels, one after another, to the chip output. The UFE boards feature a linear dynamic range of up to 1.5 pC within 1%. The gain is uniform within 3% per UFE. The increase is 2 ADCcounts/fC, which gives a dynamic range of 3000 ADC counts. With a gas gain of 3000, a MIP corresponds to about 80 ADC counts. The noise per channel is below 2 ADC counts, which corresponds to 6250 e^-. The mean pedestal lies around 400 ADC counts. These characteristics allow measurements in the range of 0.03 MIPs up to 33 MIPs. The mean of the UFE gain is shown in Figure 5.13. The UFE board is controlled and read out by the UDR2 boards in the U-Crate. It is supplied by ± 2 V, originally separated into ± 2 V analog and ± 2 V digital to avoid emission of digital noise into the analog signal. While the analog and digital supply lines are still separated on the UFE board, they had to be combined in the U-Crate to cut down the amount of linear regulators used and therefore the amount of UPSFE boards during weight reduction (see Section 5.7).
The two Viking chips are connected in parallel. A *shift_in* signal defines one of the two Viking chips to be active at a time. The peaking time of the Viking chip on the UFE boards is about 2.4 μs as can be seen in Figure 5.14. This time delay has to be taken into account when adjusting the trigger during data taking. The output of both Viking chips is connected to a 12-bit serial Analog Devices 7476 ADC located onboard the UFE to digitize the 64 signals. This is a major benefit, since the sensitive analog signals are converted directly after the Viking chip. In this way it is avoided that the analog signals have to be transported through a long cable, being exposed to electromagnetic noise, before being digitized on another board. The ADC is controlled and read out directly by the UDR2 board via LVDS signals. The control sequences for the two Viking chips are provided by an HCC[2] chip. The purpose of the HCC chip is to reduce the amount of control signals for the Viking chips coming from the UDR2 and to generate separate *shift_in*-signals for each Viking and therefore allowing to replace the daisy-chaining of *shift_in/shift_out* between the Vikings. This is an advantage, since the loss of the first chip does not imply the loss of the *shift_in* signal for the second Viking. Five HCC

[1] VA32hdr12 manufactured by IDEAS (Integrated Detectors & Electronics AS), N-1323 Høvik, Norway
[2] HCC, Hybrid Control Circuit

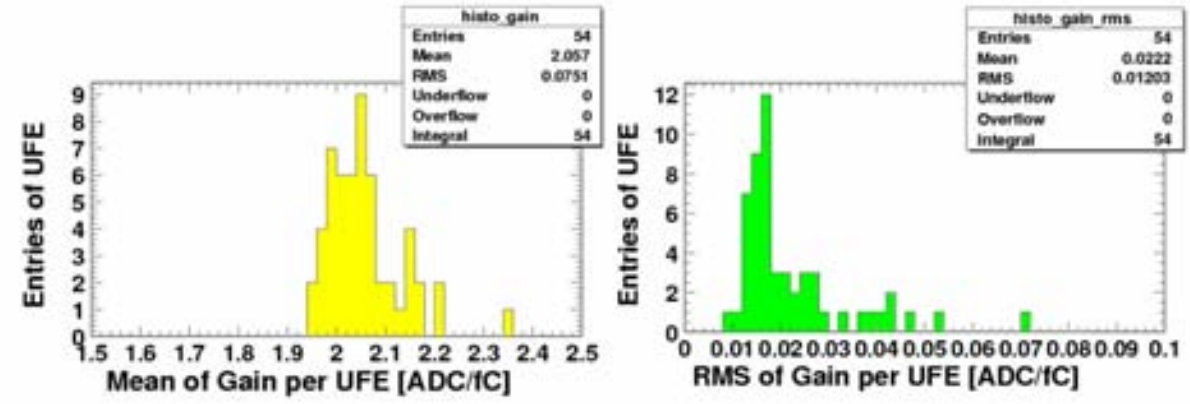

Figure 5.13: UFE production quality histograms. The mean gain is about 2 ADC/fC counts with an RMS of 0.02 ADC counts/fC. From [Chu05].

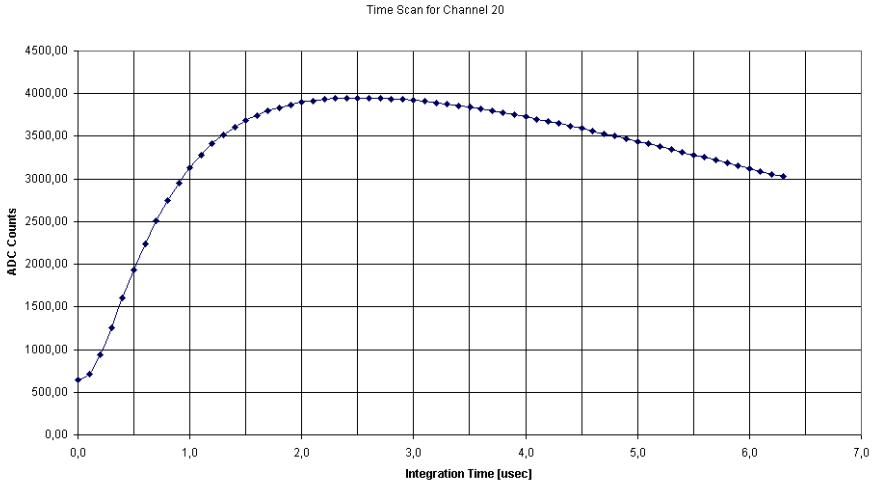

Figure 5.14: Delay scan of a UFE board. The time between physics event and the incoming trigger is varied.

output signals control the two viking chips: a *clock* signal to multiplex the channels to the chip output, a *holdVA* to hold the incoming analog signal in the chip, a *shinB* signal, or *shift_in*, to start the readout of a Viking chip, a *dreset* signal to reset the Viking and finally a *teston* signal to turn the chip into test mode. The HCC chip itself is controlled by four signals *S*, *SB*, *H*, *HB*, generated on the FPGA on the UDR2 board. Two main sequences are available: standard readout and calibration sequence. The standard readout sequence is activated as soon as a trigger arrives. It digitizes real physics data and transmits it to the UDR2 board for data reduction and further transmission. The purpose of the calibration sequence is to test the functionality and linearity of each Viking channel. A DAC[1] on the UDR2 board is used to generate a calibration pulse which is applied to a dedicated calibration input of the

[1]DAC, Digital Analog Converter

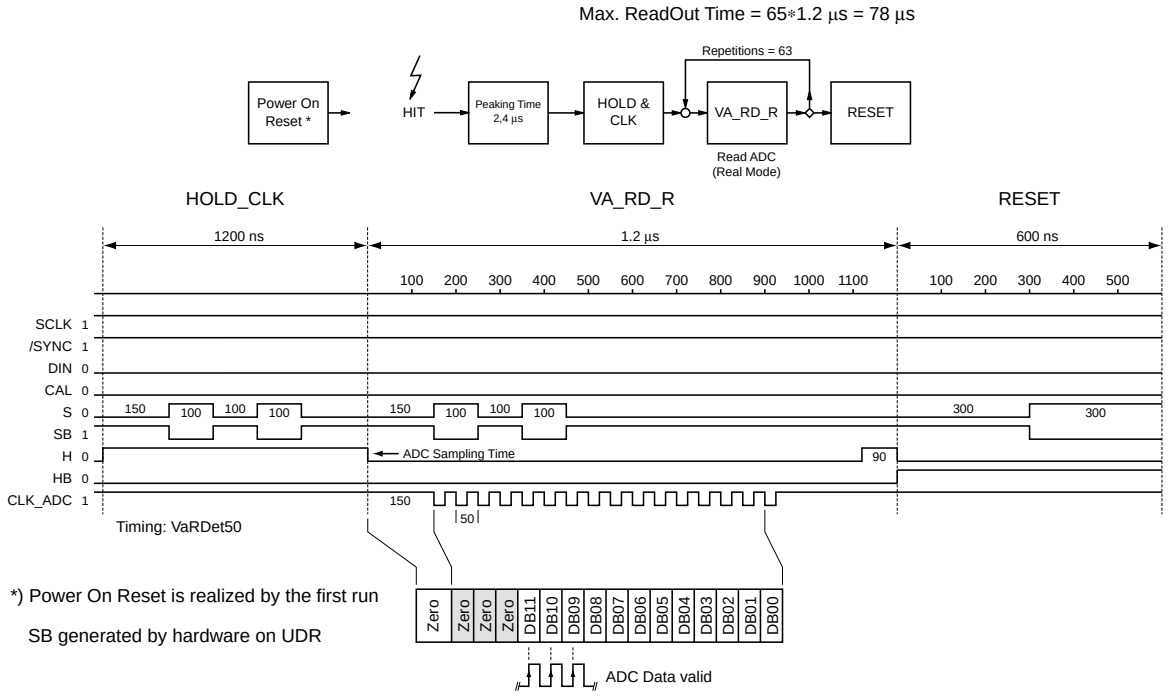

Figure 5.15: Readout sequence definition for UFE boards.

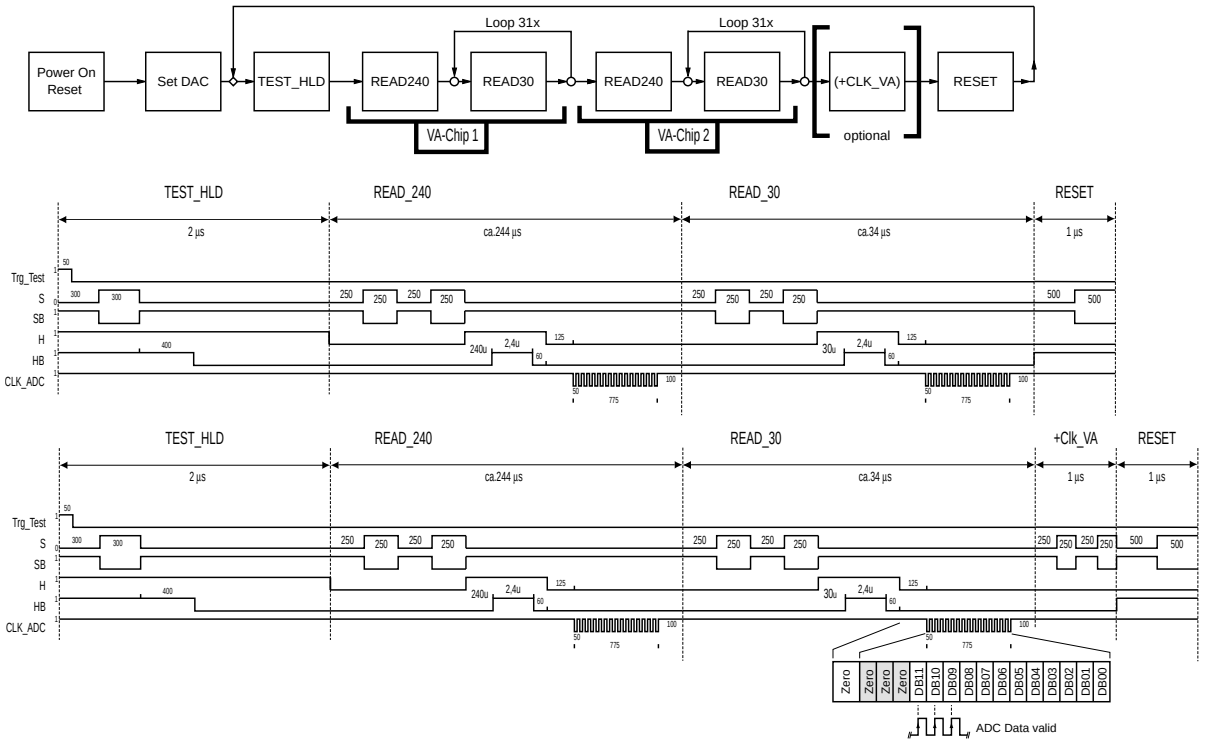

Figure 5.16: Calibration sequence definition for UFE boards.

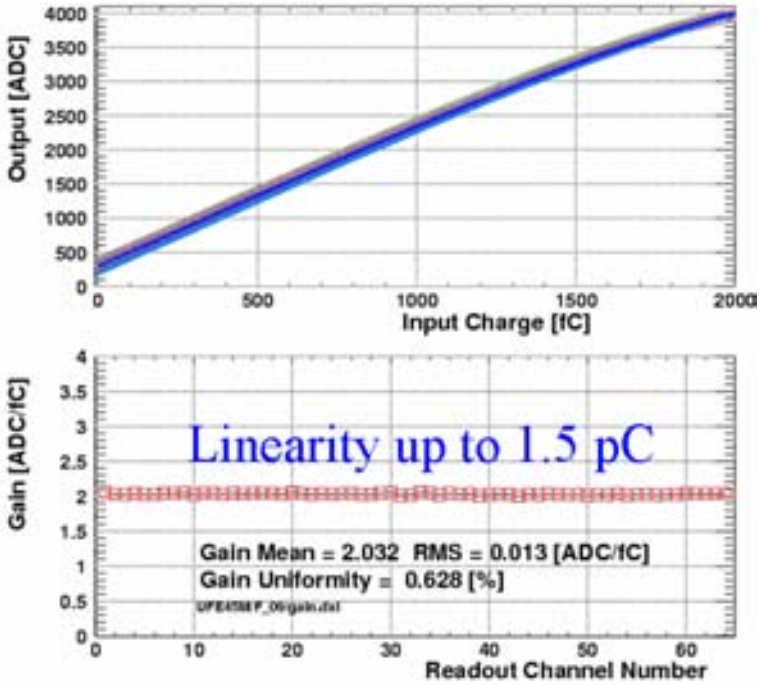

Figure 5.17: Linearity scan taken from the calibration sequence. From [Chu05].

Viking chips. From there the calibration pulse is applied to discrete channels. The standard readout sequence and the calibration sequence are illustrated in Figures 5.15 and 5.16. The readout sequence is easy to understand. After a particle has crossed the detector, the trigger is delayed for 2.4 μs to account for the peaking time. Afterwards the sequence is started with the HOLD_CLK signature. With the falling edge of the H-signal the ADC samples the analog signal and the CLK_ADC signature starts to clock the ADC to transmit the digitized value to the UDR2. After all 64 signals have been digitized, the RESET signature is sent. The attentive reader may note, that S and $\bar{S}$ are clocked twice instead of once to switch from channel to channel. The reason for this lies in the history of the HCC-chip. This chip was originally built for the tracker hybrids, which use Viking chips with 64 channels. Nevertheless it could be used in TRD electronics by reducing the amount of clock cycles from 64 to 32. This is accomplished by using a JK flip flop on the UFE board, which generates the real clock for the UFE Viking chips. The standard sequence readout time is 78 μs. The calibration sequence is a bit more complex. Before the actual start of the calibration sequence, the DAC has to be set. The TEST_HLD signature announces the start of the calibration sequence. Noteworthy are the READ240 signatures during the readout of the first channel of each Viking. A relatively large delay can be found between the first and the second channel. This large delay was introduced to reduce a cross talk problem between the first and second channel of each Viking chip. The optional CLK_VA signature at the end, just before the RESET signature prevents an accumulative problem with the last channel of the second Viking. More about Viking problems and the affiliated solutions can be found in Section 5.8.1. The output of the calibration sequence is shown in Figure 5.17. To read out one DAC pulse injected in all 64 channels, the calibration sequence takes about 2.6 ms. [AR99, Lip00, Ide00]

5.4.2 The Tube End Board UTE

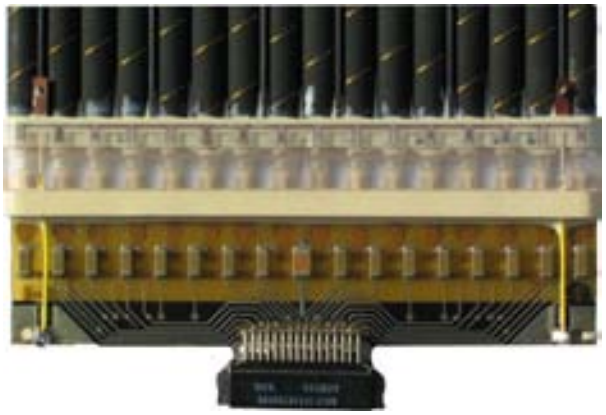

Figure 5.18: Photo of the UTE board mounted at the end of a straw module.

Figure 5.18 shows the picture of a Tube End board (UTE). It is mounted on one side of a straw tube module, where it is soldered to the CuTe endpieces. The UTE board connects the high voltage supplied by the UHVG boards via 2 MΩ resistors to each of the 16 wires of a straw tube module. Furthermore, it decouples the wire signals from the high voltage by 150 pF high voltage capacitors.

5.4.3 The High Voltage Distributor UHVD

Figure 5.19: Photo of the UHVD board.

The High Voltage Distribution Board (UHVD) as shown in Figure 5.19 is the simplest board in the front end section. It merely consists of a high voltage connector for the cables to the UHVG boards and distributes the high voltage to four UTE boards mounted on the straw tube modules.

5.5 The U-Crate: Electronics for the TRD

The U-Crate is composed of 16 U6-sized cards, 15 of them connected by 2 × 96 pin VME connectors in a backplane, one board connected by a 525-pin cPCI connector. Solid state fuses are present on each board in the U-Crate protecting against destructive single event latch-ups: as soon as a predefined current setting is exceeded this fuse cuts off the power and restores it after a certain time. Mechanically the U-Crate is made of aluminum 7075. The crate walls are machined out of single aluminum pieces. All surfaces are hardened by surface treatment. Anodizing, when no electrical and thermal contact is desired, otherwise Alodine is applied. More information about surface treatment can be found in Section 5.6. Beside the mechanical stability and the performance under vibration, the thermal transfer capability plays a major design rule. The heat generated on the electronics boards has to be removed. This is accomplished by using *wedge locks*, which are mounted close to the right and left side of each board on metalized areas (Figure 5.20). After the board is inserted into the crate, the wedge locks are splayed by adjusting a screw to establish thermal contact to the crate wall. The mechanical design drawings were created by CGS[1]. QM1 prototype U-Crate mechanics was built in Karlsruhe workshop. The surface treatment was done at CSIST[2] in Taiwan.

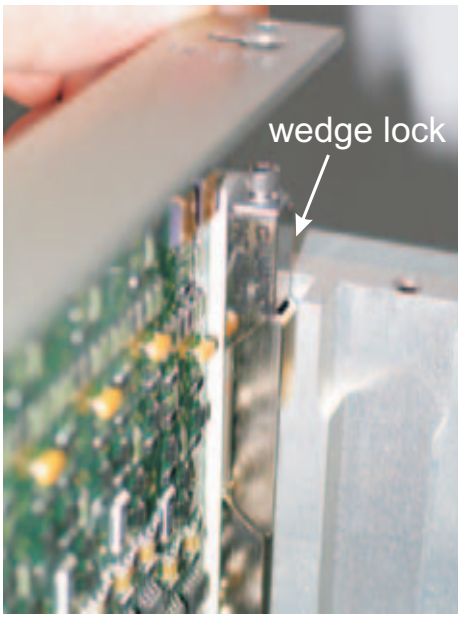

Figure 5.20: Wedge lock on UPSFEv2 during insertion into the crate.

5.5.1 The Interface Board JINFv2

The JINFv2 board represents the interface between the U-Crate and higher DAQ. It is accessed by four AMSWire connectors, which are placed on the front panel. A fifth connector on the front panel represents the trigger/busy link. Figure 5.21 shows a photo of a JINFv2 board. This board sends trigger signals to the six UDR2s of one crate. Furthermore, it gathers all physics data taken from the UDR2s, buffers it and sends it on request to the higher DAQ nodes. Additionally it issues slow control commands to the three UPSFE boards, to the six UHVG boards and to the S9011AUv2 of the UPD-Box. While the data gathering is done through AMSWire links, the slow control is performed by eight Lecroy-Bus links. The JINF board is composed of two redundant CDDCs. Two AMSWire links from the front panel are connected to each CDDC. Each CDDC has the capability to address up to 24 AMSWire slaves. This calls for an enormous amount of pins on the board connector which made it necessary to choose the cPCI standard. Since in the U-Crate just 6 UDR2s are present, only half of the available AMSWire links are used. The JINFv2 is supplied by 3.3 V power. Each CDDC can be switched on or off by its own solid state fuse through AMSWire commands. Both of them are *ON* after power up. In nominal conditions one of them is switched *OFF* to save power. The JINFv2 is a development of MIT.

[1]CGS, Carlo Gavazzi Space, Milan, Italy
[2]CSIST, Chung-Shan Institute of Science and Technology, military institute in Taiwan

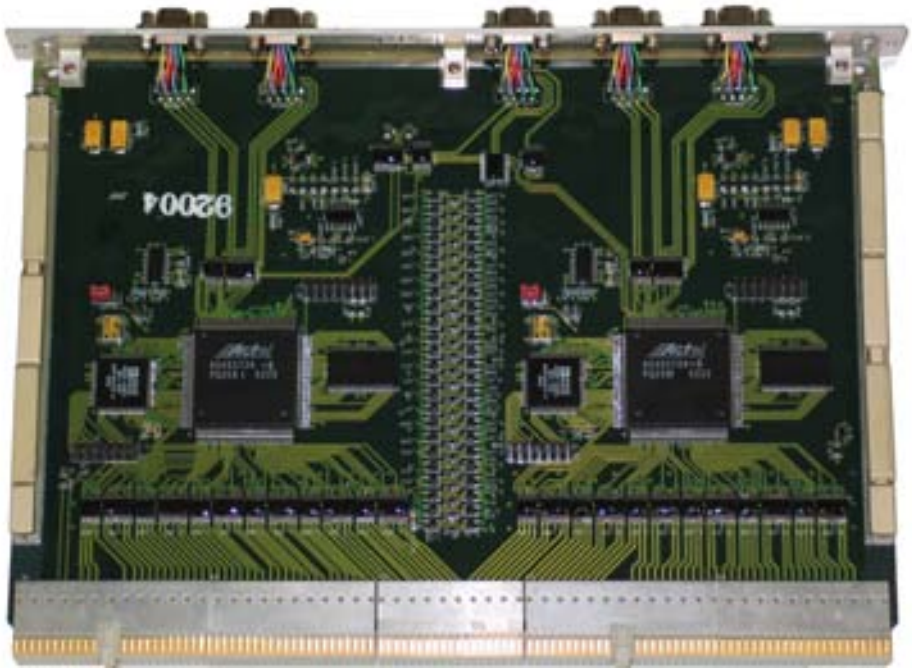

Figure 5.21: Front side of the JINFv2 board. Two CDDCs feature two-fold redundancy.

5.5.2 The Data Reduction Board UDR2

The UDR2 acquires data by sending sequence signals to the front end boards as described in Section 5.4.1. Furthermore, it performs data reduction and buffers the processed events until they are collected by the JINFv2 board. Figure 5.22 shows a photo of the front side of a UDR2 board. The UDR2 is composed of two redundant CDPs and a Detector Dependent Part (DDP). Again, each CDP is controlled and protected against single event latch-ups by its own solid state fuse. Unlike the CDDCs in the JINFv2 board, only one CDP in the UDR2 can be active at a time. This is accomplished by replacing the ON/OFF control circuitry by SWAP/OFF circuitry. If no control signal is applied, the first CDP is on, the second one stays in cold redundancy. The CDPs require 3.3 V power and the DDP ± 2 V. The DDP has to supply seven front end links with signals, generated by the sequencer, and power from the UPSFEv2. To reduce the amount of wiring, front end links 1/2, 3/4, 5/6 are merged into power sections. Link 7 stays separate. Each of these power sections is supplied by its own ± 2 V linear regulator on the UPSFEv2 board, except of channel 7 which shares its linear regulator with channel 7 of a second UDR2 board. To avoid injection of digital noise from the CDP into the DDP and from there into the front-ends, the 3.3 V for the CDP and the ± 2 V for the DDP are not referenced between each other. As a consequence, Analog Devices high speed digital isolators are used, which transmit the sequencer signals from the CDP to the DDP and the digitized signals in opposite direction. The UDR2 has been developed in cooperation with CAEN[1], MIT, INFN, RWTH Aachen and Universität Karlsruhe.

[1] CAEN, company in Viareggio, Italy, which is specialized on high energy physics electronics, microelectronics and aerospace electronics.

Figure 5.22: Front side of the UDR2 board. Two CDPs feature two-fold redundancy.

5.5.3 The Linear Regulator Board UPSFEv2

The UPSFEv2 as displayed in Figure 5.23 represents the power supply for the front ends. 14 linear regulators with ±2.0 V output and two Actel antifuse FPGAs are implemented on this board. The 14 linear regulators are split into seven primary and seven secondary linear regulators. Each linear regulator comprises its own output on the backplane connector. It is foreseen that each linear regulator of the first half is interconnected in parallel with a linear regulator on the second half to gain double redundancy on linear regulator level. One UPSFEv2 board supplies 14 UFE boards through two UDR2s. This implies that three linear regulators supply three power sections of one UDR2 and one linear regulator supplies the remaining two power sections on two UDR2s with each dedicated to only one UFE board. This scheme is illustrated later in Figure 5.32 of Section 5.5.5. The seven primary and seven secondary linear regulators are supplied by separated ±2.8 V. This allows to shut down the power for one UPSFEv2 half in nominal conditions to obtain *cold* redundancy.
Figure 5.24 shows the main schematic of one of the linear regulator circuits. Noteworthy are the diodes D_{out} at the outputs, which prevent a current flowing into an interconnected unpowered parallel linear regulator circuit. The circuit is explained on the basis of the +2.0 V part. The operational amplifier OA_1 is fed by the feedback voltage and regulates the output voltage to +2.0 V by modifying the base voltage of the NPN-transistor T_1 which controls the main PNP transistor T_2 on the +2.0 V supply line.
Each channel features overcurrent protection in order to prevent a destructive single event latch-up on the front ends and to prevent high load on the DC/DC converters, which could force the DC/DC converter to remain permanently in overcurrent protection. The current

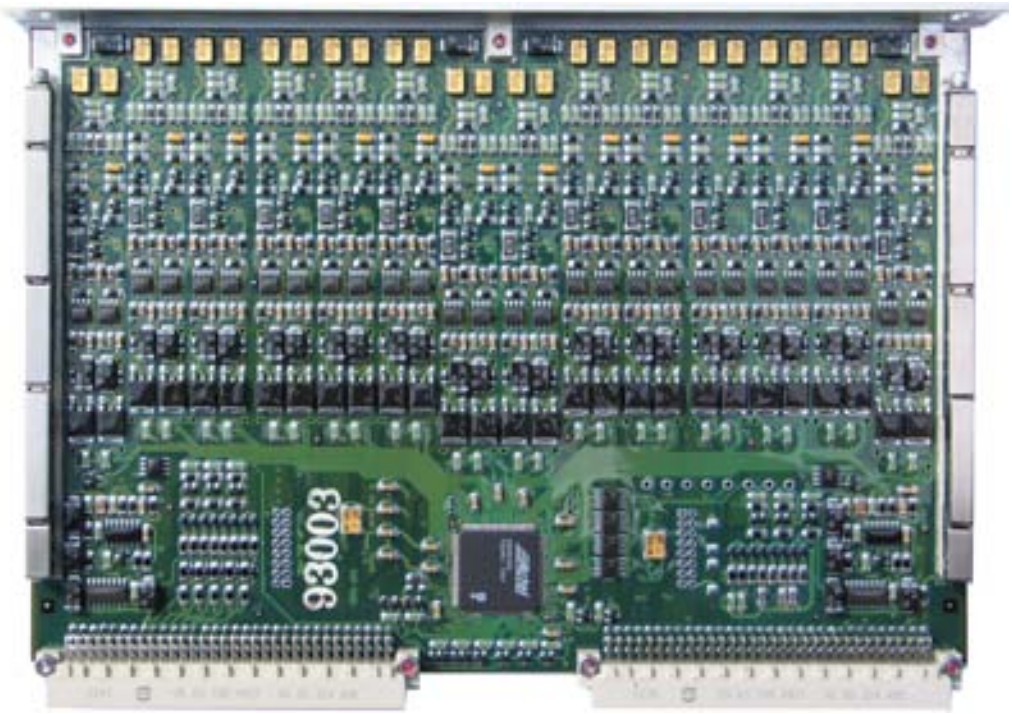

Figure 5.23: Front side of the UPSFEv2 board. This board houses two times seven linear regulators and two Actel FPGAs for twofold redundancy.

flowing through the linear regulator is sensed on the resistor R_{sense} = 270 mΩ placed in the main +2.8 V/+2.0 V supply line. The maximum current is defined by choosing the resistors R_{def} in a proper way. Equation 5.2 gives the dependency between the maximum current and the resistor value R_{def}.

$$I_{MAX} = \frac{V_{IN} \cdot R_{def}}{R_{sense}(R_{def} + 10k\Omega)} \tag{5.1}$$

The comparator OA_2 compares the voltage drop on the R_{sense} resistor to the predefined voltage setting. As soon as the maximum current is reached this comparator triggers a circuit which controls the transistor T_1: Via LIM+ the HIC circuit is activated. HIC switches T_3 and T_4 and pulls SP+ to -2.8V and SP- to +2.8V. Transistor T_1 becomes non conductive and the linear regulator is switched off by blocking the regulating transistor T_2. As shown in Figure 5.25, in case of a (simulated) latch-up both output voltages are cut off and recover after about 250 ms. To switch on/off the linear regulator and monitor its status, a link to the FPGA is realized by two optocouplers which couple the 3.3 V signals from the FPGA control logic to the +2.8 V of the linear regulator. The upper optocoupler $Opto_1$ controls the linear regulator, the lower one $Opto_2$ reads back its status. With the incoming +2.8 V and the outgoing +2.0 V, this circuit provides a conversion efficiency of 71%. The hardware jumper close to the output diode was inserted during development at the same time, when the output diodes were added. With this option it is possible to grip the feedback voltage either before or after the diode, just in case the linear regulator appears to be unstable. In this case the diodes could have been removed or the feedback could have been gripped before the diode, taking into account that the current dependent voltage drop over the diodes remains uncompensated.

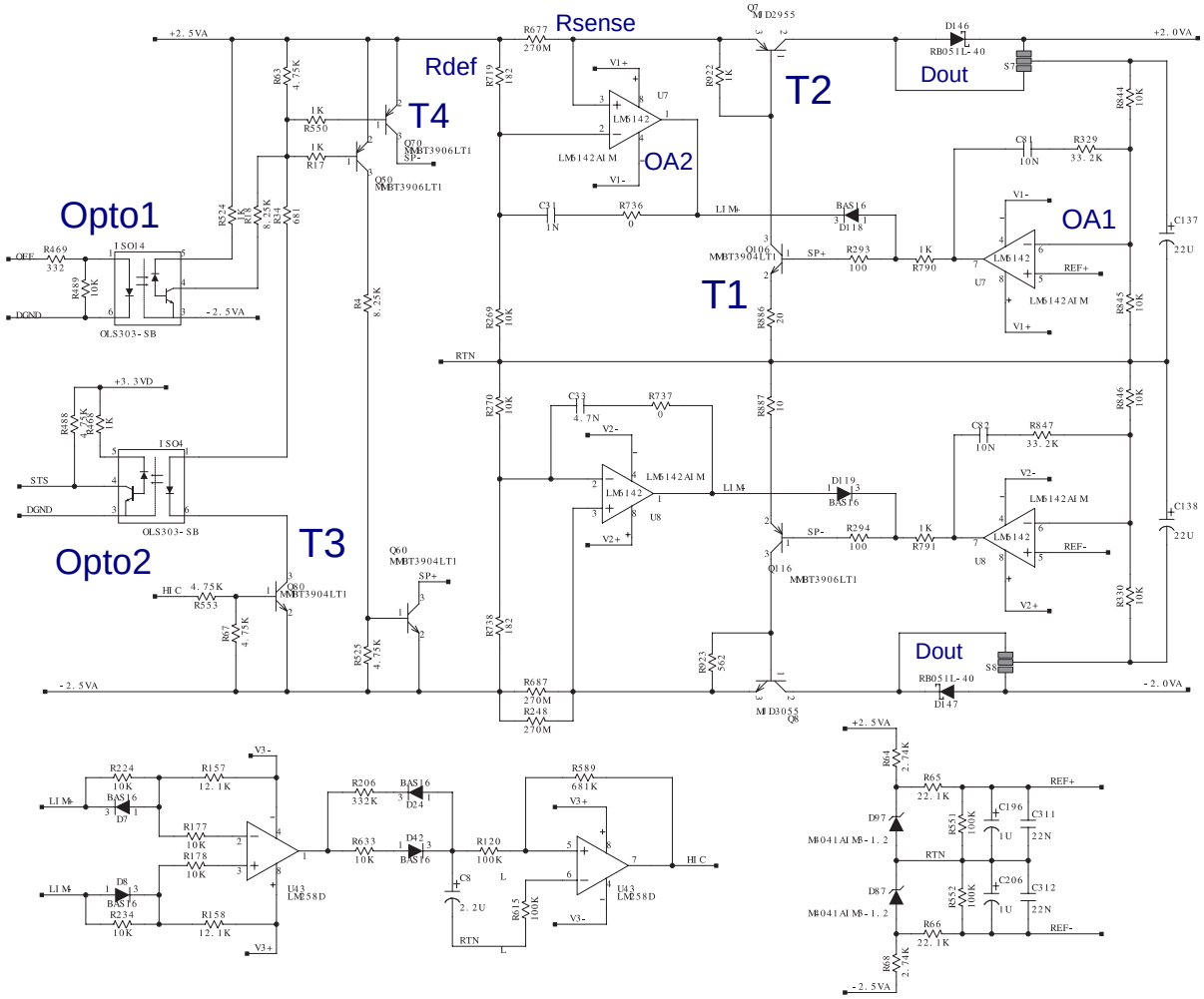

Figure 5.24: Schematics of one ±2.8 V UPSFEv2 linear regulator. $Opto_1$ and $Opto_2$ denote optocouplers, T1 to T4 stand for transistors, OA_1 and OA_2 are operational amplifiers and D_{out} indicate the output diodes. The working principle is explained in the text.

The two double redundant Actel FPGAs (A54SX32A-TQ144) do not only provide the means to control and monitor the status of the 14 linear regulators, but also control and monitor the solid state fuses of two UHVGs and two UDR2s boards. Additionally, both Actels provide the means to switch off each other to save power. As for the UHVG the FPGA control logic is accessed with the Lecroy protocol. Each FPGA is linked to a different Lecroy bus. The fact that in the U-Crate, three UPSFEs are on the same bus, calls for addressing capabilities of the UPSFEv2. This is realized by implementing a 5 bit geometric address, which is set by a jumper on the backplane. The address has been defined in a way that the address of each UPSFEv2 corresponds to its slot number on the backplane. The UPSFEv2 has been developed in cooperation with CAEN, MIT, INFN, RWTH Aachen and Universität Karlsruhe (TH).

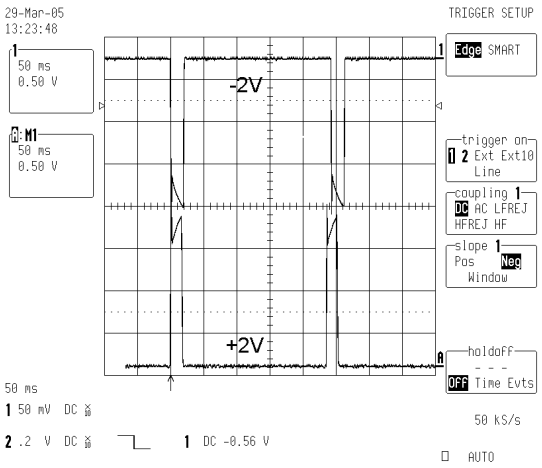

Figure 5.25: Simulated latch-up of a linear regulator channel. Both positive and negative voltages are switched off to prevent the front end electronics from being damaged.

5.5.4 The High Voltage Generator UHVG

The UHVG is the High Voltage Generator of the TRD. Six UHVG boards are present in one crate. Each UHVG provides 14 Cockroft Walton high voltage elevators, every two of them are interconnected by diodes. One of them remains off in nominal conditions to gain cold double-redundancy. In this way seven high voltage generator channels are available to supply a

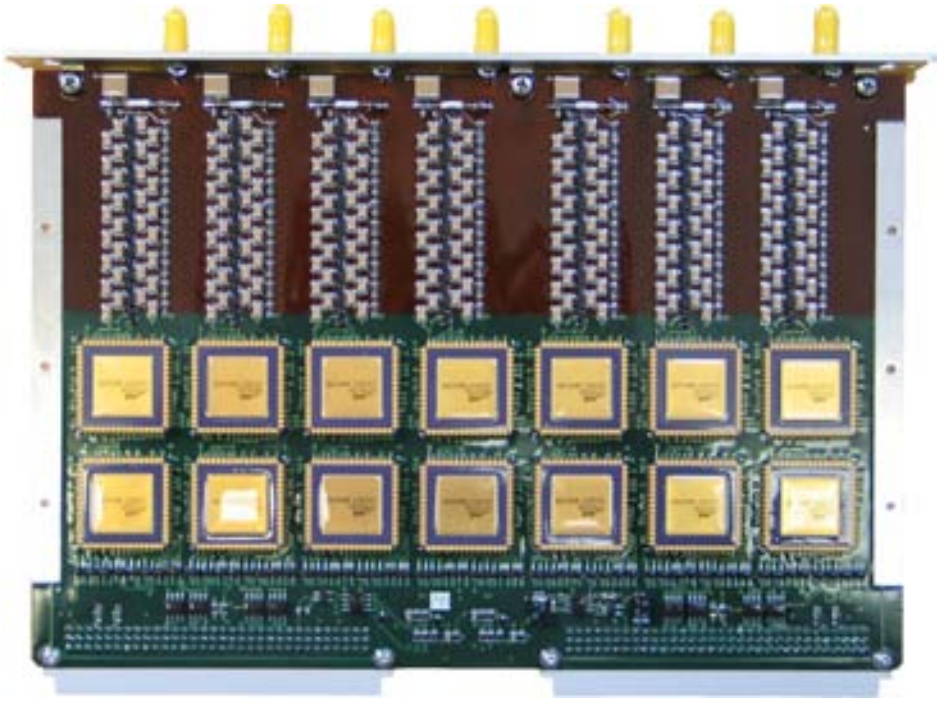

Figure 5.26: Front side of the high voltage generator card UHVG

Figure 5.27: Schematics of the UHVG high voltage elevator.

detector unit of 64 straw tubes via the seven high voltage connectors on the front panel. These are the same 64 channels which are read out by one UFE board. High voltage cables link the UHVG board channels to the UHVD boards mounted close to the UFE boards on the octagon. A Cockroft Walton Generator is built up of 16 diode/capacitor stages to rise the prime 120 V to a maximum of 1750 V. Figure 5.26 shows a photo of a UHVG board and Figure 5.27 indicates the electrical circuit of one high voltage elevator. The elevator is working in the way, that via an oscillating voltage decoupled by a capacitor, charges which enter the circuit through diodes get *pumped* to high potentials. The current which enters the circuit can be monitored at *Isense* and the resulting final voltage can be measures at *VFB*. Each cascade is controlled by a Lecroy MHV100 chip, which can be accessed using the Lecroy protocol. The Lecroy protocol is described in Section 5.13.1. Each UHVG is connected to two Lecroy links. One Lecroy link controls the primary seven Lecroy chips, the second link controls the secondary seven Lecroy chips. Since more than one Lecroy chip has to be controlled via the Lecroy bus, the chips's address capability has to be used. Three bits are used on board to select the Lecroy chip and two bits are defined on the backplane slot to select one of the three UHVG boards placed on one Lecroy bus. A Lecroy chip is composed of several DACs, an ADC and the power control logic. By setting the DACs, the desired output voltage, the overcurrent limit and the overvoltage limit is selected. Using the ADC, one can determine digitized chip temperature data, measured HV current (I_{sense}) and HV feedback voltage. Additionally, it is possible with the ADC to read back the previously mentioned DAC settings. Each HV channel needs to be calibrated. Figure 5.28 shows the linearity of a UHVG channel. Each half of the UHVG is supplied by separate +120 V serving as input for the HV elevator, separate 5 V supplying the Lecroy chips. One unique 3.3 V supplies the LVDS chips used for the Lecroy bus communication of both halves. The Lecroy chips are protected against destructive SELs by two solid state fuses on the 5 V lines. So far on QM2 level no 3.3 V SSF protection has been implemented on UHVG. During QM1 TVT of UHVG, it was found that the Lecroy chip

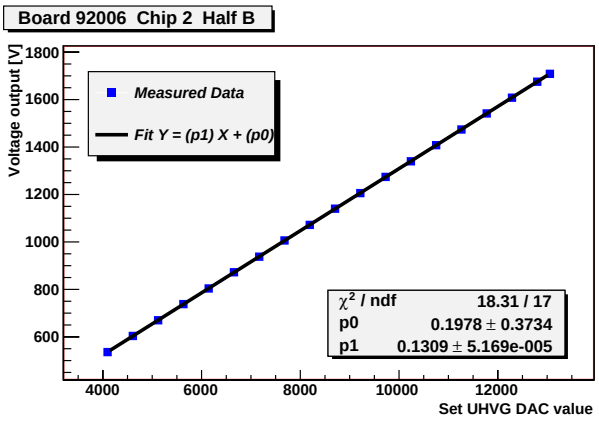

Figure 5.28: Exemplary UHVG channel calibration.

communication stopped working at -20°C. At this time it seemed that UHVG was not able to fulfill the original demands of operation between -25°C and +55°C (see Section 5.9). Later investigation showed that the Lecroy chips are able to operate at the low temperature limit by increasing the +5 V supply to +5.2 V.

5.5.5 The Backplane UBPv2

Figure 5.29: Module placement in UBPv2 after weight reduction.

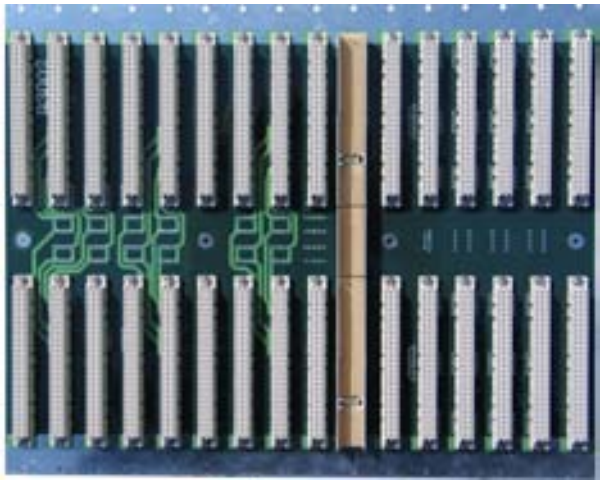

Figure 5.30: Top view of the UBPv2.

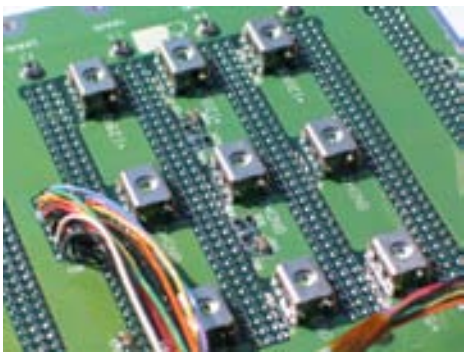

Figure 5.31: Power taps and slow control connection to the UPD-Box on the backside of UBPv2.

The U backplane or UBPv2 provides the electrical connections between the 15 boards of the U-Crate. It was developed by MIT and Universität Karlsruhe. Figure 5.29 describes the schematic layout of the UBPv2. The UBPv2 provides slots for three power groups, each composed of two UDR2s and one UPSFEv2, a slot for the JINFv2 and six slots for the UHVGs. A power group contains closed electrical interconnections in terms of front end power: one UPSFEv2 supplies the front ends connected to two UDR2s. A photo of the UBPv2 can be seen in Figure 5.30. The interconnection between the backplane and the supply lines to the UPD-Box is realized via 39 so called *power taps* located on the backside of the backplane to which the cable ring lugs are screwed. A picture of the power taps is given in Figure 5.31. Also, the slow control interconnection is provided by a 15-pin micro-d pigtail cable soldered to the backside. The distribution of the Lecroy buses to the UPSFEv2 and to the S9011AUv2 controller is described in Section 5.13.2. A schematic overview about the solid state fuse control lines can be found

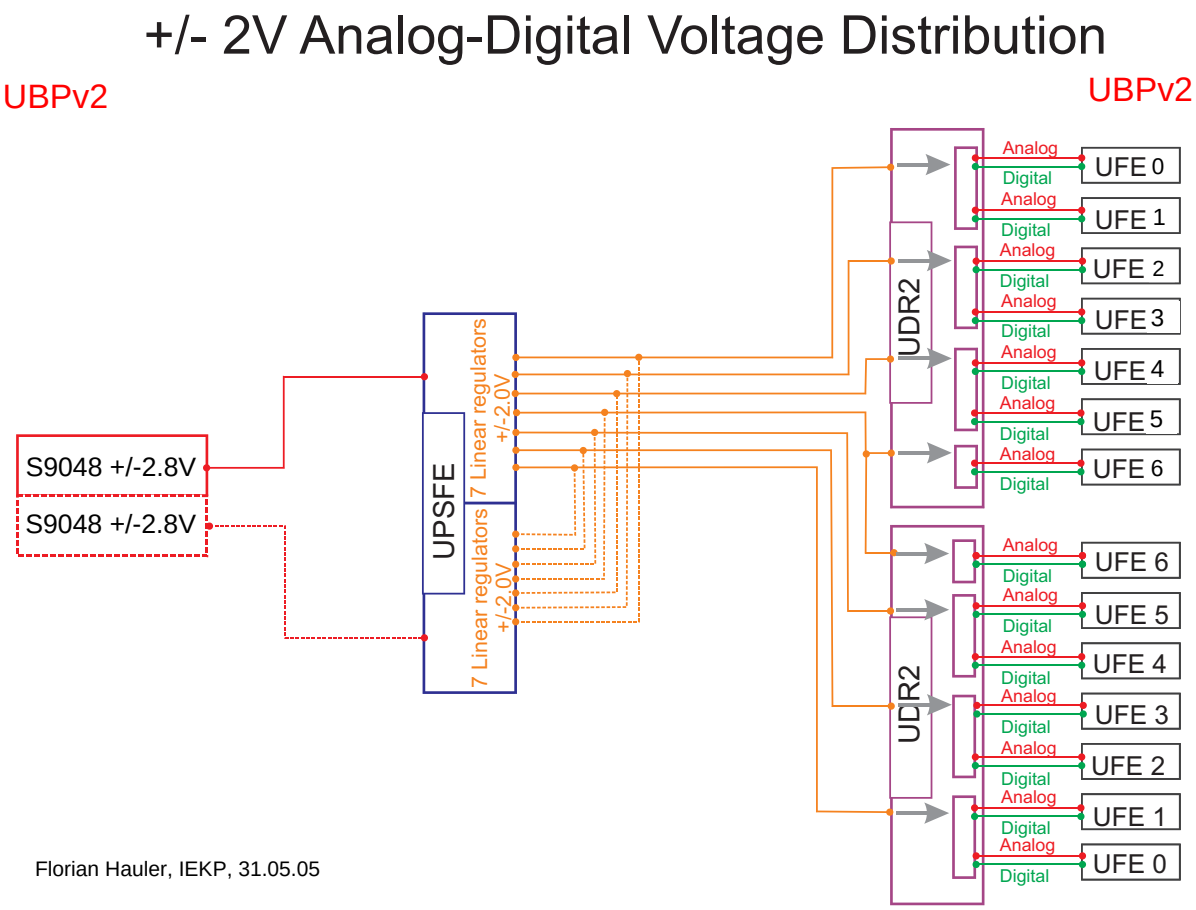

Figure 5.32: Connection scheme of one power group. The 14 linear regulators of one UPSFEv2 supply the front ends connected to two UDR2 boards.

in Section 5.13. Figure 5.32 shows the front end power interconnection. Each half of an S9048 ±2.8 V DC/DC converter supplies seven primary and seven secondary linear regulators. In nominal conditions one half stays off to gain cold redundancy. The primary and secondary linear regulators are interconnected on the backplane to provide a redundant power supply for the front ends. The ±2.0 V supply lines going from the UDR2 to the UFE boards are still separated in two supply lines named analog and digital, although they are fed by one unique linear regulator. This splitting is a remnant of the layout before weight reduction. The design of the TRD electronics subsystem and consequently of its backplane is based on the strict separation of its DC/DC converter grounds in the UPD-Box and the unification of all grounds on the octagon. In the TRD electronics subsystem several grounds are used: high voltage ground (+120 V/+5 V), low voltage ground (±2.8 V), digital ground (+3.3 V) and shield. All grounds are separated in order to prevent noise interspersion from *dirty* grounds such as the digital ground to the sensitive hybrid electronics of the front ends. With this grounding scheme a noise below two ADC counts can be reached. Whether this low noise performance can be conserved in the full configuration of the assembled AMS-02 detector has still to be verified. Appendix Figure A.1 demonstrates the shielding and grounding of the complete TRD DAQ electronics subsystem including the octagon, the U-Crate and the UPD-Box. Appendix Figures

A.2 and A.3 show the low voltage and high voltage grounding schemes. The digital ground is connected on the backplane via shield to the other grounds. The shield can be referred to as *dirty* ground since it is connected to the mechanics of the U-Crate, the UPD-Box and the outer shielding of the front end cables. Its intention is to protect the electronics against electromagnetic pollution from neighboring subsystems.

5.5.6 Temperature Readout

The temperature of the U-Crate and the UPD-Box is measured on different boards in different ways. The main temperature readout is performed by DALLAS sensors. They are powered by a 5 V and readout by a 1-wire bus. They measure temperatures between -55°C and +125°C with an accuracy of ±0.5°C between -10°C and +85°C. The sensors are calibrated in centigrade. It provides a digital resolution of 9-bit with a conversion time of maximum 750 ms. Each DS18S20 has a unique 64-bit serial code, which allows many sensors to be operated on the same bus. On each UPSFEv2 two temperature sensors are mounted, which makes six sensors per crate. Two sensors are mounted on the S9011AUv2 in the UPD-Box. Furthermore, on the UHVGs each Lecroy MHV100 chip features a temperature readout, 84 temperature sensors for all six UHVGs. Additionally, on the outer walls of the U-Crate and UPD-Box, several DALLAS temperature sensors of the global DALLAS network will be placed to determine, whether the system temperature is in the nominal operational range between -20°C and +50°C or not. By using the data from this measurement it has to be decided whether it is safe to switch the system on, or whether the system has to be switched off. Moreover, temperature sensors are placed on the straw tube modules in the octagon. There the local temperature sensors are vital for data analysis, since the gas gain depends on the temperature. The Dallas buses are controlled by USCM boards placed in other crates such as the crate of TRD gas electronics.

5.5.7 Problems Identified During Development

One of the first developments for AMS-02 was the sequencer. It was used in an evaluation setup and in the testbeam of 2002. By chance it was found that, when applying testpulses onto UFE channels and using the real time sequence for readout, the first channel behaved differently compared to other ones. Other problems were identified in the calibration sequence, which manifested in missing or noisy second and last channels. These problems were recognized as UFE hardware problems. After the delivery of QM1 boards, it was possible to test the system on crate level for the first time. A problem concerning slow control communication on the Lecroy lines was discovered, which led to a revision of all xPSFE boards and xPD boards in AMS-02.

Sequencer Problems

Figure 5.33 shows the comparison of four different channels in one UFE board. Obviously the dynamic range of the first channel seems to saturate at about 3000 ADC counts, while for the other channels the dynamic range reaches up to more than 4000 ADC counts. After investigation by comparison with the reference system at RWTH Aachen, it was found that the delay between the first S clock signal to the second clock signal is shorter than the consecutive ones, as illustrated in Figure 5.34. It was realized that the reason for this problem was a documentation mistake in the sequencer definition sheet, which had to be corrected. In the real time sequence as shown in Figure 5.15, the timing for the slot HOLDCLK was announced as 600 ns instead of 1200 ns, which caused a lower signal at the ADC sampling time and thus

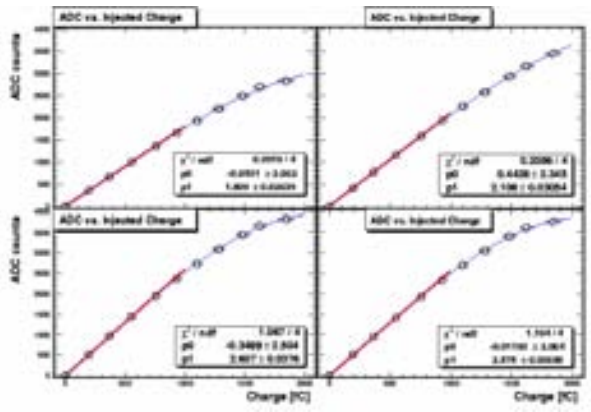

Figure 5.33: Testpulses onto different UFE channels. Channel 1 shows a limited dynamic range. Source: C. Chung, RWTH Aachen.

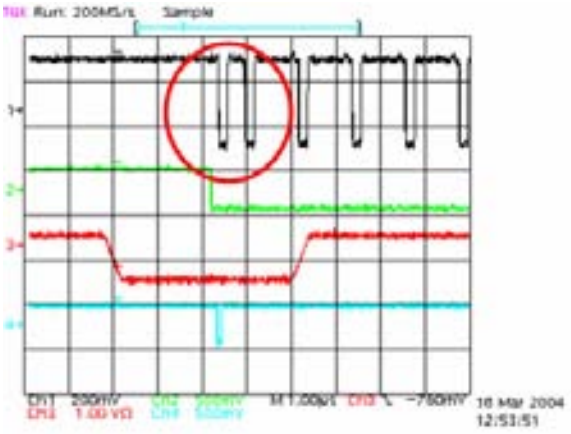

Figure 5.34: The reason for the suspicious behavior of the UFE board is a timing mistake in the sequencer.

seemed to be a charging problem. The corrected sequencer did not show this problem any more.

UFE Problems

Two problems were detected in the calibration sequence, which both manifested in missing or noisy channels. The first problem was found to be a cross talk problem on the PCB between the first and second channel of the first Viking chip on the UFE, which caused a distortion of the second channel. Consequently the UFE PCB was modified in order to spatially separate the problematic lines. Additionally a time gap between the read out of the first and second channel was inserted into the calibration sequence to avoid residual distortion.
Another problem affected the 64th channel of the UFE board. The amplitude of this channel

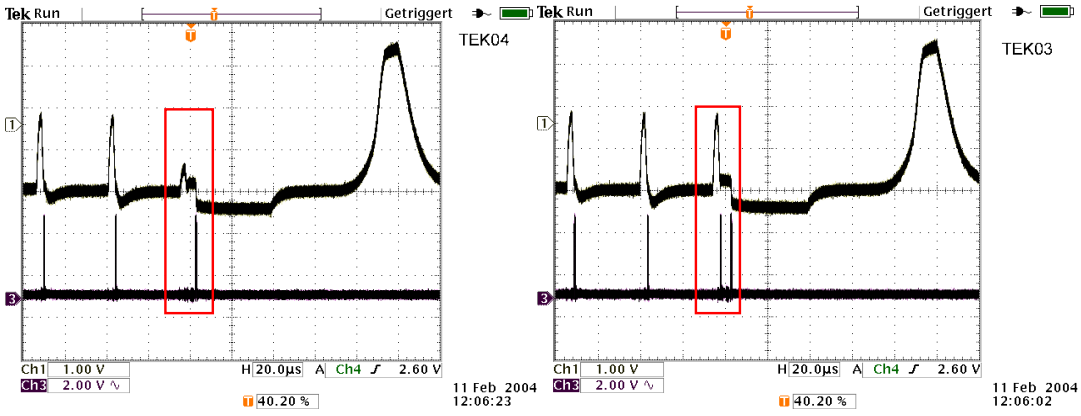

Figure 5.35: Upper line shows the Viking signal amplitude, the lower line represents the clock that switches the Viking output from channel to channel, defined by the sequencer S signal. Left picture: missing last channel amplitude. Right picture: problem recovery by clocking once more. From [Kar03].

becomes suppressed during consecutive fast readouts. Figure 5.35 shows the distortion of the last channel. This problem was found to depend on the Viking chips and appears to be enhanced, when the analog supply voltages become asymmetric. Furthermore, this problem is not visible at low readout frequencies, but evolves gradually during a number of readouts. All chips under test showed this problem when the supply power became +1.85 V/-2.00 V or +2.00 V/-2.07 V, respectively. One chip even showed this undesired behavior at nominal voltage +2.00 V/-2.00 V. The reason for this problem seems to be Viking internal and therefore cannot be investigated easily. However, it was found that this problem can be prevented by a calibration sequence modification. Two options arise. The first one is simply the introduction of a 2.2 ms time gap between the readout of the last channel and the start of the reset section in the calibration sequence. The second one, and in fact the one which has been chosen finally, is an additional 65th channel clock pulse to the Viking chip. The analog readout before and after this modification is shown in Figure 5.35. More information about the investigation of the UFE problems is available in [Kar03].

Lecroy Problems

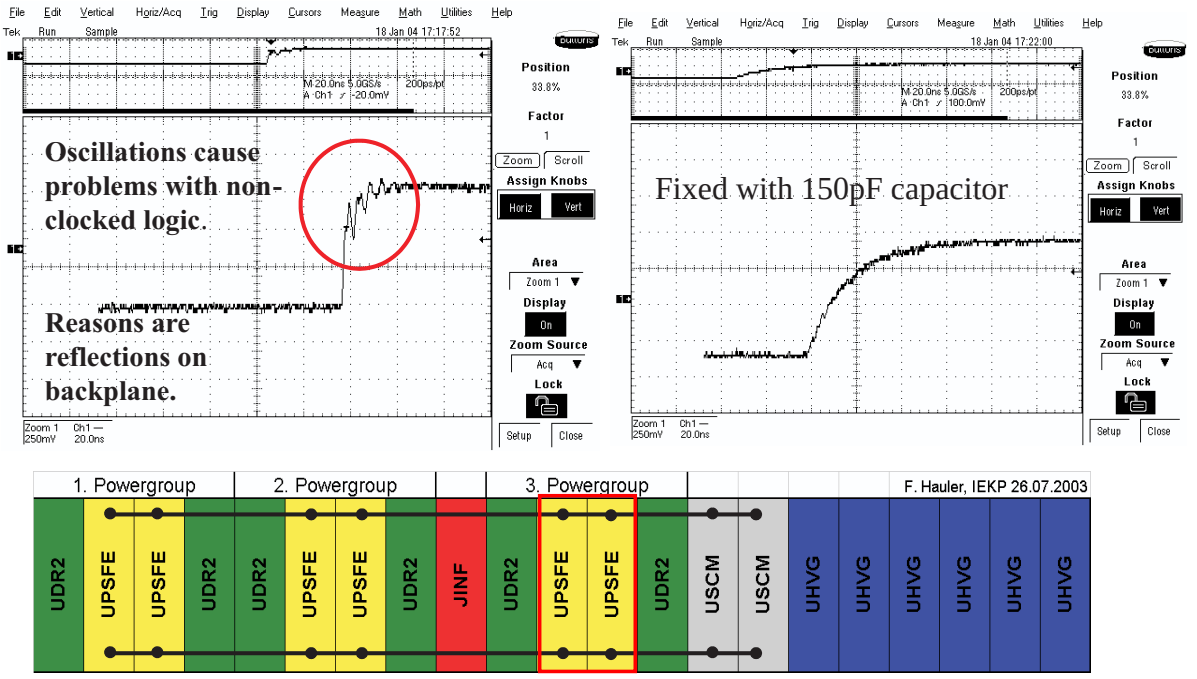

Figure 5.36: Oscillations on LVDS lines (picture left) on the marked UPSFE slots (drawing below). This problem can be fixed by placing 150 pF capacitors between the differential LVDS lines (picture right).

When testing the slow control communication on QM1 level it was found that UPSFE boards in specific slots did not respond. The U-Crate system as illustrated in Figure 5.36 was still in the configuration before weight reduction. Looking on the differential LVDS lines revealed (Lecroy Clock) signal oscillations, caused by reflections which spoiled communication. Increasing the capacitance of the bus by inserting capacitors between the two differential lines fixed the problem. Two reasons for these reflections can be considered. This is an LVDS system composed of

two USCMs and six UPSFEs with a 100 Ω termination on one end of the bus. Basically this represents a multipoint LVDS bus configuration with a single termination. Multipoint LVDS buses normally have 100 Ω terminators on both ends. The LVDS drivers on the USCMs and UPSFEs are point-to-point LVDS drivers, which do not allow to terminate the bus on both ends due to the lower bus resistance of 50 Ω. Another issue which could cause the oscillations are the relatively long bus stubs in the UPSFE boards, which ought to be kept as short as possible. To correct this problem two approaches were made. First of all the point-to-point drivers were exchanged against multipoint LVDS (MLVDS) drivers and receivers. This caused modifications on all UPSFE boards including the S9011AU boards. Since this problem was present in other crates as well, all related xPSFE and S9011Ax boards were modified. The system had to be redesigned anyway due to weight reduction and so it was decided to take out the USCMs and develop a new JINF board taking over the slow control capability. This new board could be equipped with the new MLVDS drivers and the multipoint bus could be terminated on both ends. The second approach was to correct residual reflections or other distortions by adding digital filter logic into the FPGA firmware. This firmware samples the incoming communication signals and determines the signal state by majority voting. Figure 5.37 shows the difference between a point-to-point LVDS system and a multipoint LVDS bus system. Figure 5.38 illustrates the level sampling of the UPSFE firmware.

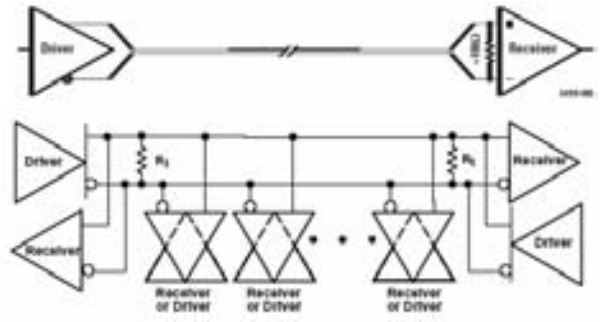

Figure 5.37: Schematic drawing of single-point LVDS (above) and multipoint LVDS (below).

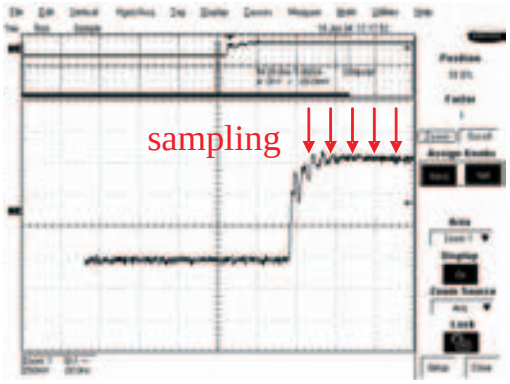

Figure 5.38: Working principle of the digital filter. The signal is sampled a few times and the state of the signal is determined by majority voting.

5.6 The UPD-Box: Power Distribution for the TRD

The UPD-Box is the power supply for the TRD electronics. Seven DC/DC converters inside the UPD-Box adapt the incoming 28 V from the power distribution system of AMS-02 to the needs of the U-Crate boards. The DC/DC converters are controlled by the S9011AUv2 board. The incoming 28 V are filtered by the S9011B board. Figure 5.39 illustrates the module placement in the UPD-Box. The S9011B filter is placed in the middle surrounded by three S9048 ±2.8 V converters. The S9011AUv2 controller board is located at the very left end of the UPD-Box, next to the S9053 3.3 V DC/DC converter, since the S9011AUv2 controller board is powered by 3.3 V. A supply cable within the box links the two boards. The three S9056 +120/5.2V converters are placed at the right end of the UPD-Box. Figure 5.40 describes the

Figure 5.39: Module placement in UPDv2-Box after weight reduction.

interconnection between the UPD-Box and the U-Crate. Each DC/DC converter is composed of two completely separated and exactly identical redundant halves. Upon start-up both halves are powered, but under nominal conditions one half is switched off. This power supply scheme is made in a way that one redundant half of a DC/DC converter powers one redundant part of the U-Crate electronics: The first half of the S9056 HV converter supplies the first half of two UHVG boards. The first UHVG half houses seven HV elevators which are brought together with the seven HV elevators of the second half by diodes at the output of each channel. The second half of the S9056 HV converter supplies the second seven redundant HV elevators. A similar scheme is applied for the S9048 LV circuits, with the only difference that one S9048 half powers one half of one UPSFEv2 board, each half containing seven linear regulators. The power

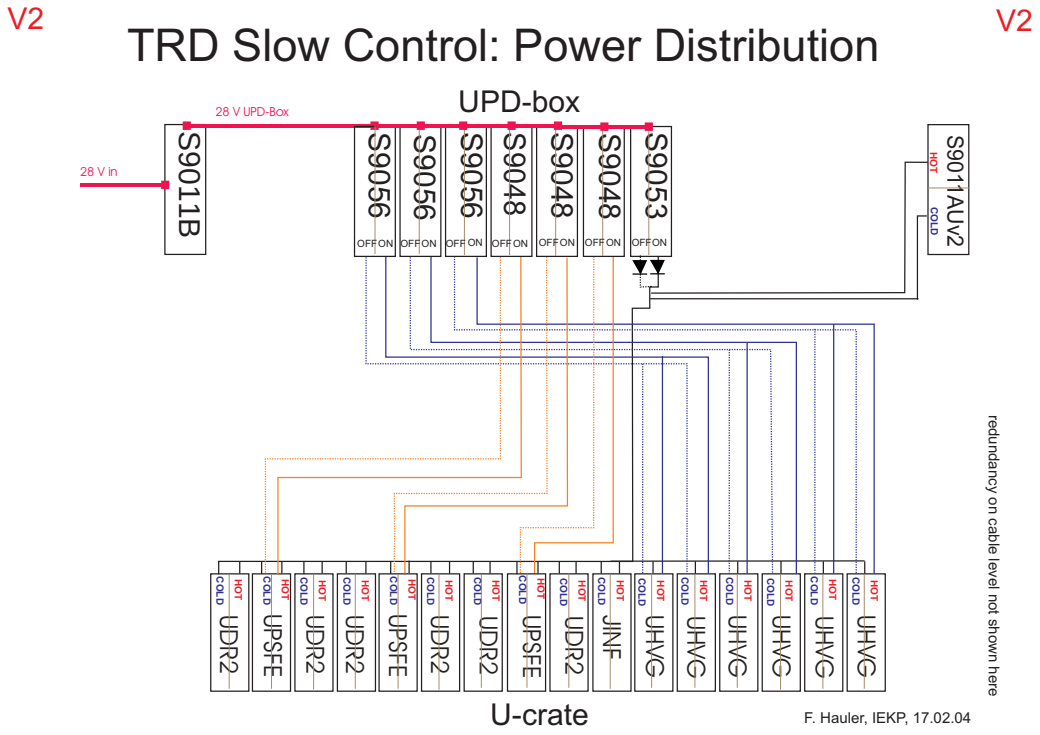

Figure 5.40: Overview of U-Crate power design.

Figure 5.41: Assembled Power Distribution Box for the TRD (UPD-Box). Mil-Spec connectors coupled the supply lines to the UPD-Box. 15-pin micro-d pigtail connectors guide the slow control communication from the UBPv2 to the UPD-Box.

Figure 5.42: Inner view of the UPD-Box assembly test. The length of the cables will be reduced to a minimum in the final QM2 assembly.

source for the digital electronics on each board of the U-Crate is certainly the 3.3 V power, supplied by the S9053 DC/DC converter. This converter also powers the S9011AUv2 board of the UPD-Box. Due to the importance of the 3.3 V power, the outputs of the two S9053 halves are brought together with diodes: in case of a S9053 half failure, still all the digital electronics of the U-Crate are operational. Almost all U-Crate electronics boards are protected against shorting the 3.3 V lines by solid state fuses.
Additionally to the electronics redundancy, even the cabling is kept redundant to avoid a system failure due to the loss of cable connections caused by the vibrations during the shuttle start. Figure 5.41 shows the outer view and Figure 5.42 the inner view of the UPD-Box. The cables between the UPD-Box and the U-Crate are crimped to ring lugs on the U-Crate side which are screwed to the power taps mounted on the UBPv2. On the UPD-Box side they are inserted in MIL-C-38999, Series II connectors which can be mated to box mounting receptacles of the same type. In order to insert the cables into the MIL-C-38999 connectors, they have to be prepared by crimping pins on their ends. The cable sizes have to be determined by calculating the nominal power flowing through it and apply the proper derating when running the cables as bundles. Each DC/DC converter module has its own receptacle and therefore its own cable bundle to the U-Crate. The two slow control and temperature buses are fed to the UPD-Box by two 15-pin micro-d connector cables soldered to the UBPv2. All cables to the U-Crate have a defined size of 1.5 m. In the UPD-Box, slow control connections between the DC/DC converter and S9011AUv2 controller are made with 9-pin micro-d pigtail connectors soldered to the DC/DC converters. The 28 V power is gripped by short cables soldered to dedicated DC/DC converter pins and screwed to two redundant 28 V/GND Ni-plated copper bar pairs. The mechanical design of the UPD-Box is led by the intention to extract defective DC/DC converters after assembly without having to disassemble the whole mechanics. Each DC/DC converter is mounted on an I-Frame which is inserted from the bottom of the UPD-Box.

Between the DC/DC converter and the I-Frame conductive but electrically isolating Chotherm[1] material is placed to ensure good thermal contact and to avoid unwanted electrical connections to the PCB. The I-Frames are fixed by screws to both walls and to the 28 V/GND Ni-plated copper bars on the top. On the bottom they are stabilized by mechanical pins mounted on the I-Frames. The UPD-Boxes will be mounted on the wake and ram radiators. The side, from where the DC/DC converters are inserted, are mounted face to the radiator with the I-frame feet touching the radiator. This allows the dissipated heat from the DC/DC converters to flow through the I-frames into the radiator. The I-Frames are built of aluminum 6061 T651, the walls are made of aluminum 7075 T7351. Two types of surface treatments are applied: *Clear Anodizing*[2] and *Alodine*[3]. Clear Anodizing is used as general surface treatment in order to harden all box surfaces. Anodizing can be performed by an electrolytic process where the part to be treated forms the anode of an electrical circuit. The principle is that the natural aluminum oxide layer on the surface is turned into a thicker oxide. Afterwards it gets sealed by using hot water or steam to turn the oxide into its hydrated form. Since this process causes the surfaces to get electrically and thermally insulating, another treatment has to be used for surfaces on interfaces which are desired to conduct electrically and thermally, such as the DC/DC converter I-Frames. *Alodine* is a chemical treatment process for aluminum used to provide corrosion protection while remaining electrically and thermally conductive. DC/DC I-Frames or all kinds of surfaces which are intended to remain electrically conducting are treated with Alodine. In order to allow the air in the UPD-Box to be vented during the shuttle start, tiny slits between the lid of the UPD-Box and the small side walls are left open. The 28 V conducting copper bars in the UPD-Box are surface treated with 20 μm Ni-plating increase wear and corrosion resistance. The QM1 UPD-Box was produced in Karlsruhe and surface treated at CSIST in Taiwan.

5.6.1 DC/DC Converters

Figure 5.43: S9053U DC/DC converter.

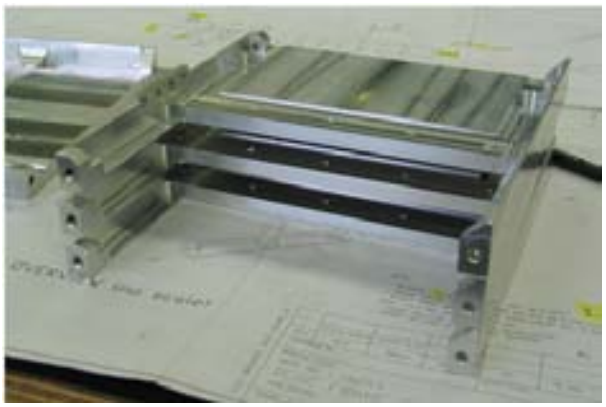

Figure 5.44: Three stacked DC/DC converter I-Frames.

The DC/DC converters were designed under contract with CAEN. Figure 5.43 shows a picture of a typical AMS-02 DC/DC converter. These DC/DC converters are switching-type DC/DC

[1] Chotherm, Chomerics Europe, Parker Hannifin PLC, UK
[2] Clear Anodizing, according to MIL-A-8625 Type II Class 1
[3] Alodine 1200, according to MIL-C-5541 Class 3

Type	Output Voltage	Nominal Load	Maximum Load	Measured Efficiency
S9053U	+3.4 V	+1522 mA	3 A	65%
S9048	±2.8 V	+950/-1447 mA	±2.4 A	estim. 71%
S9056	+120 V/+5.2 V	+18/+54 mA	35/150 mA	55%
S9054	+5 V	+200 mA	4.5 A	45%

Table 5.2: DC/DC converters used for the TRD electronics subsystem. The table provides output voltage, nominal load and measured conversion efficiency.

converters. A MOSFET hacks the incoming 28 V of a primary transformer circuit and the secondary circuit equipped with output filters produces the nominal voltage. The converters are supplied by 28.5 V ± 2 V and feature input over/undervoltage control and output overcurrent control. A solid state fuse limits the power line input current and switches off the converter if the temperature exceeds 82°±3°C. Furthermore, they feature a tunable soft start time in order to decrease in-rush current and tunable latch-delay time which allows to set the maximum time an overcurrent is allowed to last before the converter switches off. Before being inserted into the UPD-Box, they first have to be mounted on I-Frames. Figure 5.44 shows three stacked I-Frames during production at the Universität Karlsruhe. Table 5.2 gives an overview about the DC/DC converters used in the TRD electronics and provides information about their nominal load and measured efficiency. Figure 5.45 shows the DC/DC converter efficiency plots measured on QM2[1] modules.

[1]for an explanation about the QM2 production step, the reader is referred to Section 5.8

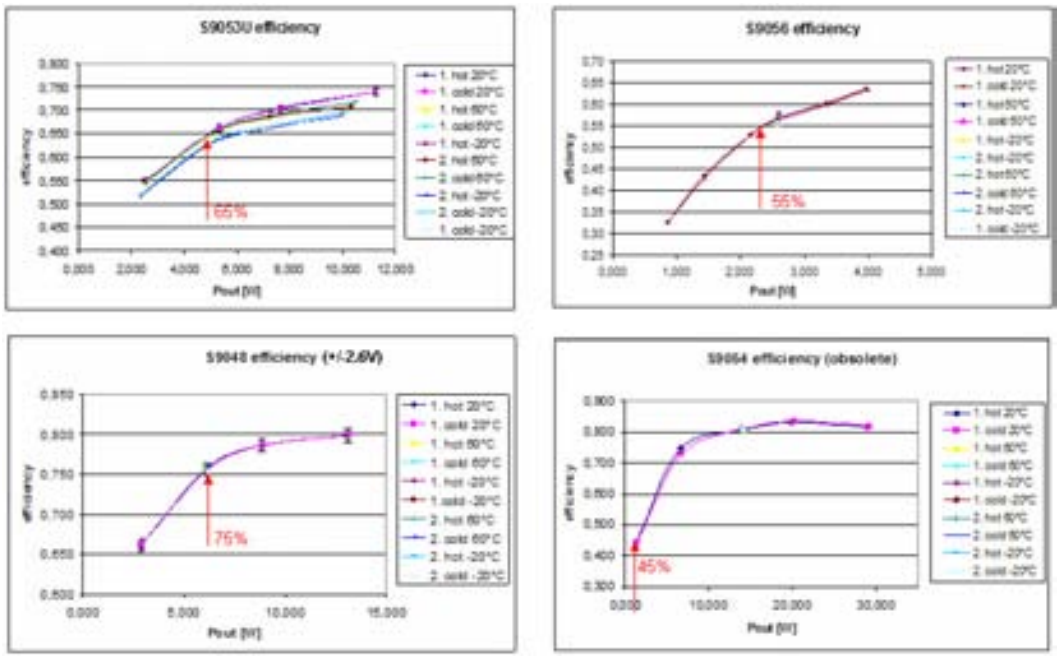

Figure 5.45: DC/DC converter efficiencies measured on QM2 modules. Nominal load is indicated by an arrow. The S9048 efficiency curve corresponds to an outdated ±2.6V version. After weight reduction the S9054 converter became obsolete.

5.6.2 S9011AUv2 and S9011B: Slow Control Electronics for the UPD-Box

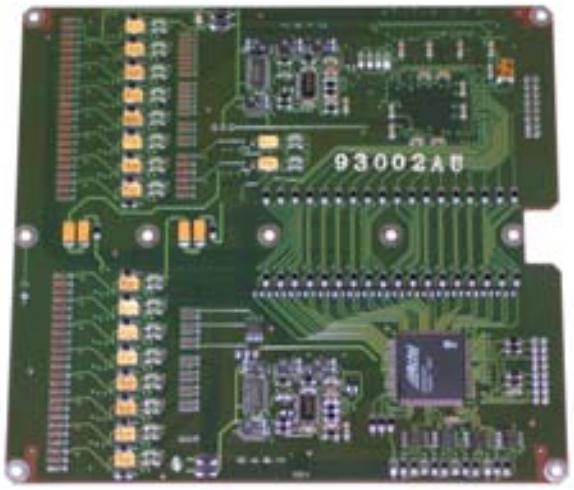

Figure 5.46: S9011AUv2 controller board.

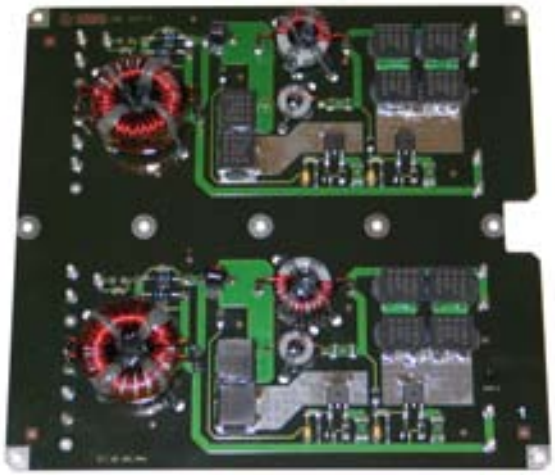

Figure 5.47: S9011B filter board.

The S9011AUv2 controller board shown in Figure 5.46 and the S9011B filter shown in Figure 5.47 were designed under contract with CAEN. The conducted susceptibility which gives information about the amount of noise getting from the 28 V line into the UPD-Box is given in Figure 5.48. The conducted emissions as shown in Figure 5.49, which describe the opposite way, give information about the reduction of possible noise generated by the DC/DC converters and transmitted back to the 28 V supply line. For example, a source of noise is the switching MOSFET of the DC/DC converters.
The double redundant S9011AUv2 board controls and monitors the seven DC/DC converters. The control logic is burnt in two Actel A54SX32TQ144 chips. Both Actels provide the means to switch off each other to save power. Each half is protected by a solid state fuse. The S9011AUv2 Actel FPGAs receive their commands from the JINFv2 board in the U-Crate through the Lecroy protocol. 9-pin micro-d receptacles are mounted on the top of the S9011AUv2 I-frame to provide connections to the DC/DC converters.

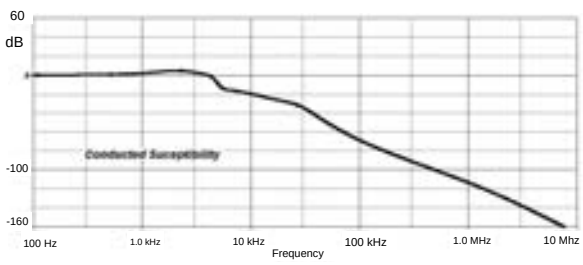

Figure 5.48: Conducted susceptibility of S9011B filter. From [CAE04].

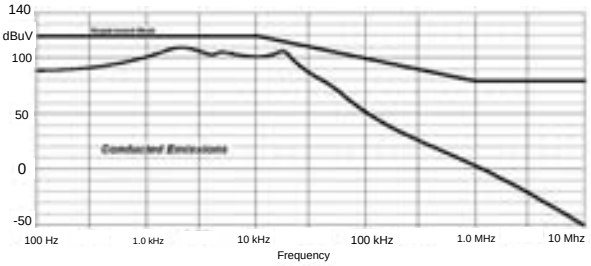

Figure 5.49: Conducted emissions of S9011B filter. From [CAE04].

5.7 Weight Reduction

In the second half of 2003, the need emerged to study AMS-02 wide weight reduction options to eliminate 60 kg weight excess over the TTCS[1] budget of 311 kg and 30 kg weight excess over electronics budget of 460 kg. AMS-02 has an expected total weight at lift-off of about 6.7 tons. To contribute to this weight reduction process several options were proposed for the TRD electronics with a target reduction of 2.3 kg per crate and box plus the savings for reducing the size of crate mechanics. Figure 5.50 and 5.51 show the changes of TRD electronics layout before and after weight reduction.

Figure 5.50: Changes of module arrangement on UBP due to weight reduction.

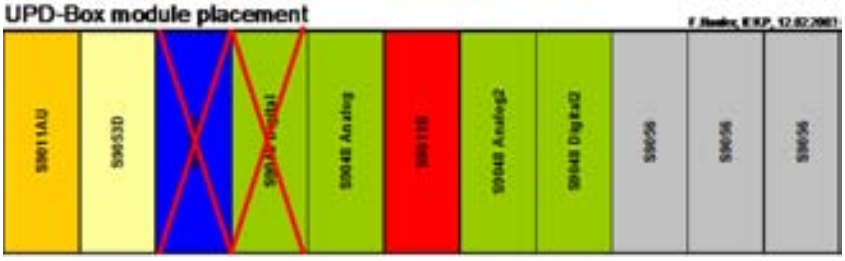

Figure 5.51: Changes of module arrangement in UPD-Box due to weight reduction.

5.7.1 Removal of two USCMs and Affiliated DC/DC Converters

Originally two redundant USCM[2] boards were the slow control master boards in the U-Crate. One USCM remained off for cold redundancy under nominal conditions. The USCMs were based on a DS80C390 microprocessor, similar to an 8051. They were controlled by a multitasking operating system and were supposed to switch off redundant hardware according to decision tables stored in the USCM memory or by direct request from the JMDC. The link between the USCMs and JMDC was realized via two CAN-bus links. Furthermore, the USCMs were supposed to read out the DALLAS sensors in the U-Crate and on the octagon. Apart from these features used by the TRD electronics, the USCMs had in fact more capabilities, such as serial interfaces or ADCs which are used by other subsystems. After evaluation it became clear that slow control could be taken over by a modified JINFv2 board, which basically acts as an AMSWire-Lecroy bus converter. Decision tables to control crate and box redundancy can be

[1]TTCS, Tracker Thermal Control System
[2]USCM, Universal Slow Control Module

stored in the JMDC main computer. The temperature readout can be performed by the TRD gas electronics, where still USCMs are used. In all DAQ-crates the USCMs were removed and a JINFv2 took over part of the original USCM tasks. With the removal of the USCMs the affiliated +5 V DC/DC (S9054) converter in the UPD-Box became dispensable, too. Originally the S9011AU controller was supplied by +5 V, but could be changed into a +3.3 V version by replacing the solid state fuse. The new board was named S9011AUv2. The removal of the USCMs had even more implications concerning start-up. Originally the redundancy control was performed by the two USCMs each supplied by one half of the +5 V S9054 converter. The second redundant side of the +3.3V S9053 converter was kept off by default and it was planned to activate it only in case the first one gets permanently damaged. To allow a proper start-up without the USCMs but using the JINFv2 board which is supplied by the +3.3 V of the S9053, clearly both converter halves must initially be on. Otherwise in case of a malfunctioning first half of S9053, the complete crate would be lost, since there would be no possibility to activate the second half. The original scheme allowed to place MOSFETs on the outputs of each S9053 half, in order to prevent current flowing from the powered half into the other. However, CAEN does not certify this DC/DC converter for a scheme, where both S9053 halves are ON at the same time, but offers a modified S9053U converter with real diodes instead of MOSFETs with the disadvantage of an increased power consumption. The minimal estimated weight saving is about 960 g.

5.7.2 Combination of Digital and Analog Front End Power Supply

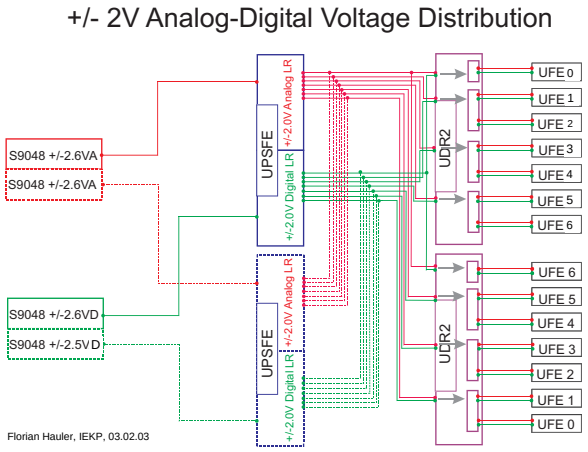

Figure 5.52: UPSFE power distribution before weight reduction.

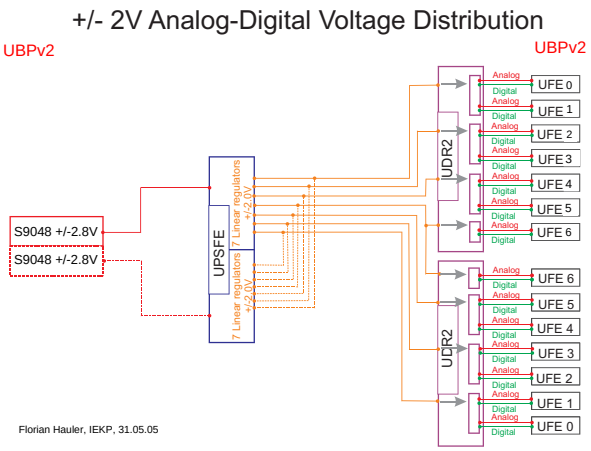

Figure 5.53: UPSFE power distribution after weight reduction.

Originally the U-Crate housed six UPSFE boards which supplied the front ends with separated power for the analog and digital front end parts parts. Seven linear regulators on one UPSFE were used as digital supplies and seven linear regulators as analog supplies. Two UPSFE boards were interconnected on linear regulator level for redundancy. This power scheme was slightly asymmetric. Two S9048 DC/DC converters, one for the analog power and one for the digital power, supplied two power groups. Further two S9048 DC/DC converters, again one for the analog power and one for the digital power, supplied the remaining power group. Figure 5.52 shows this scheme in the case for the single power group. For comparison again the latest scheme is given in Figure 5.53. After some tests, it turned out that the noise performance does not

worsen when merging digital and analog power. This allowed to halve the number of UPSFEs by drawing more power from each linear regulator. Figure 5.54 and 5.55 compare pedestal and noise before and after the unification of both linear regulators. This test was performed on the QM1 testbackplane, which is described in Section 5.10.1. The UPSFE reduction to three modules was accompanied by a reduction of the former four S9048 DC/DC converters to three, one dedicated for each power group. As a consequence each converter has to supply more current than before which resulted in an increased voltage drop on the cabling. Moreover, recent investigations show that the output of the ±2.6 V S9048 DC/DC converter has to be raised to ±2.8 V, since the increased load on each linear regulator channel causes an enhanced voltage drop on the output diodes. With the combination of analog and digital linear regulators, the UPSFE firmware had to be changed. Formerly, upon a possible trip in either the analog or digital linear regulator, the affiliated brother digital and analog linear regulator had to be switched off automatically by the firmware, in order to avoid damaging the front ends. With the combination of both supplies, the UPSFE firmware had to be changed. The minimal estimated weight saving is about 1310 g. With all the removals and changes described in the last two subsections the old 21-slot backplane had to be replaced and a new UBP backplane was developed, labelled UBPv2.

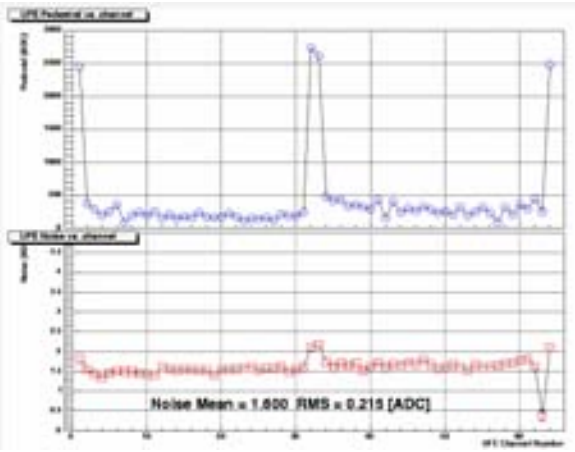

Figure 5.54: Noise performance before analog and digital power unification.

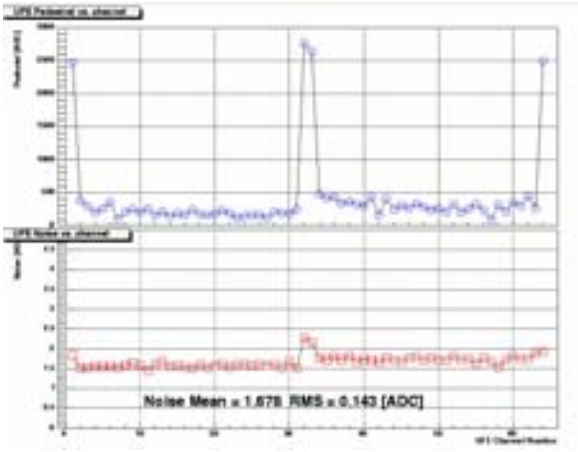

Figure 5.55: Noise performance after analog and digital power unification.

5.8 Development and Production

The development and production of the TRD electronics boards was carried out in four different steps. Depending on the step's purpose, modules were given different names: In the first step the *Engineering Modules* (EM) have been produced followed by the *Qualification Modules 1* (QM1) in the second step. Both steps were produced by the company CAEN as described in the next section. After the QM1-production step the electronics was supposed to be considered as bug free and the next two steps could be started. The boards of step three were called the *Qualification Modules 2* (QM2) and the boards of step four were the final *Flight Modules* (FM) including *Flight Spares* (FS), both produced by a defense contractor institute in Taiwan, called CSIST.

AMS-02 Transition Radiation Detector

Florian Hauler 18.4.2004

Boards for U-crate electronics

Name of board	purpose of board	EM Modules	QM1-Modules	QM2-Modules	FM-Modules	FS-Modules
UDR2	data reduction board	2	4	10	12	3
UPSFE	power supply front end	2	2	[9]	[12]	[3]
UPSFE v2	power supply front end v2			9	6	3
UHVG	high voltage generator	4	skip	14	12	3
S9011B	UPD filter		1	1	2	1
S9011AU	UPD controller		1	[1]	[2]	[2]
S9011AU v2	UPD controller v2			3	2	1
UBP v1	backplane		2	[1]	[2]	[2]
UBP v2	backplane v2			4	2	2
JINF v1	command and data distrib.	2	skip	2	[2]	[1]
JINF v2	command and data distrib. v2			4	2	1
S9048	+/-2.6V DCDC converter		2	5	6	3
S9053	+3.6V DCDC converter		1	1	[2]	[2]
S9053U	dioded +3.4V DCDC converter			1	2	2
S9054	+5.3V DCDC converter		1	1	[2]	[2]
S9056	+120V/+5V DC/DC converter		2	3	6	3

boards in brackets will not be produced

Figure 5.56: Number of boards to be produced to TRD electronics at CAEN and at CSIST.

- **Engineering Modules (EM)**
  The EM modules were the first TRD boards to be produced. In this step UPSFE and UDR2 were designed and produced under contract with the Italian company CAEN in cooperation with MIT, RWTH Aachen and Universität Karlsruhe. JINF and UHVG were developed by MIT and produced at CERN facilities. The purpose of this production step was to study and verify the design on board level and to develop the firmware codes of the PLDs on the boards. Therefore, mainly reprogrammable Altera PLDs were mounted. To save money, commercial parts were used. Recognized bugs were reported to the designer, in order to be corrected in the next electronics revision. A very limited amount of boards was produced.

- **Qualification Modules 1 (QM1)**
  The QM1 modules underwent functional tests with special emphasis on the modifications suggested in the first step. Again only a limited number of UDR2 and UPSFE boards was produced at CAEN. Additionally a UBP backplane was developed at CAEN, which allowed to test the produced boards on system level. UHVG and JINF were not produced on QM1 level but directly on QM2 level. Again, bugs were reported to the designer and corrected in the board/backplane design. The boards in this step were produced identically to the final flight electronics: Reprogrammable Altera FPGAs were replaced by Actel antifuse FPGAs. Where necessary, radiation-hard components were used. Some boards were tested in a thermo-vacuum chamber and on a vibration table. With the finalization of the QM1 step, the bug free electronics design was transferred to CSIST in Taiwan.

- **Qualification Modules 2 (QM2)**
  The QM2 modules were the first modules to be produced at CSIST. Electronics boards for at least one complete crate and one complete power supply box were produced and tested in Taiwan. The goal of this production step is to provide the necessary hardware to accomplish successful space qualification tests. Also, this step serves as a test run of the final flight module production. Once the space qualification tests are successfully finished, the final flight module production is started.

- **Flight Modules / Flight Spares (FM/FS)**
  In this step the real flight modules are produced with the experience gained by the previous steps. Hardware for two complete crates and boxes are produced. Additionally to the boards required to fill two crates and boxes, a few boards more are produced serving as spares.

Figure 5.56 summarizes the amount of boards to be produced for the TRD electronics in each production step. Once being relatively simple, this table became much more complicated, when a painstaking weight reduction program was imposed on TRD electronics, which affected both the design of the boards and the amount of boards placed in a crate or box. At the time when the weight reduction decision was taken, some of the boards were already produced and a modified *version 2* had to be reproduced, sometimes in a different quantity.
Although some EM DC/DC converters were produced at CAEN, they are not represented in this table, since they were produced for the complete collaboration and not dedicated to a specific subsystem such as TRD electronics.

5.8.1 Development at CAEN in Europe

The development of UDR2, UPSFE and the first version of UBP was done under contract with CAEN. One of the main arguments for a cooperation with CAEN was to obtain financial and technological synergy effects. The tracker subsystem, whose main money source is the Italian Space Agency ASI[1] is under contract with CAEN. Since most of the boards are common in major parts, such as the CDP, the development of UDR2 and UPSFE could be done in a collective effort together with the corresponding tracker boards TDR2 and TPSFE. For the development the same components and to a big extent the same or similar circuitry could be used, minimizing the risk of undetected subsystem specific bugs. The two EM modules of UPSFE and UDR2 were delivered fully functional, without any mounting bugs or defective components. The design of both boards was tested and possible changes to the coming QM1 modules were evaluated as described in sections for the UDR2 modules and for the UPSFE modules. In contrast to the successful delivery of EM boards, the QM1 modules of UDR2 and UPSFE were almost all faulty. Two of three defective QM1 UDR2 boards were sent back together with the two QM1 UPSFE boards to be corrected by CAEN engineers. The main faults on the UDR2 board were shorts between the dense Actel pins. One board contained a defective driver component in the detector dependent part. On the UPSFE boards missing components were the main failure source. Nevertheless, cooperation with CAEN can be summarized as convenient and successful.

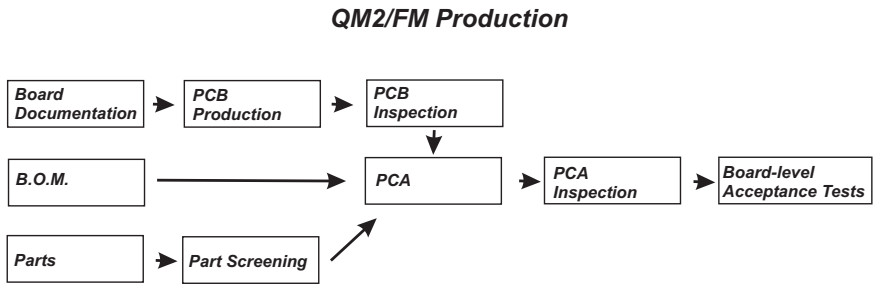

Figure 5.57: Production workflow at CSIST in Taiwan.

5.8.2 Production at CSIST in Taiwan

The production on QM2 and FM/FS level is carried out at CSIST in Taiwan. Figure 5.57 illustrates the workflow. As soon as the development process and the design verification is completed, the board designer at CAEN gets authorized by the board responsible to create the documentation files and the Bill of Material (BOM). This board documentation contains the necessary information to start the PCB production. Typically it is composed of a collection of files: The Gerber Files supply information about the layout of the board. The serigraphy files provide the board inscription which labels the space for each component by its identifier. The pick-and-place file contains information about the coordinates of the components to be placed. The drill files specify size and coordinates of drill holes in the PCB. Production information files offer information about the physical composition of the PCB such as PCB material, copper thickness and layer thickness.

As early as possible the board designer works out a preliminary BOM, which establishes

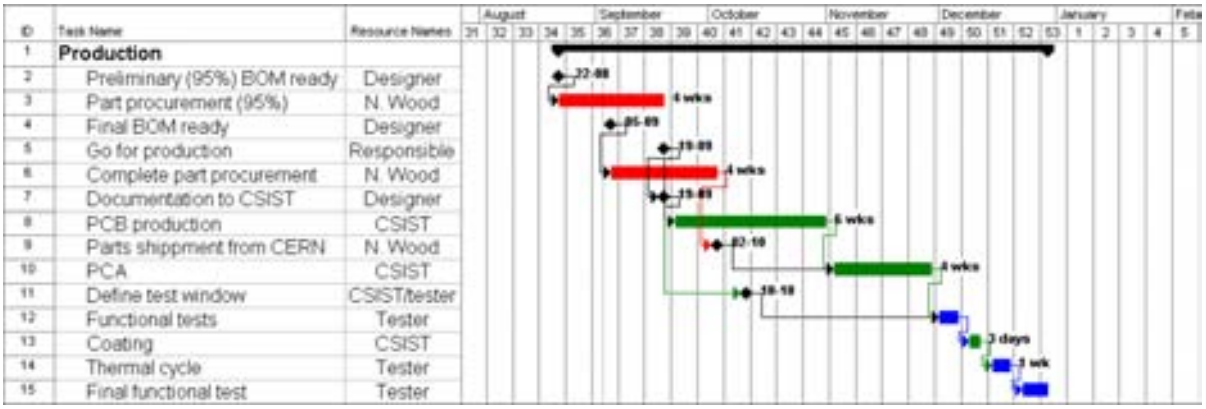

Figure 5.58: Production schedule at CSIST in Taiwan.

the link between component identifiers used in the production files and the real component product names, allowing the procurement responsible to start working. Part procurement is

[1] ASI, (italian), Agenzia Spaziale Italiana

always started as soon as possible since some components appear to have long delivery times of several weeks. A few weeks later the board designer finished the final BOM. When parts have arrived at CSIST, selected components undergo a screening process, to recognize faulty components at the earliest possible time. Complex parts such as DSPs and gate arrays are not screened at CSIST arrival but are verified during board level environmental stress screening. When PCB production is finished, the PCBs are inspected for faults before going into the PCA[1] process. After PCA the boards are inspected again and thereon handed over to subsystem testing personnel for environmental stress screening. Figure 5.58 gives an idea about the time needed for each production step. Roughly six weeks are calculated for part procurement. PCB production is scheduled with six weeks and PCA with about four weeks. CSIST and subsystem testing personnel agree on a testing window, which ideally is placed right after the end of the production process. It is important that this window is defined as early as possible, since CSIST has to arrange a part of testing equipment, such as bulky power supplies which cannot be transported conveniently by testing personnel in an airplane. Furthermore, CSIST has to arrange facilities to perform environmental stress screening.

5.8.3 Production Problems and Recovery

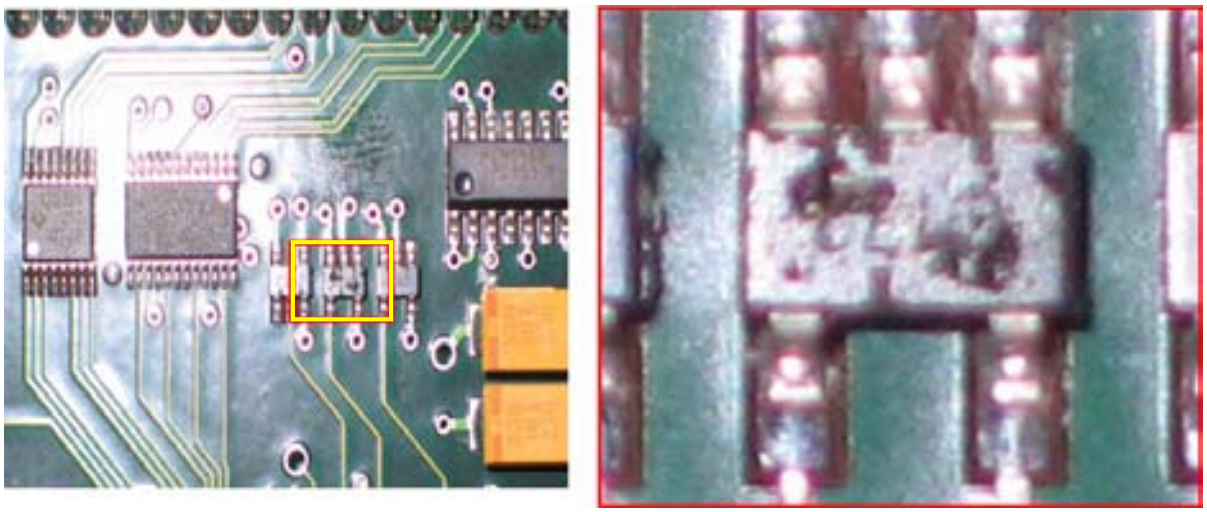

Figure 5.59: Bad component on UDR2 93005 during production. The component failed visual inspection and was replaced before board level functional tests.

After all the problems during QM1 production, QM2 production at CSIST turned out to be surprisingly reliable. No noteworthy problem was found during QM2 UPSFE production. Four of ten QM2 UDR2 boards were found to be defective. DC/DC converter problems could be traced back to missing components. The main benefit of testing on location at CSIST is that the production responsibles including the technicians are at the tester's disposal. While error fixing on QM1 level in cooperation with CAEN takes between one and two weeks including the shipment back and forth, error fixing at CSIST is a question of hours. Figure 5.59 shows a Schmitt trigger buffer component which failed visual inspection. The component was replaced before starting the functional tests and conformal coating procedure. Figure 5.60 illustrates

[1] PCA, Printed Circuit Assembly

another problem which was found similarly on four UDR2 boards with serial numbers 93005, 93006, 93008 and 93009. Some of these boards featured high currents, others exhibited SRAM memory and flash memory problems. No visible shorts were detected during visual inspection. The origin of these problems was found when the decision was taken to replace the suspicious DSPs. Below the DSP is a solder area which is used to transfer heat from the DSP to the PCB. During the DSP mounting process the still liquid solder was pushed from the heat transfer area to the via, thus causing a short. This kind of problem is particularly hard to detect, since it is not visible on a fully mounted board, with this area hidden below the DSP. On all four defective boards similar problems were found, although not all on the same via. To prevent this kind of problem during FM/FS production, it is under discussion to fill the vias with solder stop to prevent shorts between the heat transfer area and the vias. Recapitulating, the production at CSIST was a success, with an electronics yield more than enough to fill up one complete UPD-Box and U-Crate, smoothing the way to space qualification tests on crate level.

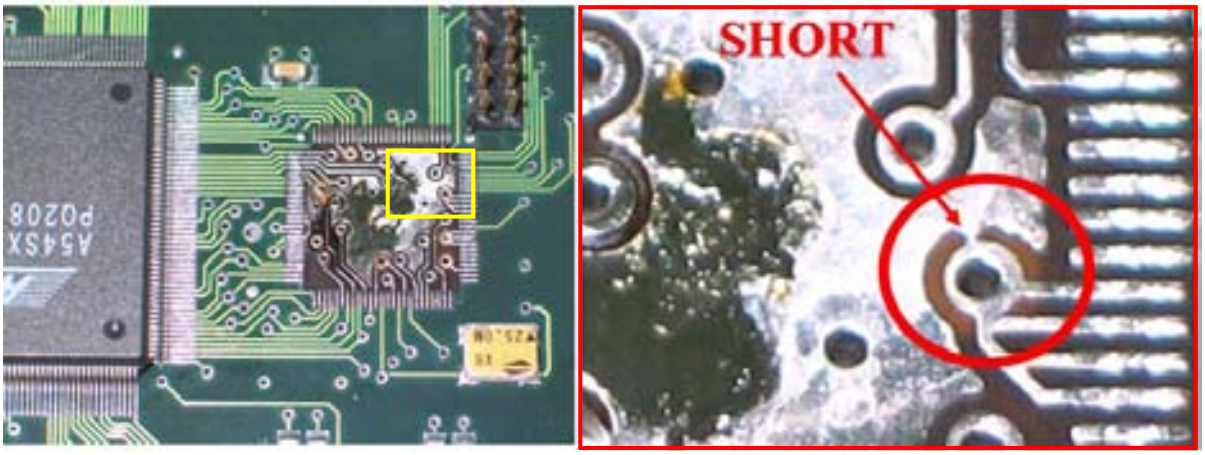

Figure 5.60: DSP solder problem during UPSFE production, found on boards 93005, 93006 and 93009. This kind of problem is especially hard to detect, since normally the failure area is covered by the DSP chip.

5.9 Space Qualification

Once the board production is finished, the produced hardware has to be tested for functionality. Moreover, it has to proof its ability to survive the launch and to work in deep space conditions. Several steps have to be performed to achieve space qualification, grossly divided into board level tests and crate level tests. As will be shown in the next sections, qualification tests for QM2 hardware and FM/FS hardware are similar but not identical. QM2 hardware is tested to absolute extreme conditions, giving information about the basic qualification of the hardware to the mission, but accepting that the hardware gets degraded during testing. Therefore, a slightly modified testing scheme is applied to the FM/FS modules in order to prevent the hardware from damage. Extreme temperature conditions and vibration durations are reduced to moderate values.

5.9.1 QM2 Qualification and FM/FS Acceptance Procedure on Board Level

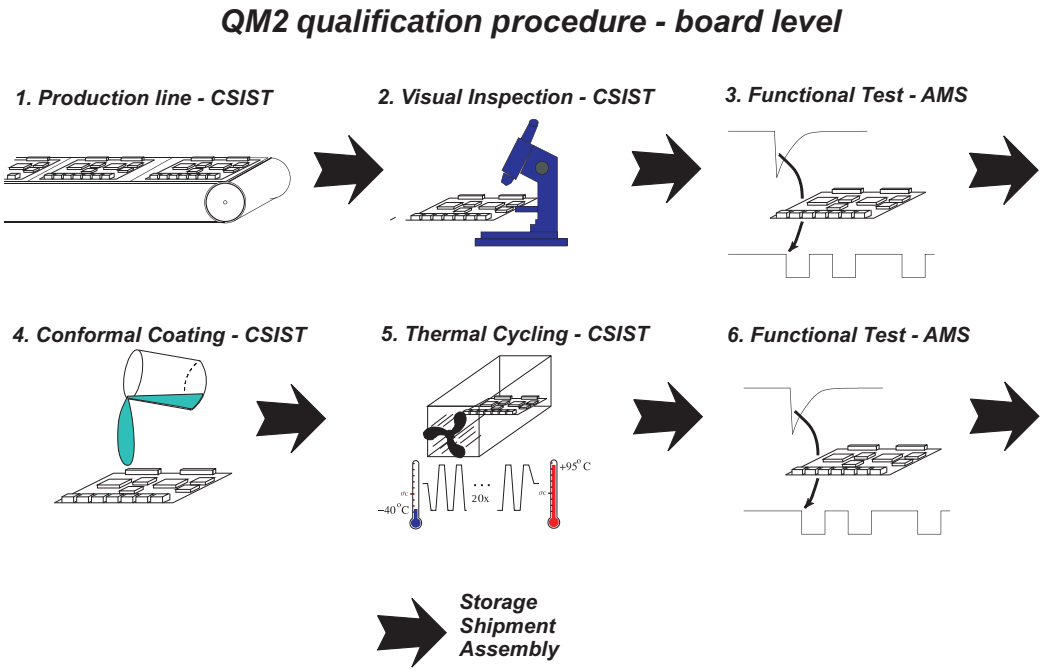

Figure 5.61: Qualification procedures for QM2 production on board level.

Figure 5.61 illustrates the space qualification procedure on board level. As soon as the assembled PCBs leave the PCA assembly line, they are inspected by CSIST personnel for missing or misplaced components or visible solder shorts. Once they are found ok, AMS-02 subsystem people take over and test the hardware for functionality. Next step is the conformal coating. Conformal coating protects the PCBs from humidity and impurities on Earth and in space prevents floaters from touching and damaging the hardware. The conformal coating requires about 2-3 days to dry. Afterwards the hardware is put into thermal-cycling climate chambers, where extreme storage temperatures simulate thermal environment on orbit. To verify that all components have survived this treatment, once again functional tests are carried out by AMS-02 subsystem personnel. Once declared as failure free the hardware is placed in storage at CSIST or shipped to Europe for assembly. Individual test procedures are explained in the following text.

Functional Tests (FT)

To start with board level testing, power is applied to the boards and the current flow is observed. Higher or lower nominal currents indicate a problem. UDR2 and UPSFEv2 can be powered using the QM1 backplane described in Section 5.10.1. The UDR2 board tests continue with an AMSWire communication test. The status of the CDP is requested by sending a *GETSTATUS* command. This request reads out the results of the DSP internal memory test routines, which were performed during start up. No answer or a corrupted answer indicates one or more

problems. In this case the DSP emulator EZ-ICE has to be connected and the hardware problem has to be traced by running the test routines manually. The proper functionality of the DDP is tested by connecting seven UFE boards and reading out pedestals and optionally perform a DAC calibration. On the UPSFEv2 board the linear regulators are tested using the UPSFEv2 test backplane described in Section 5.10.2. The voltages are measured manually, but the overcurrent protection is tested automatically using microcontrollers. The proper functionality of the FPGA is verified by sending Lecroy commands. Board level tests of JINFv2 and UHVG are under responsibility of MIT and therefore not described here.

Environmental Stress Screening on Board Level (ESS)

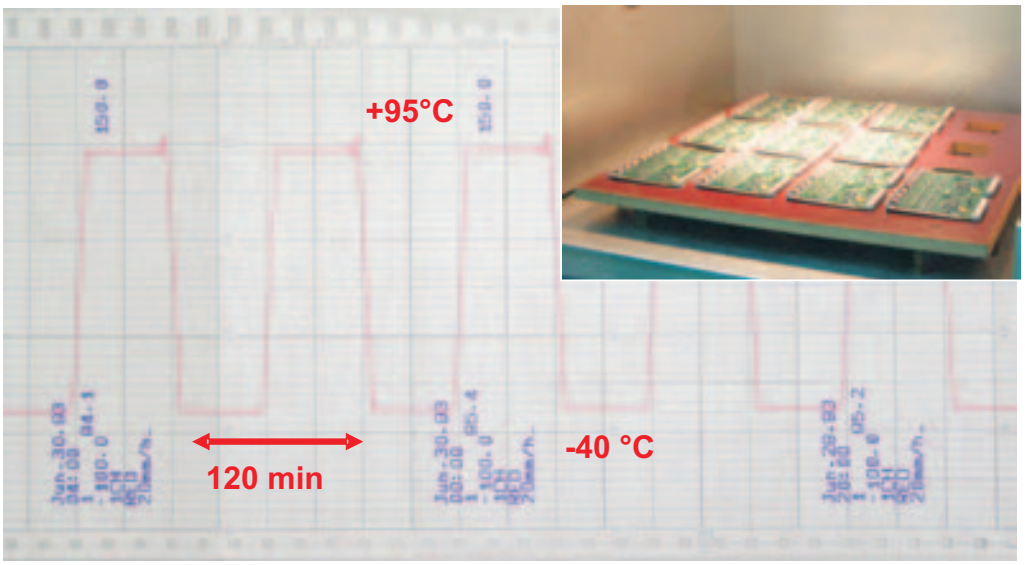

Figure 5.62: Part of the environmental stress screening profile for board level tests. Right corner: QM2 UDR2-boards during thermal cycling in summer 2004.

Figure 5.62 shows the log sheet of the QM2 UDR2 thermal-cycling. 20 cycles are conducted from -40°C to +95°C. Flight Modules are screened using the same temperature range. All boards of the U-Crate remain unpowered during thermal-cycling. Basically applying power is possible, but imposes a huge amount of preparation effort, since not only several voltages have to be applied to the 32-pin board connectors, but also communication links have to be connected to all the boards in the test. After ESS, all boards are checked again for functionality. In contrast to the boards in the U-Crate, the DC/DC converters can be tested under power. They are switched on in the beginning and in the end of thermal-cycling at +55°C and at -25°C to undergo a functional test. No TRD board or DC/DC converter failed the functional QM2 board level tests during or after ESS.

5.9.2 QM2 Qualification and FM/FS Acceptance Procedure on Crate Level

The crate level tests described in this section are the final barrier the TRD electronics has to pass. By successfully completing these tests, the electronics are space-qualified and the

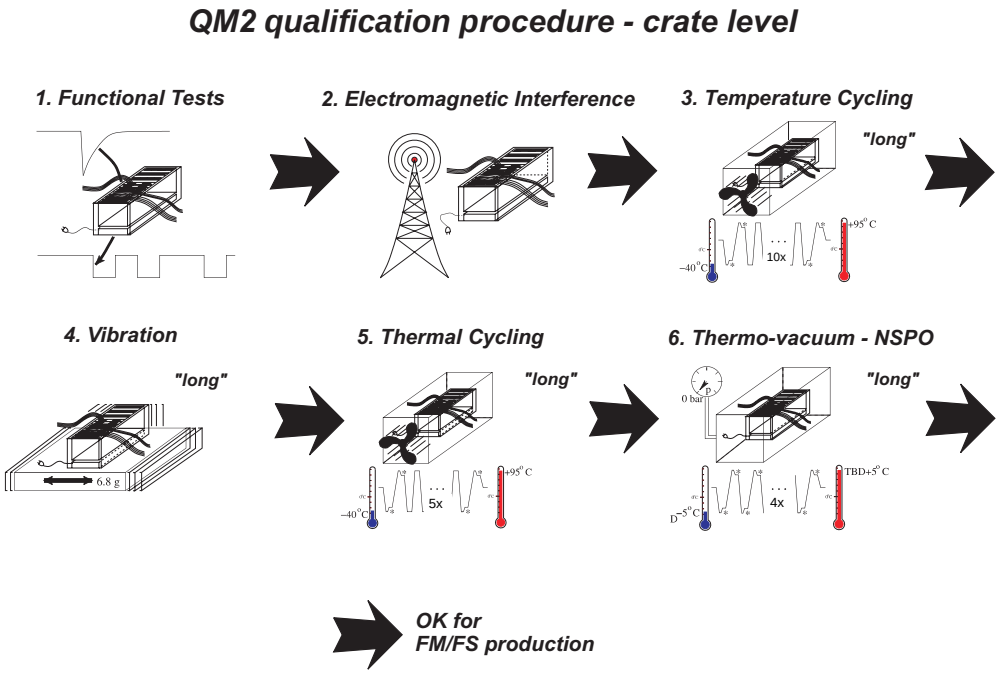

Figure 5.63: Qualification procedures for QM2 production on crate level.

flight module production can start. The procedure, as shown in Figure 5.63, starts with crate level functional tests, which proof that the system works properly. Afterwards Electromagnetic Compatibility (EMC) of the crate and the box is verified. This test is required, because the system must not emit noise in other AMS-02 subsystems, or, even worse, into Space Station systems. On the other hand it may not be affected by radiated Electromagnetic Interference (EMI) from the outside. Temperature cycling is performed before and after a vibration test, which simulates the vibrations during the start of the Space Shuttle. If a part of the crate gets affected by these vibrations because of excited resonance frequencies and an electronics board loses components, the test has certainly failed. In the end, a Thermo-Vacuum-Test (TVT) not only simulates extreme temperature conditions on orbit but also inhibits convective heat exchange, in other words it represents the dress rehearsal for operation in space.

Functional Tests (FT)

The functional tests on crate level verify the full functionality of the complete crate. AMSWire communication performance tests are carried out. High voltage is ramped. Slow control status signals are read out frequently and the ability to switch on/off all DC/DC converters and U-Crate boards is tested. To test the DAQ-chain, front end simulators (see Section 5.10.3) are connected to the UDR2.

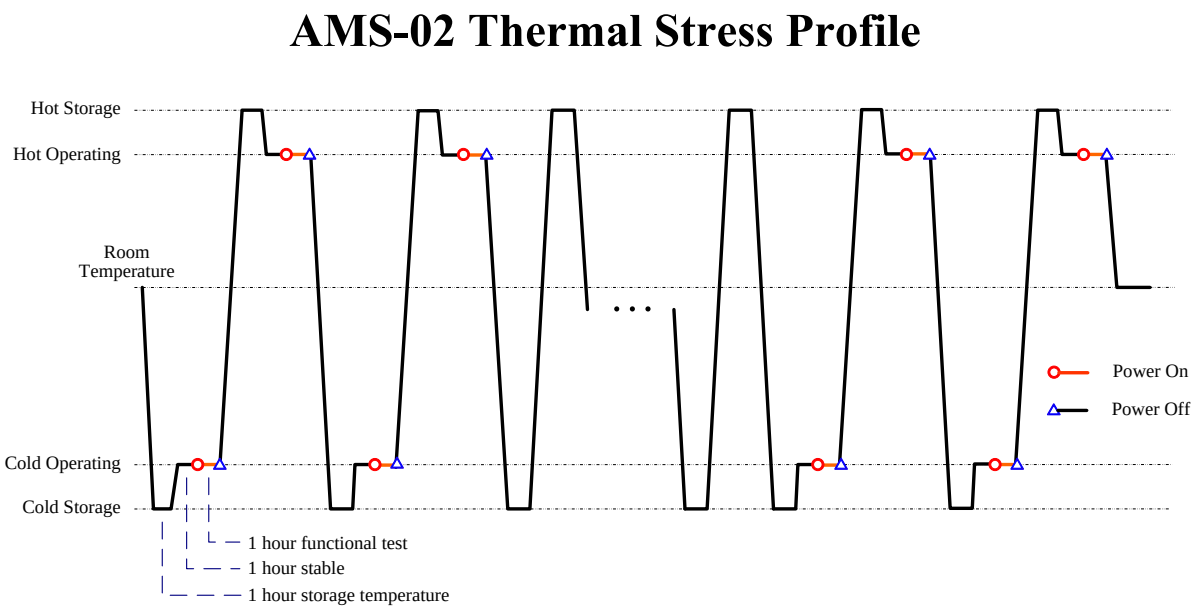

Figure 5.64: Environmental stress screening profile for crate level tests.

Environmental Stress Screening on Crate Level (ESS)

Figure 5.64 shows the thermal stress profile for crate level ESS. Four temperature levels are defined: hot storage, hot operating, cold operating and cold storage. During cycling the temperature remains constant at the cold and hot storage temperatures for one hour before being conducted to the hot and cold operating temperatures. There, the temperature is kept constant again for one hour. As soon as the operational temperature is reached again, the electronics are switched on for one hour and functional tests have to be performed. Ten cycles should be performed with functional tests during the first two cycles and the last two cycles before entering the vibration test. After the vibration test, five cycles should be taken with functional tests during the first cycle and the last two cycles. The cycles can be stopped whenever any test fails or for any other reason. But to successfully accomplish this test, the last two cycles should be failure free. Table 5.3 defines the four temperature levels for QM2 and FM/FS testing.

QM2 hot storage	QM2 hot operational	QM2 cold operational	QM2 cold storage
+85°C	+55°C	-25°C	-45°C
FM/FS hot storage	FM/FS hot operational	FM/FS cold operational	FM/FS cold storage
+80°C	+50°C	-20°C	-40°C

Table 5.3: Temperature level definitions for QM2 and FM/FS thermal cycling.

Vibrational Tests (VT)

Figure 5.65 defines the power spectral density[1] which is applied to the hardware during a vibrational test. The vertical axis is scaled in units of G^2/Hz, which at first glance is not

[1] indeed a more suitable name would be acceleration spectral density, but this nomenclature has a long history

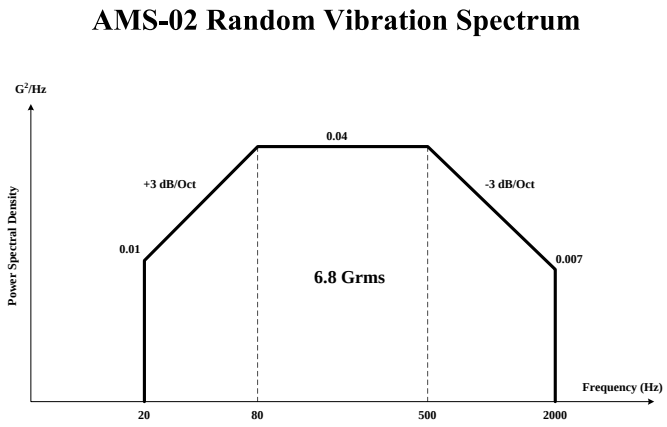

Figure 5.65: Random vibration spectrum used for vibrational tests.

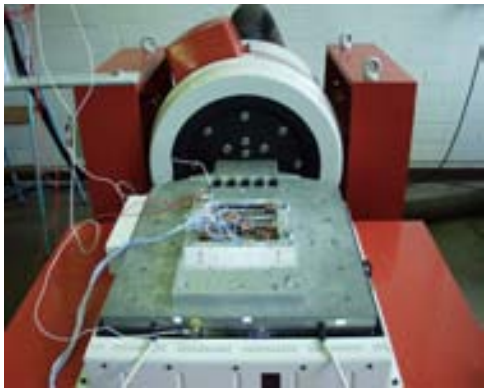

Figure 5.66: Vibrational test of a QM1 DC/DC converter at RWTH Aachen.

easy to understand. The nominator G^2 offers information about the physical quantity under consideration, namely acceleration, in units of gravitational acceleration on Earth G. The denominator Hz is used as normalization factor. When measuring a power spectral density, a power spectral density analyzer inserts the measured accelerations in a histogram, subdivided by a certain bin size. During this process the measured quantity is squared and averaged with the prior samples. The resulting quantity therefore is the average value over the bandwidth of the bin, which is called the mean square acceleration G^2. This value is afterwards divided by the bandwidth, to normalize for the bin size and gives rise to the peculiar unit of G^2/Hz, called power spectral density. The integrated area below the power spectral density plot represents the mean square acceleration over the entire frequency range. The square root of this value is simply the mean value or commonly referred to as the *rms* value. Assuming now that the vibration source emits Gaussian distributed vibrations, we can say that for a 6.8 g_{rms} spectrum almost all accelerations peaks lie within the 3σ limit of 20.4 g. For QM2 qualification tests this vibration spectrum is applied for 10 minutes in X, Y and Z direction, while powering the hardware and performing functional tests. For FM/FS acceptance tests, vibrational testing is carried out for at least 1 minute per axis and for a maximum of 2-3 minutes, while performing functional tests. During vibrational tests the hardware is powered and constantly tested in order to identify latent defects and manufacturing flaws in electronics hardware. Figure 5.66 shows a picture of a QM1 DC/DC converter vibration test at RWTH Aachen. [Gil97, Mul96b]

Thermo-Vacuum Tests (TVT)

This test represents crate level functional performance tests between and at temperature extremes. Figure 5.67 illustrates the temperature profile for a thermo-vacuum test. Again four temperature levels are defined for hot storage, hot operating, cold operating and cold storage phases. The pressure is reduced to at least 1.0 x 10^{-5} mbar. The electronics has to be switched off when exceeding the maximum allowable temperature region. The electronics has to be switched on during hot soak and cold soak and complete successful functional tests. After passing the first hot and cold soak phases consecutive cycles in the operational temperature region are conducted. From time to time successful functional tests have to be carried out, before entering a second hot storage and cold storage phase, where the electronics has to be again switched off. The test ends with cold balance and hot balance phases where measured

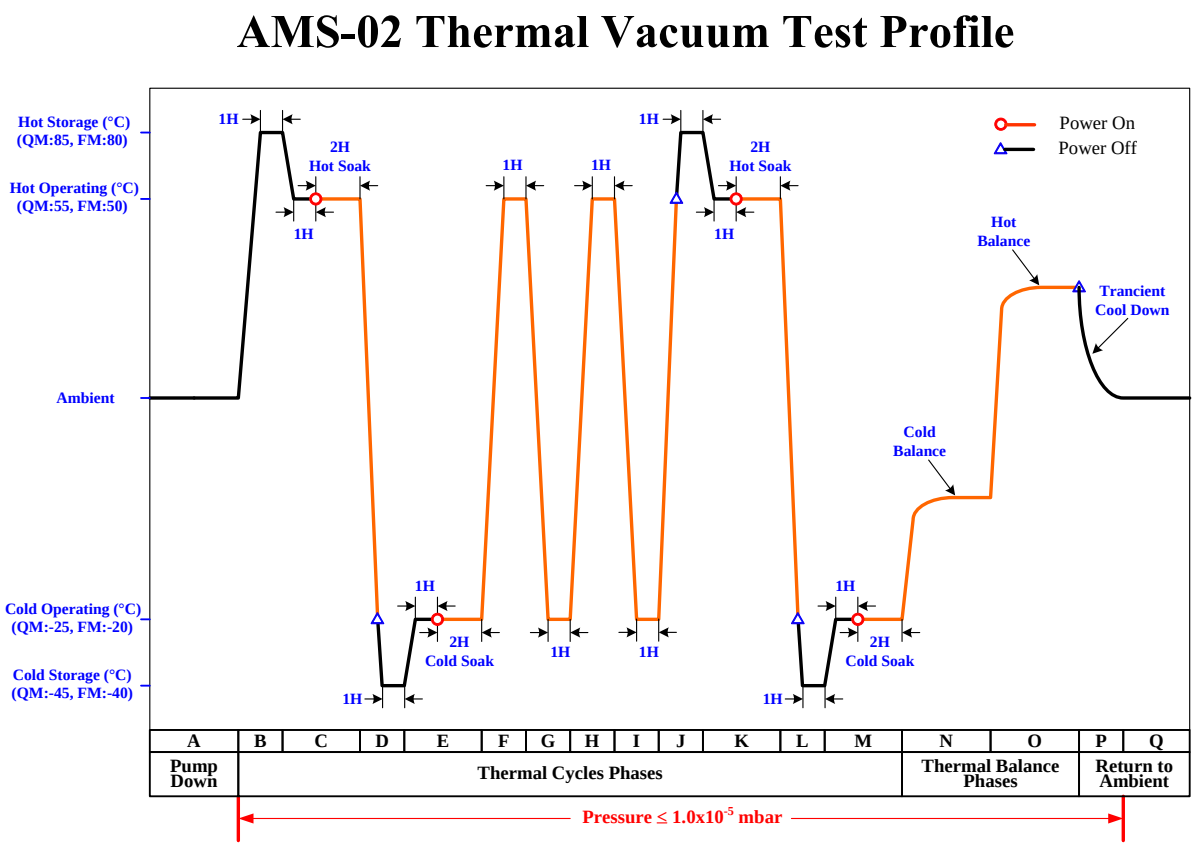

Figure 5.67: Thermo-vacuum test temperature profile.

temperature levels are used for comparison with thermal analytic models. The temperature levels for QM2 and FM/FS thermo-vacuum testing are the same as for ESS, given in Table 5.3. [Mul96a, Gil94]

Electromagnetic Compatibility (EMC) / Electromagnetic Interference (EMI) Tests

To verify that the system is not affected by conducted or radiated immissions (electromagnetic susceptibility tests) or that the system does not disturb other systems by radiated or conducted emissions an EMI/EMC test campaign was performed at CSIST. For the conducted electromagnetic susceptibility tests sinusoidal disturbances (CS01/CS02) between 30 Hz and 50 MHz at 2.8 V_{rms} and spikes (CS06) of $\pm 56V$ with a duration of 10 μs and 0.15 μs were injected into the +28V power lead. Likewise the conducted emissions during switch-on (CE01) and during normal operation (CE03) may not exceed certain thresholds.
The system may no be influenced by radiated susceptibility of spikes (RS02) of $\pm 56V$ with a duration of 10 μs and 0.15 μs and by radiated susceptibility of sinusoidal radiations (RS03) between 14 kHz and 15 GHz with field strengths of up to 250 V/m. Again, the radiated emissions during normal operations (RE02) may not exceed certain thresholds.
Figure 5.68 shows the EMI/EMC test arrangement for the U system at CSIST. The laboratory is protected against electromagnetic radiation from the environment. The electromagnetic emission of the system is shown in Figure 5.69 (EMC). The maximum allowable emission rate by NASA specification is shown as well. Similar tests for the front end boards performed by

Figure 5.68: Experimental arrangement of the QM2 EMI test in Taiwan.

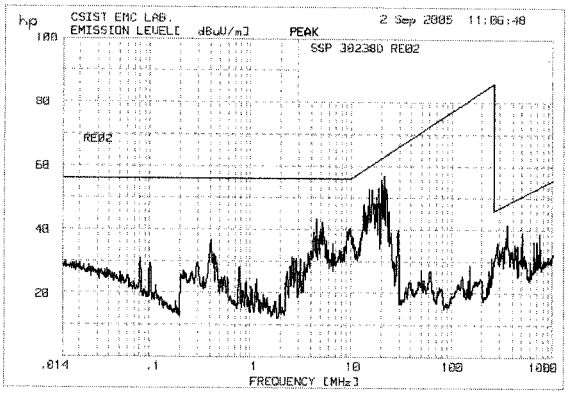

Figure 5.69: Radiated emission measurement (RE02) of the U system without cable shielding.

RWTH Aachen showed that the cabling of the UFE boards had to be modified in order to successfully pass this test. A metal screening was added around the signal cables to the UFE. In the final TRD this screening will be a netting of copper and aluminized Kapton foil. [Fop04]

The QM2 EMI/EMC test of the U-Crate and the UPD-Box has been successfully accomplished in August 2005.

5.10 Test Setups

In order to test newly developed and produced hardware, early provisions have to be made to allow an immediate start of testing upon hardware delivery. To verify the board design, an EM and a QM1 test backplane were developed. For the series production at CSIST a UPSFE testbench was designed. To simulate 82 front ends during the QM2 TVT, a front end simulator was developed, whose task is to dissipate the heat which is normally consumed by the front ends. Moreover, it simulates DAQ front end replies.

5.10.1 EM/QM1 Test Backplanes

Two test backplanes were built. The first one, called the EM test backplane, allows to test one EM UDR2 and two in parallel connected EM UPSFEs. It was used to evaluate the first prototype boards delivered by CAEN. This backplane provides connections for +3.3 V and ±2.8 V power supply, four AMSWire links to the UDR2, a trigger/busy connector and a slow control connector to the UPSFE. LEDs[1] allow to test the UPSFE slow control functionality to control the solid state fuses of other boards. The incoming LVDS trigger is converted on the backplane into an LVTTL signal accepted by the UDR2. The busy signal coming from the UDR2 is converted vice versa from LVTTL into LVDS. Jumpers can be used to set the solid state fuse control signal for the UDR2 or to simulate the solid state fuse status signal for the UPSFE. On each supply line 0.075 Ω resistors are placed to determine the nominal power consumption of each board by voltage measurement. Using this backplane a first testbeam in 2002 was successfully conducted. A picture of the EM backplane is available in Figure 5.70.

[1]LED, Light Emitting Diode

Figure 5.70: EM power group backplane.

Figure 5.71: QM1 power group backplane with UDR2 and UPSFE.

Along with the changes in the QM1 modules, the need emerged to develop a second backplane. The connector layout of the QM1 UDR2 had changed and was no longer compatible to the old EM backplane. During the design of the new QM1 test backplane, the coming series production was taken into account and a solid state fuse test circuit was implemented. Figure 5.71 shows a picture of the new QM1 test backplane and Figure 5.72 describes the features of the new backplane in detail. All of the features used in the EM backplane were taken over into the QM1 backplane. The most significant difference is the fact that the new backplane allows to test a full power group composed of two UDR2s and two UPSFEs. Consequently eight AMSWire links, four for each UDR2 are available. Each UDR2 possesses its own trigger/busy link, but it is possible to trigger both simultaneously by jumper interconnection. In this configuration the busy signals are interconnected by diodes. This power group scheme of two UDR2s and two UPSFEs was used in the QM1 U-Crate layout before weight reduction. During weight reduction the linear regulator interconnections of one power group changed, because one UPSFE was removed and the linear and analog power was combined. Although the QM1 test backplane does not support this latest layout of U-Crate electronics, it is still suitable to test UDR2s and UPSFEv2s of QM2 and FM/FS production. Figure 5.73 shows the schematic of the solid state fuse test circuit. A PC running Labview[1] accesses an I/O warrior microcontroller[2] via USB[3]. The big advantage of using this microcontroller is, that the USB protocol is already implemented in the microcontroller and drivers to access it are provided by the company. The I/O warrior is supplied by the 5 V USB bus power. By setting the microcontroller's I/O pins, the DS1803 8-bit digital potentiometer can be controlled. The communication between the I/O warrior and the digital potentiometer is performed by a 2-wire serial bus with one line used as strobe (SDA) and one line used as clock (SCL). Two ways of controlling the digital potentiometer can be chosen. The first way is to write each bit separately to the outputs, the

[1]Labview, graphical development environment by National Instruments
[2]I/O warrior USB interface microcontroller, Code Mercenaries, Germany
[3]USB, Universal Serial Bus

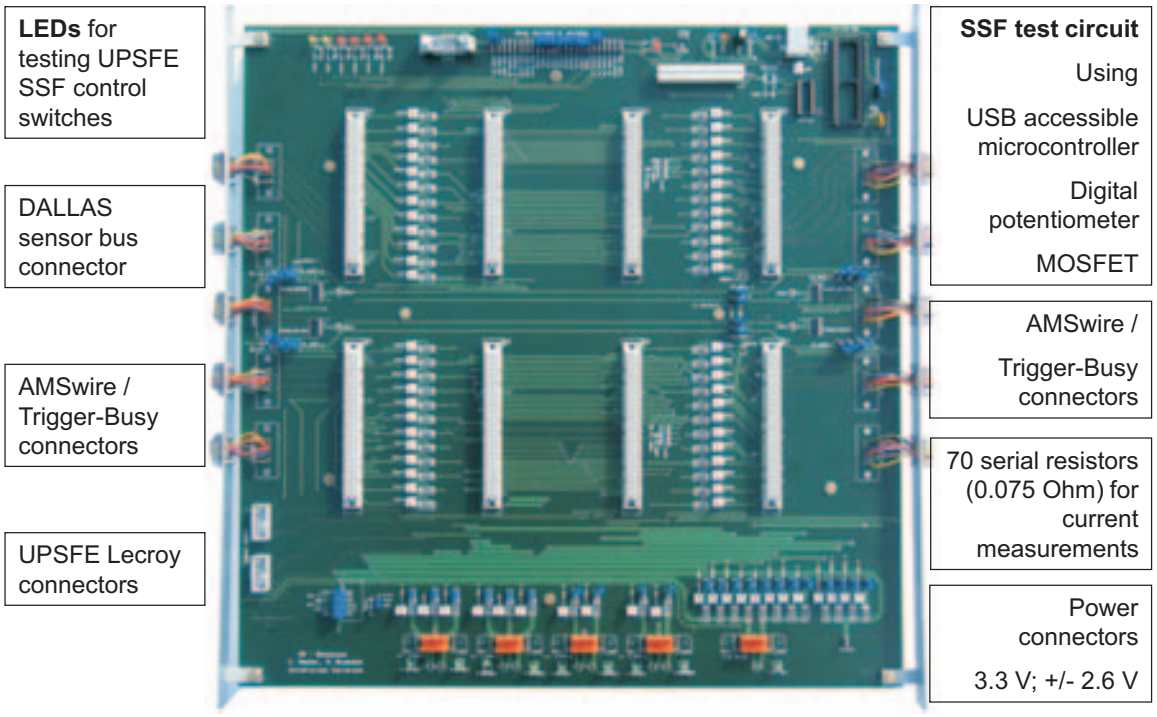

Figure 5.72: Features of the QM1 power group backplane.

second way is to use the I^2C[1] capability of the microcontroller, where a complete I^2C command is transmitted, avoiding large overhead as in the first case. The maximum reachable speed in the first way by controlling the pins individually is 30 bits/s limited by USB speed. Since 3 bytes are used to set one potentiometer value, it takes approximately one second to define the current flow through the circuit. Using the I/O warrior's I^2C pins a throughput of 750 bytes/s can be reached, since only one USB transaction is needed to send an I^2C command. A similar circuit is used in the UPSFE testbench described in the next section. While for the solid state fuse test both communication approaches are feasible, for the UPSFE testbench the I^2C communication is clearly preferable, since 14 circuits have to be controlled simultaneously [Cod04]. The digital potentiometer controls a MAX890L MOSFET current limiter which acts as a variable resistor and shorts the 3.3 V solid state fuse circuit in a defined way. The MAX890L current limit can be calculated according to Formula 5.2 [Max00]. To account for component uncertainties such as for the potentiometer, the circuit can be calibrated in order to obtain exact switching currents.

$$I_{Limit} = \frac{1.38 \cdot 10^3}{R_{Set}} \tag{5.2}$$

Here I_{limit} defines the current flowing through the circuit and R_{set} is the value of the digital potentiometer. The 3.3 V power and ground has to be gripped with a probe from two test points on each UDR2 and UPSFE board. As soon as the current limit is exceeded, the solid state fuse switches off the 3.3 V power supply. This can be detected by the microcontroller by reading an I/O pin, which senses the voltage of the protected 3.3 V power behind the solid

[1] The I^2C-bus is patented by Philips Semiconductors, the Netherlands

state fuse. To obtain precise measurements a Keithley 2000 multimeter can be connected to the circuit to read out the current as can be seen in Figure 5.74. For the PCB a four layer design was chosen. All supply and communication lines run either on the top or on the bottom layer, which allows, just in case, to correct mistakes using flying wires. The two middle layers are ground layers used for impedance matching of LVDS lines routed on the top and bottom layer. More information about the design is available in [Brü03].

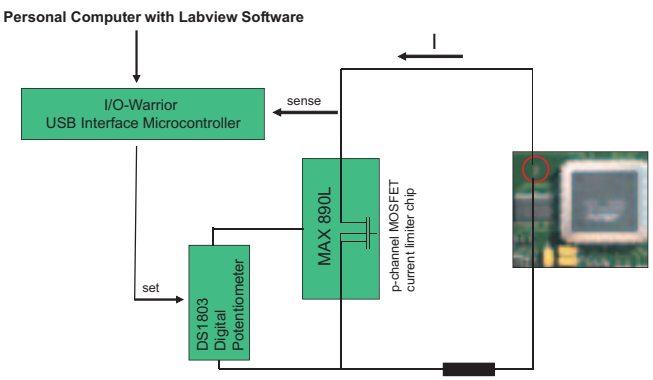

Figure 5.73: Schematic of the SSF test circuit. A microcontroller sends sequence signals to a digital potentiometer which defines the current through the MAX890L current limiter.

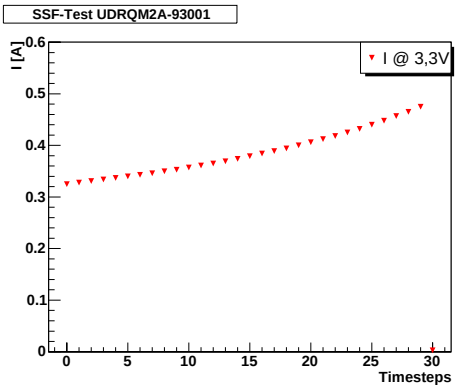

Figure 5.74: Typical output of the solid state fuse test. The current was logged using a Keithley 2000 multimeter, read out by Labview.

5.10.2 UPSFE Test Backplane

When testing the UDR2, most of the component tests such as SRAM, flash or AMSWire tests can be performed by taking advantage of the small DSP onboard computer and running appropriate test software. The result is read out either by AMSWire or by looking directly into the DSP memory via EZ-ICE, a hardware interface to the DSP. Apart from the solid state fuse test circuit, no special hardware arrangement is needed to evaluate whether the board is faultless or not. In contrast to that, the UPSFE is a rather primitive board and needs external hardware for evaluation whether all the linear regulators work properly or not. The best way to test the UPSFE linear regulators is certainly to measure the output voltages and the incoming current. The automatic overcurrent protection is tested by applying a variable load to the linear regulator outputs. While the first two tests can be done in an easy way using the QM1 testbackplane, shorting nine UPSFE boards with 14 linear regulators each can be rather cumbersome, even for the eager tester. Consequently an automatic testbench was designed which takes over the job. Figure 5.75 shows a photo of the UPSFE test bench. A circuit which is able to short a solid state fuse by applying a variable load was already implemented in the QM1 test backplane and working properly. Since time was short, a new development was not feasible and the well-known circuit was adapted. Using this circuit a testbench was designed, whose purpose is to determine the approximate switching current of the 14 linear regulators. Because each linear regulator provides ±2.0 V output, 28 of these circuits need to be placed on this board. This can be accomplished by using 28 MAX890L digital current limiter MOSFETs and 14 DS1803 digital potentiometer chips and two IO Warrior microcontrollers. 14 DS1803 chips are sufficient since one chip in fact houses two potentiometers. Two I/O Warriors are

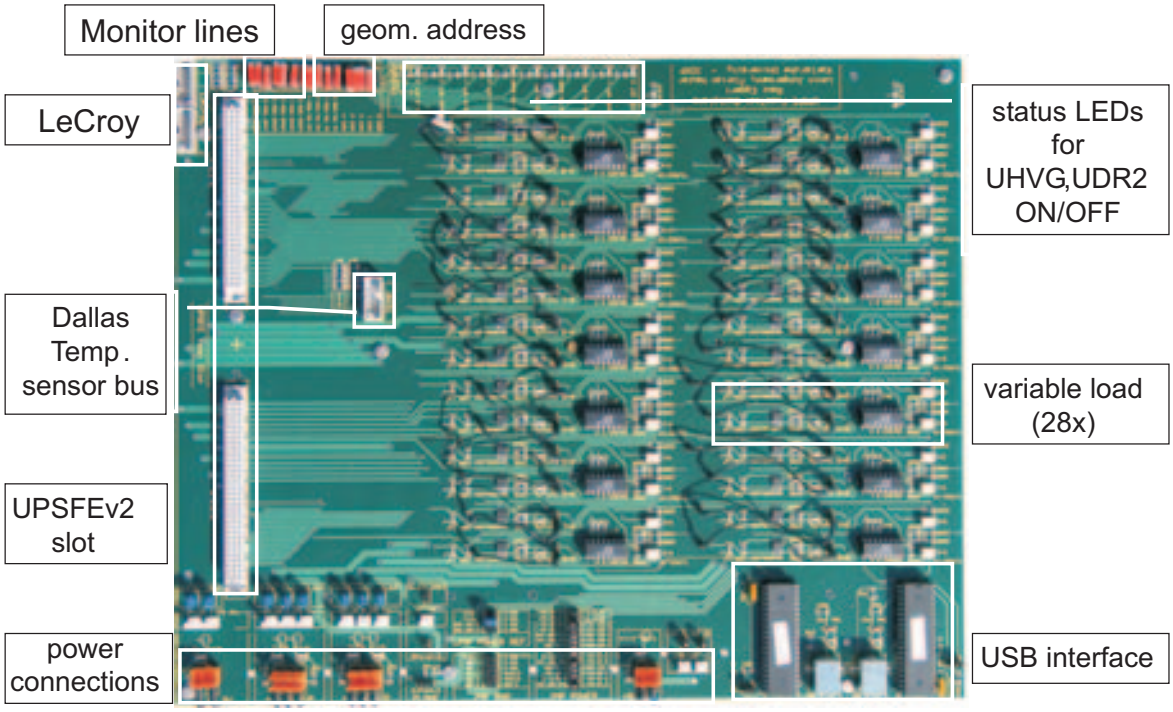

Figure 5.75: Features of the UPSFE test backplane.

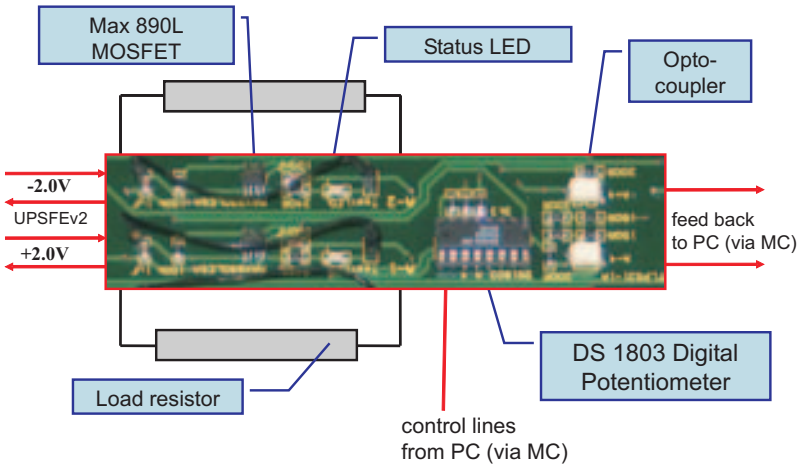

Figure 5.76: Variable load circuits consisting of MOSFETs, digital potentiometers and opto-couplers.

needed, because a maximum of seven digital potentiometer chips can be accessed on one 2-wire bus due to the limited 3-bit addressing capability of the DS1803 chip. This means half of the 14 linear regulators are tested by the first I/O warrior, the other half is tested by the second I/O warrior. To determine, whether the UPSFE overcurrent protection has switched, the ±2.0 V linear regulator output voltage is fed back as a status signal to the microcontrollers' I/O ports

via Toshiba TLP521 optocouplers. Additional test bench features are LED indicators as optical status signals for the linear regulators and solid state fuses control circuits. Figure 5.76 shows a close-up view of such a variable load circuit. Again as for the EM and QM1 test backplane a four layer design was used for the PCB. The development and production of this test bench is described in [Egg04].

5.10.3 Front End Simulator (UFS)

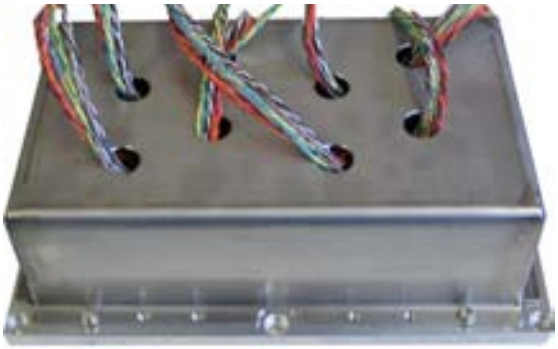

Figure 5.77: Assembled UFS-Box.

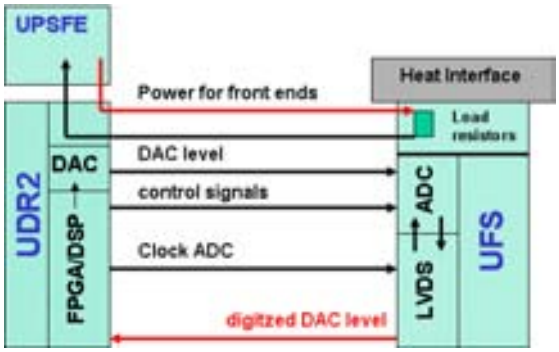

Figure 5.78: UFS schematics.

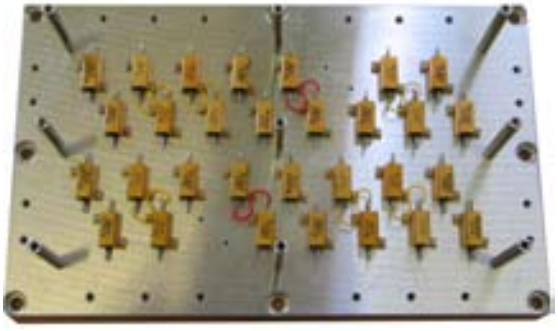

Figure 5.79: UFS support mechanics with mounted resistors.

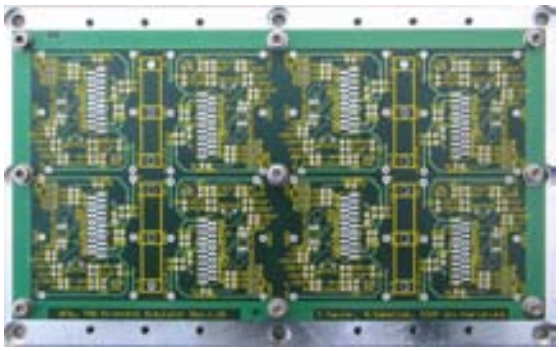

Figure 5.80: UFS PCB, mounted on support mechanics.

During thermo-vacuum tests, all electronics have to work as close as possible to real conditions in order to simulate operation in space correctly. For the TRD DAQ electronics this means that UPD-Box and U-Crate should be nominally powered to apply the proper load. To accomplish this goal, even the front ends have to be connected, since they draw about 10 W power per crate, which the DC/DC converters have to deliver via the linear regulators in the UPSFE. But, placing the 41 front ends into the thermo-vacuum chamber is not feasible for several reasons. Firstly, since 41 front ends have to be placed correctly in the chamber, a mounting jig had to be designed. Placing the front ends outside the chamber imposes the problem of interfacing 41 cables through the chamber door. Secondly there are no 41 QM front ends, but 41 FM front ends which must not be tested according to the harsher QM2 qualification procedure. As a consequence a UFS (U Front End Simulator) was built, whose task is to dissipate about 10 W (summed over three UFS boxes) of power and to provide a DAQ feedback in order to see whether the DAQ still works. Figure 5.77 shows such a front end simulator box and Figure 5.78 illustrates the basic idea of this front end simulator. Load resistors mounted on an interface plate dissipate the power

coming from the linear regulators of the UPSFE. Since during the thermo-vacuum test the UFS resides in vacuum, no convection occurs to take away the dissipated heat from the resistors. Therefore, the resistors are mounted on an interface plate, which has a good thermal contact to the temperature guidance plate of the TVT chamber. Since one linear regulator supplies two front ends which are connected to one power section of a UDR2, it is sufficient to connect only one link of a power section. Therefore, the UFS resistors are dimensioned in a way to simulate two front ends per link for three of the four power sections. The last UDR2 power section takes a special position, since it provides only one front end link. This link is connected to a UFS circuit with smaller resistor values to simulate only one front end. Reducing the amount of link cables in this way is advisable to do, since the link cables are 21-pin micro-d pigtail connectors qualified for aerospace applications, thus quite expensive. The load resistor values are given in Table 5.4. A picture of the mounted resistors can be seen in Figure 5.79. To allow more flexibility in the UFS placement and to take into account the limited cable lengths to the UFS, not all front end simulator circuits are placed on one PCB in one big box. Instead three smaller boxes were designed, each box housing the simulator for one power group. To simulate a DAQ response, advantage is taken from the DAC on the UDR2. An AD7476 ADC is placed on the front end simulator to digitize the incoming DAC level from the UDR2. The control signals are converted from LVDS to LVTTL by LVDS receivers. The digitized value is clocked as LVDS signal back to the UDR2 and confirms the proper functionality of the DAQ. Figure 5.80 shows an open UFS-Box with the PCB for eight front end simulator circuits. Figure 5.81 demonstrates the linear relation between the UFS ADC reading and the UDR2 DAC setting. The same sequences as for the UFE boards can be used since only the ADC clock, and the H signals are used (Figure 5.15) and no HCC and Viking chip control is needed. The H signal defines the digitization time of the ADC and in fact is connected to the CS[1] input of the ADC.

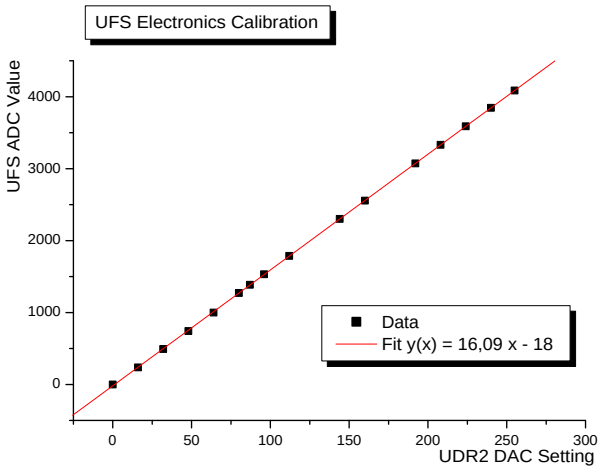

Figure 5.81: UFS ADC reading over DAC setting.

	Input [V]	$I_{circuit}$ [mA]	I_{target} [mA]	R [Ω]	I_{final} [mA]
1 UFE link	+2V	11	47	54 [27+27]	48
	-2V	11	82.6	27	85.1
2 UFE link	+2V	11	94	22.9 [27‖150]	98.4
	-2V	11	165.2	12.7 [10+2.7]	168.5

Table 5.4: UFS resistor values for I_{target} current consumption. $I_{circuit}$ is the power consumption of one UFS simulator circuit, which has to be considered for the final current consumption I_{final}.

[1]CS, chip select

5.11 Power Consumption and Weight

The exact knowledge of power consumption and weight of each subsystem is of utmost importance. Certain weight and power budgets are provided by NASA, which the experiment must adhere to. Each subsystem has to deliver correct values, in order to be able to determine the mass at lift-off and the power consumption onboard the ISS. Moreover, these values serve as input for thermal calculations of the subsystem and AMS-02. Again, this has impact on the mechanical design. As an example, the size of the DC/DC converter I-Frames is dependent on the power dissipation, since it has to be able to transfer all heat to the radiators. Figure 5.82 shows the total power consumption and the weight of the TRD electronics subsystem. As

U-Crate+UPD — **FLIGHT QTY=2**

Resp F Hauler — 10 Jul 05

Slot	Board	State	3,35	2,0	2,0	2,0	120	5,2	120	5,2	120	5,2	Heat	Mech	Wght
1	UDR2	1H1O	0,12	0,27									0,93	2,5	0,33
2	UPSFE	1H1C	0,04	0,77									1,68	2	0,35
3	UDR2	1H1O	0,12	0,27									0,93	2	0,33
4	UDR2	1H1O	0,12		0,27								0,93	2	0,33
5	UPSFE	1H1C	0,04		0,77								1,68	2	0,35
6	UDR2	1H1O	0,12		0,27								0,93	2,5	0,33
7	UDR2	1H1O	0,12			0,27							0,93	2	0,33
8	UPSFE	1H1C	0,04			0,72							1,57	2	0,35
9	UDR2	1H1O	0,12			0,27							0,93	2	0,33
10	JINF	1H1O	0,29										0,97	2	0,35
11	UHVG	1H1C	0,03				0,01	0,03					1,33	2,5	0,35
12	UHVG	1H1C	0,03				0,01	0,03					1,33	2	0,35
13	UHVG	1H1C	0,03						0,01	0,03			1,33	2	0,35
14	UHVG	1H1C	0,03						0,01	0,03			1,33	2	0,35
15	UHVG	1H1C	0,03								0,01	0,03	1,33	2	0,35
16	UHVG	1H1C	0,03								0,01	0,03	1,33	2,5	0,35
90	UBP	Passive												12	1,33
99	U Crate Mech	Passive												4	2,79
16	**Total Crate**		1,33	1,30	1,30	1,25	0,02	0,05	0,02	0,05	0,02	0,05	19,5	0	9,60
														0	
	UFE (4 units)			*1,38*	*1,38*	*1,28*							5,1		
			3,40	2,8	2,8	2,8	120	5,2	120	5,2	120	5,2			
			0,65	0,71	0,71	0,71	0,55	0,55	0,55	0,55	0,55	0,55			
0	59011AU (PD elec)	1H1C	0,10										0,34	C	0,10
1	59053U(+3,35)	1H1C	1,43										3,21	M	0,34
2	59048(+-2,8)	1H1C		1,97									2,30	M	0,26
3	59048(+-2,8)	1H1C			1,97								2,30	M	0,26
4	59011B (filter)	Passive												S	0,20
5	59048(+-2,8)	1H1C				1,87							2,14	M	0,26
6	59056(120,+5,2)	1H1C					0,02	0,05					2,00	M	0,26
7	59056(120,+5,2)	1H1C							0,02	0,05			2,00	M	0,26
8	59056(120,+5,2)	1H1C									0,02	0,05	2,00	M	0,26
90	UPD wiring	Passive													0,40
99	UPD mech	Passive													3,19
9	**Total xPD**												16,3		5,79

Note: 20 Layers=82 Modules, 64 wires/module,7 module per UDR2, UHVG
V= 2.0 means V= + - 2.0, etc.

Figure 5.82: TRD electronics flight design summary sheet.

calculated in this figure the power dissipation of two U-Crates amounts to 2×19.5 W and in the two UPD-Boxes 2×16.3 W are dissipated. Distributed around the Octagon, 82 front ends dissipate 16.2 W. The complete TRD electronics subsystem therefore consumes below 100 W.

The U-Crate is estimated to weigh about 9.60 kg and the UPD-Box 5.79 kg. A more detailed power calculation table can be found in Appendix Figure B.1.

5.12 Data Acquisition (DAQ)

As soon as trigger signals arrive, the DAQ is activated. This means that the UDR2 sends sequences to the front ends, where the incoming data in digitized and sent back. The UDR2 compresses the data by zero-subtraction in the DSP and buffers it until the JINFv2 requests the processed event. Before actually being able to process the event, the pedestals have to be known. The pedestal calculation is performed by a calibration routine. This calibration routine and the data compression routine are under subdetector responsibility. The DAQ framework in which the above mentioned routines are embedded is provided by MIT. The complete DAQ software is stored in the flash memory. Three copies of a basic program, called the *ROM monitor* and does not contain any of the subdetector specific routines, are stored in protected flash sectors. Each of the three is protected by a Frame Check Sequence (FCS), which is calculated using a 16-bit CRC algorithm. A boot loader loops over these three versions, checks the FCS and loads the first one which passed this test. If all three versions fail, majority logic is used to reconstruct a new ROM monitor out of the three available versions. This ROM monitor looks for a subdetector specific default program in the flash memory and loads it. If there is no default program, the ROM monitor keeps on running. These subdetector specific programs in the flash memory are not protected and can be overwritten. Section 6.3 offers more information about these routines and about DSP programming of the UDR2. The next two sections describe the DAQ communication with the U-Crate on an introductory base. More detailed information about ROM monitor and the flash file system can be found in [KK05].

5.12.1 AMSWire Commanding

AMSWire commanding to the U-Crate in the laboratory can be performed in different ways. Firstly there is a small interface box, which connects to the EPP[1]-Port of a PC. It provides four AMSWire links. The communication throughput is limited by the EPP communication speed of maximum 2 MBit/s. Another option is an AMSWire PCI card, which provides four links but can be upgraded to eight links. The data throughput is higher and is limited by the theoretical PCI communication speed of 133 MByte/s. This card requires Linux drivers to be operated. Due to the ease of operating, the EPP-Box is commonly preferred for hardware testing and testbeams. AMSWire represents a point to point communication. To address a node in the hierarchy a command is routed through different slave nodes to the slave destination node. The answer is routed back to the master. This procedure is reflected in the addressing scheme. Any address information is added in front of the actual command. The more routing slaves are between the master and the slave destination node, the more address information is added. As soon as an intermediate slave routes a command, the corresponding address information used by it is stripped and the next slave just sees the next address information dedicated to him. To address any AMSWire node directly the address identifier `2E` is placed before the actual command. `2E` means that the destination address is the node itself. As an example, to request an event from a JINFv2 node, the command would be used:

[1] EPP, Enhanced Parallel Port

`2E01 - get event`

If it is necessary to talk to the UDR2 node through a JINFv2 directly as an intermediate node in between, further address identifiers are required. Four bytes containing the slave ID and the port ID have to be added in front of the command. The slave ID may be any of the 24 possible links a CDDC in the JINFv2 provides. The port ID nominates the port to be used and may be 0 or 1. Any other value means that any port can be used. To request an event from a UDR2 board on link 4 through a JINF board, with any port to be used, the command would be:

`043f 2E01 - get event on link 4 using any port`,

where 3f has been chosen as "don't care" value. Each reply is protected by a frame check sequence using CRC algorithm. The most important commands are given in Table 5.5. Apart from this simple addressing scheme there are group addressing commands which may or may not require the definition of mask IDs. More information can be found in [KK05].

Category	HEX code	Request
General	0x40	Boot
	0x01	Read Event
	0x02	Read Last Event Number
	0x42	Reset Event FIFO
	0x0C	Read Node Status
	0x0D	Ping
	0x4E	Enter Power Down State
DAQ control	0x52	Set Processing Mode
	0x12	Read Processing Mode
	0x53	Perform Calibration
	0x13	Read Calibration Results
	0x54	Execute SD Proc. Results
	0x14	Read SD Proc. Results
Flash	0x45	Write FLASH file
	0x05	Read FLASH file
	0x06	Test FLASH file
	0x46	Load FLASH file
	0x47	Erase FLASH file/sector
	0x07	Read FLASH summary
	0x48	Write file attribute
I/O	0x10	Read Program Memory
	0x50	Write Program Memory
	0x11	Read Data Memory
	0x51	Write Data Memory
Test	0x55	Program Test
	0x56	Slave Test
	0x16	Read Slave Test Results

Table 5.5: Shorted list of AMSWire commands. Some commands require appended parameters. From [KK05].

5.12.2 Control GUI

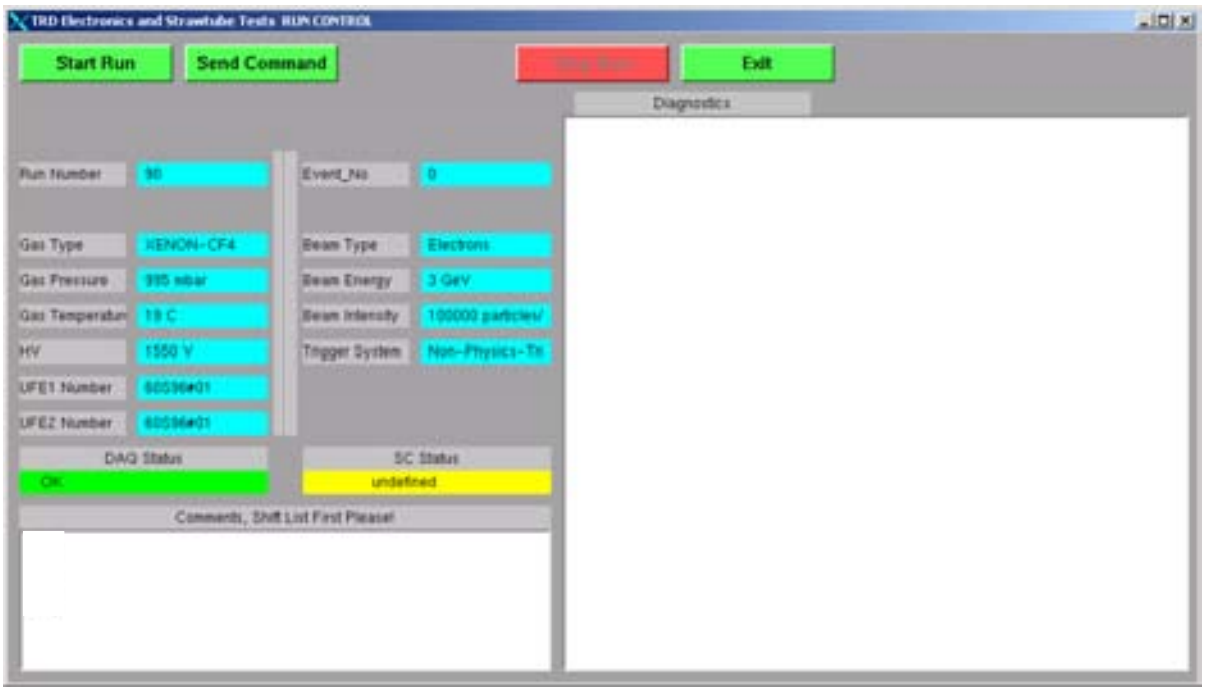

Figure 5.83: Screenshot of Runcontrol GUI.

Figure 5.83 shows a screenshot of the RUNCONTROL GUI, which was created to facilitate the commanding of UDR2 nodes during a testbeam. Simple commands like `get event`, or `Perform Pedestal Calibration` can be executed, without the actual knowledge of the composition of AMSWire commands. It provides certain logging options such as temperature, gas type, gas pressure, beam type and beam energy. On request a certain amount of events can be read out.
Runcontrol was written in the programming language QT[1]. It interfaces to a command shell program named PCAMSW which accesses the EPP-Box via the parallel port. Since this GUI was dedicated for testbeam usage to control a maximum of one UDR2, efforts are ongoing to develop a more flexible GUI which is able to control the UDR2s and the JINFv2 of a full crate.

5.13 Slow Control

The term *slow control* refers to all procedures which are not directly associated to data acquisition. This term particularly describes tasks which are needed to configure the system to perform data acquisition, to gather information which could be of importance for data analysis and which describes the health of the system. In the case of the TRD DAQ electronics, this is

- *HV control and readout*
  Before the start of data taking, 82 high voltage channels have to be ramped and parameters such as HV current and measured HV voltage have to be logged. While HV current

[1]QT by Trolltech, Norway. C++ application framework.

offers certain information about the health of the UHVG modules and straw tubes and indicate possible corona discharge problems, measured HV voltage is essential for data analysis since the gas gain strongly depends on the applied high voltage. High voltage control is performed via Lecroy bus communication between the JINFv2 and UHVGs.

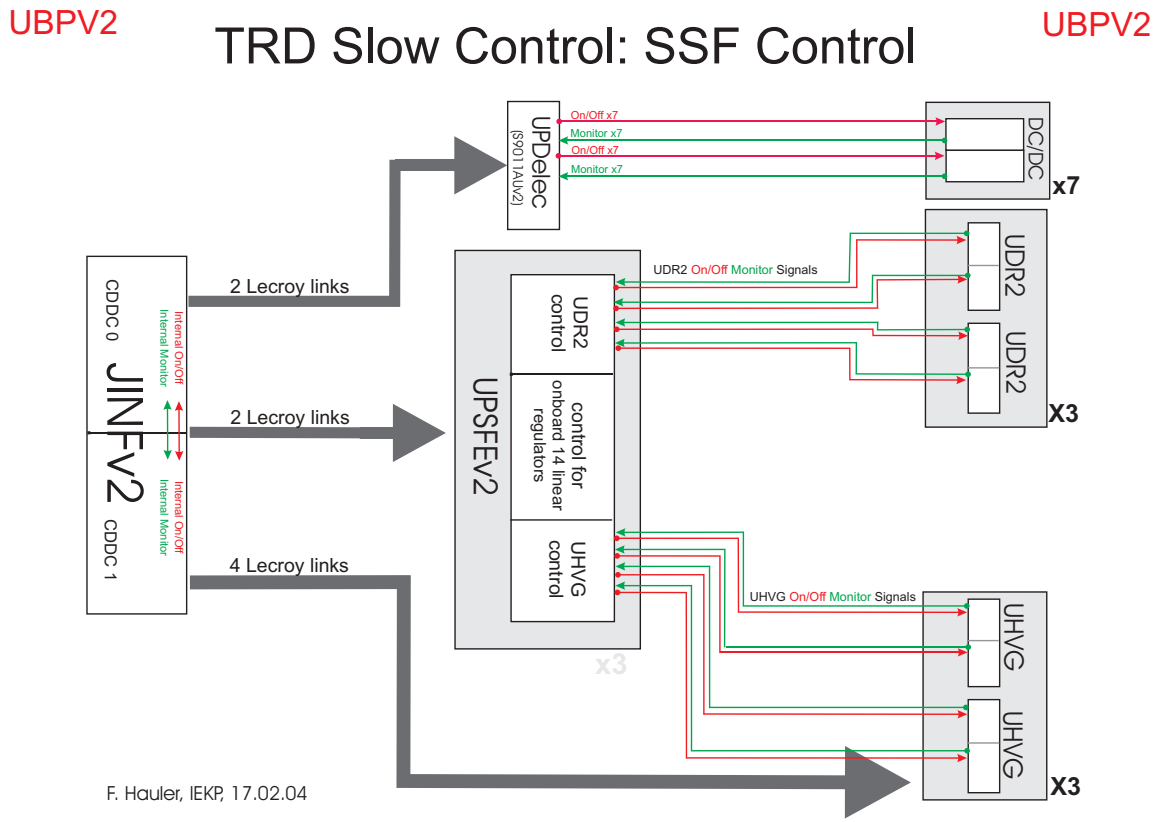

Figure 5.84: Overview of slow control communication links.

- *Redundancy control*
  To safe power, redundant hardware will be switched off using the onboard solid state fuses. The DC/DC converters are controlled by the S9011AUv2, which is addressed by the JINFv2 via Lecroy buses. The UDR2 and the UHVG solid state fuses are controlled by the UPSFEv2, which is also accessed by the JINFv2 via Lecroy buses.

Figure 5.84 summarizes the Lecroy bus slow control links to the UHVGs, S9011AUv2s and UPSFEv2s. The Lecroy protocol is described in the next subsection.

5.13.1 The Lecroy Protocol

Data on the Lecroy buses is transmitted by a clock line and a data line. The Lecroy buses use master slave architecture. The clock line is always clocked by the master. The data line can be accessed by both master and slave. In the U-Crate the Lecroy master is the JINFv2. The UPSFEv2, S9011AUv2 and UHVG boards act as slaves. Figure 5.85 describes the bit order of a typical Lecroy transaction. The complete Lecroy transaction comprises 64 bit. The first 32

Header Frame [16 bit]							DATA Frame [16 bit]	Echo Header Frame [16 bit]							Reply Data Frame [16 bit]
1	Parity	Power	Broadcast	ADR[8]	Write/Read	Register[3]	DATA[16]	0	Echo Parity	Echo Power	Echo Broadcast	Echo ADR[8]	Echo Write/Read	Echo Register[3]	DATA[16]
1	0	1	0	00110000	0	010	0000 0000 0000 0000	0	0	1	0	00110000	0	010	0000 0000 0000 0001

Figure 5.85: Lecroy command bit order.

bits represent the actual command, subdivided into a 16-bit header frame and a 16-bit data frame. It starts with the bit '1' followed by the parity bit and a broadcast bit. The broadcast bit causes all slaves on the bus to execute the command sent. The next eight bits are used to address the slaves. Write/Read defines whether the command writes to or reads from the registers. The following three bits provide the register address. This is followed by 16 bits of data. The last 32 bits represent the answer from the slave. It starts with the bit '0' and transmits the original header frame back to the master. The final 16 bits represent the actual answer int the reply data frame.

5.13.2 Slow Control Commanding

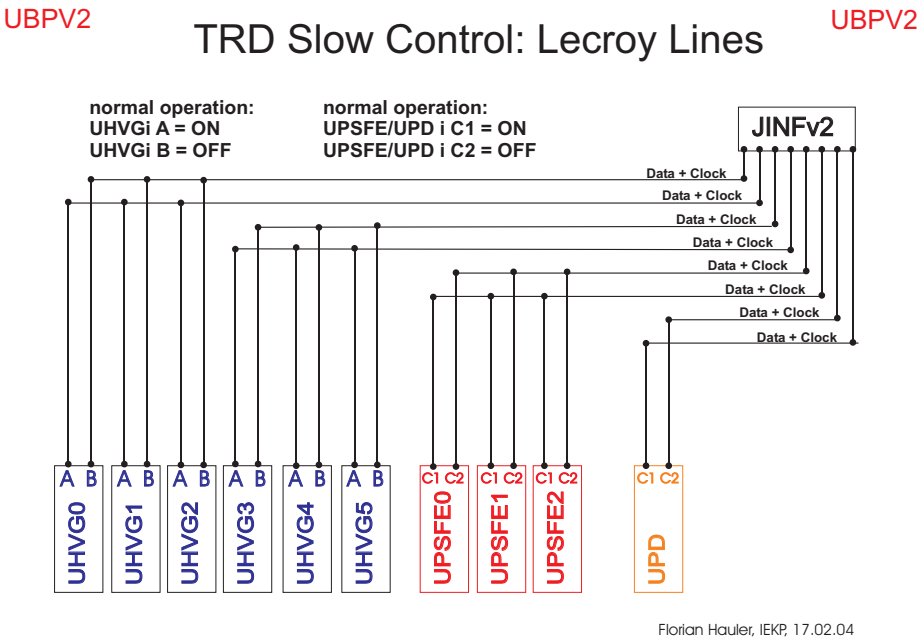

Figure 5.86: Lecroy line distribution between JINFv2 and UHVG, UPSFEv2 and S9011AUv2.

Figure 5.86 describes the routing of the Lecroy lines in the U-Crate and UPD-Box. There are eight Lecroy links, each composed of a DATA and a CLOCK line. Both signals are driven by MLVDS drivers and receivers[1]. There are eight Lecroy links. Four links are used to communi-

[1]except of UHVG, which still uses point-to-point LVDS drivers at QM2 level. A change to multi-point drivers for the flight modules is under evaluation.

cate with six UHVGs: two links for three UHVGs. One of these two links communicates with one half of Lecroy chips mounted on the three UHVGs. Two other Lecroy links are routed to three UPSFEs. Again, one link communicates with one control half of the three UPSFEs. The last two links are routed by twisted pair cable to the S9011AUv2 in the UPD-Box: one link for one S9011AUv2 control half. The JINFv2 receives slow control commands by AMSWire. It has to strip the Lecroy information from an AMSWire command and redirect it to the correct Lecroy link. Two AMSWire slow control commands are existing:

Lecroy Write: `2E5D - initializes the Lecroy link`
Lecroy Read: `2E1D - writes or reads registers from Lecroy slaves`

For both commands the information containing the Lecroy link has to be appended. The correct syntax for the first 32 command bits is therefore:

```
2E1D B000 HHHH DDDD ,
```

where `B` is the bus link, `HHHH` the 16 bit of the header frame, followed by the 16 bits of the data frame. The answer is clocked immediately back as the following 32 bit.
As an example we read out one of the DC/DC converter status registers. We address the first control part of the UPD, which is placed on Lecroy bus 3 with the Lecroy slave address 3 and the register address 010 bin. The correct command is therefore:

```
2E1D 3000 A302 0000
```

The bit order of this Lecroy communication is displayed in detail in the lower line of Figure 5.85. The answer is simply "1", meaning that the first DC/DC converter is switched off, the other ones are on.

5.13.3 Slow Control Features

While the features and therefore the registers of the UHVG Lecroy chips are fixed and cannot be changed, the control features of UPSFEv2 and S9011AUv2 had still to be designed under responsibility of the Universität Karlsruhe. The firmware for the UPSFEv2 contains registers to control all its 14 linear regulators, the two UHVGs, two UDR2s and its redundant brother Actel FPGA. Furthermore, it can read back their status lines coming back from the controlled hardware. By monitoring these lines it is able to detect trips and remembers them in trip count registers. As a feature which is normally switched off but can be activated any time, trip thresholds can be activated, which define the amount of allowed trips before the hardware is supposed to be switched off permanently until the trip counters are reset. The S9011AUv2 basically has similar features, although the hardware to be controlled is different. This board controls and monitors the seven DC/DC converters and its brother Actel FPGA. A detailed description of the slow control features implemented in the firmware of S9011AUv2 and UPSFEv2 can be found in [Jun05]. Since setting, reading out and interpreting firmware registers manually by command line software can be quite cumbersome, a first GUI[1] control software for the TRD electronics, written in Xforms[2], was provided by MIT. Figures 5.87, 5.88, 5.89 show

[1] GUI, Graphical User Interface
[2] Xforms, Graphical User Interface toolkit for X

the GUIs to control UHVG, UPSFEv2 and S9011AUv2. The board to be controlled is chosen by the setting in the upper left corner. Then, Lecroy buses and board addresses are completed automatically. All GUIs provide a simple push-button interface allowing to set and read out every register.

Figure 5.87: Screenshot of S9011AU commander.

Figure 5.88: Screenshot of UHVG commander

Figure 5.89: Screenshot of UPSFE commander.

Chapter 6

Working with the U System: Testbeams, Cosmics and DSP Programming

This chapter begins with an overview about the two testbeams that were conducted in 2002 and 2003 within the framework of this thesis. One section describes a cosmics stand which was built up at IEKP in Karlsruhe. These tests were performed to verify the proper functionality in physics data taking. The chapter ends with a description of the DSP data reduction code and the calibration code written in assembler.

6.1 Testbeams at CERN, East Area, T9

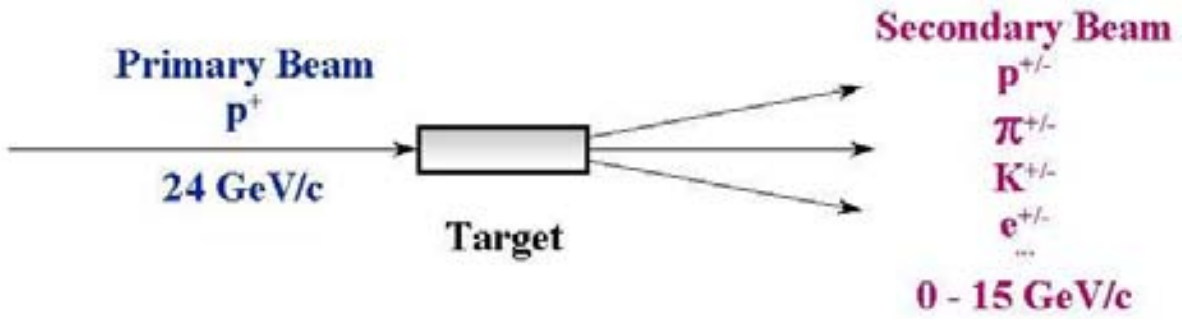

Figure 6.1: CERN T9 beam. A primary proton beam hits a target, where the particles for the secondary beam are created.

The two testbeams took place at CERN, East Area, T9 irradiation facility. The beam is composed of secondary particles created during the interaction of the primary CERN PS[1] 24 GeV/c beam on an exchangeable fixed target (see Figure 6.1). The secondary beam consists mainly of protons, π^+, π^-, K^+, K^- at 0 to 15 GeV/c. To increase the electron yield special targets are available.
Secondary beam control and particle selection has to be done by the user. Dipole magnets are used to select positive and negative particles, to define the desired momentum and to control the beam location. Quadrupole magnets are used to define the beam focus. Collimators are available to limit the size and intensity of the beam. Also, there are MWPCs[2] which can be used to monitor the beam location in order to steer the beam. Cherenkov counters were used for particle identification.

[1] PS, Proton Synchrotron
[2] MWPC, Multi Wire Proportional Chamber

6.1.1 Testbeam 2002

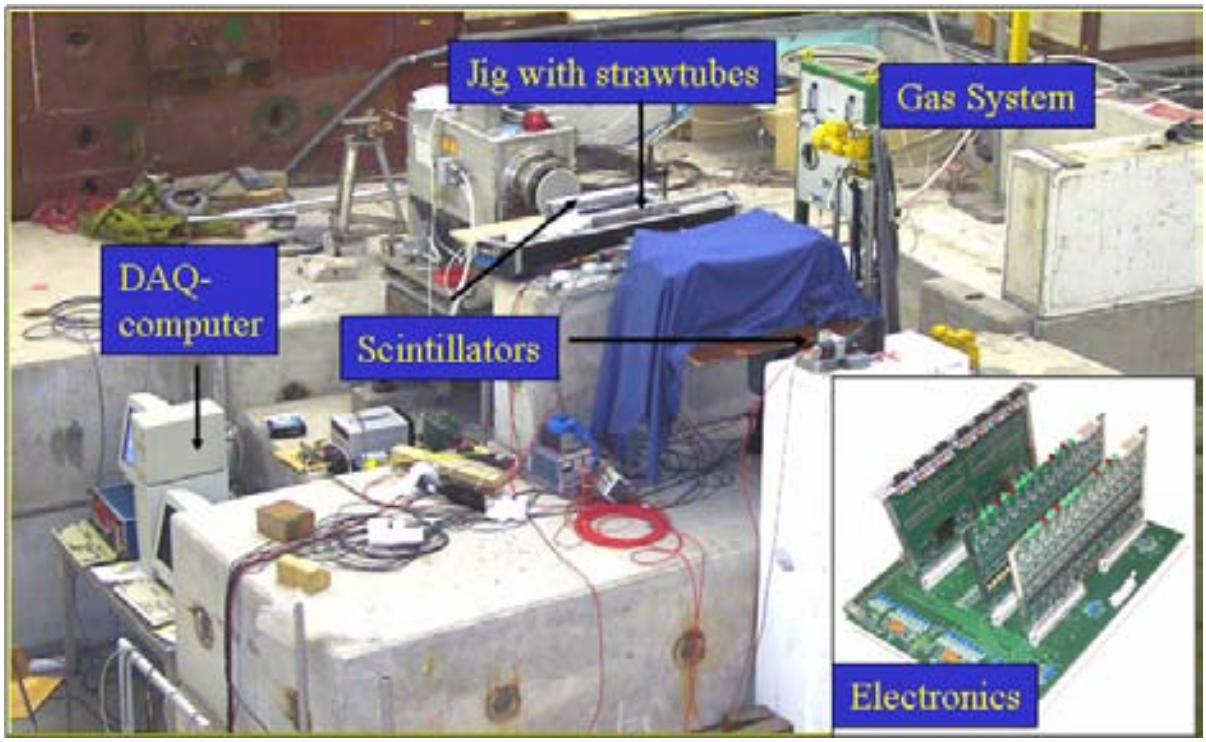

Figure 6.2: Testbeam 2002 arrangement.

The testbeam in 2002 served as the first test for U-Crate electronics. An EM UDR2 together with two EM UPSFE boards on the EM test backplane were used. Since at that time no UHVG was available, the detector was biased with a custom high voltage power supply. A DAQ PC was placed in the beam area and remote controlled over network. Figure 6.2 gives an overview about the testbeam arrangement. Scintillation detectors were placed in front of and behind the 4-layer straw tube jig. Cherenkov counters were located upstream. The trigger electronics was placed outside the beam area. From the electronics point of view the testbeam was a full success. Moreover, the physics data could be used to clarify another issue. At that time, during straw tube production at RWTH Aachen the problem arose, that a very high quantity of straw tube modules were leaky. This was unacceptable since the amount of gas that can be taken to the ISS is limited. The problem was faced by applying additional 10 μm of Parylene-C coating, which was supposed to seal the leaky tubes. To verify that the new straw tube layout could be correctly described by GEANT3[1] software, Parylene-C coated prototypes were used in this testbeam. Figure 6.3 shows the γ attenuation length of Parylene-C compared to Polyimide and the comparison of the GEANT 3 simulation to the taken data. Obviously, the GEANT simulation describes the testbeam data well. However, after some time it turned out that even the Parylene-C coated straw tubes became leaky and this idea was discarded. Later the problem was solved by performing single straw tube tests to select only the most gastight ones for module production.

[1]GEANT, Detector Description and Simulation Tool

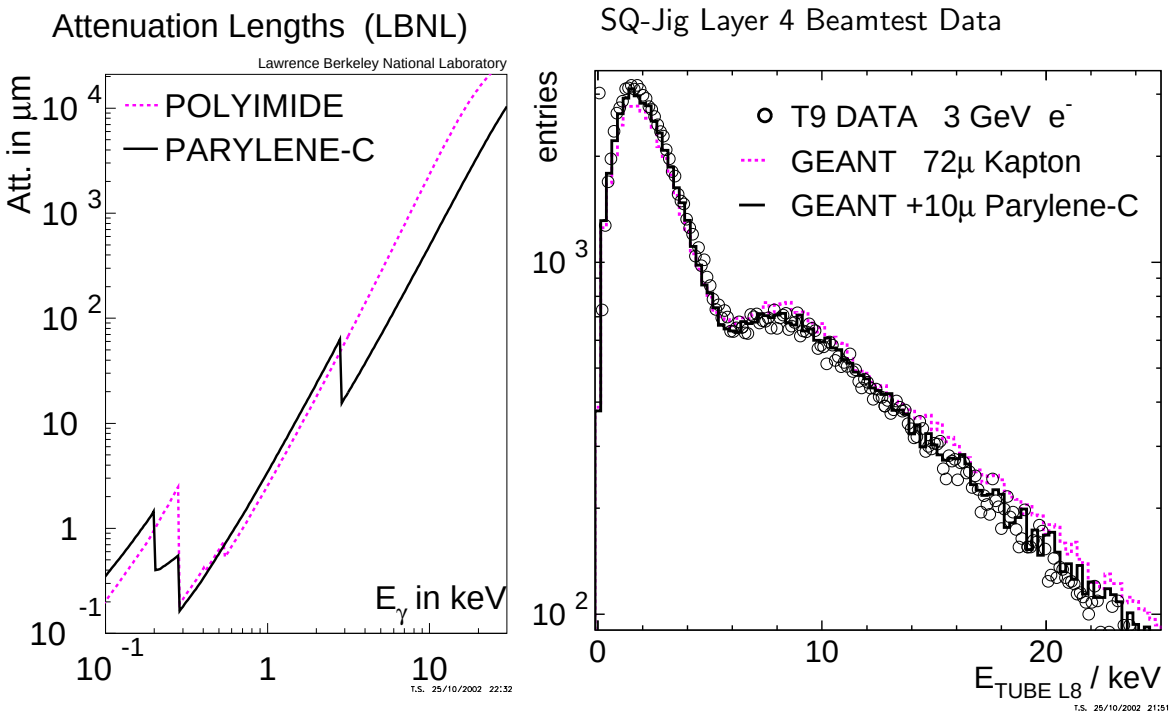

Figure 6.3: Attenuation length of Polyimide and Parylene-C (left). Comparison between data and GEANT3 simulation (right). From [Kir02].

6.1.2 Testbeam 2003

One year later, after the EM to QM1 transition the need emerged to verify the QM1 electronics on system level. This testbeam was performed again with the cooperation of RWTH Aachen. The first pre-weight reduction UBP was available which was equipped with two USCMs, one UHVG, two UPSFEs, one UDR2 and one JINF. For comparison and as a backup, the QM1 test backplane was used to power UPSFE and UDR2. All in all the electronics worked properly, although minor bugs were identified and corrected. The test beam was a success, demonstrating the proper operation of all the boards. The arrangement is shown in Figure 6.4. Again two main scintillation detectors were placed in front of and behind the 4-layer straw tube jig. Two crossed finger scintillation detectors were used to define the correct beam window. For particle identification two Cherenkov detectors upstream were used. A remote controlled DAQ PC was present in the beam area. Trigger electronics were located outside. Two gas mixtures were available: Ar/CO_2 (80/20) and Xe/CO_2 (80/20).
For the following plots only *clean* tracks were used. A straight line fit through at least three tubes that showed a 3σ excess was used to define such a clean track, as illustrated in Figure 6.5. The test beam started with a delay scan of the trigger electronics: a delay unit was inserted into the trigger timing. This delay scan is necessary since the front ends require a peaking time of 2.4 μs and the lengths of all the cabling in the beam area were unknown.
The *Most Probable Value* (MPV) was determined by fitting a Landau distribution to the histogram data. Depending on the peaking time, which reflects basically the charging of an internal capacitor of the Viking chip, this MPV moves to higher ADC values or to lower, in this way modifying the *visible* deposited energy in the detector. All MPVs were corrected for

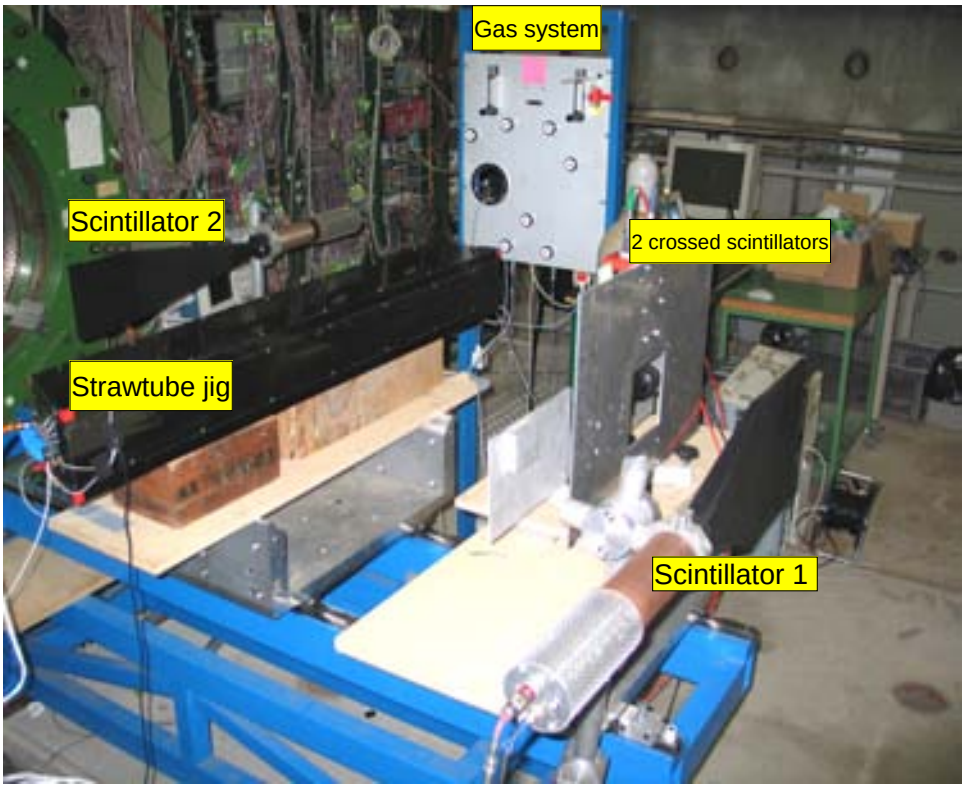

Figure 6.4: Testbeam 2003 arrangement.

gas gain variations. This procedure is described in more detail in the next section. Figure 6.6 shows the result of the delay scan. The peak is observed around 2.0 - 2.1 μs, which yields that the cabling delay in the beam area amounted to about 0.3 - 0.4 μs.
When comparing the amount of hits in the straw tubes to the neighboring ones, the beam profile becomes visible. Figure 6.7 and Figure 6.8 show the beam profile for the proton and electron runs, respectively. The change of beam location is due to the forced reconfiguration of the magnets when switching from positive to negative beam. It is observable that both, electron and positron beam, have a small asymmetric intensity distribution.

Figure 6.9 shows the difference in the single straw energy deposition histogram between a 12 GeV proton run and a 3 GeV electron run. Clearly observable is the additional energy deposition of the transition radiation photons in addition to the energy deposition due to primary particle ionization in the gas (dE/dx).

Figure 6.10 shows the variation in shape of the normalized energy deposition histograms over applied voltage at a 3 GeV electron run. With increasing voltage the gas gain rises. Therefore, the entries are pushed to higher ADC values.

Figure 6.11 plots the most probable values measured from the voltage scans of 3 GeV protons using Ar/CO_2 and of 3 GeV electrons and 15 GeV protons using Xe/CO_2. In this plot, the units of the vertical axis have been recalibrated into charge units since for the UFE boards the following relation is valid: $1\ fC\ =\ 2\ ADC\ counts$. Nicely observable is the different gas gain

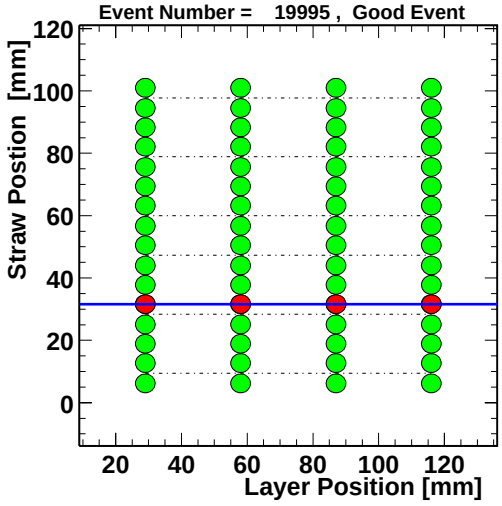

Figure 6.5: Good event definition. At least three hits on track were required for the analysis. [Chu05].

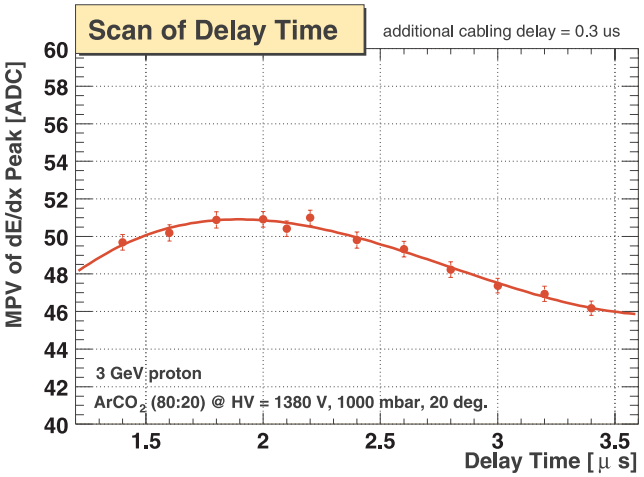

Figure 6.6: Delay scan to set the additional trigger delay. The polynomial red line serves to emphasize the slope of the data points. [Chu05]

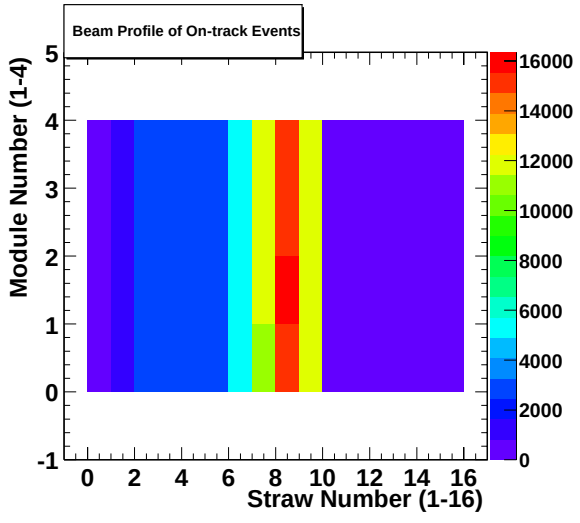

Figure 6.7: Beam profile during proton runs. [Chu05]

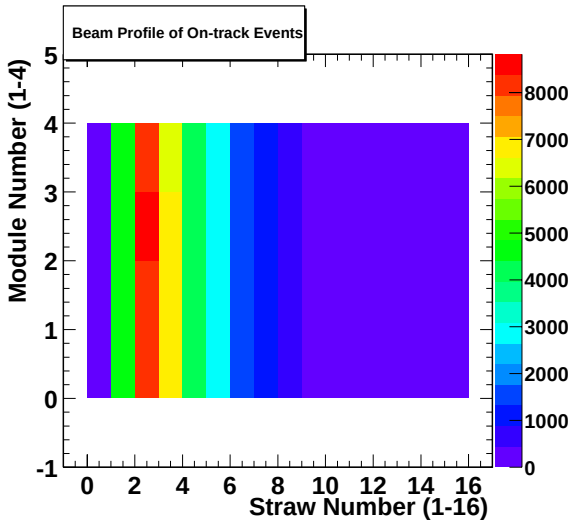

Figure 6.8: Beam profile during electron runs. [Chu05]

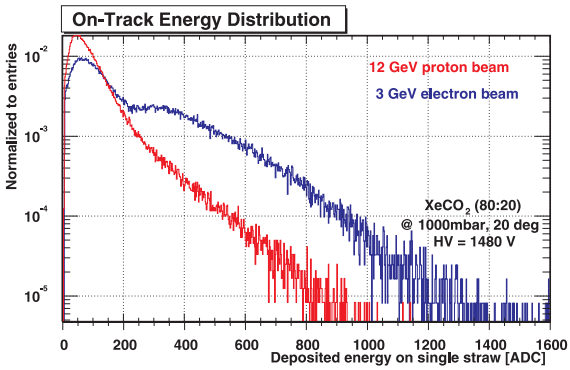

Figure 6.9: Normalized histogram of an electron and proton run. [Chu05]

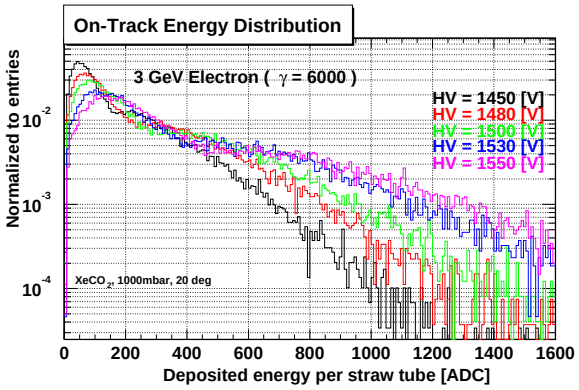

Figure 6.10: Voltage scan during electron runs. [Chu05]

of Ar/CO_2 and Xe/CO_2 resulting from the different gas density. The higher density of Xe/CO_2 causes a lower gas gain, since at a certain voltage the mean free path of the electrons between collisions is reduced and therefore, a lower percentage of electrons gains enough energy from the electric field to ionize further gas atoms and to create more electrons by the avalanche effect. The advantage of the higher density of Xe/CO_2 is the higher photoabsorption probability. Finally Figure 6.12 demonstrates the signal to noise ratio at a 15 GeV proton run over different voltages. With these results the data taking capability and the ability of the UHVG board

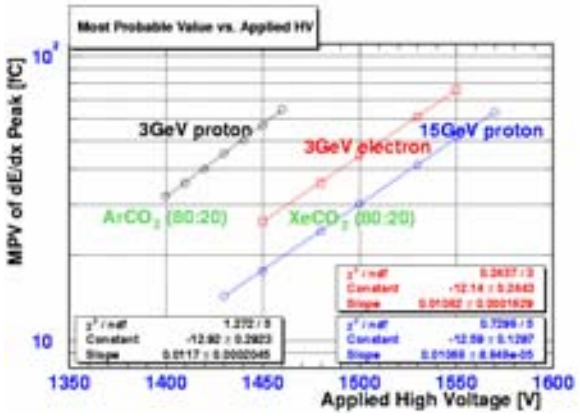

Figure 6.11: Most Probable Value (MPV) in UFE charge units over voltage. [Chu05]

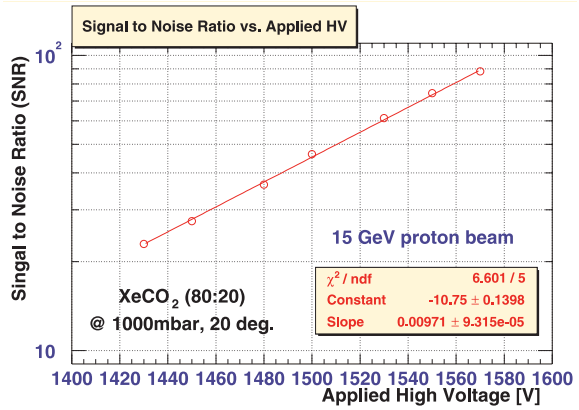

Figure 6.12: Signal to noise ratio over voltage. [Chu05]

to provide stable high voltage at room temperature to the straw tube modules was proven at QM1 level.

6.2 Cosmics

A cosmic test stand was set up at IEKP, Universität Karlsruhe to further test the TRD electronics and to get experience with the system. The next subsections describe the setup, the necessity to correct the gas amplification for temperature and pressure variations[1], the deter-

[1] as was already done in the testbeam analysis previously described

mination of the correct delay timing, a voltage scan and a rough energy calibration by means of an Fe^{55}-source.

6.2.1 Setup

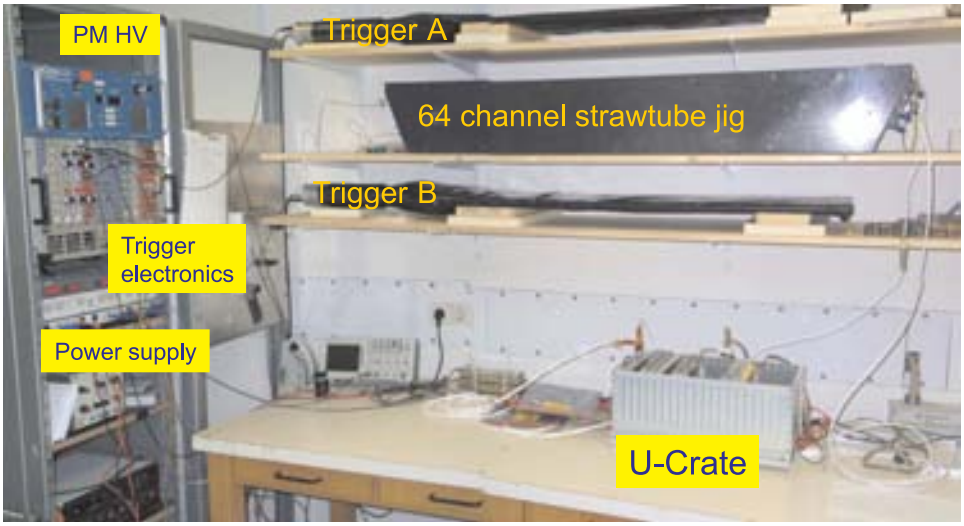

Figure 6.13: Cosmics test stand. This test stand was operated with the U-Crate, the UPD-Box (not visible) and a two layer trigger system. A third trigger layer based on Avalanche Photo Diode (APD) technology on top of trigger layer B was added later.

Figure 6.13 shows the cosmics setup. A 64 channel straw tube jig, provided by RWTH Aachen, was used as detector. The fleece radiator layers were removed, therefore only the energy deposition due to dE/dx and no transition radiation was measured. The gas to be used for the proportional straw tubes was premixed Ar/CO_2 (80/20). Gas temperature and pressure monitoring was available using a Keithley 2000 device, based on an automatic readout via GPIB[1] and a QT software on a Linux operating system. The trigger system was set up using custom NIM[2] electronics. In the beginning two scintillation layers were available connected in coincidence (Trigger A and B). Later the system was enhanced with a third trigger layer (Trigger C) based on Avalanche Photo Diode (APD) technology placed between the straw tube jig and Trigger B. The complete electronics setup used for cosmics data taking plus the 3 UFS-Boxes is shown in Figure 6.14. As shown in Figure 6.15, an online monitor was developed, that displays a 3-D Open-GL image of the 64 straw tubes. Hits are visualized with a color coding depending on the height of the ADC counts.

6.2.2 Temperature and Pressure Correction of the Argon/CO_2 Mixture

The gas amplification is strongly depending on temperature and pressure variations. Consequently the data taken has to be corrected. A theoretical description of the gas amplification and the derivation of the Diethorn formula was given in Section 4.4. Figure 6.16 shows the Diethorn plot for an Ar/CO_2 (82/18) gas mixture, prepared by RWTH Aachen. From this plot,

[1] GPIB, General Purpose Interface Bus, IEEE-488.2
[2] NIM, Nuclear Instrumentation Module

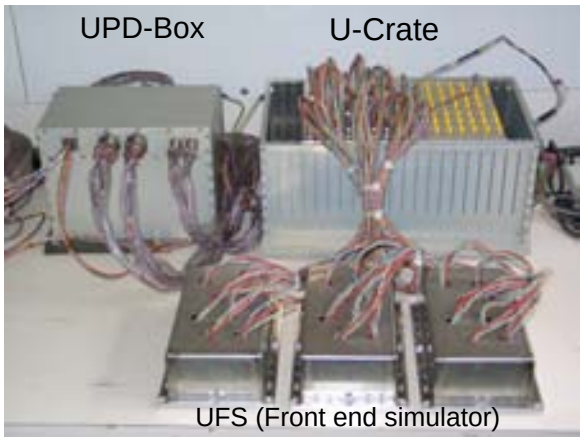

Figure 6.14: Complete TRD electronics setup consisting of the U-Crate, the UPD-Box and three UFS-Boxes.

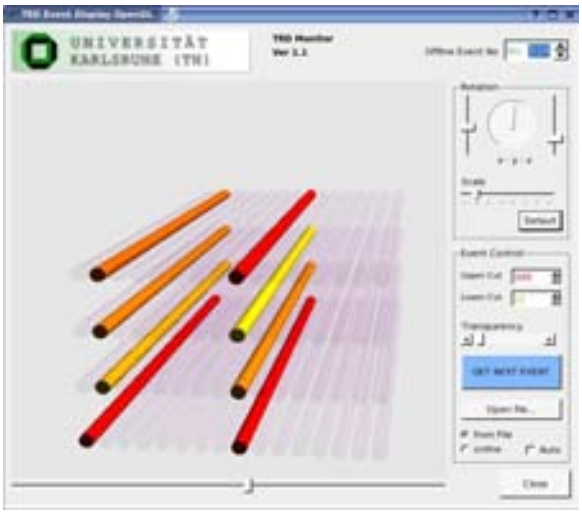

Figure 6.15: Four layer double event visualized by the TRD online monitor.

the Diethorn parameters ΔV and E_{min} can be derived by fitting. Using these parameters, the gas gain for this gas mixture can be plotted against the bias voltage as shown in Figure 6.17. Since this gas mixture is similar[1] to the one which was used in the cosmics test stand, these Diethorn parameters were used for temperature and pressure corrections:

$$\Delta V = 26.88\ V \tag{6.1}$$

$$E_{min} = 45.09\ kV/cm \tag{6.2}$$

All measurements were corrected to gas standard conditions of $T_0 = 20°C$ and $p_0 = 1013$ mbar

[1]This Diethorn measurement was performed using a self-triggered readout using an Fe^{55} source. Since such a readout is not available at Karlsruhe, this measurement from RWTH Aachen had to be used.

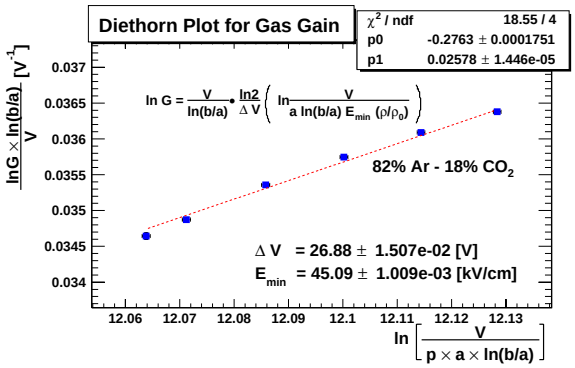

Figure 6.16: Diethorn plot for Ar/CO_2 (82/18). From [Chu05].

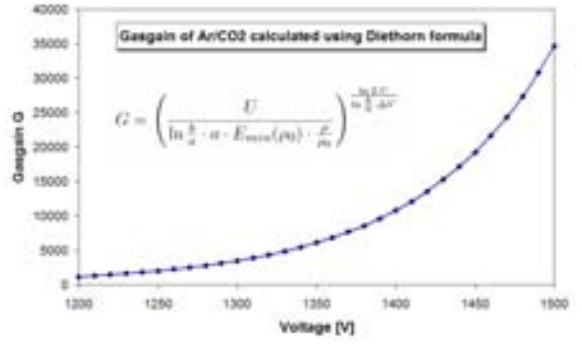

Figure 6.17: Calculated gas gain from Diethorn formula using parameters from Figure 6.16.

with a gas amplification G_0 according to

$$ADC_{corr} = ADC \frac{G_0}{G(T,p)} \tag{6.3}$$

at the voltage under consideration.

6.2.3 JINFv2 Delay Scan

On a custom cosmics test stand usually a timing unit has to be used to adjust the trigger timing to the Viking peaking time of about 2.4 μs. The TRD electronics features a tunable delay onboard the JINFv2, which is able to delay the trigger signal according to a setting between 0x00 hex and 0xff hex (0 to 256 decimal). A first test run was made to determine this optimal setting.
The analysis software to be used was the same one as in testbeam 2003. Hits were identified if they showed a 3σ excess above the pedestal. Only clean tracks were used further on in the event analysis with the following constraints:

- no multiple hits in one layer
- minimum 3 hits on a fitted straight line in 4 layers.
- no hits off-road, that means beyond the physical dimension of the straw tubes lying on the straight line.

From the remaining events, the measured energy deposition of each single straw was inserted in a histogram and the most probable value was determined with a Landau fit. An example histogram is given in Figure 6.18.
The optimum setting was determined in Figure 6.19 to be 0x70 hex. This delay in addition to a negligible delay in the ns range due to the cabling of the cosmics stand yields the total delay request of 2.4 μs.

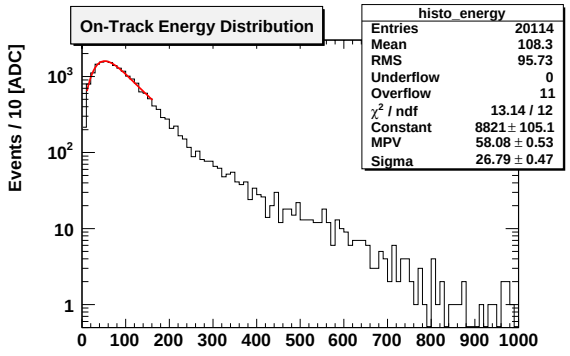

Figure 6.18: Single straw on-track Energy distribution at 1370 V. Determination of the MPV by Landau fit.

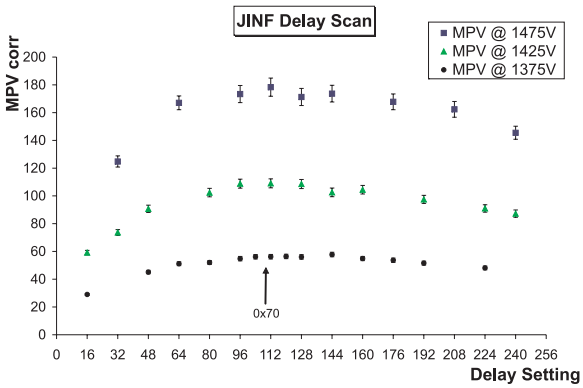

Figure 6.19: JINFv2 delay scan using physics. MPVs were determined from Landau fits.

6.2.4 Voltage Scan

Figure 6.20 shows the MPV dependence on the bias voltage. The corrected data for temperature and pressure variations is drawn in solid boxes, the uncorrected data is drawn in open circles. An extrapolated line using Diethorn's formula, normalized on the lowest ADC value shows the theoretical expectation. It is clearly visible, that the corrected data points lie much closer on this line than the uncorrected ones.
The tracking efficiency can be defined as the ratio of accepted events over total events:

$$Eff = \frac{accepted\ events}{total\ events}. \tag{6.4}$$

As can be seen in Figure 6.21, it is depending on the bias voltage and therefore on the gas gain. The lower the bias voltage, the smaller the ADC signal gets and the more it is likely that the energy deposition falls below the 3σ tracking constraint. On the other hand, a higher bias voltage than the optimum causes more straw tubes to show a signal slightly above 3σ so that an increased number of events does not pass the tracking constraints. Using the gas mixture Ar/CO_2 (80/20) together with this basic analysis approach, it can be seen that the optimum gas gain factor is approximately 3000. Evidently, the efficiency measurement depends on the analysis software to be used. It is planned that finally the TRD in space will be operated with a Xe/CO_2 gas admixture at a gas gain of about 3000.

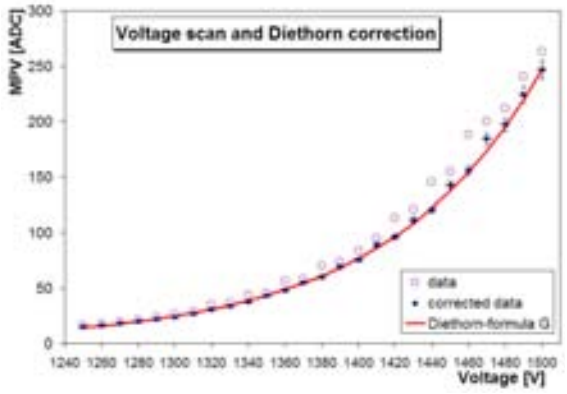

Figure 6.20: Cosmics voltage scan. Uncorrected and temperature/pressure corrected data. The Diethorn expectation is drawn as solid line.

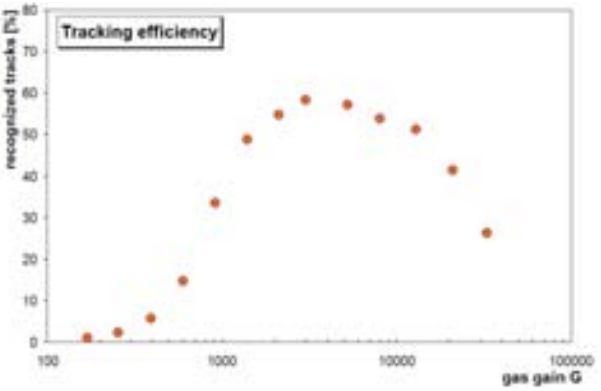

Figure 6.21: Tracking efficiency at different gas gains.

6.2.5 Fe^{55} Energy Calibration

Up to now, all measurements were presented in terms of MPVs in ADC count units. In order to explicitly relate an ADC count to the real energy deposition in the straw tubes, measured by the UFE ADC, an energy calibration is required. A good approach is to apply a photon source with a well-defined energy to the detector. The photons release their complete energy to the detector gas by the photoelectric effect, thus freeing electrons. These are accelerated towards the anode wire through the electric field created by the bias voltage, on their way ionizing gas atoms and therefore liberating more electrons by the avalanche effect. Since the electrons

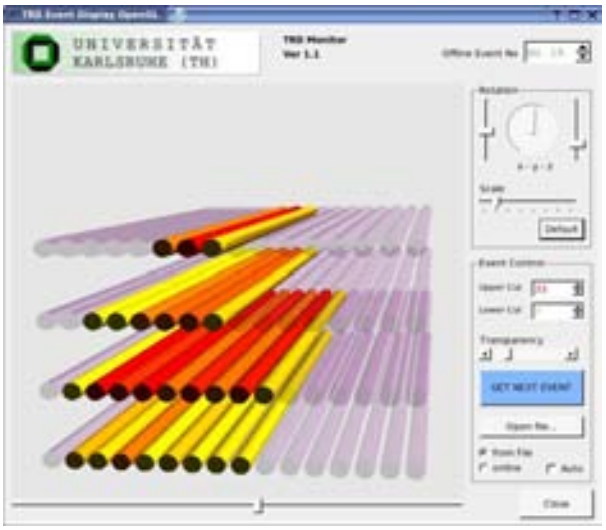

Figure 6.22: Fe^{55} source radiation profile, averaged and visualized by a modified version of the TRD online monitor.

traveling through the electric field cause the voltage drop on the UTE bias resistors which is measured by the ADC, the amount of electrons and therefore the gas gain is a major factor in this energy calibration. As a consequence the energy calibration is given as a function of gas gain.
Unfortunately this approach is not applicable without any problems. It is not possible to trigger on photons by means of scintillator detectors as used in the cosmics stand, since upon detection through the photoelectric effect, the photon disappeared and therefore cannot be detected in a straw tube any more. Principally this problem can be avoided by using a self-triggered readout chip, but the Viking chip VA32HDR12 on the UFE boards does not feature a self-triggered mode.
Nevertheless, a rough calibration can be done even with a random readout, when applying a source with a well-defined photon energy, such as an Fe^{55} source. The well-defined Fe^{55} γ-radiation of 5.9 keV (24%) originates from a K-shell electron capture:

$$Fe^{55} + e^{-} \rightarrow Mn^{55} + \nu \tag{6.5}$$

The radiation profile of the Fe^{55} source can be recognized using the averaged mode of the TRD online monitor as shown in Figure 6.22. From the technical point of view, using random readout means that one has to take into account that the photons almost never fall exactly into the peaking time of the Viking chip. Most of them are detected either before or after the peaking time and therefore their signals suffer degradation. Looking on the single straw energy deposition histogram as shown in Figure 6.23, a continuum of entries up to an edge which corresponds to the maximum energy, can be recognized. Solely the photons at maximum energy fall into the peaking time. The measured energy value corresponds to the non-degraded 5.9 keV energy deposition. From that, taking into account the energy resolution of the detector, the calibration can be performed.
Normally one would choose a strong Fe^{55} source and randomly read out as fast as possible in order to quickly obtain data. Unfortunately the UFE pedestal is not stable at a very high particle flux, but is smeared against lower ADC counts, since it was designed for a flux of

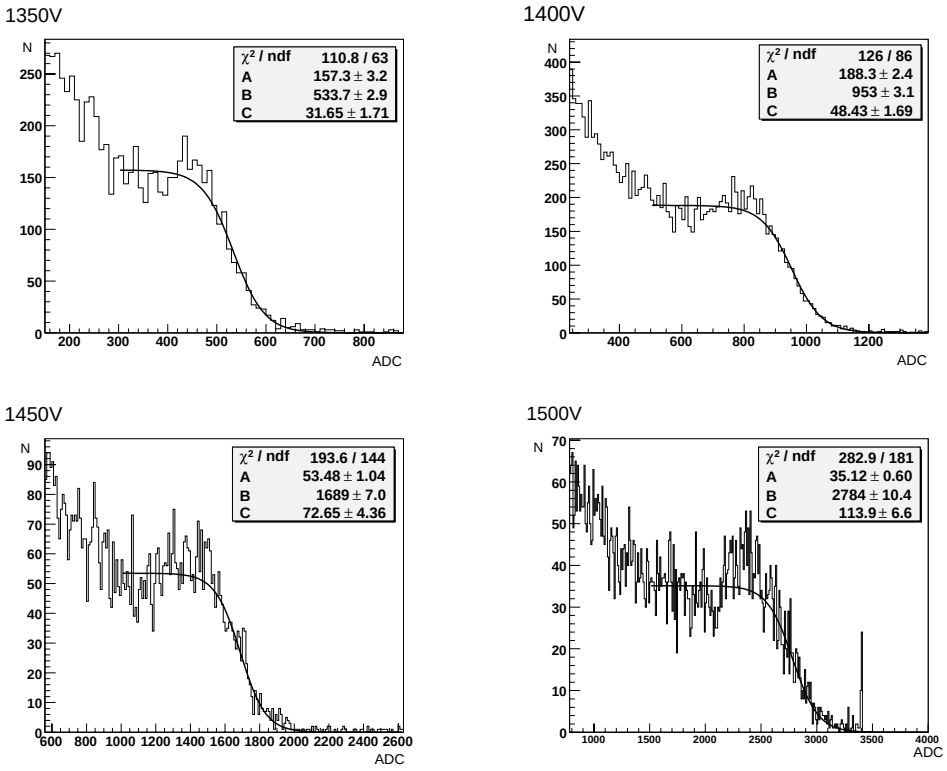

Figure 6.23: Histograms of randomly triggered readout with an Fe^{55} source at different voltages.

about 2000 Hz. Therefore it is advisable to use a weak Fe^{55} source. But using a week source in comparison to a strong source reduces the detection yield. In order to increase the detection yield, the detector should be readout out as fast as possible. Often the readout speed is limited by the data transfer rate to the readout computer. In our case it is limited by the data transfer rate of the EPP-box or the AMSWire PCI card. The amount of data can be significantly reduced, and the data throughput maximized, when using the data reduction in the DSP. Only the data of tubes showing a signal greater than 5 σ are transmitted. The theoretical readout limit is defined by the sequencing time, which is in our case about 80 μs or in other words 12.5 kHz.
To analyze the shape of the histograms, a Fermi function was fitted on the edge of maximum energy:

$$f(x) = \frac{A}{e^{(x-B)/C} + 1}, \tag{6.6}$$

where B is the point of inflexion and C describes the softness of the Fermi edge. From RWTH Aachen Monte Carlo studies [Kir00], it was found that the Fe^{55} peak energy position can be determined using the relation:

$$ADC_{cal} = B - 2.92 \cdot C + 0.007 \cdot C^2. \tag{6.7}$$

A similar result can be obtained when taking the point which corresponds to 90% of the Fermi function height:

$$ADC_{cal} = B - 2.2 \cdot C. \tag{6.8}$$

We take ±C as an upper error estimate in addition to the error coming from the pressure and temperature measurement. Figure 6.24 shows the determined ADC_{cal} edges over voltage and Figure 6.25 plots these values versus gas gain. From the slope, the calibration factor can be derived which defines the amount of ADC counts per keV. For this calculation the point at

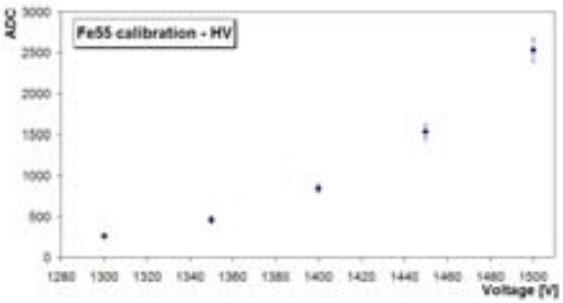

Figure 6.24: Randomly triggered readout with an Fe^{55} source at different voltages.

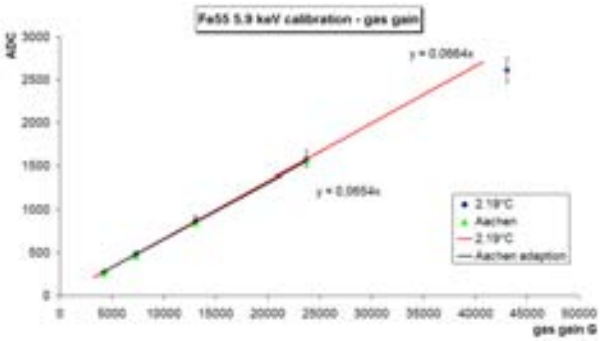

Figure 6.25: Randomly triggered readout with an Fe^{55} source at different gas gains.

highest gas gain was not considered, since it already touches the non-linear amplification of the Viking. The determined calibration factor normalized to the gas gain G = 1 is:

$$CAL = 11.3 \times 10^{-3} ADC/keV \tag{6.9}$$

Using this calibration factor it is possible to derive the most probable MIP energy deposition in one straw tube from the MPV cosmics data of the voltage scan in Section 6.2.4.

$$\Delta E^W = ADC^{MPV}/G/CAL \approx 0.623keV \pm 0.015keV \tag{6.10}$$

The theoretical energy deposition dE/dx of a MIP in a straw tube can be approximated by a layer of Argon (d=0.47 cm) gas with the same volume. Using the most probable energy loss dE/dx of Argon 1.2 keV/cm, the energy loss in this layer amounts to $\Delta E^W = 0.57\ keV$. This value lies close to the measured one, although it is slightly higher, which can be explained by the fact that cosmics do not consist entirely of MIPs, but also of higher energetic radiation.

6.3 DSP Programming on UDR2

Digital signal processing is a powerful technology, which is used in a broad range of engineering fields including communications, medical imaging, high fidelity music reproduction, radar & sonar, and geologic oil prospecting. In our scope, DSP is used for online data reduction and pedestal calibration to keep the amount of data to be transferred to the Earth as small as possible. This is accomplished by comparing the electronic channel offset, called the pedestal, to the channel content of one triggered event. A discrepancy indicates that a particle has deposited energy in a straw tube. It is only this information that is supposed to be used for further physics analysis and the contents of the remaining channels, which are identical to the pedestal, are discarded.

This section gives a short overview of the Analog Devices Digital Signal Processor (DSP 2187L) architecture and then describes the pedestal calibration and data reduction routines, written in assembler.

6.3.1 Analog Devices A2187L-DSP Architecture

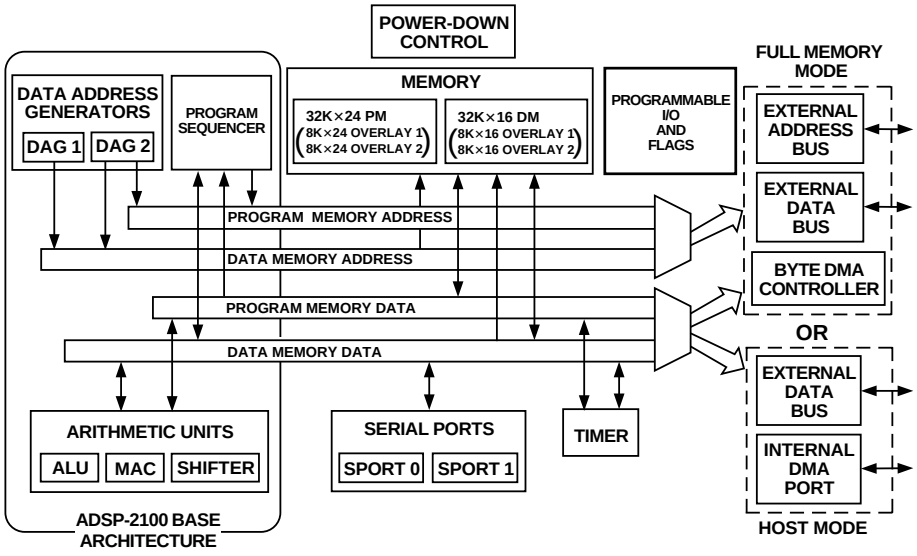

Figure 6.26: Functional block diagram of the Analog Devices DSP 2187L. From [Ana98]

Figure 6.26 illustrates the Analog Devices DSP 2187L functionality. The processor is composed of three independent computational units: an Arithmetic Logic Unit (ALU), a Multiplier/ACcumulator (MAC) and a Shifter unit. All three units have 16 bit inputs. The ALU is able to directly perform a standard set of arithmetic and logic computations with 16 bit result data. The MAC calculates multiply, multiply/add, multiply/subtract operations in a single cycle with a result of up to 40 bits. The shifter performs logical and arithmetic shifts with a 32 bit output field. The internal result bus interconnects all three computational units. In this way the output of any unit may be the input of any unit on the next operational cycle.
The processor features 32K of 24 bit program memory and 32K of 16 bit data memory. Two data address generators (DAGs) provide the means to simultaneously fetch two operands from data memory and program memory - a feature that is widely used in the data reduction code in order to save processing time. Each DAG maintains four address pointers, which are post-modified after each memory access, in the same processor cycle. All in all there are five internal buses: a program memory address bus, a program memory data bus, a data memory address bus, a data memory data bus and the above mentioned result bus.
With this flexible architecture the DSP can perform multiple operations in parallel. This is of special interest, when creating the data reduction code. The processing time to perform the data reduction of a single event directly defines the subdetector dead time. Therefore, the subdetector with the longest processing time defines the dead time of the whole experiment. Intelligent code creation by using the multifunction instructions can reduce this dead time significantly. The amount of channels play a major role in the data reduction processing time, since all routines have to loop over this number. Therefore it is clear that the subdetector with the most channels takes the longest dead time. In our case this is the tracker with 192 ladders $\times$ 1024 channels = 196608 channels, compared to the TRD with 82 UFE $\times$ 64 channels = 5248 channels. More information about further features of the AD DSP 2187L can be found in [Ana98] or in Section 5.2.5.

Arithmetic Logical Unit (ALU)

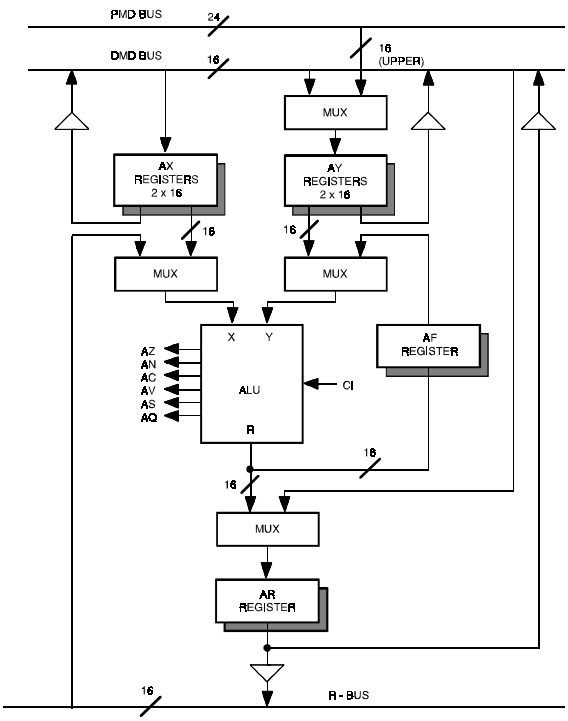

Figure 6.27: Arithmetic Logic Unit (ALU) of the Analog Devices DSP 2187L. From [Dev01].

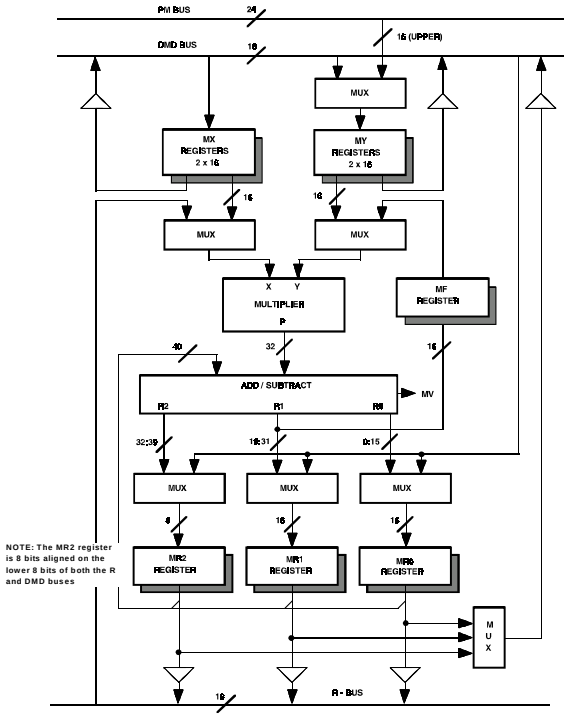

Figure 6.28: Multiplier Accumulator (MAC) unit of the Analog Devices DSP 2187L. From [Dev01].

Figure 6.27 describes the ALU composition. Two times two 16 bit registers AX[0..1] and AY[0..1] are available as operand inputs for the ALU. A 16 bit feedback register AF can be used to feed the ALU result back to its input. Otherwise the result is saved into the 16 bit result register AR, which is linked to the result bus (R-Bus). Six status signals define the status of the ALU after its last operation and a carry-in signal is available. Registers are read at the beginning of a processor clock cycle and written at the end of it. Therefore a register can serve as the input of one instruction and then can be updated at the end of the same cycle from the memory in a multifunction instruction.

Multiplier Accumulator (MAC)

Figure 6.28 shows the MAC composition. Two times two 16 bit registers MX[0..1] and MY[0..1] are available as operand inputs for the MAC. A multiplier and an add/subtract unit perform operations of the form MR = MR ± MX*MY. A feedback register MF feeds the result back to the input of the multiplier. Three output registers, two 16 bit registers MR0 and MR1 and an 8 bit register form the 40 bit output.

Barrel Shifter

The shifter unit is shown in Figure 6.29. The 16 bit shifter input register SI provides input to the shifter array and the exponent detector. The 8 bit shifter exponent register SE holds

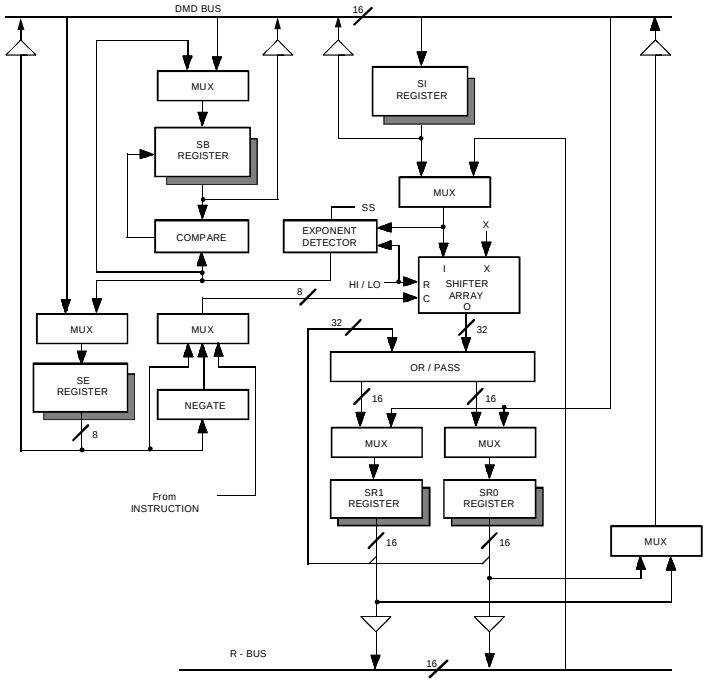

Figure 6.29: Shifter unit of the Analog Devices DSP 2187L. From [Dev01].

the exponent during normalize and denormalize operations; the 5 bit shifter block register SB holds the block exponent value and is used for block floating point operations. So far both are not used in calibration and data reduction code. The 32 bit result is saved in the two 16 bit output registers SR0 and SR1. Both registers are fed back to the OR/PASS logic.

6.3.2 Data Reduction

The data reduction code in its version 0.6 has the functionality described in the following points:

- *pedestal subtraction*
  Read the event from the raw event buffer and subtract the pedestals, which are calculated by the pedestal calculation routine and saved in program memory. Do this separately for the first Viking and the second Viking of each UFE, since this offers the opportunity to use a time-saving algorithm
  $$X_i = RAW_i - PED_i. \tag{6.11}$$

- *common mode correction*
  The common mode is separately calculated for each Viking
  $$CM = \frac{1}{32}\sum_{i=1}^{32} X_i. \tag{6.12}$$
  Then, correct the amplitudes of each Viking according to this information
  $$Y_i = X_i - CM. \tag{6.13}$$

- *hit identification*
  If the remaining amplitude fulfills the condition and the channel is not flagged noisy,

$$|Y_i| \geq 5 * \sigma_i, \tag{6.14}$$

  this amplitude together with the channel number information is saved, otherwise discarded.

The data reduction code v0.6 has a processing time of about 131μs maximum. In this version it is foreseen to save negative amplitudes, caused by very fast consecutive triggers, so that a previous particle is seen as negative trace. If one decides to discard this information, a further reduction of processing time can be achieved.
Furthermore, in one of the next versions, a feature will be included that checks for large amplitudes that could falsify the common mode calculation. The data reduction code v0.6 can be found in Appendix C.

6.3.3 Pedestal Calibration

The pedestal calibration code calculates the pedestal and the noise of each channel. This information is used later in the data reduction code. The calculation in version 0.6 is performed in the following steps:

- *pedestal calculation*
  The pedestal is the electronic offset of each channel. It has to be corrected for in order to recognize particle hits which add to this offset. The pedestal of each channel is calculated as the average over 512 samples according to the formula:

$$PED_i = \frac{1}{512} \sum_{j=1}^{512} RAW_i^j \tag{6.15}$$

- σ_{raw} *calculation*
  The σ_{raw} is a gaussian noise on each channel. It is calculated according to the formula:

$$\sigma_{raw\ i} = \sqrt{\overline{X_i^2} - \overline{X_i}^2} \tag{6.16}$$

  Averages are taken over 512 samples. A table is defined, which indicates dead or noisy channels. Therefore the averaged σ of each Viking chip is calculated according to

$$\overline{\sigma_{Viking}} = \frac{1}{32} \sum_{i=1}^{32} \sigma_i \tag{6.17}$$

  Dead or noisy channels are flagged according to the conditions:

$$X_{dead} < \frac{1}{4} \sigma_{Viking} \tag{6.18}$$

$$X_{noisy} > 3\sigma_{Viking} \tag{6.19}$$

- σ_{final} *calculation*
  This time a common mode correction is taken into account excluding flagged channels determined at the end of σ_{raw} calculation. Here a verification is made that no particle crossed the detector by chance and deposited energy:

$$|X_i| \geq 4 * \sigma_{raw\ i}. \tag{6.20}$$

  The first 16 channels of each Viking that pass these restrictions are used for the common mode calculation:

$$CM = \frac{1}{16}\sum_{i=1}^{16} X_i. \tag{6.21}$$

  This is used to correct the 32 amplitudes of the corresponding Viking:

$$Y_i = X_i - CM. \tag{6.22}$$

  Finally σ_{final} is calculated using averages over 512 samples:

$$\sigma_{final\ i} = \sqrt{\overline{Y_i^2} - \overline{Y_i}^2} \tag{6.23}$$

  For completeness the flag table is updated by calculating $\sigma_{Viking\ final}$

$$\overline{\sigma_{Viking\ final}} = \frac{1}{32}\sum_{i=1}^{32} \sigma_{final\ i} \tag{6.24}$$

  and using the restrictions:

$$Y_{dead} < \frac{1}{4}\sigma_{Viking\ final} \tag{6.25}$$

$$Y_{noisy} > 3\sigma_{Viking\ final} \tag{6.26}$$

The pedestal calibration code can be found in Appendix D.

Chapter 7

Summary

In the framework of this thesis the actions were taken to successfully develop, test and produce the AMS-02 TRD readout and slow control electronics and the associated mechanics.

The responsibility for the financial and organizational planning, especially concerning the time schedule, was taken. A close cooperation with the Italian company CAEN - a NASA certified company to build space-qualified electronics - was required to communicate the needs for a working space-qualified electronics system to be used in high energy physics. This information was used by the CAEN engineers to successfully design the electronics boards for the system. An attentive tracking of the engineer's work in the development of the design led to various changes and finally to a perfectly working system. The design is based on flexible, radiation hard Free Programmable Gate Arrays (FPGAs) used to control the data flow from the detector and to manage the slow control.
The data reduction code of the DSP in the main electronics board was written. The system proofed its functionality together with real detector modules in two testbeams, carried out in the 4th quarter of 2002 with engineering modules (EM) and in the 4th quarter of 2003 with qualification modules (QM1). The testbeams were prepared and the readout software had to be written. The results of the testbeam 2002 helped to verify that the Monte Carlo software Geant 3 is able to describe the performance of Parylene-C coated strawtubes well. In the testbeam 2003 for the first time each type of electronics board was present in the system and the electronics could proof its functionality as a whole.
To develop and produce the space-qualified mechanics of the U-crate housing the readout and slow control electronics and the UPD-box housing the power supply for the crate, close cooperation with MIT and the Italian company in charge CGS (Carlo Gavazzi Space) was essential. Under tight supervision the mechanics not only for the TRD but also for the tracker were produced at the IEKP mechanical workshop. Obscurities in the drawings were adjusted in co-operation with CGS.
To verify the qualification for space applications several thermo-vacuum tests and vibration tests were carried out on board level at RWTH Aachen and MPE Garching.
The overweight of the whole AMS-02 detector required a painstaking weight reduction program. The TRD electronics had to be reduced from 21 boards down to 16 boards in a smaller crate and from 9 DC/DC converters down to 7 in a smaller box. This required a substantial rethinking of the whole electronics and a new design of the backplane and the mechanics, which resulted in a development and production delay of at least 1.5 years.
Several bugs were found in the control sequences for the front end boards and on the electronics boards, which were corrected. After the confirmation that the produced prototypes were faultless and suitable for space applications the electronics design was transferred to CSIST, a semi-governmental institute in Taiwan with experience in the production of space-qualified electronics. Here the QM2 series production was done. Although the series production was

carried out by an external institute, still the verification that the produced electronics works properly had to be done by our institute.
To prepare this testing in Taiwan several test benches had to be designed and produced. The necessary software to execute the tests was written. Finally a three week scientific visit in Taiwan was done to verify the proper functionality of the hardware. Minor production problems were discovered and corrected on the spot.
In Europe the complete system could be assembled and tested. In the beginning of 2005 a cosmics stand was set up at the Universität Karlsruhe in order to perform long term tests and to verify the noise performance of the complete system composed of a fully assembled power supply box (UPD-Box) and a fully assembled readout electronics crate (U-Crate). The noise of the electronics channels could be confirmed to two ADC counts and a rough energy calibration with Ar/CO_2 (80/20) could be performed.
To simulate thermal properties of the whole system during a thermo-vacuum test scheduled in the end of 2005, a front-end simulator, consisting of dissipation resistors, a heat interface and a DAC-ADC feedback circuit were developed and produced. This front end simulator allows to simulate power consumption and data acquisition of the front ends.

With the successful accomplishment of the different development and production steps, referred to as engineering modules (EM) and qualification modules (QM), and the associated tests, namely functional tests including beamtests and cosmics data taking, vibration tests and thermo-vacuum tests, the outcome of this thesis is a fully working space-qualified DAQ electronics system for a transition radiation detector to be mounted on the International Space Station. This detector is able to achieve a proton rejection factor of 10^2 to 10^3 in the energy range between 5 and 300 GeV at a 90 % positron detection efficiency. Together with the AMS-02 electromagnetic calorimeter a proton rejection factor of 10^5 to 10^6 can be reached.

Acknowledgements

First of all I would like to thank Prof. Dr. Wim de Boer for the assignment to this interesting and challenging project. His confidence in my work and his encouraging advice made me passionately push for the advance of the TRD electronics system development. For taking over the Korreferat my thanks go to Prof. Dr. Thomas Müller, our institute leader.

My special thanks go to my doctorate companions Dr. Levin Jungermann, Dipl.-Phys. Hannes Bol, Dipl.-Phys. Mike Schmanau, Dr. Alexander Dierlamm, Dipl.-Phys. Christian Piasecki, and Dipl.-Phys. Alexander Furgeri who successfully worked with me during the last years. Together with them even the longest measurement shift was fun.

Certainly I do not want to forget our diploma students Dipl.-Phys. Martin Brückel, Dipl.-Phys. Andreas Sabellek and master student Dipl.-Ing.(FH) Rawi Eggert who significantly supported the development of the TRD electronics with their manpower. Thank you for joining me in running the thermo-vacuum tests, vibration tests and in the design of the various test benches.

As well, I would like to thank the staff of our institute. Dr. Hans-Jürgen Simonis for keeping the main computer system running reliably, Dr. Peter Blüm for his cooperation as team leader in the practical training for students and Dr. Frank Hartmann for his advices while I was writing this thesis. Tobias Barvich and Pia Steck for their technical support. Herr König and Herr Theel together with their excellent crew from the mechanical workshop for manufacturing the space-qualified mechanics for our electronics. Herr Atz and his crew from the electronics workshop for their assistance in time consuming cabling work. Frau Haas, Frau Fellner and Herr Fuchs for dealing with all the administrative obstacles. All other members of the Institut für Experimentelle Kernphysik, including Dr. Valery Zhukov and Dr. Eugene Grigoriev, for the nice atmosphere in the last years.

Furthermore, my thanks go to my collaboration colleagues at CERN, where I spent 1.5 years together with the MIT group around Dr. Mike Capell, Dr. Vladimir Koutsenko, Dr. Alexei Lebedev, Dr. Andrei Kounine and Dr. Xudong Cai. From their experience I profited most. For the nice collaboration I would like to say thank you to my colleagues from the tracker collaboration Dr. Giovanni Ambrosi, Dr. Eduardo Cortina and Dr. Daniel Haas.

From RWTH Aachen I would like to give special thanks to Dr. Georg Schwering for advising me in several decisions concerning TRD electronics, Dr. Chanhoon Chung for his productive collaboration.

A big thank you goes to my family, especially to my parents, for their love and support in all my years of education. Another one goes to my brother Felix who kept an eye on my company when I was busy with this thesis.

The most grateful I am to Nadine who was with me since the time I began to work at CERN. She experienced all my ups and downs in the last three years and stood by me in every situation. Without too many complaints she beard the numerous times when I was on business trips at CERN, Aachen, Taiwan or the US. I am sure, without her, the enthusiasm for my work would have suffered.

List of Figures

List of Tables

Bibliography

[A+02] M. Aguilar et al. The Alpha Magnetic Spectrometer (AMS) on the International Space Station: Part I results from the test flight on the space shuttle. *Physics Reports*, 366:331–405, 2002.

[Act05] Actel Corporation. *SX-A Family FPGAs v5.1*, February 2005. http://www.actel.com/documents/A54SXADS.pdf.

[Aer05] The Aerospace Corporation. *Single Event Effects Testing*, 5:00 pm, March 3nd, 2005. http://www.aero.org/capabilities/seet/primer.html.

[Alt04] Altera. *Altera Apex 20K data sheet*, March 2004. http://www.altera.com/literature/ds/apex.pdf.

[AMS05] AMS-02 collaboration. AMS on ISS, Construction of a particle physics detector on the International Space Station. to be published, 2005.

[AN05] National Aeronautics and Space Administration (NASA). *Space Station Assembly*, May 2005. http://spaceflight.nasa.gov/station/assembly/.

[Ana98] Analog Devices Inc. *DSP Microcomputer ADSP-2187L*, 1998. http://www.analog.com.

[Ana00] Analog Devices Inc. *AMD Am29LV004B CMOS 3.0 Volt-only Boot Sector Flash Memory*, November 2000. http://www.amd.com/us-en/assets/content_type/white_papers_and_tech_docs/21522.pdf.

[AR99] G. Ambrosi and D. Rapin. Protocol for the TDR (Tracker Data Reduction) to TFE (Tracker Front-end or Hybrid) connection. HCC (Hybrid Control Circuit) specifications. Technical report, University of Geneva, November 1999.

[Atk90] P. W. Atkins. *Physikalische Chemie*. VCH Verlagsgesellschaft GmbH, 1990. ISBN 3-527-25913-9.

[AYM75] X. Artru, G.B. Yodh, and G. Mennessier. Practical theory of the multilayered transition radiation detector. *Physical Review D*, 12(5):1289–1306, 1975.

[B+00] B. Blau et al. Status of AMS02 detectors and the superconducting magnet. *Grav. Cosmol. Suppl.*, 6:168–179, 2000.

[B+02] B. Blau et al. The superconducting magnet of AMS-02. *Nucl. Phys. Proc. Suppl.*, 113:125–132, 2002.

[B+03] M. Buénerd et al. The AMS-02 RICH Imager Prototype In-Beam Tests with 20 GeV/c per Nucleon Ions. In *28th International Cosmic Ray Conference (ICRC)*. Universal Academy Press Inc., 2003.

[B+04] B. Blau et al. The superconducting magnet system of the Alpha Magnetic Spectrometer AMS-02. *Nucl. Instrum. Meth.*, A518:139–142, 2004.

[Bat02] R. Battiston. Astroparticle Physics in Space with AMS-02. In *Talk at 1st Space Part Conference, Elba*, May 2002.
http://www.pg.infn.it/spacepart/presentazioni/presentazioni.html.

[BR93] W. Blum and L. Rolandi. *Particle Detection with Drift Chambers*. Springer Verlag, 1993.

[Brü03] M. Brückel. The Transition Radiation Detector of the AMS-02 Experiment - Development and test of Read-out Electronics. Master's thesis, Institut für Experimentelle Kernphysik, Universität Karlsruhe, 2003. IEKP-KA/2003-9.

[C+02] F. Cadoux et al. The AMS-02 electromagnetic calorimeter. *Nucl. Phys. Proc. Suppl.*, 113:159–165, 2002.

[C+03a] D. Casadei et al. The AMS-02 Time of Flight System. Final Design. In *28th International Cosmic Ray Conference (ICRC)*. Universal Academy Press Inc., 2003.

[C+03b] E. Cortina et al. The AMS-02 Tracker Performance. In *28th International Cosmic Ray Conference (ICRC)*. Universal Academy Press Inc., 2003.

[CAE04] Technical Information Manual Mod S9011. Technical report, CAEN, March 2004. Rev. 1.

[CAN05] CAN in Automation (CiA). *Can in Automation*, 20:40 pm, March 7nd, 2005.
http://www.can-cia.org/.

[Car03] Carso, Center for Advanced Research in Space Optics. *Carso brochure*, 2003.

[Car05] Carso, Center for Advanced Research in Space Optics. *Amica - Astro Mapper for Instrument Check of Attitude*, 5:40 pm, February 10th, 2005.
http://carso.area.trieste.it/.

[Cec03] C. Cecchi. The AMS-02 tracker. In *28th International Cosmic Ray Conference (ICRC)*. Universal Academy Press Inc., 2003.

[Cec04] C. Cecchi. The silicon tracker of the AMS02 experiment. *Nucl. Instrum. Meth.*, A518:145–146, 2004.

[Che78] M. L. Cherry. Measurements of the spectrum and energy dependence of x-ray transition radiation. *Physical Review D*, 17(9):2245–2260, 1978.

[CHMP74] M. L. Cherry, G. Hartmann, D. Müller, and T. A. Prince. Transition Radiation from relativistic electrons in periodic radiators. *Physical Review D*, 10(11):3594–3607, 1974.

[Chu05] C. Chung, 2004/2005. Information from Chanhoon Chung, RWTH Aachen.

[Cod04] IOWarrior. Technical report, Code Mercenaries, May 2004. V1.0.5.

[dB94] W. de Boer. Grand unified theories and supersymmetry in particle physics and cosmology. *Prog. Part. Nucl. Phys.*, 33:201–302, 1994.

[dB04] W. de Boer. Indirect evidence for WIMP annihilation from diffuse galactic gamma rays. 2004. arXiv.org astro-ph/0412620.

[dB05] W. de Boer. personal conversation, 2005.

[dBGK$^+$] W. de Boer, A.V. Gladyshev, D.I. Kazakov, M. Herold, C. Sander, and V. Zhukov. Dark matter not so dark: first evidence for Galactic gamma rays from dark matter annihilation. to be published.

[dBHSZ03] W. de Boer, M. Herold, C. Sander, and V. Zhukov. Indirect evidence for the supersymmetric nature of dark matter from the combined data on galactic positrons, antiprotons and gamma rays. 2003. arXiv.org hep-ph/0309029.

[dBHSZ04] W. de Boer, M. Herold, C. Sander, and V. Zhukov. Indirect evidence for neutralinos as dark matter. *Eur. Phys. J.*, C33:s981–s983, 2004. arXiv.org hep-ph/0312037.

[Dev01] Analog Devices. *ADSP-218x DSP Hardware Reference*. Analog Devices, Digital Signal Processor Division, One Technology Way, Norwoord, Mass, 02062-9106, February 2001.

[Div98] Mission Operations Directorate/Space Flight Training Division. International Space Station Familiarization. Technical Report NASA/TM-2001-211291, National Aeronautics and Space Administration (NASA), July 1998.

[Dol86] B. Dolgoshein. Transition radiation detectors and particle identification. *Nuclear Instruments and Methods in Physics Research A*, 252:137–144, 1986.

[Dol93] B. Dolgoshein. Transition radiation detectors. *Nuclear Instruments and Methods in Physics Research A*, 326:434–469, 1993.

[Egg04] R. Eggert. Development of a Fuse-Test Backplane for a Multi-Channel Power Supply (UPSFE) within the AMS Project. Master's thesis, Institut für Experimentelle Kernphysik, Universität Karlsruhe, 2004. IEKP-KA/2003-9.

[ESA00] V. Egorytchev, V. Saveliev, and S.J. Aplin. Particle identification via transition radiation and detectors. *Nuclear Instruments and Methods in Physics Research A*, 453:346–352, 2000.

[Eur00] European Cooperation for Space Standardization (ECSS). *SpaceWire - Links, Nodes, Routers and Networks*, November 2000. ECSS-E-50-12 Draft F(2).

[Fop04] S. Fopp. *Entwicklung und Bau eines auf Proportionalkammern basierenden Übergangsstrahlungsdetektors für das AMS-02-Weltraumexperiment.* PhD thesis, RWTH Aachen, 2004.

[G$^+$03] S. Gentile et al. The Performance of the Transition Radiation Detector of the AMS-02 Experiment. In *Nuclear Science Symposium, Portland, Oregon, USA*, 2003.

[Gar60] G. M. Garibyan. Transition radiation effects in particle energy losses. *Soviet Physics JETP*, 37(10)(2):372–376, 1960.

[Gar71] G. M. Garibyan. Contribution to the theory of formation of transition X-radiation in a stack of plates. *Soviet Physics JETP*, 33(1):23–29, 1971.

[Gil94] D. G. Gilmore, editor. *Satellite Thermal Control Handbook*, chapter Thermal Testing. The Aerospace Corporation, 1994.

[Gil97] K. Gilman. *A Random Vibration Primer - Part 1-3.* Lansmont, Monterey, CA93940, USA, 1996-1997. http://www.lansmont.com/NewsLetters/.

[Gil02] D. G. Gilmore. *Spacecraft Thermal Control Handbook.* The Aerospace Press, 2002.

[Gru93] C. Grupen. *Teilchendetektoren.* BI Wissenschaftsverlag, 1993. ISBN 3-411-16571-5.

[H+01] T. Hams et al. ^{10}Be/^{9}Be ratio up to 1.0 GeV/nucleon measured in the ISOMAX 98 balloon flight. In *Proc. of the 27th ICRC, Hamburg*, volume 5, page 1655, 2001.

[H+04] T. Hams et al. Measurement of the abundance of radioactive Be-10 and other light isotopes in cosmic radiation up to 2-GeV/nucleon with the balloon-borne instrument ISOMAX. *Astrophys. J.*, 611:892–905, 2004.

[Haa04] D. Haas. The Silicon Tracker of AMS02. *Nucl. Instrum. Meth.*, A530:173–177, 2004.

[Hau04] F. Hauler. The AMS-02 TRD for the International Space Station. *IEEE Trans. Nucl. Sci.*, 51:1365–1372, 2004.

[HZ+98] D. Haidt, P.M. Zerwas, et al. *The European Physical Journal C - Particles and Fields.* Springer, 1998.

[Ide00] VA32_HDR12. Technical report, Ideas ASA, Norway, December 2000.

[JKG96] G. Jungman, M. Kamionkowski, and K. Griest. Supersymmetric dark matter. *Phys. Rept.*, 267:195–373, 1996. hep-ph/9506380.

[Jun05] L. Jungermann. *Space Qualified Electronics for AMS02 and Medical Radiation Imaging.* PhD thesis, Institut für Experimentelle Kernphysik, Universität Karlsruhe, June 2005.

[K+01a] T. Kirn et al. The AMS-02 TRD - A detector designed for space. In *Workshop on advanced Transition Radiation Detectors for accelerator and space applications, Bari*, volume XXV, page 161. Frascati Physics Series, 2001.

[K+01b] T. Kirn et al. The AMS-02 TRD - A detector designed for space. In *Workshop on advanced Transition Radiation Detectors for accelerator and space applications, Bari*, volume XXV, page 161. Frascati Physics Series, 2001.

[K+04] T. Kirn et al. Status of the AMS-TRD-Straw Modules. *Nucl. Instrum. Methods.*, A522:69–72, 2004.

[Kar03] W. Karpinski. VA-Chip und UFE-Board Untersuchungen. internal note, 2003.

[Kir00] T. Kirn. Testbeam results. Talk, Johnston Space Center, Houston, 2000.

[Kir02] T. Kirn. Status of AMS TRD. Talk at Johnston Space Center, Houston, October 2002.

[KK05] A. Kounine and V. Koutsenko. AMS-2 DAQ software organisation, xDR and JINx nodes. internal note, October 2005.

[KS+04] T. Kirn, T. Siedenburg, et al. The AMS-02 Transition Radiation Detector. In *10th Vienna Conference on Instrumentation, Austria*, 2004.

[Lam03] G. Lamanna. Astroparticle Physics with AMS-02. In *28th International Cosmic Ray Conference (ICRC)*. Universal Academy Press Inc., 2003.

[Lin01] C.H. Lin. AMS-II DAQ Link Protocol Ver 3.0. internal note, January 2001.

[Lip00] M. Lippi. Specifiche Tecniche (SPT), HCC32 (bybrid Control Circuit). Technical Report TC/SPT/00-002.0, Aurelia Microelectronics and CAEN, November 2000.

[M+03] B. Monreal et al. Gas Slow Control System for AMS-02 Transition Radiation Detector on ISS. Poster, presented on the Nuclear Science Symposium, Portland, Oregon, USA, 2003.

[Max00] Max890L, High-Side P-Channel Switch with Thermal Shutdown. Technical report, Maxim Integrated Products, USA, 2000.

[ME-05] ME-Messsysteme GmbH, 16761 Henningsdorf, Germany. *Grundlagen zum CAN Bus*, 12:00 pm, March 6th, 2005. http://www.me-systeme.de/canbus.html.

[Moo02] A. A. Mooty. Attached Payloads Accommodation Handbook. International Space Station Program. Technical report, National Aeronautics and Space Administration (NASA), September 2002.

[Mul96a] D. R. Mulville. Payload Test Requirements. Technical Report NASA-STD-7002, National Aeronautics and Space Administration (NASA), USA, July 1996. http://klabs.org/DEI/References/design_guidelines/content/nasa_specs/7002.pdf.

[Mul96b] D. R. Mulville. Payload Vibroacoustic Test Criteria. Technical Report NASA-STD-7001, National Aeronautics and Space Administration (NASA), USA, June 1996. http://klabs.org/DEI/References/design_guidelines/content/nasa_specs/7001.pdf.

[Nat88] National Aeronautics and Space Administration (NASA). *NSTS 1988 News Reference Manual*, 1988. http://science.ksc.nasa.gov/shuttle/technology/sts-newsref/.

[Nat05a] National Aeronautics and Space Administration (NASA), Goddard Space Flight Center. *Introduction to Liquid Helium in Space*, May 2005. http://cryowwwebber.gsfc.nasa.gov/introduction/helium_space.html.

[Nat05b] National Aeronautics and Space Administration (NASA), Goddard Space Flight Center. *Radiation Effects and Analysis*, 5:00 pm, March 3th, 2005. http://radhome.gsfc.nasa.gov/top.htm.

[Orb03] J. Orboeck. *The final 20-Layer-Prototype for the AMS Transition Radiation Detector: Beamtests, Data-Analysis, MC-Studies*. PhD thesis, RWTH Aachen, 2003.

[Per03] D. Perkins. *Particle Astrophysics*. Oxford University Press, 2003.

[Rob91] Robert Bosch GmbH. *CAN Specification Version 2.0*, September 1991.

[S+02] T. Siedenburg et al. A Transition Radiation Detector For AMS. *Nucl. Phys. Proc. Suppl.*, 113:154–158, 2002.

[S+03] D. N. Spergel et al. First Year Wilkinson Microwave Anisotropy Probe (WMAP) Observations: Determination of Cosmological Parameters. *Astrophys. J. Suppl.*, 148:175, 2003.

[Sav03] C. J. Savage. *Spacecraft Systems Engineering*, chapter Thermal Control of Spacecraft. Wiley, 2003.

[Sci05] Science Directorate Marshall Space Flight Center. *Solar Physics*, 5:00 pm, March 2nd, 2005. http://science.msfc.nasa.gov/ssl/pad/solar/default.htm.

[She01] Ronald Cintra Shellard. Cosmic Accelerators and Terrestrial Detectors. *Brazilian Journal of Physics*, 31(2), June 2001.

[Sta03] J. P. W. Stark. The Spacecraft Environment and its effect on design. In *Spacecraft Systems Engineering*. Wiley, 2003.

[TM61] M. L. Ter-Mikaelyan. Emission of fast particles in a heterogeneous medium. *Nuclear Physics*, 24:43–61, 1961.

[Wik05a] Wikimedia Foundation Inc. *Wikipedia, The Free Encyclopedia*, 4:40 pm, January 27th, 2005. http://en.wikipedia.org/wiki/Space_shuttle_program.

[Wik05b] Wikimedia Foundation Inc. *Wikipedia, The Free Encyclopedia*, 5:00 pm, January 31st, 2005. http://en.wikipedia.org/wiki/International_Space_Station.

[WPM+04] S.P. Wakely, S. Plewnia, D. Müller, J.R. Hörandel, and F. Gahbauer. Transition radiation detectors for energy measurements at high Lorentz factors. *Nuclear Instruments and Methods in Physics Research A*, 531:435–444, 2004.

Index

Glossary

A

ACC AntiCoincidence Counter, subdetector of AMS-02.

ACOP AMS Crew Operations Post, placed in the ISS to record AMS-02 data.

ADC Analog Digital Converter.

ALICE A Large Ion Collider Experiment, experiment at CERN.

Alodine Alodine 1200, surface treatment process, according to MIL-C-5541 Class 3.

ALU Arithmetic and Logic Unit.

AMS-02 Alpha Magnetic Spectrometer 02.

Anodizing Clear Anodizing, surface treatment process, according to MIL-A-8625 Type II Class 1.

AOA Abort Once Around, Space Shuttle abort mode.

APD Avalanche Photo Diode, technology used for trigger layer C in cosmics test stand.

ASI Agenzia Spaziale Italiana.

ASIC Application-Specific Integrated Circuit.

AST AMICA Star Tracker, subsystem of AMS-02.

ATLAS ATLAS, A Toroidal LHC ApparatuS, experiment at CERN.

ATO Abort To Orbit, Space Shuttle abort mode.

ATV Autonomous Transfer Vehicle.

B

BDMA Byte Memory Direct Memory Access.

BESS Balloon-borne Experiment with a Superconducting Spectrometer.

BOM Bill of Material, part of electronics production files.

C

CAEN company in Viareggio, Italy, which is specialized on high energy physics electronics, microelectronics and aerospace electronics.

CAN Controller Area Network.

CAPRICE The Cosmic Anti Particle Ring Imaging Cherenkov Experiment.

CCD Charge Coupled Device.

CDDC Command Distributor and Data Concentrator on JINF/JINFv2 board and higher DAQ nodes.

CDP Common Digital Part, on UDR2 board.

CGRO Compton Gamma Ray Observatory.

CGS Carlo-Gavazzi-Space, Milano, Italy.

CMOS Complementary Metal Oxide Semiconductor.

CMS Compact Muon Solenoid, experiment at CERN.

COBE Cosmic Background Explorer.

CRC Cyclic Redundancy Check.

CSA/ASC Canadian Space Agency.

CSIST Chung-Shan Institute of Science and Technology, Taiwan.

D

DAC Digital Analog Converter.

DAG Data Address Generator, functional part of the DSP 2187L.

DAQ Data Acquistion.

DDP Detector Dependent Part, on UDR2 board.

DM Dark Matter.

DMA Dark Matter Annihilation.

DRAM Dynamic Random Access Memory.

DSP Digital Signal Processor.

E

ECAL Electromagnetic Calorimeter, subdetector of AMS-02.

EGRET Energetic Gamma Ray Emission Telescope.

EM Engineering Modules.

EMC Electromagnetic Compatibility.

EMI Electromagnetic Interference.

EMU Extravehicular Mobility Unit, US spacesuit on the ISS.

EPP Enhanced Parallel Port.

ESA European Space Agency.

ESS Environmental Stress Screening on board level.

EVA Extravehicular Activity.

F

FCS Frame Check Sequence.

FM Flight Modules.

FPGA Field Programmable Array.

FS Flight Spares.

FT Functional Tests.

G

Gerber Files part of electronics production files, which describes the PCB layout.

GPS Global Positioning System.

GUI Graphical User Interface.

H

HCC Hybrid Control Circuit.

HEAT High Energy Antimatter Telescope.

HERA-B large-aperture high-rate spectrometer in the proton-electron accelerator HERA (Hadron Elektron Ring Anlage) at DESY in Hamburg.

HRDL High Rate Data Link.

HV High Voltage.

I

IAS Internal Audio Subsystem, ISS.

IMAX Isotope Matter Antimatter Experiment.

IRAS Infrared Astronomical Satellite.

ISO Infrared Space Observatory.

ISOMAX Isotope Magnetic Experiment.

ISS International Space Station.

J

JAXA Aerospace Exploration Space Agency, Japan.

JINF link to higher DAQ.

JINFv2 link to higher DAQ version 2.

JMDC J Main DAQ Computer.

JTAG Joint Test Action Group.

K

KASCADE KArlsruhe Shower Core and Array DEtector.

L

LED Light Emitting Diode.

LET Linear Energy Transfer.

LHC Large Hadron Collider, collider at CERN.

LRDL Low Rate Data Link.

LVDS Low Voltage Differential Signal.

M

MAC Multiplier, Accumulator.

MIP Minimum Ionizing Particle.

MIPS Million Instruction per Second.

MLI MultiLayer Insulation.

MLVDS Multipoint Low Voltage Differential Signal.

MOSFET Metal Oxide Semiconductor Field Effect Transistor.

MPLM Multi-Purpose Logistics Module, transportation module for the Space Shuttle built by ASI.

MPS Main Propulsion System, Space Shuttle.

MPV Most Probable Value, determined by a Landau fit.

MWPC Multi Wire Proportional Chamber.

N

NASA National Aeronautics and Space Administration, USA.

NIM Nuclear Instrumentation Module.

O

OMS Orbital Maneuvering System, Space Shuttle.

P

PAMELA a Payload for Antimatter Matter Exploration and Light-nuclei Astrophysics.

PCA Printed Circuit Assembly.

PCB Printed Circuit Board.

PDS Power Distribution System.

PLD Programmable Logic Device.

PMT PhotoMultiplier Tube.

Q

QM1 Qualification Modules 1.

QM2 Qualification Modules 2.

R

RCS Reaction Control System, Space Shuttle.

RICH Ring Imaging Cherenkov Counter, subdetector of AMS-02.

ROM Read Only Memory.

RTLS Return to Launch Site, Space Shuttle abort mode.

S

S9011AU DC/DC controller board in UPD-Box.

S9011AUv2 DC/DC controller board version 2 in UPD-Box.

S9011B Filter board in UPD-Box.

S9048 ±2.8 V DC/DC converter.

S9053U dioded +3.4 V DC/DC converter.

S9054 +5.2 V DC/DC converter, dedicated to USCMs, obsolete in U-Crate.

S9056 +120 V/+5.2 V DC/DC converter.

SEB Single Event Burnout.

SEE Single Event Effect.

SEL Single Event Latchup.

SEU Single Event Upset.

Shifter unit that moves data in an output field to the right or to the left, functional part of the DSP 2187L.

SHOOT Superfluid Helium On-Orbit Transfer, experiment as part of the space shuttle STS-57 mission in June, 1993.

SRAM Static Random Access Memory.

SSF Solid State Fuse, protection on U-Crate boards against destructive SELs.

T

TAL Transatlantic Landing, Space Shuttle abort mode.

TID Total Ionizing Dose.

TOF Time Of Flight, subdetector of AMS-02.

TRD Transition Radiation Detector, subdetector of AMS-02.

TVT Thermo-Vacuum-Test, space qualification test.

U

UBP U BackPlane.

UBPv2 U BackPlane version 2.

UDR2 U Data Reduction Board 2, 2 indicates that actually two redundant UDRs are placed on one board.

UFE U Front End Board.

UFS U Front End Simulator.

UHF Ultrahigh Frequency Subsystem, ISS.

UHVD U High Voltage Distributor.

UHVG U High Voltage Generator.

UPD-Box U Power Distribution Box.

UPSFE U Power Supply For Front End board.

UPSFEv2 U Power Supply For Front End board version 2.

USB Universal Serial Bus.

USS Unique Support Structure.

V

VDS Video Distribution Subsystem, ISS.

VT Vibrational Tests.

W

WIMP Weakly Interacting Massive Particle.

WMAP Wilkinson Microwave Anisotropy Probe.